

7. TAG-1 AREA¹

Shipboard Scientific Party²

HOLE 957C

Date occupied: 1 October 1994
Date departed: 14 October 1994
Time on hole: 4 days, 12 hr
Position: 26°8.226'N, 44°49.555'W
Bottom felt (drill-pipe measurement from rig floor, m): 3648.0
Distance between rig floor and sea level (m): 11.38
Water depth (drill-pipe measurement from sea level, m): 3636.6
Total depth (from rig floor, m): 3697.2
Penetration (m): 49.2
Number of cores (including cores having no recovery): 6
Total length of cored section (m): 49.2
Total core recovered (m): 21.88
Core recovery (%): 44.1
Hard rock:
 Depth (mbsf): 49.2
 Nature: Massive sulfide and sulfide-anhydrite breccias
Comments: HRB relocated from Hole 957B. Wash Cores 4W, 6W, and 8W

HOLE 957D

Date occupied: 14 October 1994
Date departed: 15 October 1994
Time on hole: 1 day, 9 hr, 45 min
Position: 26°8.220'N, 44°49.562'W
Bottom felt (drill-pipe measurement from rig floor, m): 3648.5
Distance between rig floor and sea level (m): 11.54
Water depth (drill-pipe measurement from sea level, m): 3637.0
Total depth (from rig floor, m): 3677.9
Penetration (m): 29.4
Number of cores (including cores having no recovery): 0
Total length of cored section (m): 0.0
Total core recovered (m): 0.0
Core recovery (%): 0
Comments: Drilling only from 0.0 to 29.4 mbsf; no cores recovered

HOLE 957E

Date occupied: 15 October 1994
Date departed: 27 October 1994
Time on hole: 10 days, 6 hr, 30 min
Position: 26°8.219'N, 44°49.560'W
Bottom felt (drill-pipe measurement from rig floor, m): 3646.0
Distance between rig floor and sea level (m): 11.51
Water depth (drill-pipe measurement from sea level, m): 3634.5
Total depth (from rig floor, m): 3771.7
Penetration (m): 125.7
Number of cores (including cores having no recovery): 18
Total length of cored section (m): 94.2
Total core recovered (m): 4.03
Core recovery (%): 4.3
Hard rock:
 Depth (mbsf): 125.7
 Nature: Massive sulfide breccias and hydrothermally altered basalts
Comments: Drilled without coring to 31.5 mbsf; first hole occupation: 2230 hr, 15 October 1994, to 1415 hr, 20 October 1994 (4 days, 6 hr, 30 min); second hole occupation (after Holes 957F and 957G): 0700 hr, 22 October 1994, to 2145 hr, 27 October 1994 (5 days, 14 hr, 45 min)

HOLE 957F

Date occupied: 20 October 1994
Date departed: 21 October 1994
Time on hole: 14 hr, 45 min
Position: 26°8.212'N, 44°49.564'W
Bottom felt (drill-pipe measurement from rig floor, m): 3648.6
Distance between rig floor and sea level (m): 11.54
Water depth (drill-pipe measurement from sea level, m): 3637.1
Total depth (from rig floor, m): 3658.6
Penetration (m): 10.0
Number of cores (including cores having no recovery): 2
Total length of cored section (m): 9.0
Total core recovered (m): 0.95
Core recovery (%): 10.5
Hard rock:
 Depth (mbsf): 10.0
 Nature: Massive granular sulfide and nodular pyrite-anhydrite breccia
Comments: Bit penetrated 1.0 m into the seafloor when set down

¹Humphris, S.E., Herzig, P.M., Miller, D.J., et al., 1996. *Proc. ODP, Init. Repts.*, 158: College Station, TX (Ocean Drilling Program).

²Shipboard Scientific Party is given in the list preceding the Table of Contents.

HOLE 957G**Date occupied:** 21 October 1994**Date departed:** 22 October 1994**Time on hole:** 1 day, 2 hr**Position:** 26°8.213'N, 44°49.558'W**Bottom felt (drill-pipe measurement from rig floor, m):** 3646.0**Distance between rig floor and sea level (m):** 11.57**Water depth (drill-pipe measurement from sea level, m):** 3634.4**Total depth (from rig floor, m):** 3671.0**Penetration (m):** 25.0**Number of cores (including cores having no recovery):** 3**Total length of cored section (m):** 13.0**Total core recovered (m):** 1.12**Core recovery (%):** 8.6**Hard rock:**

Depth (mbsf): 25.0

Nature: Massive granular pyrite, and massive-nodular pyrite-anhydrite breccia

Comments: Drilled from 0 to 12 mbsf**HOLE 957L****Date occupied:** 2 November 1994**Date departed:** 8 November 1994**Time on hole:** 5 days, 18 hr, 30 min**Position:** 26°8.215'N, 44°49.565'W**Bottom felt (drill-pipe measurement from rig floor, m):** 3711.6**Distance between rig floor and sea level (m):** 11.69**Water depth (drill-pipe measurement from sea level, m):** 3699.9**Total depth (from rig floor, m):** 3778.2**Penetration (m):** 66.6**Comments:** Attempts to set a reentry cone with casing terminated (bad hole)**Principal results:** Holes 957C, 957E, 957F, and 957G are located on the upper terrace of the TAG active hydrothermal mound approximately 20 m southeast of the Black Smoker Complex. The objective of drilling at this location was to recover a stratigraphic section of hydrothermal deposits and underlying stockwork beneath the most active part of the mound.

The two most complete sections through the mound were cored in Holes 957C (from 10 to 49 mbsf) and 957E (from 30 to 125 mbsf), with recoveries of 44% and 4%, respectively. The upper part of the section was cored in Hole 957F (from the surface to a depth of about 8 mbsf, with recovery of 10.5%) and in Hole 957G (from 12 to 22 mbsf, with recovery of 8.5%). Holes 957D and 957L were also drilled in this area but with no recovery.

Because all the holes are within 10–15 m of each other, their stratigraphy is considered together to form a composite section through the hydrothermal mound and into the upper portions of the stockwork zone. Based on recovery from Holes 957F and 957G, the upper few meters of core contain fragments of massive granular pyrite and chalcopyrite, which likely represent near-surface hydrothermal precipitates derived from sulfide crusts and chimney talus. From the surface to a depth of 15 m, the mound consists dominantly of porous to granular pyrite ± chalcopyrite and pyrite breccias. The pyrite breccias appear to be partly derived from this sulfide crust material and from pieces of black smoker chimneys. From 15 to 30

mbsf, there is a zone of pyrite-anhydrite-rich breccias, which grades into pyrite-silica-anhydrite breccias that extend down to about 45 mbsf. These make up the bulk of the anhydrite-rich zone. Altered basalt clasts are first encountered at about 20 mbsf and become increasingly common below about 30 mbsf. Abundant quartz-pyrite mineralization and quartz veining immediately beneath the anhydrite-rich zone represent the top of the stockwork, suggesting that the thickness of the mound in this area is about 30 m. A quartz-rich zone composed mainly of pyrite-silica breccias near the top and silicified wallrock breccias toward the bottom occurs between 45 and 100 mbsf. This quartz-rich zone grades downward into a chloritic stockwork below about 100 mbsf, and chloritized and weakly mineralized basalt is the dominant lithology to the maximum depth cored (125 mbsf). The transitions between zones are gradational, and some lithologies at depth within the section also occur as clasts higher up in the stratigraphy.

Anhydrite veining is abundant throughout the vertical extent of the section, but it is best developed in the pyrite-anhydrite and pyrite-silica breccias (15–50 mbsf), where veins up to 45 cm in width are present. These veins comprise complex, multistage fracture fillings and cavity linings, some of which include disseminated, fine-grained pyrite and chalcopyrite, and trace amounts of hematite. The occurrence and size of veins decrease downward and correspond to an increase in the amount of quartz cement. The abundance of veining, brecciation, and quartz cementation, and the presence of widespread silicified and chloritized basalt clasts below about 30 mbsf, indicate that Holes 957C and 957E intersected a portion of the main subseafloor stockwork.

Most of the sulfides occur in the upper part of the section, with pyrite making up 50–80 vol% of the rock down to about 30 mbsf. Large ranges in the chemical compositions of different rock types reflect the extreme heterogeneity of the samples and the variable proportions of sulfides, anhydrite, and silica. The Fe contents of the samples range from 20.1 to 40.8 wt% and reflect the dominance of pyrite in the sulfide section. Cu contents are significantly lower, ranging from 0.01 to 6.0 wt%, and Zn concentrations are also generally low (<700 ppm). The most striking feature of the sulfides in the TAG-1 area is their very low concentrations of Pb, Ag, and Cd, which are close to their detection limits.

Apart from the massive granular pyrite and chalcopyrite that occur in the upper 5 m of the section, pyrite breccias dominate the lithology between 15 and 45 mbsf. The different types—massive pyrite breccia, pyrite-anhydrite breccia, and pyrite-silica-anhydrite breccia—are distinguished primarily on the basis of the relative abundances of pyrite, anhydrite, and silica. Massive pyrite breccia (from 0 to 15 mbsf) contains >75% pyrite and is largely clast supported. These breccias, some of which are nodular, consist of subrounded clasts of massive, granular pyrite in a porous, sandy pyrite matrix that is cemented by anhydrite (<25% of the rock by volume). Clastic material in these breccias resembles porous and granular massive pyrite found in the sulfide talus from the surface of the mound. These massive pyrite breccias grade downsection into matrix-supported pyrite-anhydrite breccias that dominate the lithology between 15 and 30 mbsf. These breccias typically consist of rounded pyrite clasts in a matrix of semi-massive anhydrite (>25% of the rock by volume). The clasts (ranging in size from 0.5 to 2 cm) are composed of massive granular pyrite, but siliceous clasts, quartz-pyrite clasts, and altered basalt fragments become increasingly common with depth.

Pyrite-silica-anhydrite breccias occur at the base of the anhydrite-rich zone and are intermediate in character between pyrite-anhydrite breccias above and pyrite-silica breccias below. The subangular to subrounded clasts, consisting of siliceous pyritic material, quartz-pyrite aggregates, and massive granular pyrite, are cemented mainly by quartz, with most of the anhydrite related to crosscutting anhydrite veins. The quartz appears dark gray because of inclusions of abundant, fine-grained disseminated pyrite. This matrix is also commonly brecciated and veined by a later generation of quartz and anhydrite, forming larger breccia fragments of up to 10 cm in size.

As the amount of anhydrite veining decreases, pyrite-silica breccias become the dominant lithology. These consist of large (up to 10 cm) fragments of fine-grained, gray siliceous material and smaller fragments of

quartz-pyrite set in a matrix of very fine-grained quartz. The gray siliceous clasts appear to be fragments of preexisting mineralized and silicified wallrock similar to that occurring deeper in the section; these clasts, however, generally have more diffuse boundaries and are partially replaced by the quartz matrix.

The silicified wallrock breccias differ from the overlying pyrite-silica breccias in that they are dominantly clast supported and contain significantly less pyrite. They consist of angular siliceous clasts, 1–5 cm in size, veined and cemented by white to gray quartz and pyrite. The clasts are hard, silicified basalt fragments that are identical to the isolated silicified basalt clasts that occur higher in the stratigraphic column. They are totally recrystallized to quartz, pyrite, and clay; locally, they contain relict igneous textures with plagioclase microlites being replaced by quartz \pm a tan to brown phyllosilicate (as yet unidentified), and groundmass being replaced by the same clay and fine-grained, disseminated pyrite and quartz. Vesicles are filled by clay, pyrite, and quartz.

Below about 100 mbsf, this quartz-rich zone grades downward into a chloritic stockwork where chloritized and weakly mineralized basalt is the dominant lithology. The rocks range from gray chloritized basalt breccias to gray plus green chloritized basalt breccias below 111 mbsf. The gray chloritized basalt breccias consist of 1- to 5-cm clasts of altered basalt in a fine-grained matrix of intergrown, white to gray quartz and pyrite. The chloritized basalt clasts are softer and less silicified than those in the overlying silicified wallrock breccias. Plagioclase microlites are replaced mainly by chlorite(?) and to a lesser extent by quartz. The basalt groundmass is replaced by chlorite(?); locally, however, feathery groundmass clinopyroxenes are replaced by orange Fe-oxides or oxyhydroxides plus chlorite(?). In many cases, the margins of altered basalt clasts are rimmed by 1- to 4-mm-wide zones of pyrite and, locally, chalcopyrite.

Altered clasts in the green chloritized basalt breccias are pervasively altered to chlorite + pyrite + quartz. Plagioclase microlites and microphenocrysts are replaced by quartz, brown chlorite(?), and pyrite; rare olivine microphenocrysts are replaced by orange Fe-oxides or oxyhydroxides and quartz. Fine-grained interstitial material is replaced by brown chlorite(?) and quartz. Pyrite is abundant as disseminated grains and as a replacement of plagioclase; quartz commonly surrounds many of the pyrite grains and aggregates.

Veins of pyrite, quartz, and quartz + pyrite commonly cut the basalt clasts and appear to follow a sequence, from early pyrite and quartz + pyrite veins, to later quartz veins that cut the earlier veins. Many pieces have 1- to 3-mm coatings of anhydrite on broken surfaces, which may represent remnants of anhydrite veins that were lost during coring. The anhydrite veins appear to be relatively late, cutting other vein types or as the last mineral to form at the center of sulfide veins.

The physical properties of sulfide samples from the TAG-1 area are typical for this type of material and yielded bulk densities that range from 2.85 to 4.51 g/cm³ and porosities from 2.4% to 16.2%. Compressional (*P*-wave) velocities are generally high (4.85–5.66 km/s), and electrical resistivities are low (0.11–2.01 Ω m). Thermal conductivities generally range from 5.7 to 8.7 W/(m·K). In contrast, anhydrite samples have lower bulk density (2.79 and 2.85 g/cm³) and thermal conductivity (5.4 W/(m·K)) values and distinctly higher electrical resistivity (2.77 Ω m) values than the sulfides, but porosity values (4.9% and 9.6%) are similar.

Paleomagnetic measurements indicate that cores recovered from the upper part of the section (0–25 mbsf) have a low intensity of natural remnant magnetization, whereas those from depths of 30–35 mbsf have a stable component of magnetization consistent with the location of the TAG mound. Preliminary data from unblocking temperatures and coercivity determinations suggest that maghemite is the most likely magnetic carrier in these rocks.

Fluid sampling in Hole 957C indicates that borehole fluids are dominated by surface seawater introduced during the drilling processes; no evidence exists for the upflow of hydrothermal fluids. However, elevated concentrations of magnesium, calcium, and sulfate in the sample suggested that dissolution of calcium and magnesium sulfate solids may be occurring. This is most likely an artifact of the drilling process, but it could also be the result of an ongoing process in the mound.

STRATIGRAPHY

Introduction

Holes 957C, 957E, 957F, and 957G, in the TAG-1 area, are located on the upper terrace of the mound, within about 10 m of each other and approximately 20–30 m southeast of the Black Smoker Complex. Holes 957D and 957L were also drilled in this area, but they had no recovery. The holes were drilled from a depth of 3647 m and penetrated to a maximum depth of 125 mbsf. The two most complete sections of stratigraphy through the mound were cored in Holes 957C (10–49 mbsf) and 957E (30–125 mbsf), with recovery of 44% and 4%, respectively. The upper part of the section was cored in Hole 957F from the surface of the mound to a depth of approximately 8 mbsf, and in Hole 957G from 12 to 22 mbsf. Graphic logs of the most complete core sections are shown in Figure 1, and Table 1 lists the different rock types and their distribution in each core. For more detailed descriptions of the rock types encountered in the TAG-1 area, see the “Sulfide Petrology and Geochemistry” section (this chapter).

Distribution of Lithologies

From the surface to a depth of 15 m, the mound consists predominantly of massive pyrite and pyrite breccias. A zone of pyrite-anhydrite breccias occurs from 15 to 30 mbsf, and pyrite-silica breccias with abundant anhydrite veining occur between 30 and 45 mbsf. A quartz-rich zone composed mainly of pyrite-silica breccias and silicified wallrock breccias occurs between 45 and 100 mbsf, and chloritized basalt breccias occur below 100 mbsf. The transitions from one zone to another are gradational, and some lithologies at depth within the mound may also occur as clasts or unreplaced remnants higher up in the stratigraphy. The abundance of anhydrite veining, brecciation, and quartz cementation, and the presence of widespread silicified and chloritized basalt clasts below about 30 mbsf suggests that Holes 957C and 957E intersected a portion of the main seafloor stockwork.

The first few meters of core recovered from the surface of the mound (Core 158-957F-1N) contain fragments of massive granular pyrite and chalcopyrite, which likely represent near-surface hydrothermal precipitates derived from sulfide crusts or chimney talus. Massive pyrite breccias and pyrite-anhydrite breccias with sandy pyrite in the matrix are the dominant lithologies to a depth of about 15 mbsf. Although recovery of core from Hole 957C was poor in this interval, small pieces of massive pyrite were cored in Section 158-957C-4W-1 at about 10 mbsf. These samples are likely fragments of the same pyrite breccias recovered in Core 158-957G-1N and resemble parts of the massive pyrite section between 1 and 5 mbsf in Cores 158-957F-1N and 2N. Below 15 mbsf, anhydrite- and quartz-cemented breccias are the dominant lithologies and include nodular pyrite-anhydrite breccias and nodular, siliceous pyrite-anhydrite breccias. These rocks are matrix supported and make up the bulk of the anhydrite-rich zone. Altered basalt clasts were first encountered at about 20 mbsf (Core 158-957C-7N and Cores 158-957G-2N and 3N) and are increasingly common below the anhydrite-rich zone. Abundant quartz-pyrite mineralization and quartz veining immediately beneath the anhydrite-rich zone represent the top of the stockwork, suggesting that the thickness of the mound in the TAG-1 area is about 30 m. The quartz stockwork extends for about 70 m below the anhydrite-rich zone; it consists of pyrite-silica breccias near the top and silicified wallrock breccias toward the bottom. This zone grades downward into a chloritic stockwork below about 100 mbsf, and chloritized and weakly mineralized basalt is the dominant lithology to the maximum depth cored (125 mbsf). This chloritic zone grades from gray to gray plus green rocks below 111 mbsf, and may be part of a broader alteration envelope that extends up the flank of the quartz stockwork (see “Stratigraphy” section, Chapter 8, this volume).

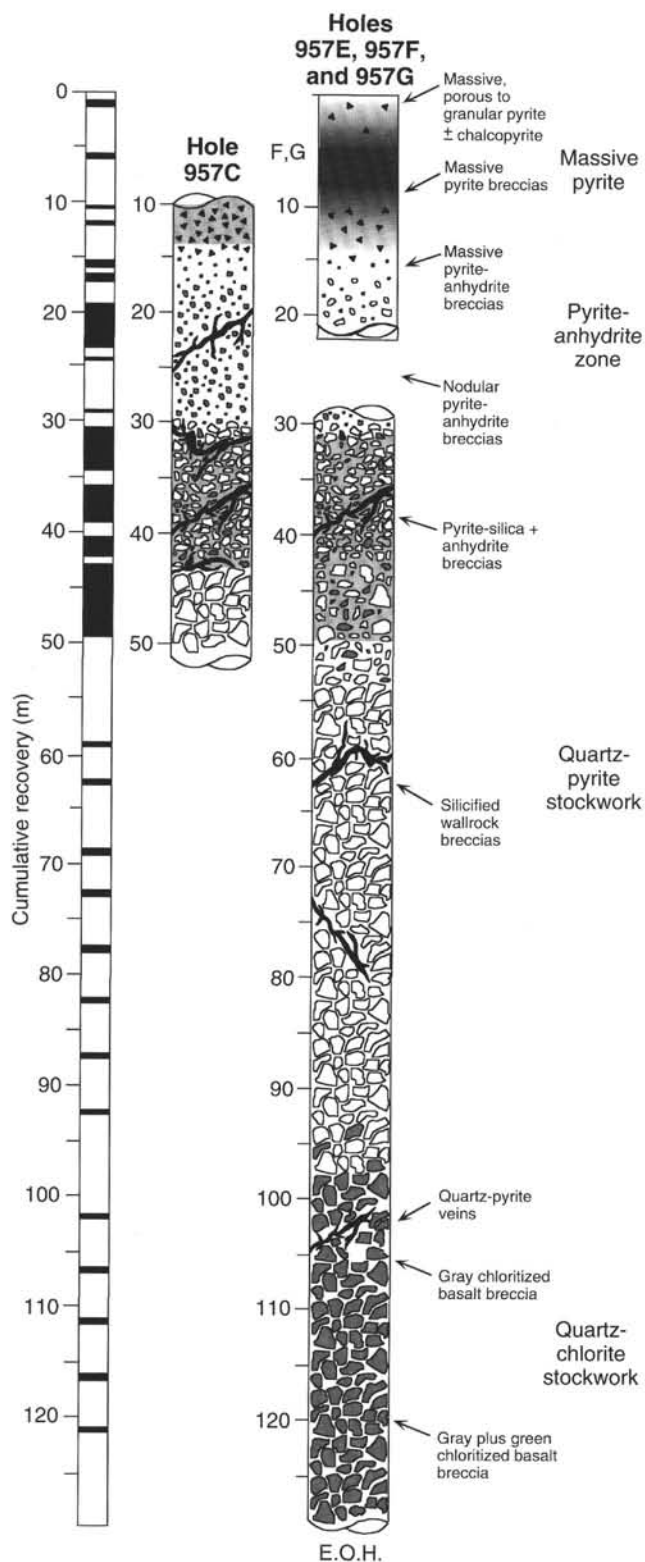


Figure 1. Schematic stratigraphic section of the mound in the TAG-1 area showing the distribution of the principal rock types in cores from Holes 957C, 957E, 957F, and 957G. E.O.H. = end of hole.

Veining

Large anhydrite veins (up to 45 cm in width) were first intersected in the anhydrite-rich zone at 21 mbsf (Section 158-957C-7N-2) and persist in the core to a depth of about 45 mbsf. Anhydrite veining was less common in core from Hole 957E even over similar depth intervals; this may reflect the significantly lower recovery. Quartz veining increases dramatically below about 50 mbsf and is the dominant vein fill in the silicified wallrock breccias to a depth of about 100 mbsf.

Mineralization

Most of the sulfides in the TAG-1 area occur in the upper 30 m of the mound, above the quartz-rich stockwork zone. Pyrite accounts for about 80 vol% of the rock in the upper 15 m of the mound, dominantly as massive pyrite breccias, and about 50 vol% in the anhydrite-rich zone between 15 and 30 mbsf. The bulk of the pyrite and chalcopyrite mineralization in the anhydrite zone and upper stockwork is associated with anhydrite veining and occurs as halos and discrete selvages on the veins. Pyrite abundance decreases from about 30 to 40 vol% in the central part of the quartz-rich stockwork to about 20 vol% in the chloritized basalt breccias. Mineralization in this zone consists predominantly of quartz-pyrite veins and disseminated pyrite in the adjacent wallrock breccias. Preliminary chemical analyses indicate that bulk metal contents also decrease from about 3 wt% Cu in the upper 15 m of massive pyrite to about 2 wt% Cu in the anhydrite-rich zone, 1 wt% Cu in the pyrite-silica breccias from the upper part of the quartz-rich stockwork, and <0.5 wt% Cu in the silicified wallrock breccias and chloritized basalt breccias. Concentrations of Zn are uniformly low (<0.1 wt%) in sulfides from the TAG-1 area.

Interpretation

The complex assemblage of rock types that make up this section of the TAG mound is a product of its multistage development, in which sulfide breccias that are now at the base of the mound were formed at the seafloor during an earlier stage of deposit growth and have since been buried and overprinted by later hydrothermal events. The sulfide breccias likely accumulated at the seafloor through the collapse of large sulfide chimneys and by dissection of massive sulfides along active fault scarps. This debris has been overgrown by later generations of chimneys and progressively cemented or replaced by quartz, sulfides, and sulfates. Therefore, the apparent stratigraphy within the mound, from clast-supported massive pyrite breccias to matrix-supported, pyrite-anhydrite and pyrite-silica breccias, reflects different degrees of brecciation, cementation, hydrothermal reworking, and replacement of preexisting sulfides. The presence of altered basalt clasts from the base of the mound to higher up in the section may indicate periodic dislocation and partial erosion of the mound/stockwork complex by faults during the growth of the deposit. Alternatively, the basalt clasts may be remnants of lava flows that partially buried the deposit early in its development, or relics of the original pillow talus on top of which the sulfides accumulated.

SULFIDE PETROLOGY AND GEOCHEMISTRY

Introduction

The TAG-1 area, located 20 m east-southeast of the Black Smoker Complex, includes Holes 957C, 957D, 957E, 957F, 957G, and 957L (see Fig. 3, Chapter 1, this volume). These holes are aligned in a northeasterly direction in an area measuring roughly 10 × 5 m. No core was recovered from Holes 957D and 957L. Hole 957E had the deepest penetration (125 m) into the TAG hydrothermal system, and the most continuously cored sections from Site 957 were recovered

Table 1. Distribution of dominant lithologies in core from the TAG-1 area.

Dominant lithology	Intervals recovered		Approximate location		Estimated total thickness (m)
			Top (mbsf)	Bottom (mbsf)	
Massive pyrite ± chalcopyrite (Type 5)	158-957F-1N-1	(0–0.3 m)	1.0	1.3	1
Massive pyrite breccias (Type 6)	158-957F-1N-1	(0.3–0.7 m)	1.3	1.7	15
	158-957F-2N-1	(0–0.4 m)	5.5		
	158-957C-4W-1	(0–1 m)	10.0	10.5	
	158-957G-1N-1	(0–0.4 m)	12.0	12.3	
Pyrite-anhydrite breccias (Type 7) with anhydrite veins	158-957C-5N-1	(0–0.5 m)	15.5	16.0	15
	158-957C-7N-1	(0–1.5 m)	19.5	20.8	
	158-957C-7N-2	(0–1.5 m)	20.8	22.1	
	158-957C-7N-3	(0–0.7 m)	22.1	23.5	
	158-957C-9X-1	(0–0.1 m)	24.0	24.2	
	158-957C-10N-1	(0–0.3 m)	28.7	29.0	
	158-957G-2N-1	(0–0.1 m)	16.5	16.6	
	158-957G-3N-1	(0–0.8 m)	21.0	21.7	
Pyrite-silica breccias (Types 8 and 9) with anhydrite veins	158-957C-11N-1	(0–1.4 m)	30.7	32.0	15–20
	158-957C-11N-2	(0–1.5 m)	32.1	33.5	
	158-957C-11N-3	(0–1.4 m)	33.6	34.9	
	158-957C-12N-1	(0–1.3 m)	35.2	35.8	
	158-957C-12N-2	(0–1.4 m)	35.8	36.5	
	158-957C-12N-3	(0–1.0 m)	36.5	36.9	
	158-957C-13N-1	(0–1.4 m)	37.2	38.5	
	158-957C-13N-2	(0–0.6 m)	38.6	39.1	
	158-957C-14N-1	(0–0.7 m)	40.2	40.9	
	158-957C-14N-2	(0–0.9 m)	40.9	41.7	
	158-957C-15N-1	(0–1.2 m)	42.2	42.9	
	158-957E-1R-1	(0–0.3 m)	31.5	31.7	
	158-957E-2R-1	(0–0.4 m)	37.0	37.4	
	158-957E-3R-1	(0–0.2 m)	41.7	41.9	
	Silicified wallrock breccias (Type 10a) with anhydrite and quartz-pyrite veins	158-957C-15N-2	(0–1.5 m)	43.2	
158-957C-15N-3		(0–1.5 m)	44.5	45.6	
158-957C-15N-4		(0–0.5 m)	45.8	46.2	
158-957C-16N-1		(0–1.4 m)	46.2	47.6	
158-957C-16N-2		(0–1.1 m)	47.6	48.5	
158-957E-4R-1		(0–0.2 m)	49.0	49.2	
158-957E-5R-1		(0–0.4 m)	58.6	59.0	
158-957E-6R-1		(0–0.4 m)	63.3	63.6	
158-957E-7R-1		(0–0.3 m)	68.3	68.6	
158-957E-8R-1		(0–0.2 m)	72.8	73.0	
158-957E-9R-1		(0–0.3 m)	77.8	78.2	
158-957E-10R-1		(0–0.2 m)	82.0	82.2	
158-957E-11R-1		(0–0.5 m)	87.1	87.6	
158-957E-12R-1		(0–0.5 m)	91.8	92.3	
Chloritized basalt breccias (Type 10b)		158-957E-14R-1	(0–0.5 m)	101.5	102.0
	158-957E-15R-1	(0–0.5 m)	106.5	107.0	
	158-957E-16R-1	(0–0.2 m)	111.1	111.3	
	158-957E-17R-1	(0–0.4 m)	116.1	116.4	
	158-957E-18R-1	(0–0.5 m)	120.7	121.2	

by MDCB from Hole 957C (Cores 158-957C-7N, 11N, and 15N to 16N).

The holes in the TAG-1 area form a composite section through the hydrothermal mound and into the upper portions of the stockwork zone (see Fig. 1). The rock types are, with increasing depth, massive porous to granular pyrite ± chalcopyrite, pyrite breccias and pyrite sand, pyrite-anhydrite breccias, pyrite-silica breccias, silicified wallrock breccias, and chloritized basalt breccias. Anhydrite veining is abundant throughout the vertical extent of the core, but it is best developed in the pyrite-anhydrite and pyrite-silica breccias. A quartz stockwork occurs within the silicified wallrock and chloritized basalt breccias.

This section describes the spatial distribution, mineralogy, and textural features of sulfides and other hydrothermal precipitates in Holes 957C, 957E, 957F, and 957G and separates each rock type according to the sulfide and hydrothermal precipitates classification scheme as listed in Table 3 in Chapter 5 (this volume). The breccias and anhydrite veins are further subdivided into subtypes on the basis of texture and mineralogy, and these are described in detail below.

Hole 957C

Hydrothermal precipitates and sulfides were recovered in Cores 159-957C-4W to 16N, corresponding to 10.5 to 49.2 mbsf. Four prin-

cipal rock types were identified in core from Hole 957C: massive pyrite (Type 5), pyrite breccias (Types 6, 7, 8, and 9), silicified wallrock breccias (Type 10), and anhydrite veins (Type 11). A schematic section of Hole 957C illustrating the distribution of the different rock types is shown in Figure 1, and an overview of the sulfide stratigraphy is given in the preceding section. The visual core descriptions from Hole 957C are listed in Table 2 (back pocket), and Figure 2 shows the distribution of core recovery, the various core numbers referred to in the text, and graphic logs of the most complete core sections.

Massive Granular Pyrite (Type 5c)

Massive pyrite was recovered as small drill cuttings, rollers, and unoriented pieces between 10 and 15 mbsf. Based on recovery from cores in Holes 957F and 957G, the fragments of massive pyrite are interpreted to be clasts from pyrite breccias that were incompletely cored. The clasts are similar in size and shape (subrounded fragments up to 5 cm in diameter) to large pyrite clasts in pyrite breccias below 15 mbsf. The pyrite is fine to medium grained, granular, and homogeneous; it typically lacks significant visible porosity. In polished specimen, the pyrite is commonly euhedral and appears to have been partially recrystallized. Primary, colloform-banded textures are pre-

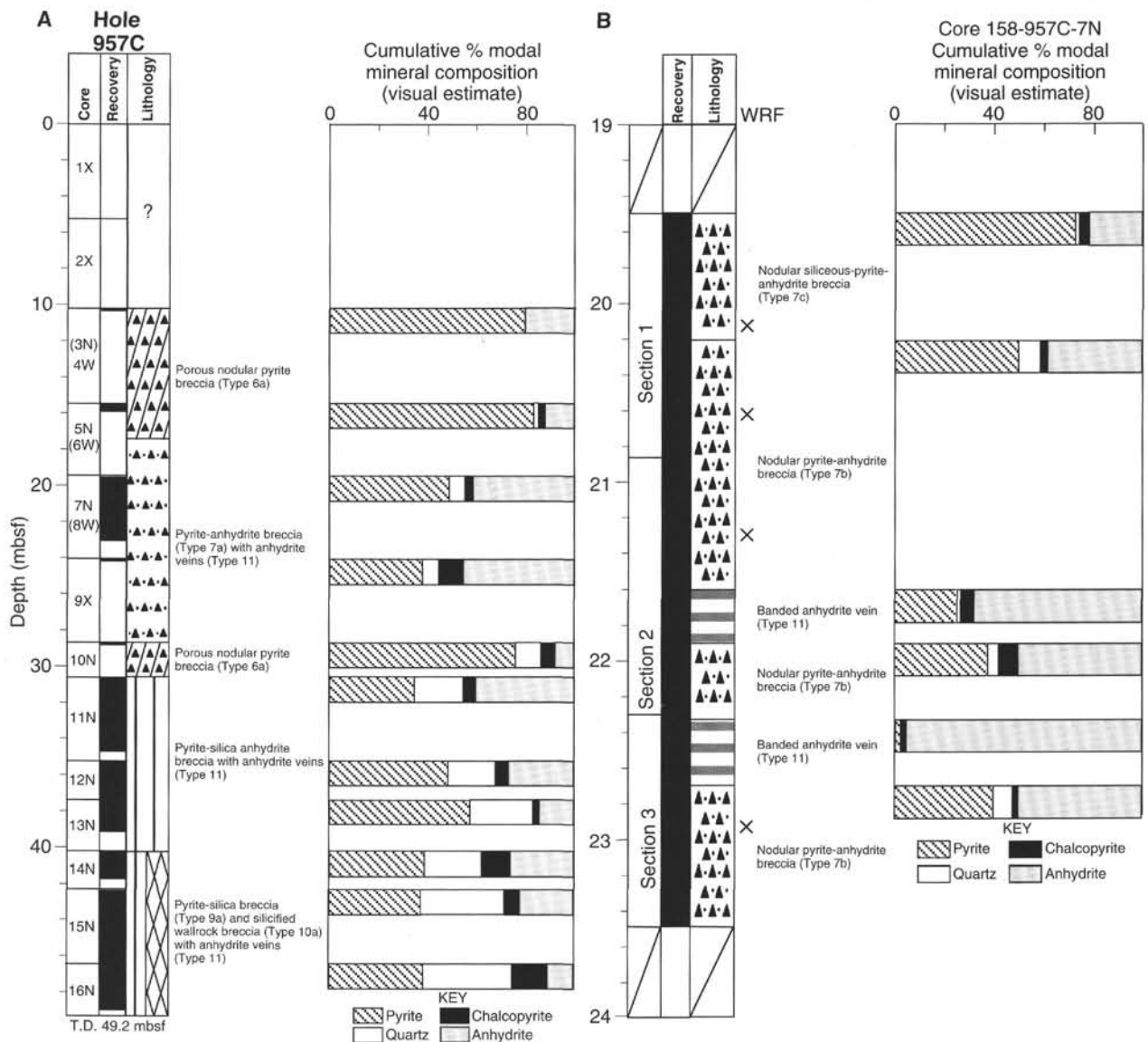


Figure 2. **A.** Idealized lithostratigraphic column for Hole 957C showing the distribution of principal rock types encountered. T.D. = total depth. **B, C, D.** Detailed stratigraphic sections of the most complete intervals in Hole 957C are shown. Mineral abundances, based on visual estimates, are given for each cored interval. WRF = presence of wallrock fragments.

served only locally in the more massive fragments. Table 3 lists the minerals identified, and their relative proportions in each thin section.

Pyrite Breccias (Types 6, 7, 8, and 9)

Pyrite breccias are the dominant lithology between 15 and 40 mbsf. They comprise massive pyrite breccias (Types 6a and 6b), pyrite-anhydrite breccias (Types 7a, 7b, 7c, and 7d), pyrite-silica-anhydrite breccias (Type 8), and pyrite-silica breccias (Types 9a and 9b). The different types are distinguished primarily on the basis of the relative abundances of pyrite, anhydrite, and silica, but they are gradational in character. Massive pyrite breccias contain >75% pyrite and are largely clast supported. They occur in the uppermost sections of Hole 957C and grade downcore into matrix-supported, pyrite-anhydrite breccias. Pyrite-anhydrite breccias contain <75% pyrite, dominantly as clasts in a matrix of semi-massive anhydrite, and occur throughout the central part of the core between 15 and 30 mbsf. These breccias

are the dominant rock type in the anhydrite-rich zone depicted in Figure 1. Pyrite-silica-anhydrite breccias and pyrite-silica breccias occur mainly beneath the anhydrite-rich zone, below about 30 mbsf, and above the silicified wallrock breccias. These are dominantly quartz-pyrite breccias with variable amounts of anhydrite matrix. The pyrite-silica-anhydrite breccias (Type 8) consist mainly of pyritic and siliceous clasts cemented by quartz and anhydrite veins. Pyrite-silica breccias (Types 9a and 9b) consist mainly of quartz-pyrite clasts in a quartz matrix. Although nodular pyrite and quartz-pyrite clasts are the dominant clast types, a variety of other fragments were also observed. A listing of the different clast types identified in Hole 957C is given in Table 4.

Nodular Pyrite Breccias (Type 6a)

The uppermost sections of Hole 957C contain porous, nodular pyrite breccias (Type 6a) consisting of subrounded clasts of massive,

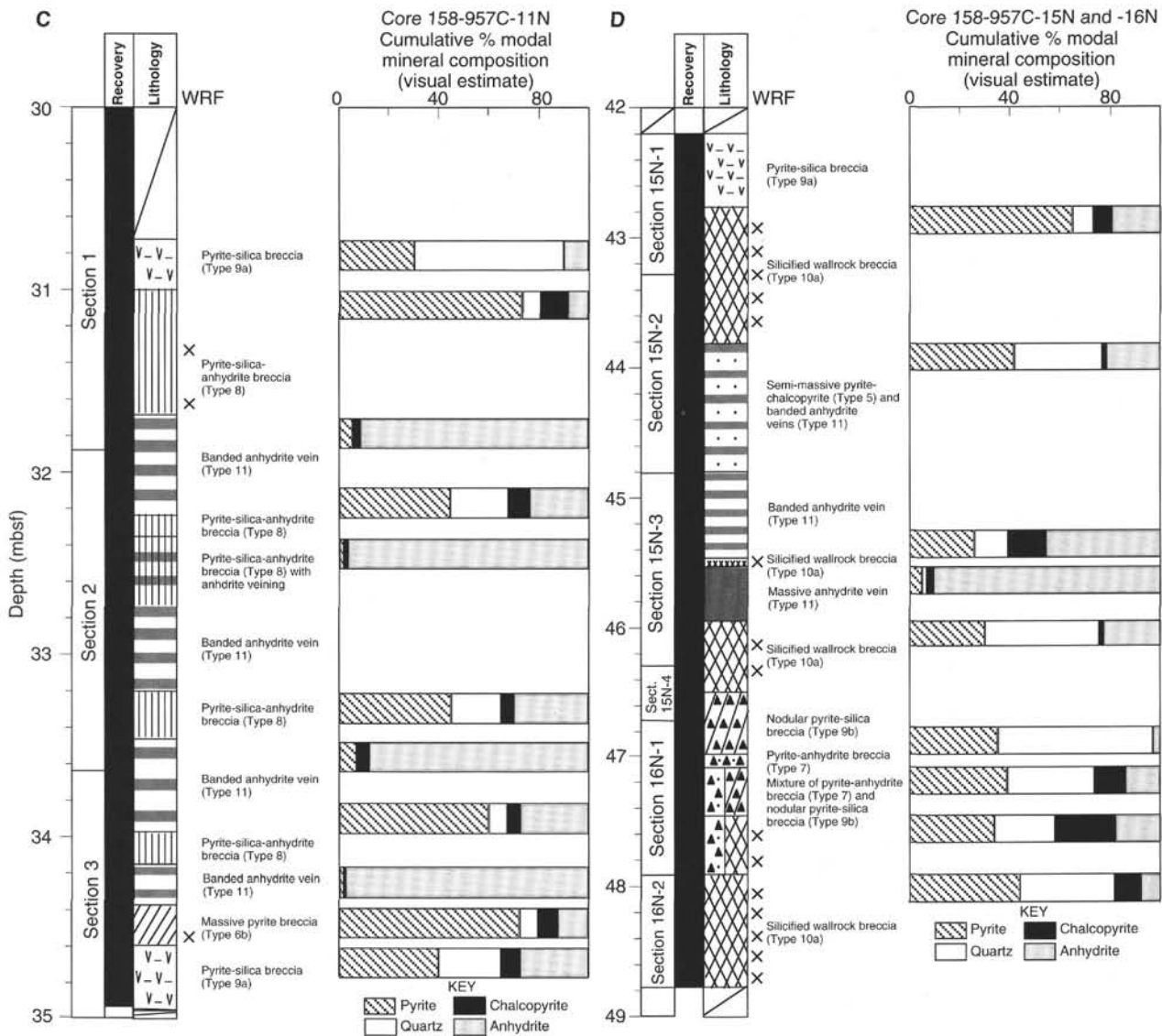


Figure 2 (continued).

granular pyrite in a porous, sandy, pyrite-anhydrite matrix (Fig. 3). These breccias are dominantly framework supported. Individual pyrite clasts are between 0.5 and 1 cm in diameter, although the matrix contains abundant sand-sized pyrite grains that may also be clastic (i.e., detrital) in origin. The sandy pyrite is cemented by fine- to medium-grained anhydrite, but the anhydrite accounts for less than 25 vol% of the rock. Clastic material in these breccias resembles porous and granular massive pyrite found in sulfide talus from the surface of the mound (e.g., Thompson et al., 1988; Rona et al., 1993).

Pyrite-Anhydrite Breccias (Types 7a, 7b, 7c, and 7d)

Pyrite-anhydrite breccias from the central part of Hole 957C consist of massive pyrite clasts and siliceous pyrite clasts in a matrix of anhydrite. These breccias range from matrix to framework supported; they typically contain >25 vol% anhydrite in the matrix. Several subtypes of pyrite-anhydrite breccias were recognized, which include matrix-poor, pyrite-anhydrite breccias (Type 7a), nodular pyrite-anhydrite breccias (Type 7b), nodular, siliceous pyrite-anhydrite breccias (Type 7c), and vein-related, pyrite-anhydrite breccias (Type 7d).

Below about 30 mbsf, these breccias grade into more quartz-rich assemblages (i.e., pyrite-silica-anhydrite and pyrite-silica breccias) and, ultimately, into silicified wallrock breccias.

Massive Pyrite-Anhydrite Breccias (Type 7a)

Matrix-poor, massive pyrite-anhydrite breccias (Type 7a) occur in Section 158-957C-5N-1 and are intermediate in character between massive pyrite breccias near the top of the core and matrix-supported breccias in the underlying anhydrite-rich zone. Individual pyrite clasts are angular and range in size from 0.5 to 2 cm (Fig. 4). These clasts are similar to fragments of massive, granular pyrite recovered at 15–20 mbsf. Pyrite within the clasts comprises fine- to medium-grained, euhedral aggregates containing interstitial quartz, minor amounts of disseminated chalcopyrite (5%–15%), and trace inclusions of sphalerite (Fig. 5A–B). In thin section, the euhedral pyrite grains are typically zoned, with chalcopyrite and sphalerite distributed along growth bands. Remnants of colloform pyrite and marcasite occur in several clasts, but overall primary colloform textures appear to have been extensively recrystallized and overgrown by later gen-

Table 3. Semiquantitative mineralogy of sulfide samples from Leg 158 thin-section descriptions.

No.	Sample	Piece no.	Type	Rock type	Py	Mc	Po	Cp	Sp	Anhyd	Qtz	Chalc	Am Si	Clay	Chl	Fe-oxide	Other
1	158-957A-3X-1	9	2	Red chert	***	tr	—	tr	tr	—	—	*****	—	—	—	tr	—
8	158-957B-4-1	5	2	Red and gray chert	*	—	—	—	—	—	****	***	—	*	—	***	—
43	158-957J-1X-1	3	2	Gray and red chert	***	tr	—	—	tr	—	—	***	*	**	—	**	Hem
57	158-957N-1W-1	2	2	Dark gray chert	**	—	—	*	tr	—	*****	**	tr	—	—	—	Bn, Cv, Dg, Cc, Hem
2	158-957A-3X-1	10	3	Gray chert	*	—	—	tr	tr	—	—	*****	—	—	—	tr	—
4	158-957A-3X-1	8	3	Gray silica	**	—	—	tr	tr	—	—	—	*****	—	—	—	—
3	158-957A-3X-1	11	5a	Porous massive pyrite	*****	***	—	tr	**	—	—	—	—	—	—	tr	—
28	158-957E-2R-1	2	5	Massive sulfide	*****	—	—	**	tr	**	**	—	—	—	**	—	—
41	158-957I-1N-1	8	5a	Porous massive pyrite-marcasite	****	*****	—	tr	**	—	—	—	—	—	—	—	Bn-Cv
44	158-957K-1X-1	2	5a	Porous massive pyrite	****	**	—	—	tr	—	—	—	*****	—	—	—	—
45	158-957K-1X-1	4	5a	Porous massive pyrite	**	***	—	—	tr	—	—	—	***	—	—	tr	—
59	158-957M-2R-1	4	5a	Porous massive pyrite-marcasite	**	****	—	—	*	—	—	—	—	—	—	tr	—
61	158-957P-8R-1	7	5a	Porous massive pyrite	*****	tr	*	**	*	—	—	—	tr	tr	—	—	—
5	158-957B-1R-2	1	5b	Porous massive sphalerite	**	—	—	*	****	—	—	—	***	—	—	tr	—
6	158-957B-3R-1	1	5c	Massive granular pyrite	*****	—	—	tr	tr	—	—	—	—	—	—	—	—
29	158-957F-2N-1	5	5c	Massive granular pyrite	*****	—	—	*	tr	*	tr	—	tr	tr	—	—	—
31	158-957G-1N-1	3	5c	Massive granular pyrite	*****	—	—	*	tr	tr	*	**	—	tr	—	tr	—
46	158-957K-2N-1	9	5c	Massive granular pyrite	*****	**	—	**	tr	—	—	—	—	—	—	—	Bn, Cv, Dg
47	158-957K-3X-1	6	5	Massive pyrite	****	****	—	—	**	—	*	*	tr	—	—	—	—
48	158-957K-3X-1	7	5	Massive pyrite	****	****	—	tr	*	—	*	*	—	—	—	tr	Unknown
24	158-957C-14N-2	1D	5	Massive sulfide	*****	—	—	*	tr	**	tr	—	—	—	—	—	—
30	158-957F-1N-1	10C	6a	Nodular pyrite breccia	****	—	—	*	tr	****	tr	—	—	—	—	—	—
37	158-957H-1N-1	13	6a	Porous nodular pyrite breccia	**	—	—	**	tr	****	—	—	—	—	—	tr	Hem + ?
36	158-957H-1N-1	13	6a	Porous nodular pyrite breccia	*****	—	—	*	tr	tr	—	*	—	*	—	—	—
38	158-957H-3N-1	1	6a	Porous nodular pyrite breccia	*****	****	—	tr	*	—	—	—	tr	tr	—	tr	—
11	158-957C-5N-1	2	7a	Massive pyrite-anhydrite breccia	*****	—	—	**	tr	****	tr	—	—	tr	—	—	—
12	158-957C-5N-1	6	7a	Massive pyrite-anhydrite breccia	*****	—	—	*	tr	*	**	—	—	tr	—	tr	—
13	158-957C-5N-1	7	7a	Massive pyrite-anhydrite breccia	*****	—	—	**	tr	tr	****	—	—	tr	—	tr	—
60	158-957O-2R-1	5	7b	Nodular pyrite-anhydrite breccia	*****	—	—	**	tr	**	—	—	—	—	—	—	—
14	158-957C-7N-1	6F	7c	Nodular siliceous pyrite-anhydrite breccia	****	—	—	**	tr	****	*	—	—	—	—	—	—
15	158-957C-7N-1	8D	7c	Nodular siliceous pyrite-anhydrite breccia	****	—	—	**	tr	**	****	—	—	tr	—	tr	—
27	158-957C-7N-1	6G	7c	Nodular siliceous pyrite-anhydrite breccia	*****	—	—	**	tr	**	*	—	—	—	—	—	—
16	158-957C-7N-2	1E	7c	Nodular siliceous pyrite-anhydrite breccia	****	—	—	**	tr	****	**	—	—	tr	—	—	—
20	158-957C-12N-2	12	8	Pyrite-silica-anhydrite breccia	****	—	—	tr	—	**	****	—	—	tr	—	—	—
58	158-957N-1W-1	4	8	Pyrite-silica-anhydrite breccia	****	-	-	**	tr	**	**	—	—	*	—	tr	—
18	158-957C-11N-1	3A	9a	Pyrite-silica breccia	****	—	—	tr	—	**	*****	—	—	tr	—	—	—
23	158-957C-14N-1	2	9a	Pyrite-silica breccia	****	—	—	tr	tr	**	****	—	—	—	—	—	—
33	158-957E-11R-1	9	9a	Pyrite-silica breccia	*****	—	tr	*	tr	—	****	**	—	*	—	—	Hem
40	158-957H-8N-1	14	9a	Pyrite-silica breccia	*****	—	—	*	tr	*	—	****	—	—	—	tr	—
42	158-957I-1N-1	12	9a	Pyrite-silica breccia	****	—	—	*	tr	—	****	**	—	*	—	tr	—
50	158-957M-1R-2	7	9a	Pyrite silica breccia	**	—	—	**	—	—	*****	—	—	*	—	—	—
51	158-957M-3R-1	30	9a	Pyrite silica breccia	*****	*	—	**	tr	—	****	tr	—	tr	—	—	—
21	158-957C-15N-4	4	9b	Nodular pyrite-silica breccia	****	—	—	tr	—	—	*****	—	—	tr	—	tr	—
22	158-957C-15N-2	1B	10a	Silicified wallrock breccia	****	—	—	—	tr	tr	****	—	—	**	tr	—	—
25	158-957C-16N-2	3C	10a	Silicified wallrock breccia	****	—	—	—	—	*	****	—	—	**	tr	—	—
26	158-957C-16N-2	1B	10a	Silicified wallrock breccia	****	—	—	tr	tr	tr	****	—	—	—	—	—	—
32	158-957E-4R-1	3	10a	Silicified wallrock breccia	**	—	—	tr	tr	tr	****	*	—	**	—	—	—
39	158-957H-5N-2	3A	10a	Silicified wallrock breccia	*****	—	—	tr	—	*	****	—	—	*	—	tr	—
34	158-957E-18R-1	5	10b	Chloritized basalt breccia	**	—	tr	**	tr	—	****	—	—	tr	****	—	—
35	158-957E-14R-1	11	10b	Chloritized basalt breccia	**	—	—	—	tr	—	****	—	—	tr	****	tr	—
19	158-957C-11N-2	9	11	Massive anhydrite vein	tr	—	—	tr	—	*****	—	—	—	—	—	—	—

Notes: Asterisks defined as follows: ***** = dominant (>50%), **** = major (26%–50%), *** = abundant (11%–25%), ** = minor (6%–10%), and * = rare (2%–5%). tr = trace. The number in the first column represents the thin-section number. Py = pyrite, Mc = marcasite, Po = pyrrothite, Cp = chalcopyrite, Sp = sphalerite, Anhyd = anhydrite, Qtz = quartz, Chalc = chalcodony, Am Si = amorphous silica, Clay = unidentified clay, Chl = chlorite, and Fe-oxides = iron oxides. Hem = hematite, Bn = bornite, Cv = covellite, Dg = digenite, and Cc = chalcocite.

Table 4. Dominant clast types identified in breccias from Hole 957C.

	Clast type	Description	Size range (cm)	Shape	Abundance
i	Porous pyrite	Fine- to medium-grained pyrite; commonly colloform, with significant porosity (>10 vol%)	0.5–1	Subrounded	Common
ii	Granular massive pyrite	Very fine- to medium-grained pyrite with minor visible pore space	0.5–2	Subrounded	Abundant
iii	Fine-grained pyrite-chalcopyrite	Fine-grained intergrown pyrite and chalcopyrite	0.5–1	Subrounded	Rare
iv	Fine-grained chalcopyrite	Fine-grained porous to granular chalcopyrite; locally with dark gray siliceous matrix	0.5–1	Subrounded	Rare
v	Nodular, siliceous pyrite	Very fine-grained disseminated pyrite in gray siliceous matrix; commonly brecciated and veined by late anhydrite	1–3	Subrounded	Abundant
vi	Quartz-pyrite	Sand-sized aggregates of euhedral pyrite grains cemented by clean quartz; common as fine-grained recrystallized clastic material throughout anhydrite- and quartz-cemented breccia	<0.5	Subrounded	Abundant
vii	Red chert	Clasts of cryptocrystalline quartz with abundant Fe-oxide inclusions; commonly as minor clasts within larger pyritic fragments	0.5–1	Angular to subrounded	Common
viii	Gray chert	Clasts of gray cryptocrystalline quartz with very fine, disseminated pyrite	0.5–1	Subangular subrounded	Common
ix	Buff-colored, altered basalt	Clay-rich fragments of altered basalt with relict primary igneous textures; commonly intensely silicified and with minor disseminated pyrite	1–2	Angular to subangular	Rare
x	Gray siliceous clasts	Fragments of silicified wallrock with primary igneous textures completely destroyed; intensely silicified, but with only trace disseminated pyrite (generally restricted to the bottom of the hole)	Up to 5	Angular to subangular	Common

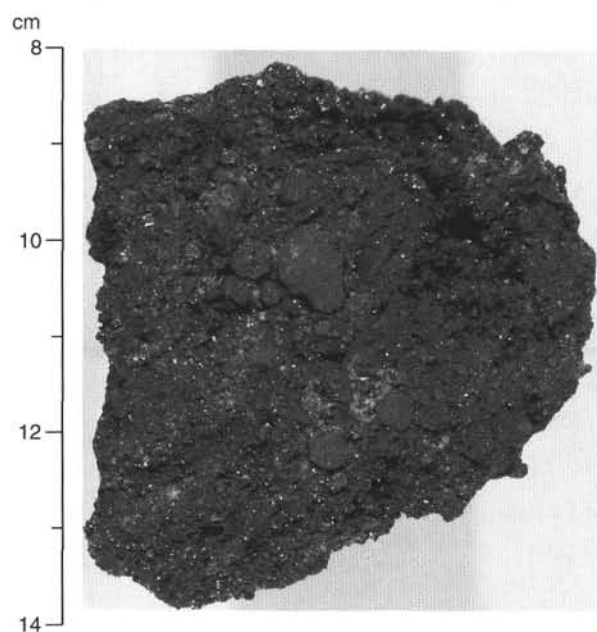


Figure 3. Porous, massive nodular pyrite breccia (Type 6a) containing sub-rounded clasts of massive granular and porous pyrite. Sample 158-957C-4W-1 (Piece 3, 8–13.5 cm).

erations of pyrite (Fig. 5C). Marcasite is rare in the recrystallized material. Anhydrite in the matrix typically consists of fine- to medium-grained euhedral aggregates (Fig. 5D).

Nodular Pyrite-Anhydrite Breccias (Type 7b)

Nodular pyrite-anhydrite breccias (Type 7b) and nodular, siliceous pyrite-anhydrite breccias (Type 7c) are the principal sulfide types in the anhydrite-rich zone. As much as 50% of the anhydrite intersected in Hole 957C occurs as matrix material in these breccias. The nodular pyrite-anhydrite breccias (Type 7b) consist of rounded pyrite clasts in a massive anhydrite matrix and occur mainly in Sections 158-957C-7N-2, 7N-3, 8W-1, and 9X-1 (Figs. 6, 7). These breccias are matrix supported with minor, disseminated sulfides

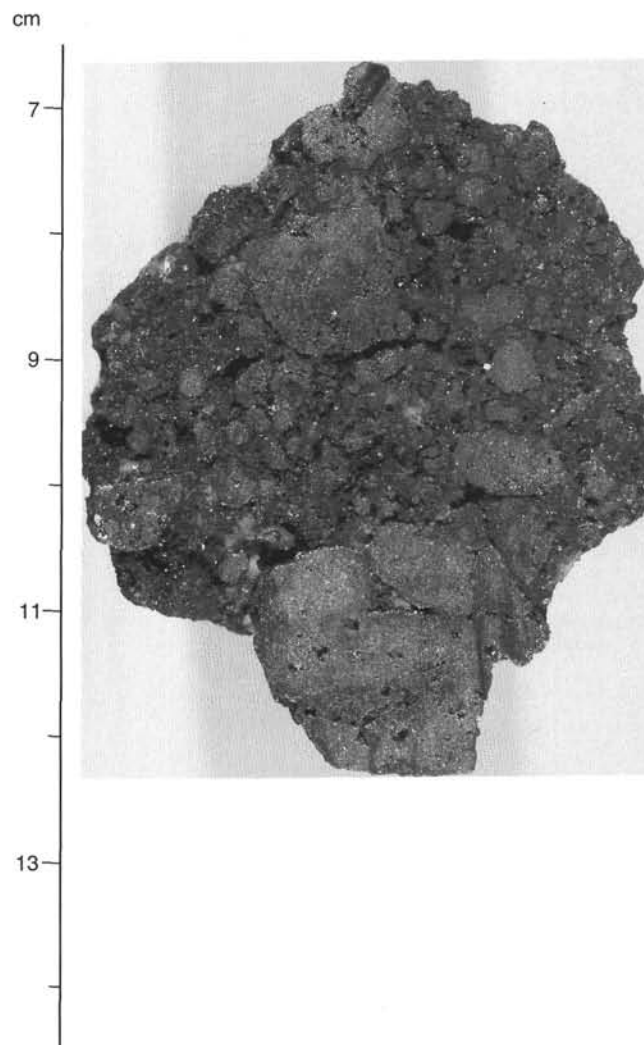


Figure 4. Porous, pyrite-anhydrite breccia (Type 7a) with clasts of massive granular pyrite. Sample 158-957C-5N-1 (Piece 2, 6.5–14.5 cm).

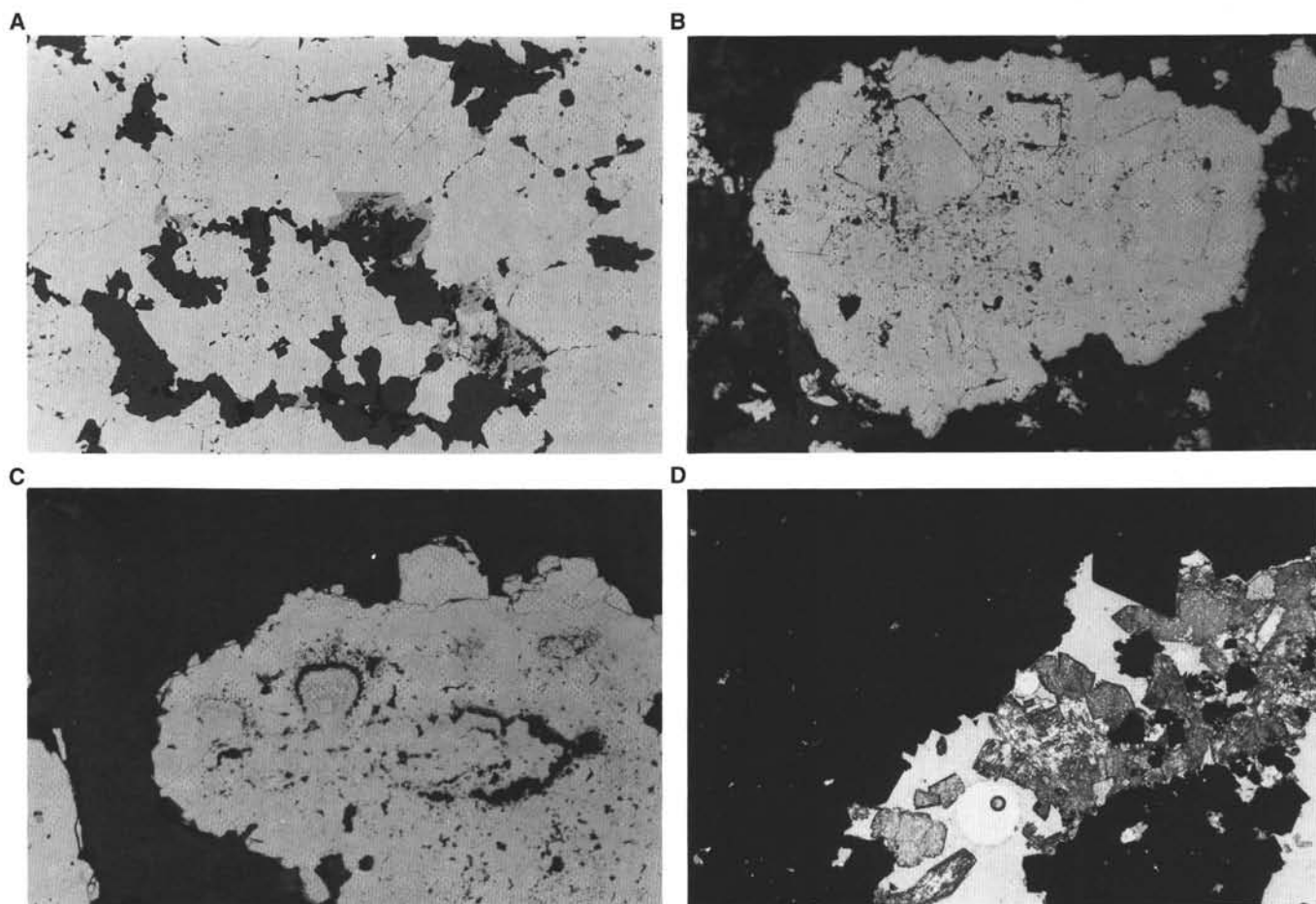


Figure 5. Representative photomicrographs of textures in massive pyrite-anhydrite breccias (Type 7a). **A.** Recrystallized pyrite (white) with interstitial chalcopyrite (gray) and quartz (dark gray). Sample 158-957C-5N-1 (Piece 7, thin section from 49 to 52 cm.). Reflected light, field of view = 1.5 mm. **B.** Granular pyrite aggregate surrounded by quartz and anhydrite consisting of euhedral pyrite (white) with minor sphalerite inclusions (gray). The aggregate is partly recrystallized and overgrown by a later generation of pyrite. Sample 158-957C-5N-1 (Piece 2, thin section from 7 to 15 cm). Reflected light, field of view = 1.5 mm. **C.** Remnant colloform textures of pyrite and marcasite overgrown and partially replaced by later euhedral pyrite (white) and intergrown with quartz (dark gray). Sample 158-957C-5N-1 (Piece 7, thin section from 49 to 52 cm). Reflected light, field of view = 1.5 mm. **D.** Granular anhydrite matrix between massive pyrite aggregates pyrite (black). Sample 158-957C-5N-1 (Piece 2, thin section from 7 to 15 cm). Transmitted light, field of view = 6 mm.

throughout the anhydrite matrix. The nodular clasts consist of massive, granular pyrite, ranging in size from 0.5 to 2 cm, but siliceous clasts and quartz-pyrite clasts become increasingly common at greater depths (see below). Buff, altered basalt fragments also occur locally, starting at about 20 mbsf.

Nodular, Siliceous Pyrite-Anhydrite Breccias (Type 7c)

Nodular, siliceous pyrite-anhydrite breccias (Type 7c) consist of nodular pyrite clasts and rounded siliceous clasts, in a matrix of dark gray anhydrite and quartz (Fig. 8). This breccia type is most common in Sections 158-957C-7N-1 and 7N-2. The matrix material ranges from barren, massive anhydrite (Figs. 8, 9), to semi-massive anhydrite with abundant disseminated sulfides (Fig. 10), and semi-massive anhydrite with patches of gray silica (Figs. 11, 12). The gray color of the matrix is generally caused by an abundance of fine-grained, disseminated pyrite (up to 10%) and locally minor chalcopyrite (up to 5%) (Fig. 10). The nodular, siliceous clasts consist of disseminated grains and aggregates of pyrite in a dark-gray silica matrix and resemble fragments of pyrite-silica breccia occurring farther downcore (see below). These clasts are subrounded and are similar in size (0.5–2 cm) and shape to the massive pyrite clasts in the same rock. Smaller, sand-sized, quartz-pyrite clasts consisting of granular aggregates of pyrite in a euhedral quartz matrix occur throughout the

breccias and appear to be remnants of an earlier generation of quartz-pyrite mineralization. Gray and red chert clasts are also present in this breccia type (Fig. 13), and buff clasts of altered basalt up to 2 cm in diameter occur in nodular, siliceous pyrite-anhydrite breccias from Section 158-957C-7N-1 (see Fig. 10 and “Hydrothermal Alteration” section, this chapter). The presence of basalt fragments, together with clasts of red chert, suggest that the anhydrite-rich zone may contain relics of preexisting wallrock breccias. In thin section, the matrix is dominantly fine- to medium-grained anhydrite, but it includes abundant quartz and disseminated, fine-grained pyrite and chalcopyrite (Fig. 14A–C). Quartz in the matrix occurs as euhedral overgrowths on the clasts and as diffuse patches of gray quartz (Fig. 14D). This material may have been introduced during veining or may be the partially replaced remnants of preexisting silicified wallrock. Sand-sized, quartz-pyrite clasts or aggregates in the matrix are commonly rimmed by coarse, euhedral pyrite and quartz (Fig. 14E–G). Locally, they appear to have been partially recrystallized or overgrown by multiple generations of later pyrite. Rare clasts of chalcopyrite also occur (Fig. 14H).

Vein-related Pyrite-Anhydrite Breccias (Type 7d)

A fourth type of pyrite-anhydrite breccia occurs mainly below the anhydrite-rich zone and is associated with anhydrite veins that cross-

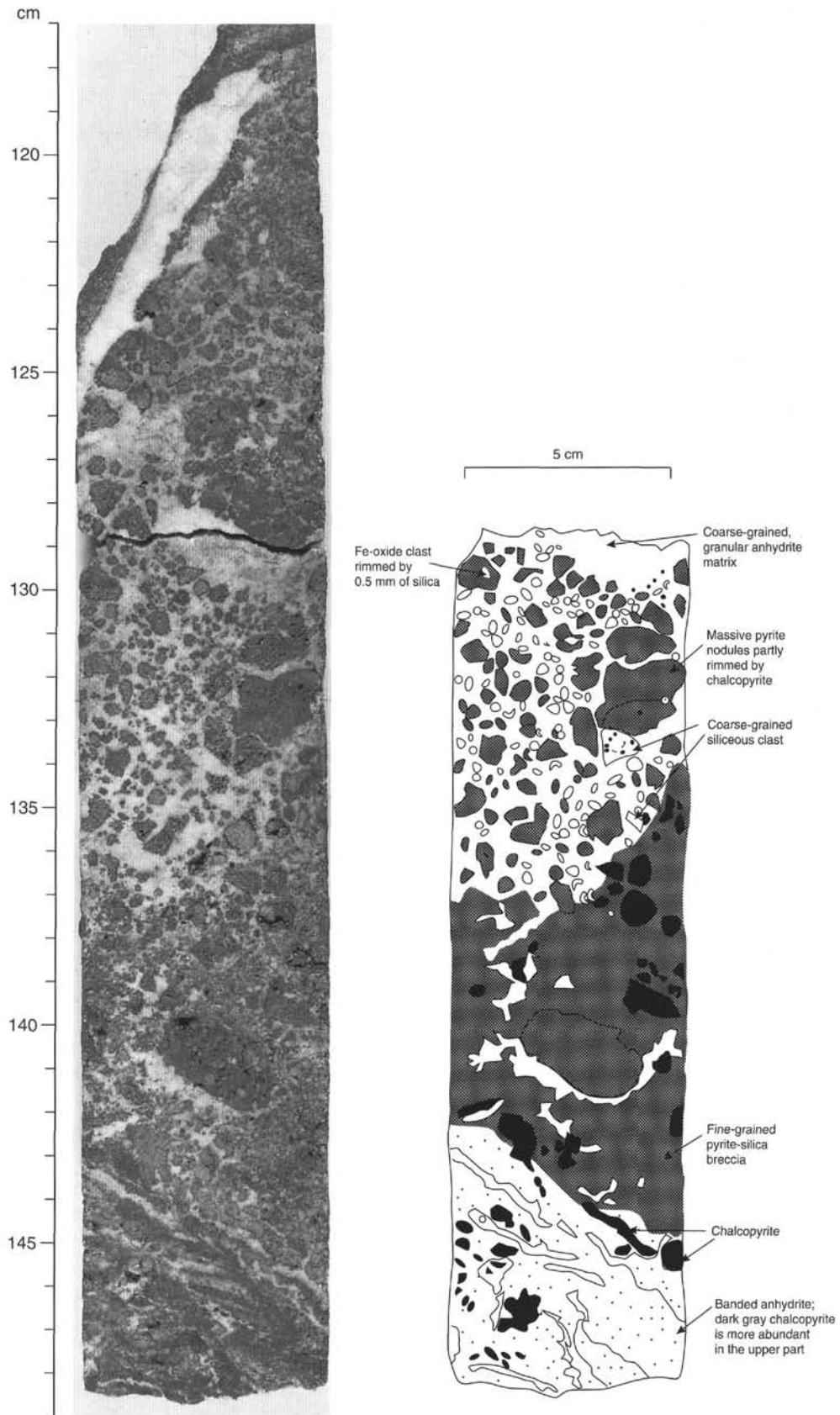


Figure 6. Photograph and sketch of nodular pyrite-anhydrite breccia (Type 7b), showing anhydrite as veins and as matrix throughout the breccia. Sample 158-957C-7N-2 (Pieces 1J and 1K, 120–150 cm).

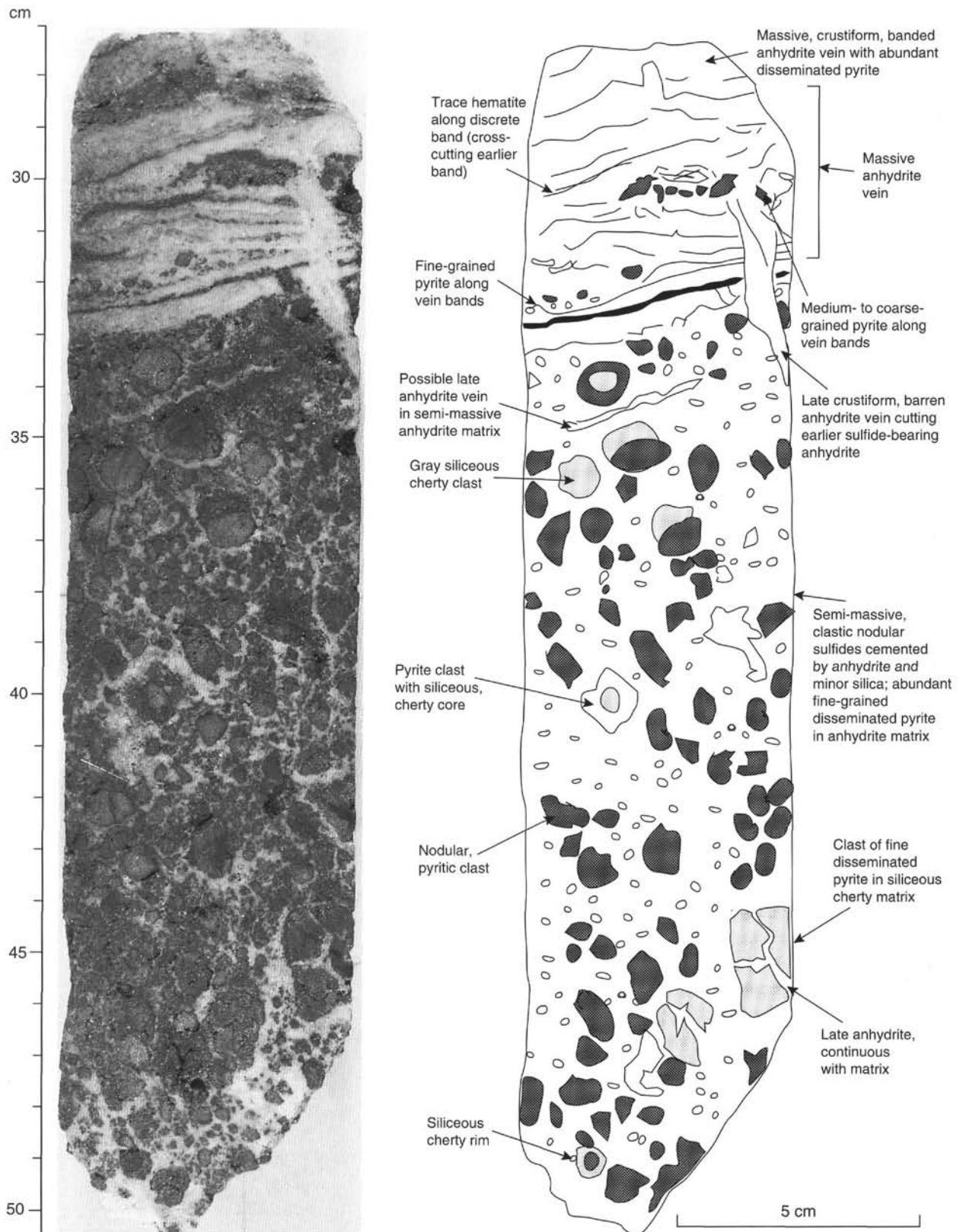


Figure 7. Photograph and sketch of massive granular pyrite clasts in nodular pyrite-anhydrite breccia (Type 7b), showing two generations of anhydrite veins (crustiform-banded anhydrite and later, crosscutting barren) cutting the breccia. Sample 158-957C-7N-3 (Piece 4A, 28–50 cm).

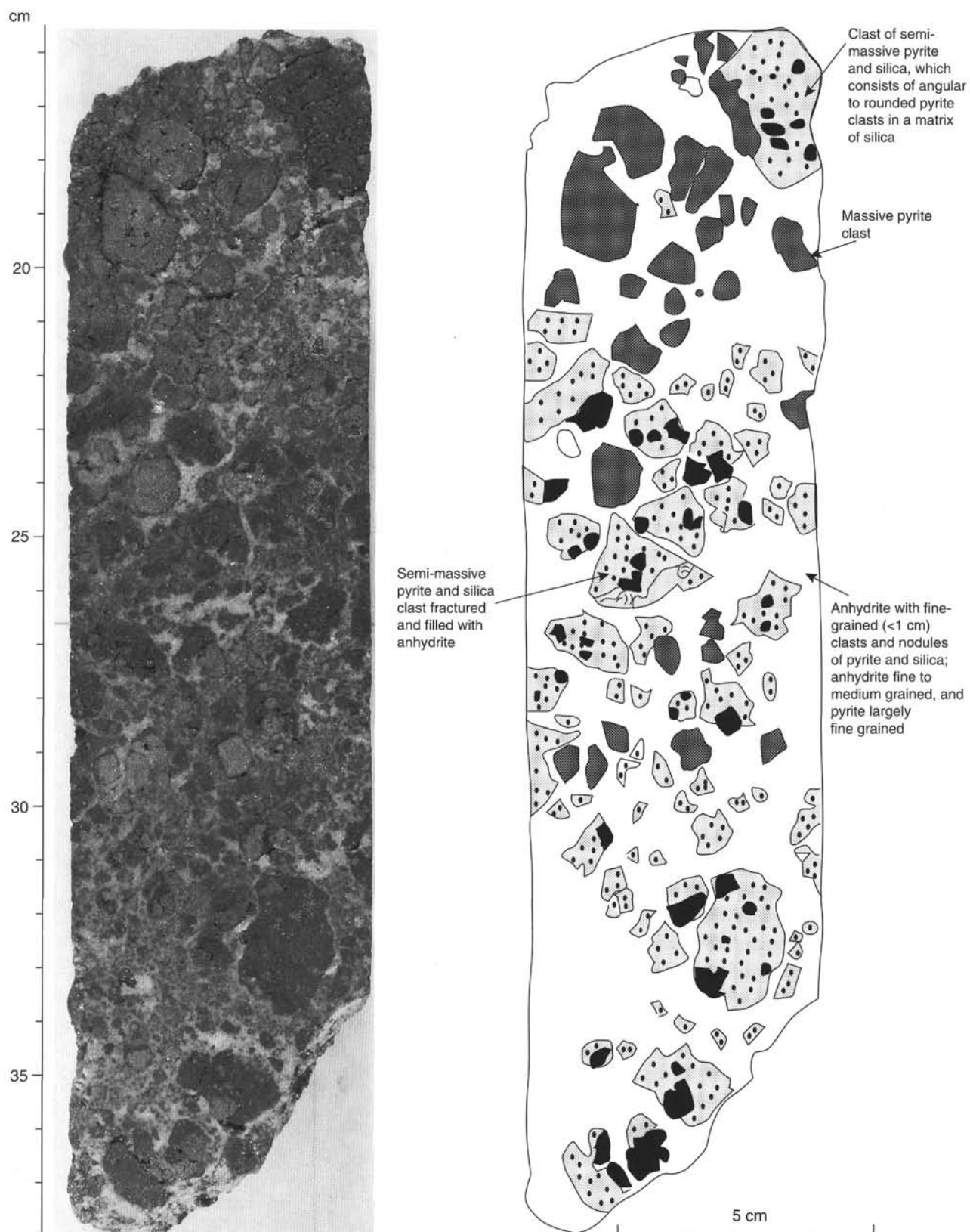


Figure 8. Photograph and sketch of massive granular pyrite clasts and siliceous clasts in nodular, siliceous pyrite-anhydrite breccia (Type 7c) with anhydrite matrix. Sample 158-957C-7N-2 (Piece 1B, 16–38 cm).

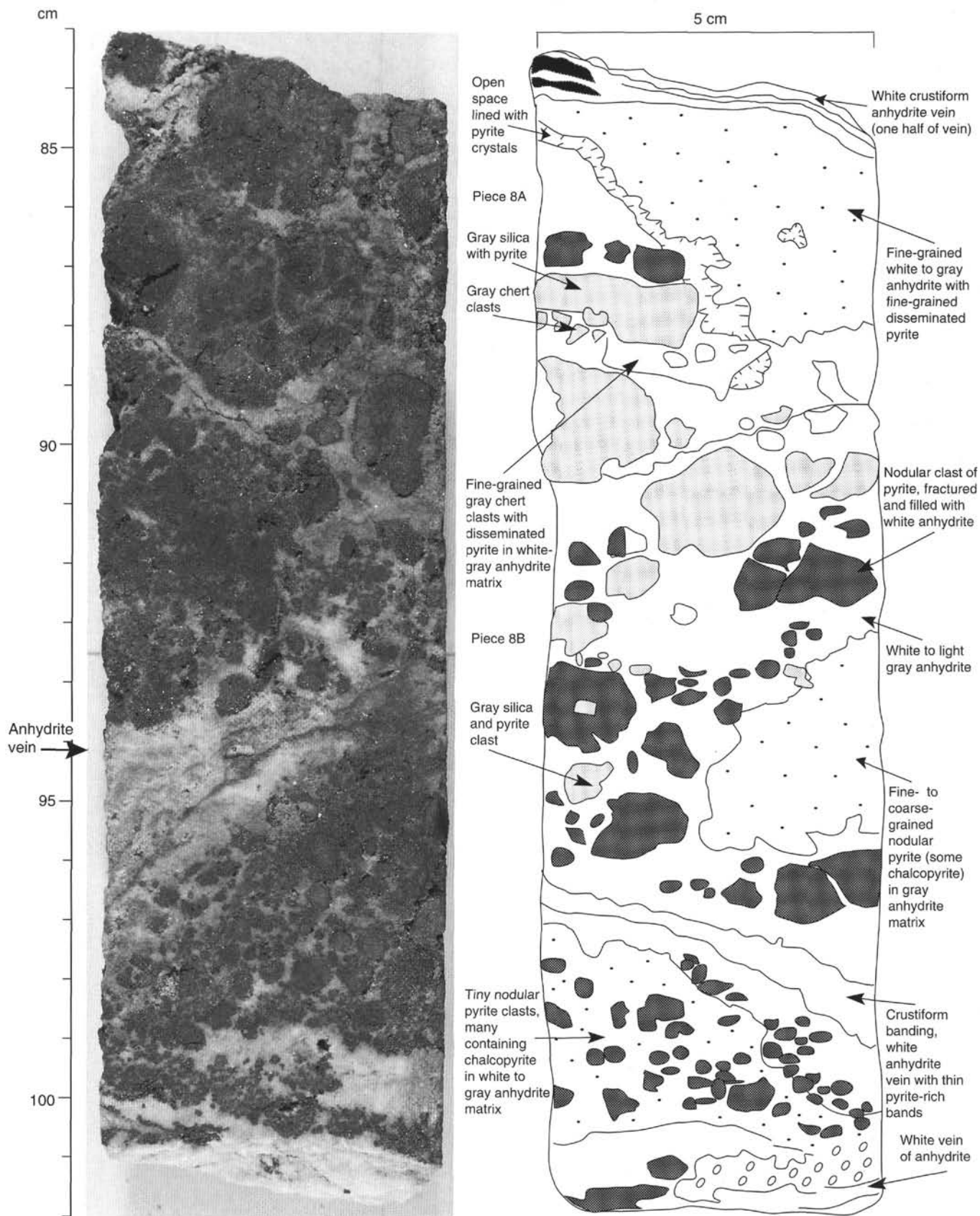


Figure 9. Photograph of archive half and sketch of working half of Sample 158-957C-7N-1 (Pieces 8A and 8B, 83–102 cm), showing the relationship between late anhydrite veins and the anhydrite matrix in nodular, siliceous pyrite-anhydrite breccia (Type 7c).

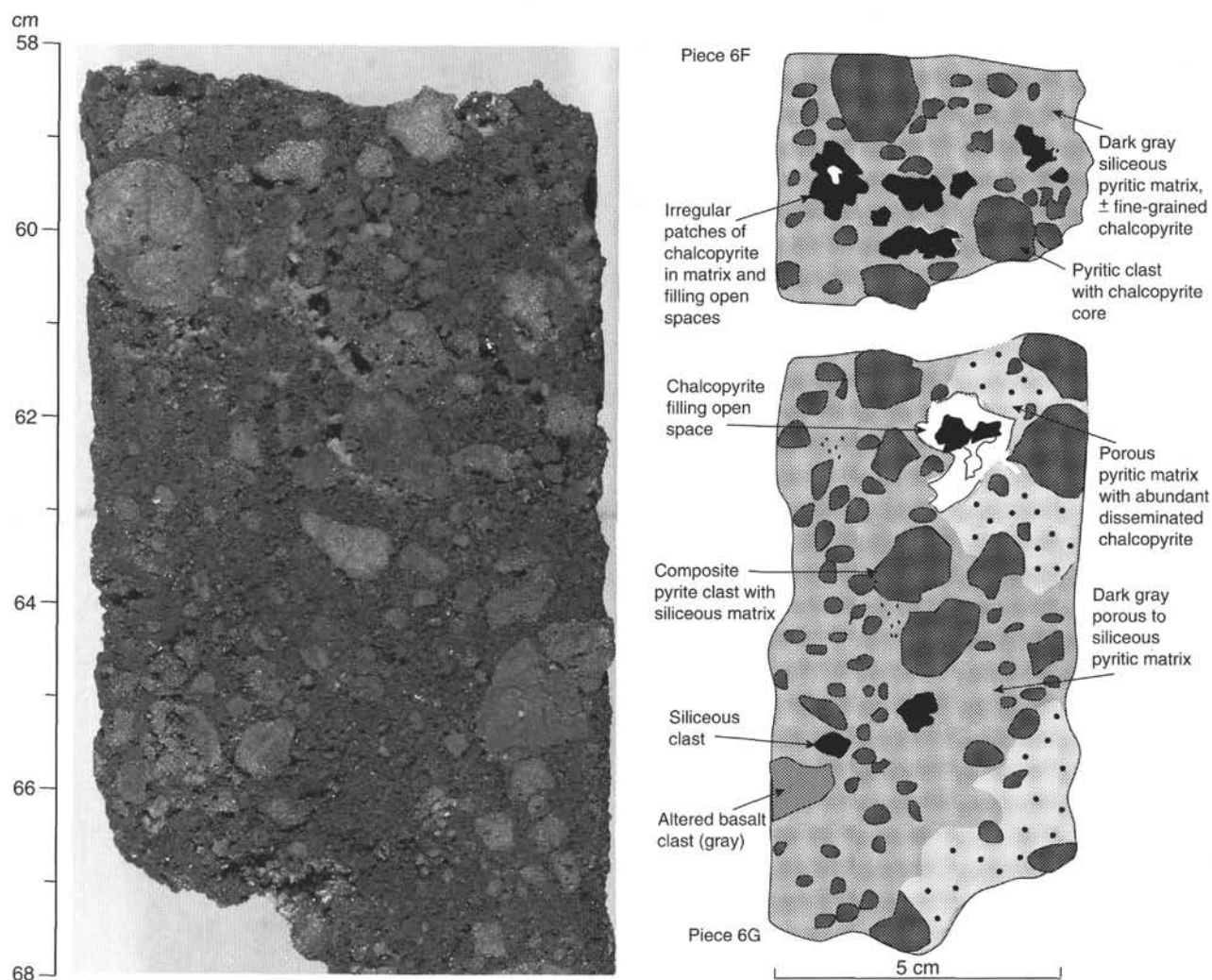


Figure 10. Photograph of archive half of Sample 158-957C-7N-1 (Piece 6G, 58–68 cm), and sketch of working half of Pieces 6F and 6G (54–68 cm), showing nodular, siliceous pyrite-anhydrite breccia (Type 7c) with abundant disseminated sulfides in the anhydrite matrix. This sample contains abundant chalcopyrite in the matrix and is one of the first altered basalt fragments encountered in the core.

cut preexisting breccias. Vein-related, pyrite-anhydrite breccias (Type 7d) are in situ and consist of massive and semi-massive, fine-grained pyrite and chalcopyrite that have been infilled by anhydrite along the vein margins (Fig. 15). These breccias account for much of the chalcopyrite downsection (e.g., below about 30 mbsf). The pyrite and chalcopyrite appear to have been precipitated as part of the vein selvage or halo, and they overgrow or replace preexisting breccia fragments in the adjacent wallrock (see discussion of anhydrite veins below). In places, the pyrite halo is massive (e.g., Figs. 16, 17), and fragments of this material are logged as brecciated massive pyrite and massive pyrite breccias (Type 6b). The brecciated appearance of the pyrite is partly inherited from the surrounding wallrock and partly induced by anhydrite veining.

Pyrite-Silica-Anhydrite Breccias (Type 8)

Pyrite-silica-anhydrite breccias (Type 8) are similar to nodular, siliceous pyrite-anhydrite breccias (Type 7c) except that they are cemented mainly by quartz, with most of the anhydrite related to cross-cutting anhydrite veins (Figs. 18, 19). These rocks occur at the base of the anhydrite-rich zone and are intermediate in character between

pyrite-anhydrite breccias (above) and pyrite-silica breccias (below). The clasts consist of siliceous pyritic material, quartz-pyrite aggregates, and massive granular pyrite, ranging in size from 0.5 to 2 cm, and they are typically subangular to subrounded. The siliceous clasts commonly have diffuse boundaries, suggesting partial replacement by the quartz matrix. The dark-gray quartz is a result of inclusions of abundant, fine-grained, disseminated pyrite. In some pieces, the gray siliceous matrix is also brecciated and veined by a later generation of quartz and anhydrite, forming larger breccia fragments of up to 10 cm in size (see Fig. 20).

Pyrite-Silica Breccias (Types 9a and 9b)

Below about 35 mbsf, pyrite-silica-anhydrite breccias grade into pyrite-silica breccias (Type 9a) as the amount of anhydrite veining decreases. These breccias occur mainly in Cores 158-957C-13N, 14N, and 15N and are gradational with silicified wallrock breccias at greater depths (below about 40 mbsf). The pyrite-silica breccias consist of large fragments (up to 10 cm) of fine-grained, gray siliceous material and smaller fragments of quartz-pyrite set in a matrix of euhedral quartz (Fig. 21). Large remnants of nodular pyrite clasts are

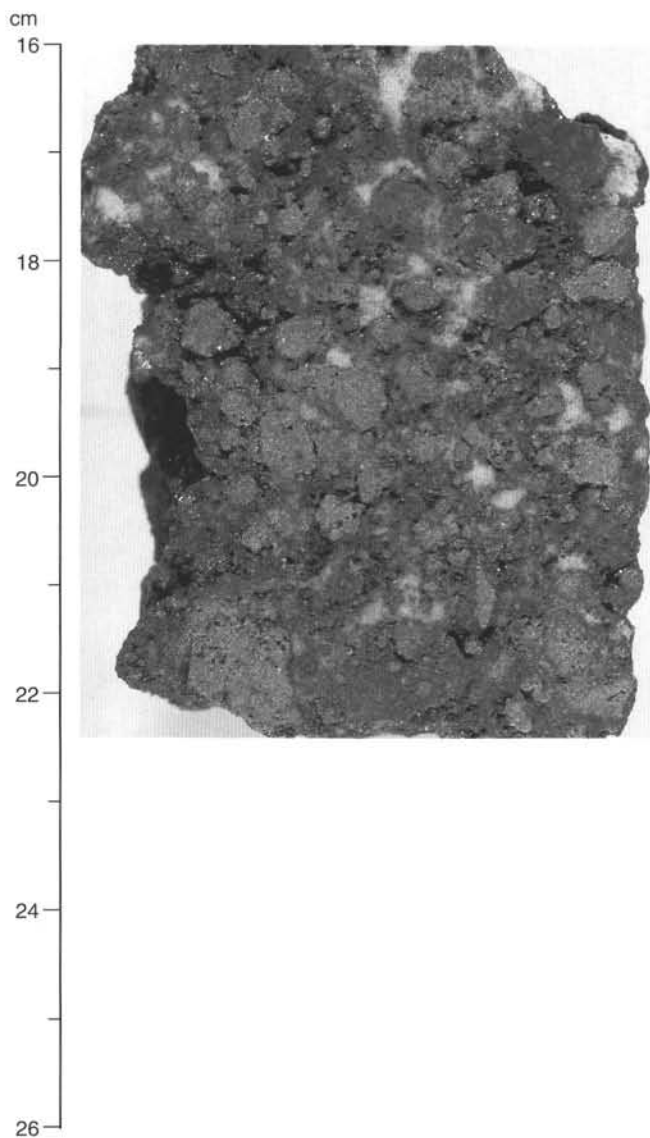


Figure 11. Nodular, siliceous pyrite-anhydrite breccia (Type 7c) with a porous matrix of anhydrite and patchy gray silica. Sample 158-957C-7N-1 (Piece 5, 16–26 cm).

also present locally (Fig. 22). The gray siliceous clasts appear to be fragments of preexisting, mineralized and silicified wallrock, similar to that occurring deeper in the core (see below), but the clasts generally have more diffuse boundaries and are partially replaced by the quartz matrix (Fig. 23). Patches of phyllosilicates (clay?) and traces of red chert (i.e., Fe-oxides) occur locally in thin section, but primary igneous textures have generally been completely destroyed. However, clasts with recognizable igneous textures in both hand specimen and thin section are present in increasing abundance downward from 20 mbsf to the bottom of the core (see “Hydrothermal Alteration” section, this chapter). Euhedral quartz occurs throughout the samples as rims on large breccia fragments and quartz-pyrite clasts or aggregates, as overgrowths on disseminated pyrite grains, and as veinlets and cavity linings (Fig. 24A–D). Multiple generations of euhedral and colloform-banded quartz are present within individual quartz-pyrite clasts and in the surrounding matrix. Trace amounts of pyrite and chalcopyrite are disseminated throughout the quartz matrix, but individual quartz crystals are typically free of sulfide inclusions.

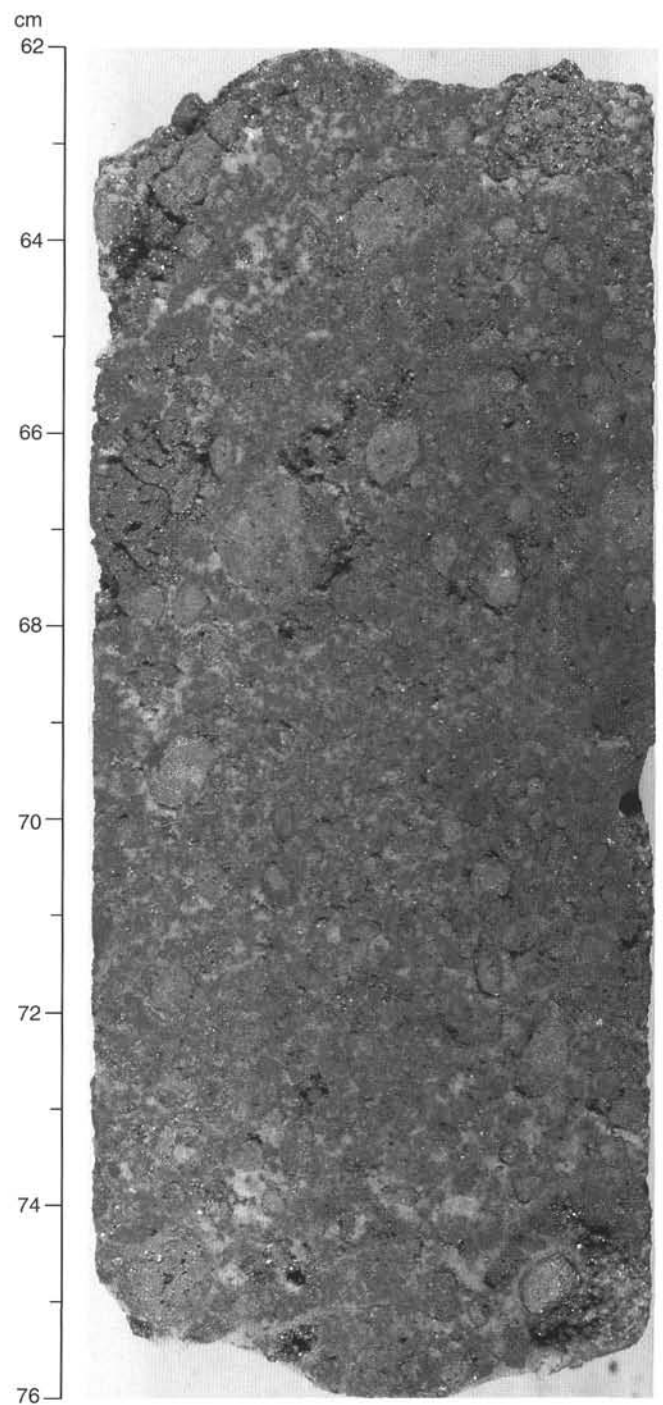


Figure 12. Nodular, siliceous pyrite-anhydrite breccia (Type 7c) with a matrix of anhydrite and gray silica. Sample 158-957C-7N-2 (Piece 1E, 62–76 cm).

Nodular, pyrite-silica breccias (Type 9b) also occur in Cores 158-957C-13N, 14N, and 15N. They consist of large siliceous clasts (up to 10 cm) containing well-rounded, nodular pyrite and quartz-pyrite aggregates (Figs. 25, 26). These breccias are texturally similar to nodular pyrite-anhydrite breccias (Type 7b), which occur upsection and may represent an earlier generation of pyrite-anhydrite that has been re-cemented by quartz. In some cases, quartz clearly replaces

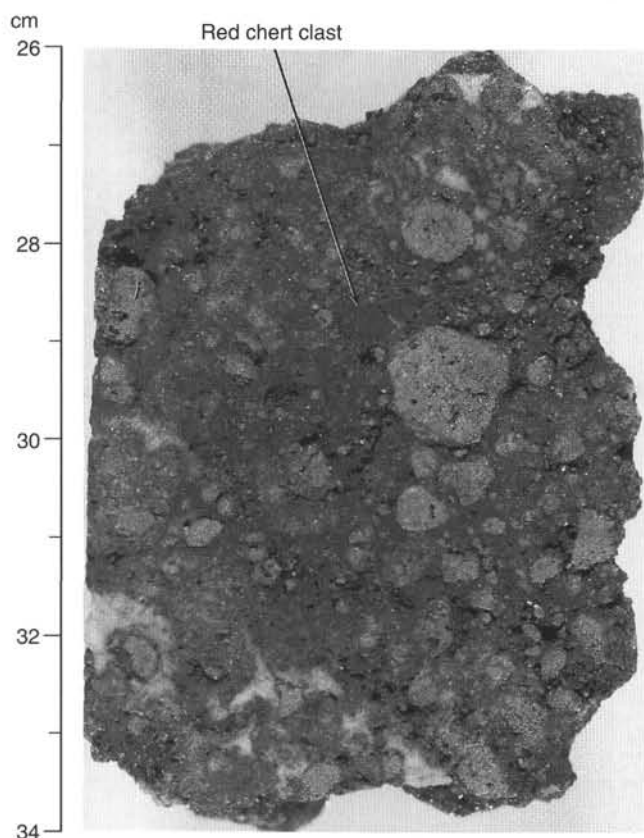


Figure 13. Nodular, siliceous pyrite-anhydrite breccia (Type 7c) with anhydrite and silica matrix and containing a clast of red chert (labeled). Sample 158-957C-7N-1 (Piece 6A, 26–34 cm).

pyrite clasts at their margins, with the original outline of the clast preserved in the quartz (Fig. 24C).

Silicified Wallrock Breccias (Type 10a)

Silicified wallrock breccias occur mainly below 40 mbsf. They differ from the overlying pyrite-silica breccias in that they are dominantly clast supported, have more distinct clast boundaries, and contain significantly less pyrite. Recognizable portions of the silicified wallrock breccia first occur in Section 158-957C-14N-2 and continue throughout most of Cores 158-957C-15N and 16N. The breccias consist of fine-grained, gray siliceous clasts, up to 5 cm across, in a quartz-rich matrix (Fig. 27). Larger fragments of wallrock are intensely fractured and veined by quartz; they contain widespread disseminated pyrite and small pyrite aggregates (Figs. 28, 29). Much of the quartz is introduced along millimeter-scale fractures, possibly generated during an early stage of silicification. Similar millimeter-scale quartz veins occur in siliceous clasts higher up in the core. Fine-grained, disseminated pyrite and chalcopyrite occur within larger quartz veins (up to 0.5 cm across) and rimming the wallrock fragments. Late anhydrite veins containing disseminated pyrite and chalcopyrite also crosscut the breccias locally (Fig. 30), but they are much less common than in higher sections of the core.

Quartz has replaced much of the original rock material in these breccias. Although distinct wallrock fragments are recognizable throughout this part of the core, some fragments are almost completely replaced by quartz (Fig. 31). Quartz also overgrows and partially replaces disseminated pyrite within the fragments (Fig. 32). In thin

section, tan claylike minerals, possibly chlorite, illite, or mixed layers with smectite, occur within some fragments, and relict igneous textures occur locally (see “Hydrothermal Alteration” section, this chapter). Traces of chlorite occur in some quartz veinlets cutting the silicified wallrock but not within the clasts themselves. Although brittle fracturing of the wallrock is common along quartz veins, sulfides within these veins and in the adjacent wallrock are rarely fractured.

Anhydrite Veins (Type 11)

Description of Vein Types

Numerous large anhydrite veins (up to 45 cm in width) are present between 20 and 40 mbsf. The veins comprise complex, multistage fracture fillings and cavity linings and consist of three main types: (1) massive, crustiform, banded veins with fine-grained pyrite and chalcopyrite disseminated along growth bands; (2) massive, granular anhydrite with uniformly disseminated, intergranular pyrite and chalcopyrite; and (3) late-stage, barren anhydrite veins, typically cutting earlier massive anhydrite. The dominant vein networks are composite in nature, and it is difficult to establish crosscutting relationships that can be extrapolated over an entire core or section.

Crustiform-banded veins display textures typical of open-space filling, and individual growth bands (0.5 up to 1 cm in width) reflect sequential precipitation within cavities or repeated opening of fractures. Veins of only a few centimeters width may have up to 10 growth bands, and these are commonly lined by aggregates of fine-grained pyrite, chalcopyrite, and rare hematite (see Fig. 33). A number of large, complex veins of more than 10 cm width occur at approximately 22, 31 and 36 mbsf (Figs. 34–37). These veins display as many as 20 discrete growth bands. Massive and semi-massive pyrite and chalcopyrite also occur locally within vugs and cavities, within the veins themselves (Fig. 37), rimming breccia fragments adjacent to the veins, and as selvages or halos in the anhydrite-rich matrix of breccias adjacent to the veins (e.g., vein-related pyrite-anhydrite breccias) (Figs. 38, 39).

Massive granular anhydrite, with disseminated pyrite and chalcopyrite, veins are less common but occur locally in the cores or as discrete bands within large anhydrite veins (see Figs. 34–36). This material is coarsely crystalline, commonly lacks well-defined growth bands, and is gray as a result of the presence of abundant fine-grained pyrite and chalcopyrite.

Late-stage, barren (devoid of sulfide) anhydrite veins cut across both earlier anhydrite and the sulfide breccias (see Figs. 40, 41). These veins are typically narrow fracture fillings of less than 1–2 cm width with concentric bands of euhedral anhydrite crystals; they appear to have formed during fewer than two or three episodes of vein filling. Locally, they may have pyritic halos but do not typically contain sulfides (e.g., see Fig. 41).

Variations in Vein Characteristics with Depth

The nature of the vein selvages and degree of hydrothermal interaction with the adjacent wallrock varies systematically with depth, and many of the textural and mineralogical characteristics of the pyrite breccias described above can be directly related to late-stage anhydrite veining (Fig. 42).

High-level Veins (Cores 158-957C-7N to 10N)

In the upper sections of the core from about 20 to 30 mbsf, the veins consist dominantly of anhydrite and are either crustiform banded or massive, often showing multiple generations of vein fill (see Fig. 41). These veins range from a few millimeters up to 40 cm in thickness. Wallrock contacts are sharp to diffuse and irregular, and commonly it is difficult to define the exact vein boundary. Pyrite and chalcopyrite occur in minor to trace quantities in the thicker veins,

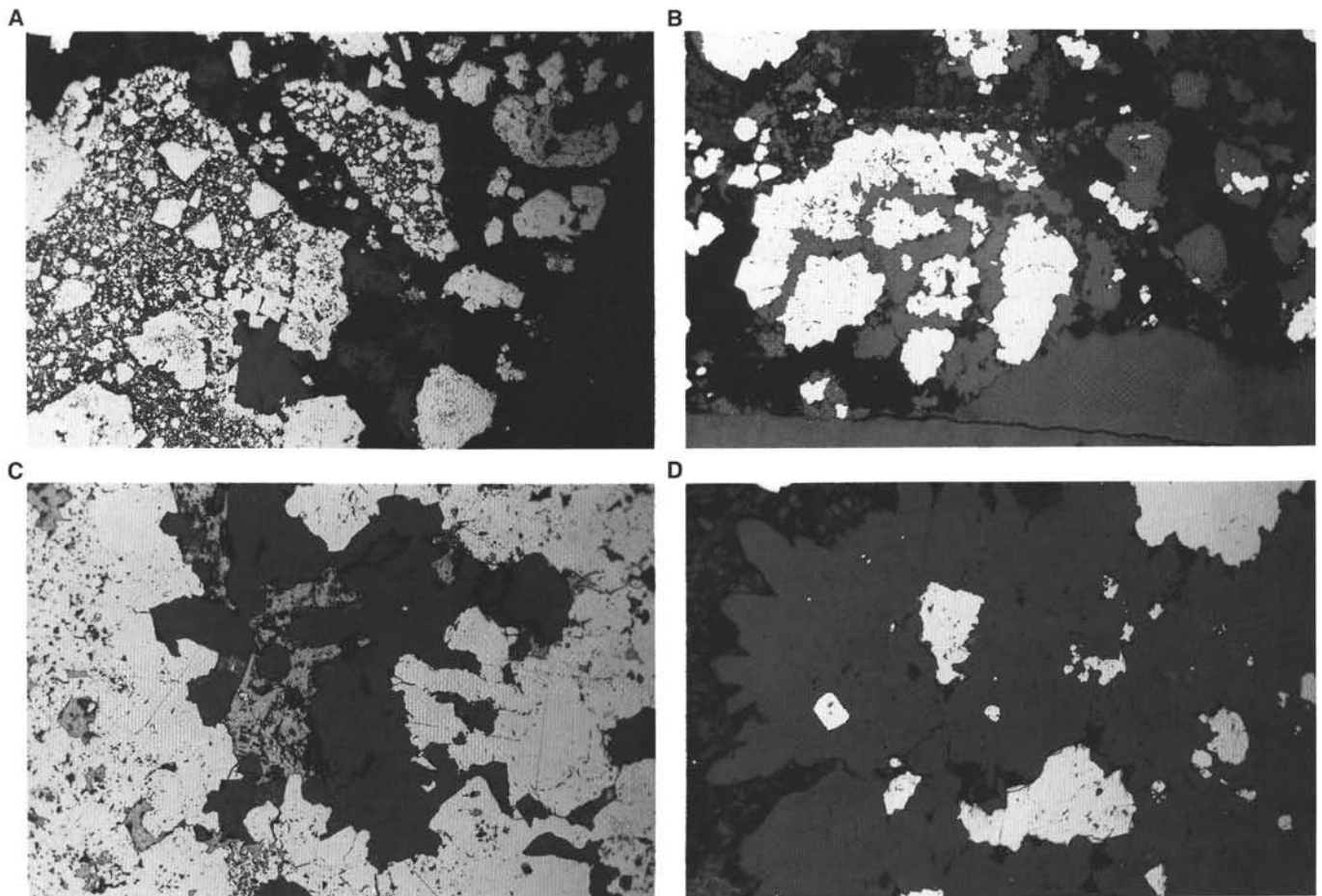


Figure 14. Representative photomicrographs of textures in nodular, siliceous pyrite-anhydrite breccias (Type 7c). **A.** Sand-sized, quartz-pyrite clasts rimmed by euhedral pyrite (white) and smaller pyrite-chalcopyrite aggregates in a matrix of anhydrite (dark gray with cleavage). Quartz (dark gray) occurs throughout the matrix. Sample 158-957C-7N-2 (Piece 1E, thin section from 64 to 77 cm). Reflected light, field of view = 6 mm. **B.** Sand-sized, pyrite-quartz clast in a matrix of anhydrite, pyrite, and quartz. The pyrite (white) and quartz (light gray) are overgrown by two generations of pyrite. Sample 158-957C-7N-1 (Piece 6F, thin section from 53 to 57 cm). Reflected light, field of view = 6 mm. **C.** Nodular pyrite clast with interstitial quartz (dark gray) and chalcopyrite (light gray). Sample 158-957C-7N-1 (Piece 6F, thin section from 53 to 57 cm). Reflected light, field of view = 1.5 mm. **D.** Close-up of euhedral quartz (dark gray) overgrowing and partially replacing disseminated pyrite (white) in a quartz-pyrite clast. Sample 158-957C-7N-1 (Piece 8D, thin section from 110 to 117 cm). Reflected light, field of view = 1.5 mm. **E.** Margin of a quartz-pyrite clast showing recrystallized pyrite rims (white) surrounded by euhedral quartz (gray). Similar quartz-pyrite clasts occur in pyrite-silica breccias (Type 9) and siliceous wallrock breccias (Type 10a) further downsection. Sample 158-957C-7N-1 (Piece 8D, thin section from 110 to 117 cm). Reflected light, field of view = 1.5 mm. **F.** Coarse granular, quartz-pyrite clast containing abundant disseminated, euhedral pyrite. Some of the larger aggregates of disseminated pyrite within the clast may also be detrital in origin, derived from earlier generations of pyrite sand. The quartz-pyrite clast is rimmed by euhedral pyrite with abundant chalcopyrite inclusions. Sample 158-957C-7N-2 (Piece 1E, thin section from 64 to 77 cm). Reflected light, field of view = 6 mm. **G.** Nodular pyrite clast showing recrystallized pyrite boundary and abundant interstitial chalcopyrite and euhedral quartz. Note the absence of inclusions in the outer recrystallized rim. Sample 158-957C-7N-2 (Piece 1E, thin section from 64 to 77 cm). Reflected light, field of view = 1.5 mm. **H.** Chalcopyrite-rich clast in the matrix of a nodular, siliceous pyrite-anhydrite breccia. The chalcopyrite clast is part of the disseminated sulfides in the anhydrite-rich cement of the breccia. The clast consists of porous chalcopyrite (light gray) with euhedral pyrite (white) and anhydrite (dark gray with cleavage) filling the pore spaces. Sample 158-957C-7N-1 (Piece 6F, thin section from 53 to 57 cm). Reflected light, field of view = 6 mm.

but thin veins are generally devoid of sulfides. Most veins show simple symmetrical zonation with crystal growth perpendicular to the walls of the veins (see Fig. 34). One thick vein displays multiple crosscutting generations of crustiform and massive anhydrite (see Fig. 34).

Fracturing adjacent to the veins is limited, implying a relatively incompetent wallrock, and the high porosity of the breccias favors diffuse flow of fluids outward from the veins. Widespread infiltration of anhydrite into the surrounding breccias is common (e.g., Fig. 7), replacing preexisting silica or anhydrite matrix and filling void space. Much of the anhydrite matrix in the pyrite-anhydrite breccias was

likely introduced in this manner. One vein contained in Samples 159-957C-7N-1 (Pieces 1D through 1H) displays a 1-cm-thick chalcopyrite selvage and a 4-cm-thick zone of pyritization, but this style of mineralization is not commonly associated with high-level veins.

Mid-level Veins (Cores 158-957C-11N to 13N)

Further downsection in Hole 957C, from about 30 to 40 mbsf, the anhydrite veins are thicker, up to 45 cm, with well-developed crustiform banding. These veins often show multiple generations of massive and crustiform-banded anhydrite, and an excellent example is seen in Samples 158-957C-11N-1 (Pieces 3I through 3L) (see Figs.

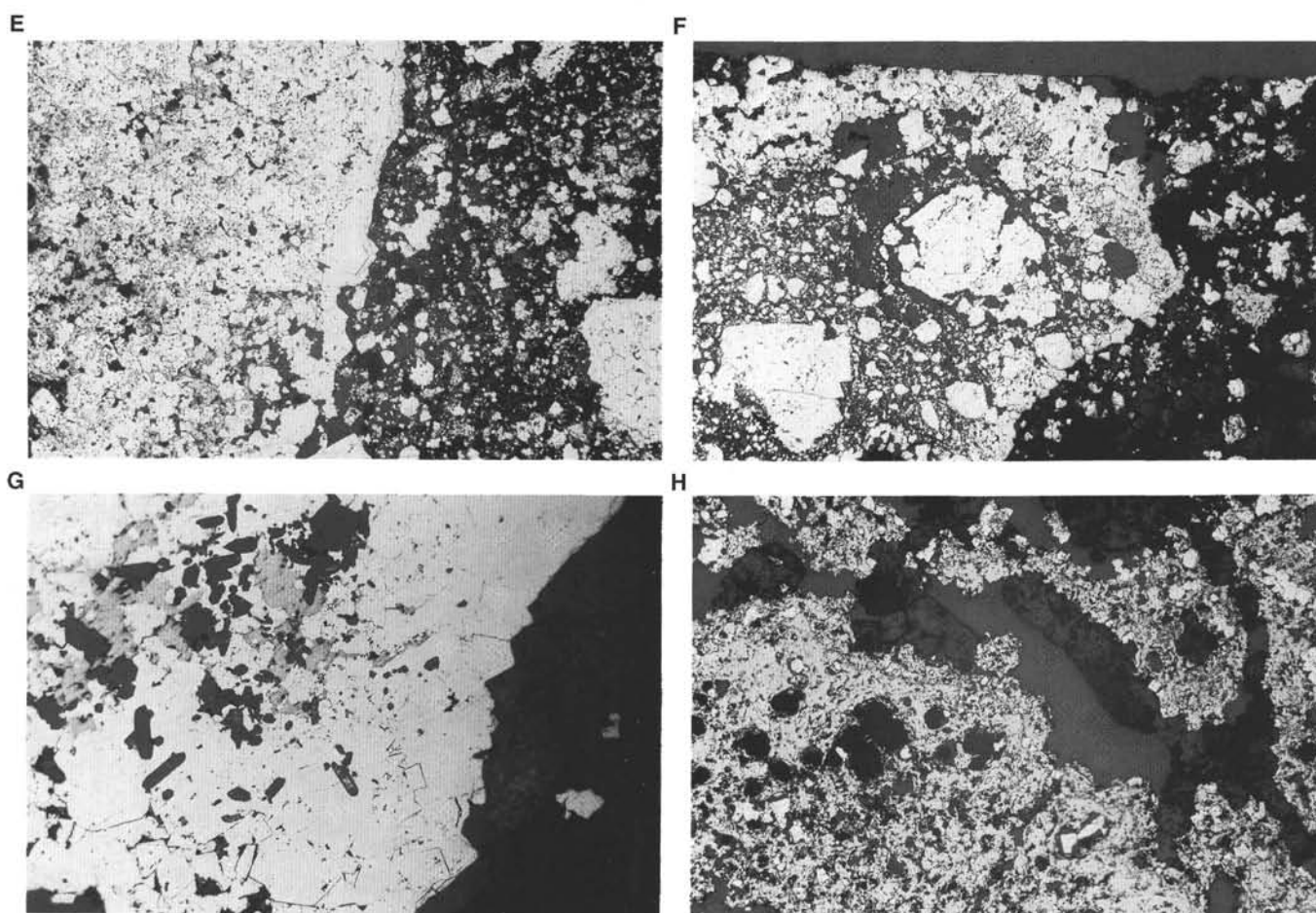


Figure 14 (continued).

35, 36). Wallrock contacts are sharp to diffuse and irregular. Fine-grained pyrite and chalcocopyrite occur in the veins and are often restricted to discrete bands near the wallrock contacts. Traces of hematite are present locally in the last generation of vein fill, and vugs with coarse-grained anhydrite crystals are common.

Mid-level veins are generally similar to the high-level veins but have extensive selvages and replacement halos. The selva generally consists of a 0.5- to 2-cm-thick band of chalcocopyrite that either rims or replaces pyrite in the wallrock. A broader pyritization halo extends up to 10 cm outward from the selva and replaces either silica or anhydrite in the clasts and matrix, giving the rock surrounding these veins a coarse-grained and semi-massive to massive appearance. The pyrite in this halo is often fractured and healed by anhydrite, which also extends outward from the vein. Microveinlets of anhydrite in the pyritization halo also commonly have discrete pyrite-chalcocopyrite selvages (Fig. 43). An excellent example of the chalcocopyrite selva and pyrite halo surrounding a crustiform anhydrite vein is seen in Samples 158-957C-13N-2 (Pieces 3B and 3C) (see Fig. 33). Small cavities, occasionally lined with pyrite grains, occur in many of the veins (see Fig. 35). These cavities may be a result of anhydrite dissolution similar to that occurring in massive anhydrite samples from the Black Smoker Complex on the surface of the mound (Tivey et al., 1995).

Deep-level Veins (Cores 158-957C-14N to 16N)

Anhydrite veining within the silicified wallrock breccias, below ca. 40 mbsf in Hole 957C, consists of relatively thin (several centi-

meters), crustiform-banded, white and gray anhydrite veins that are confined to well-defined, tight fractures (Fig. 44). Wallrock contacts are sharp and generally planar, and some veins contain angular clasts of wallrock, suggesting hydraulic fracturing. This style of veining is indicative of a fairly competent low-porosity wallrock.

Deep-level veins are commonly devoid of sulfides, but pyrite and chalcocopyrite occur locally on the selvages of the veins. The sulfides do not extend more than a few millimeter into the wallrock, and the broad pyritization halo is absent. The silicified wallrock breccias are not as extensively fractured as the pyrite breccias farther up section, and infiltration of anhydrite from the veins into the wallrock is rare. Examples of this style of veining are in Samples 158-957C-16N-1 (Pieces 3 and 5) and Sample 158-957C-15N-1 (Piece 11) (e.g., see Figs. 30, 45). In samples with multiple veins (see Fig. 45), the host rock is commonly shattered and healed by late anhydrite.

All anhydrite vein orientations were measured using the method outlined in the "Sulfide Petrology and Geochemistry" section of Chapter 5 (this volume), and the data are presented in Table 5. Relative to the core axis, the veins have dips that range from horizontal to subvertical with no preferred orientation dominating at any particular depth or within a particular set of anhydrite veins (Fig. 46). Without a reference marker, however, all orientations are artificial.

Hole 957E

Hole 957E penetrated to the greatest depth in the TAG hydrothermal system (125.7 mbsf) and gives the best record of the geology of

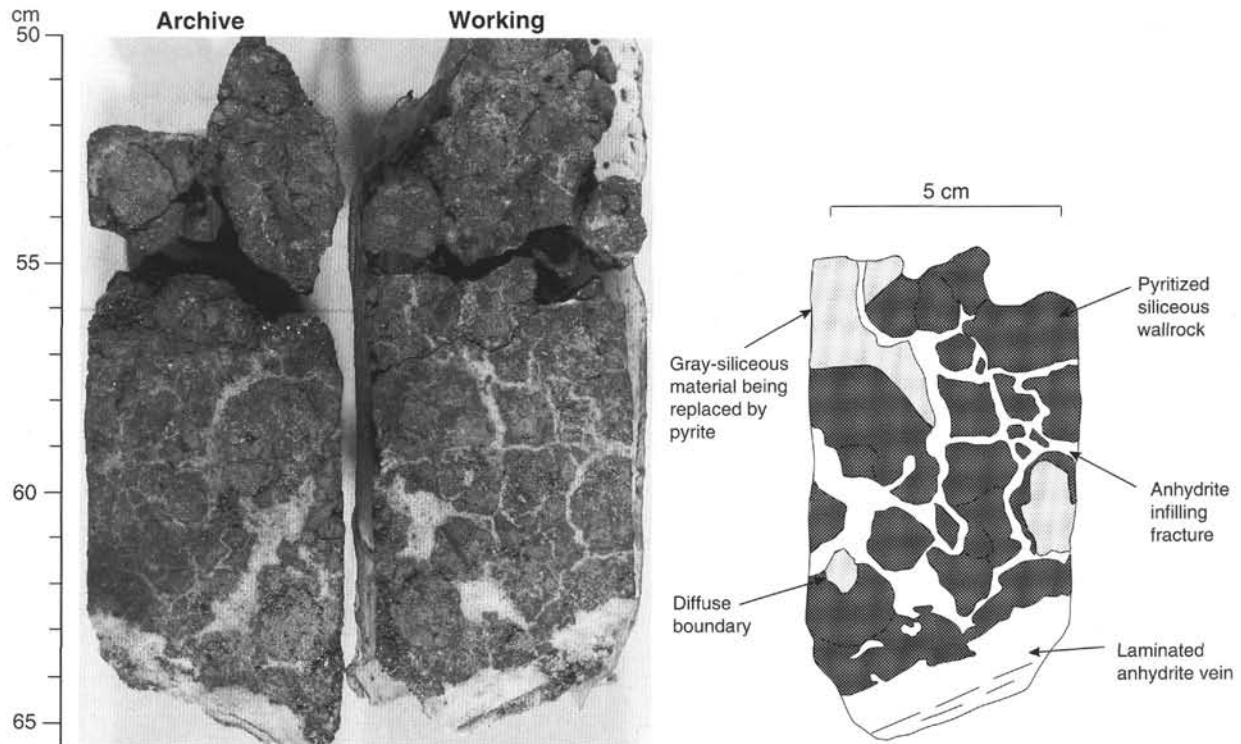


Figure 15. Photograph of archive and working halves and sketch of working half of vein-related pyrite-anhydrite breccia (Type 7d), showing infiltration of anhydrite into massive, brecciated pyrite adjacent to the vein. Sample 158-957C-12N-1 (Piece 6, 50–65 cm).

the lower portion of the hydrothermal mound and the upper portion of the stockwork zone. A listing of the visual core descriptions for Hole 957E is given in Table 6 (Sulfide Log, see back pocket) and an interpretive section of the hole is illustrated in Figure 1. Figure 47 is a detailed log of the core. Rock types recovered in Hole 957E include massive granular pyrite (Type 5c), pyrite-silica breccia (Type 9a), nodular pyrite-silica breccia (Type 9b), silicified wallrock breccia (Type 10a), and chloritized basalt breccia (Type 10b).

In general, nodular pyrite-silica breccias and light gray pyrite-silica breccias were the dominant rock types from 31.5 to 75 mbsf, with lesser amounts of silicified wallrock breccia and massive granular pyrite. Between 75 and 101 mbsf, silicified wallrock breccias were the dominant rock type recovered. In addition, minor amounts of massive granular pyrite and pyrite-silica breccias were recovered; these are a darker gray compared to pieces recovered from depths of <75 mbsf. Chloritized wallrock breccias dominate from 101 to 125.7 mbsf. In these cores, minor amounts of semi-massive granular pyrite, nodular pyrite-silica breccia, and pyrite-silica breccia were also recovered. Sample types are described below. Veins are common throughout the core from Hole 957E. Anhydrite is present on the exteriors of nearly all samples, suggesting a prevalence of anhydrite veins of unknown width (thickest layers on the exteriors of samples are 3 mm, but all samples are rollers). It is possible that samples preferentially broke along these veins.

Massive Granular Pyrite (Type 5c)

Pieces of massive granular pyrite (Type 5c) occur from 30 to 111 mbsf (Cores 158-957E-1R, 2R, 6R, 8R, 9R, 10R, 11R, and 15R). Massive granular pyrite samples are similar to those observed in cores from Hole 957C. In Hole 957E, very fine- to coarse-grained, colloform and euhedral pyrite makes up 60% to 95% of the samples, with minor amounts of chalcopyrite and anhydrite, <2%–30% quartz,

and trace amounts of iron oxide, sphalerite, and chlorite (Fig. 48). In thin section, colloform bands and aggregates of pyrite (Fig. 49) contain 1-mm anhedral chalcopyrite inclusions and trails of sphalerite inclusions that outline former pyrite grain boundaries. Inclusions of euhedral quartz and aggregates of chlorite are common, the latter filling void spaces within pyrite aggregates. Anhydrite is locally enriched within the interstices and around the rims of pyrite aggregates. The texture and mineralogy of samples in thin sections resemble those in clasts of pyrite-silica breccias in core from Hole 957C.

Pyrite-Silica Breccia (Types 9a and 9b)

Pyrite-silica breccias are found sporadically throughout the vertical extent of the core. Pyrite occurs as very fine- to medium-grained disseminated grains, aggregates, and masses in a matrix of very fine-grained white to gray quartz (Fig. 50). In thin section, fine- to coarse-grained pyrite and pyrite aggregates (with minor overgrowing chalcopyrite) are present in a matrix of quartz with low pore space (Fig. 51). Patches of smectite (50–500 μm) plus fine-grained granular quartz and pyrite are common and may represent highly altered basalt fragments. Traces of sphalerite and pyrrhotite occur as very small (<5–20 μm) anhedral inclusions in pyrite. These breccias resemble some of the silicified wallrock breccias found deeper in the core from Hole 957E (discussed below) and may represent more intensely silicified equivalents where the wallrock fragment textures have been completely overprinted. A variety of veins consisting of quartz, quartz-pyrite, and anhydrite-pyrite-chalcopyrite (discussed below) were observed in the pyrite-silica breccias. Pyrite-silica breccias in the core from Hole 957E are similar to those observed from 30.7 to 49.2 mbsf in core from Hole 957C.

Nodular pyrite-silica breccias (Type 9b) are primarily confined to the upper sections (Sections 158-957E-1R to 8R, 31.5–77.8 mbsf) of the core, although one occurrence was observed in Core 158-957E-

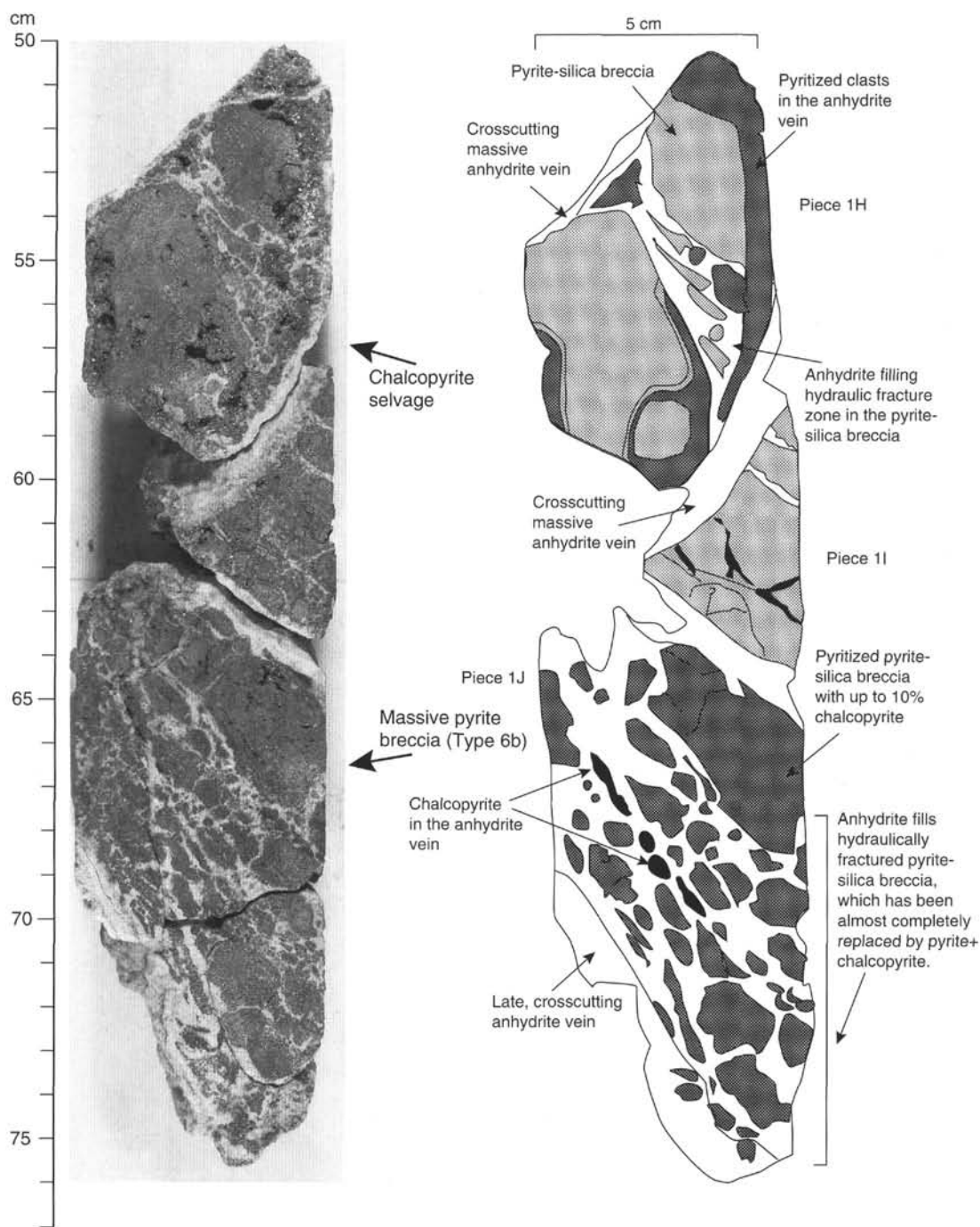


Figure 16. Photograph and sketch of massive to semi-massive, brecciated pyrite (Type 6b) associated with vein-related, pyrite-anhydrite breccias (Type 7d). Angular clasts of fine-grained, massive pyrite occur along the edges of the anhydrite veins and are extensively fractured. Interval 158-957C-11N-2 (Pieces 1H through 1K, 50–77 cm).

15R. These matrix-supported breccias are gray green and consist of small nodules and aggregates of pyrite in a matrix of white to gray quartz (Fig. 52). Pyrite nodules, up to 1 cm in diameter, contain pyrite and quartz with minor concentrations of disseminated chalcopyrite, and occasional rims of chalcopyrite or a second generation of pyrite. Rare, very fine-grained, soft green material (chlorite?) fills the pore space in pyrite. Dissolution(?) rims surround some pyrite clasts. Anhydrite veins with chalcopyrite selvages and pyritization halos are common.

Silicified Wallrock Breccia (Type 10a)

Silicified wallrock breccias occur below the pyrite-silica breccias in Hole 957E (Fig. 1). They consist of partially to completely silicified fragments of wallrock with individual grains and aggregates of pyrite set in a matrix of gray quartz with variable amounts of pyrite. Some wallrock clasts possess clear relict basaltic textures, but fragments can even appear as totally silicified clasts that retain little or no basaltic texture. Pyrite is present as 0.1- to 10-mm grains and aggre-

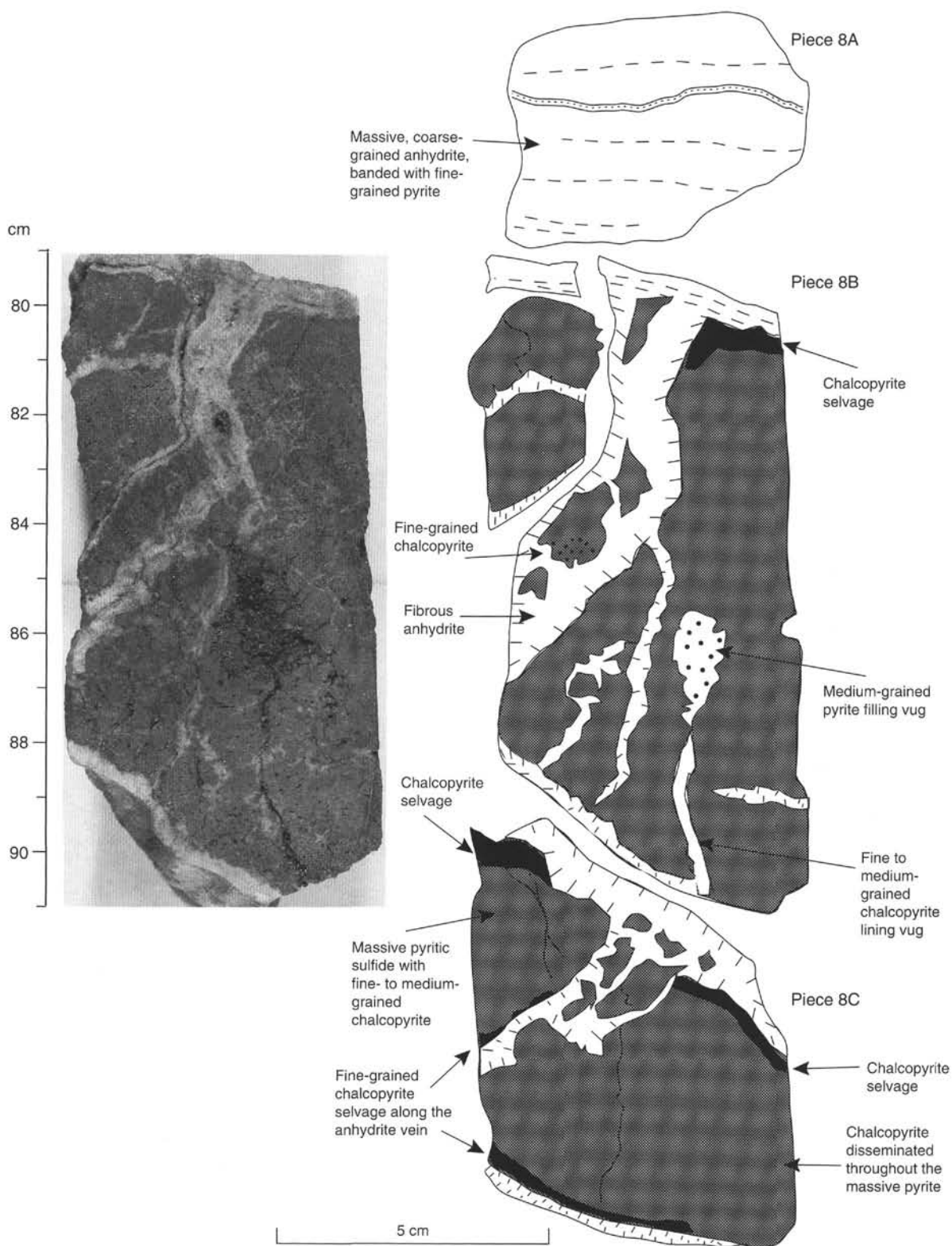


Figure 17. Photograph of the archive half of Sample 158-957C-11N-3 (Piece 8B, 79–91 cm) and sketch of the working half of Sample 158-957C-11N-3 (Pieces 8A and 8C), showing massive brecciated pyrite in Type 7d pyrite-anhydrite breccia. Fine-grained granular chalcopyrite (selvage) and pyrite (pyritization halo) occur adjacent to the veins.

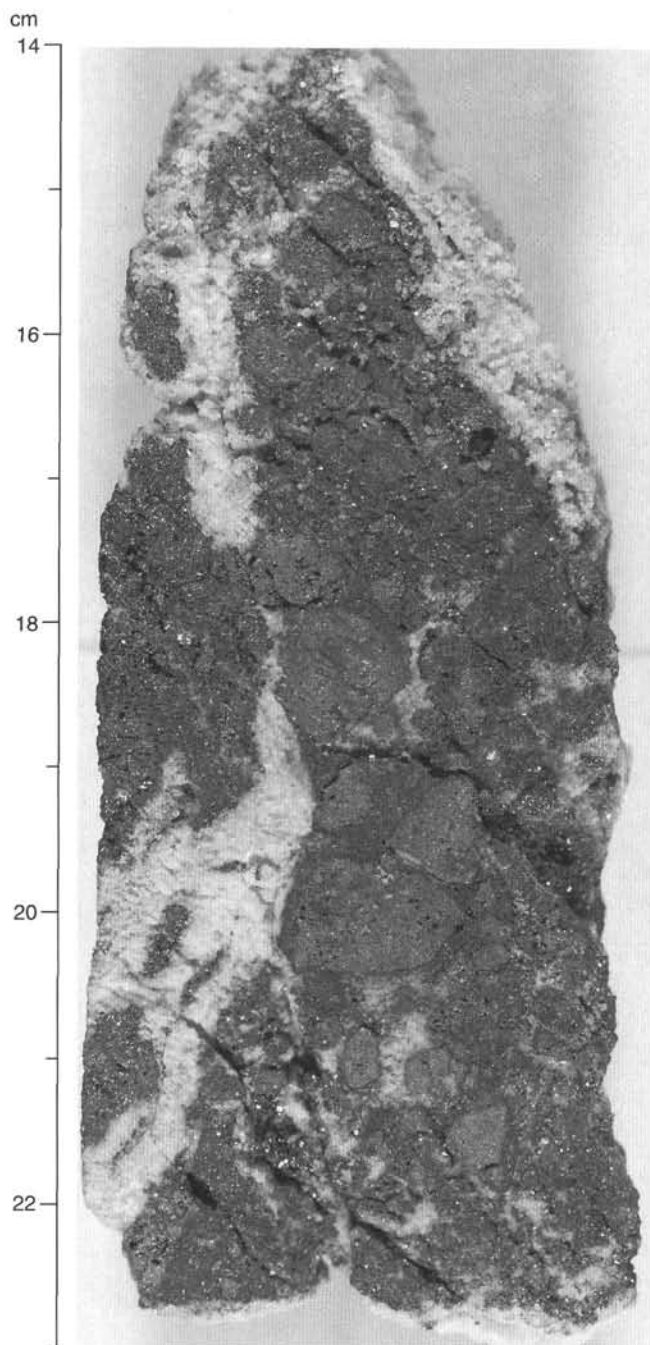


Figure 18. Pyrite-silica-anhydrite breccia (Type 8) with anhydrite veining. These breccias are similar to Type 7c nodular, siliceous pyrite-anhydrite breccias but are cemented by quartz and extensively veined by anhydrite. Sample 158-957C-12N-3 (Piece 2, 14–23 cm).

gates disseminated within the matrix of gray fine-grained quartz, and with white quartz in 0.1- to 5-mm veins that crosscut both clasts and matrix. Massive to semi-massive siliceous pyrite, with or without chalcopyrite, occurs both as isolated pieces and on the margins of some silicified wallrock breccia material (in Cores 158-957E-6R, 8R, 9R, and 11R) (Fig. 53). In thin section, pyrite grains replace basalt and are subsequently surrounded by quartz (Fig. 54). In some places, the replacement process appears to have started in vesicles of the ba-

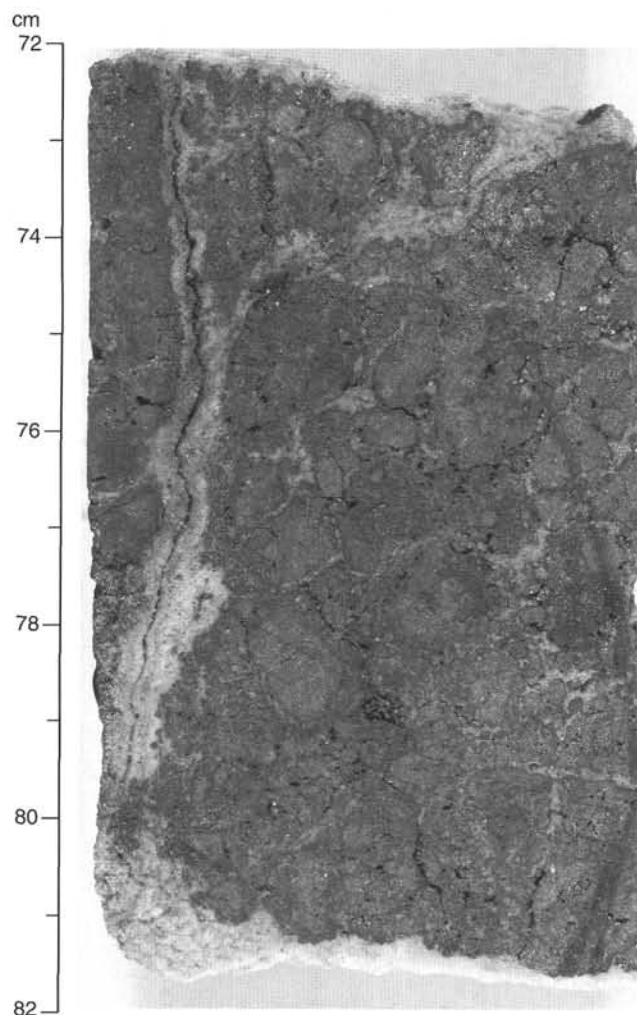


Figure 19. Pyrite-silica-anhydrite breccia (Type 8) showing a dense, gray silica matrix veined by anhydrite. Sample 158-957C-11N-1 (Piece 3G, 72–82 cm).

salt that have been preserved along with igneous textures (e.g., quartz pseudomorphs of plagioclase) in the pyrite (Fig. 55). Chalcopyrite and sphalerite inclusions in pyrite are rare relative to pyrite from cores recovered from higher up in Hole 957E. Trace amounts of anhydrite have been observed in the interstices between quartz and pyrite. The silicified wallrock breccias recovered from Hole 957E are similar to those from Hole 957C. A detailed description of the silicified wallrock breccias and their alteration characteristics is given in the “Hydrothermal Alteration” section (this chapter).

Chloritized Basalt Breccia (Type 10b)

Chloritized basalt breccias were recovered from Hole 957E and occur below the silicified wallrock breccias from 101 to 125.7 mbsf (Cores 158-957E-14R to 18R) (Fig. 1). Basalt fragments are recognizable through pervasive chlorite, clay (sericite?), and/or quartz alteration and are contained in a gray quartz-pyrite matrix and a vein stockwork. The alteration characteristics are discussed in the “Hydrothermal Alteration” section (this chapter). Pyrite occurs as 1- to 4-mm-wide zones, and chalcopyrite occurs as rims on the margins of altered basalt clasts (Fig. 56).

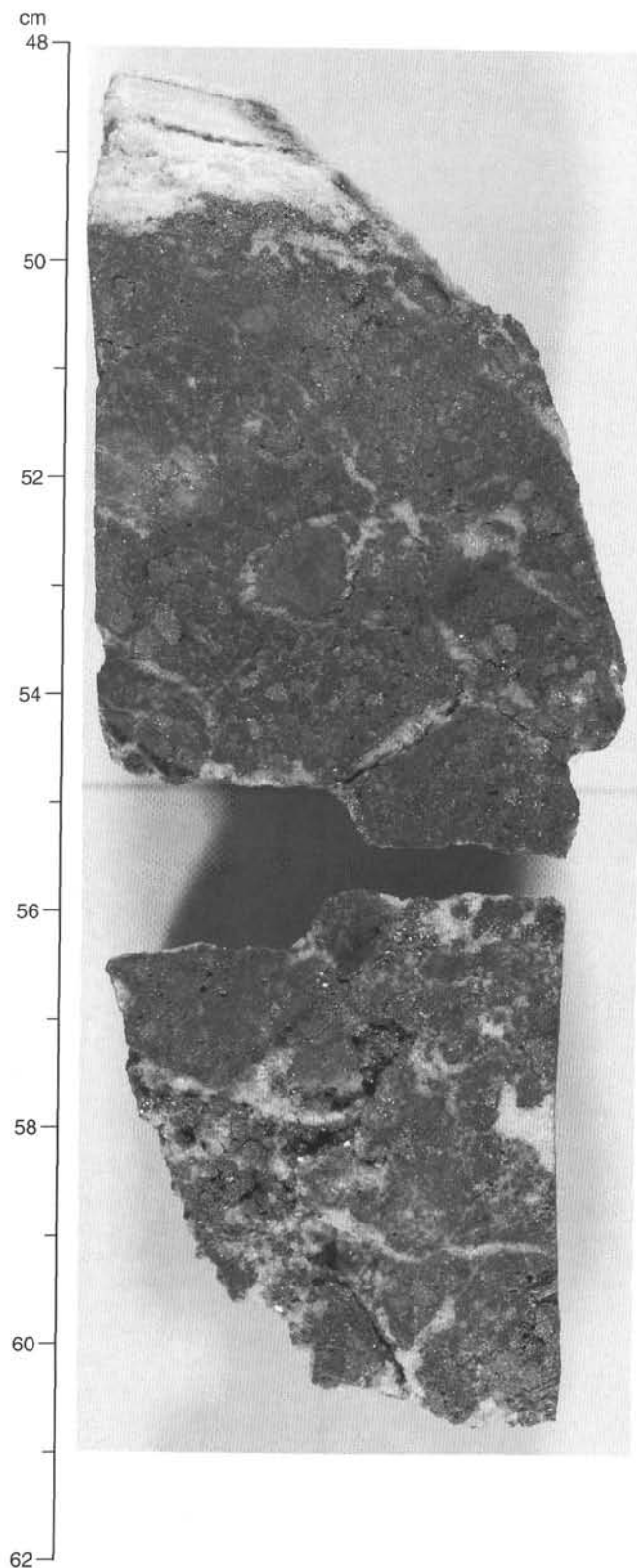


Figure 20. Pyrite-silica-anhydrite breccia (Type 8) showing late-stage brecciation of the gray siliceous matrix material. Sample 158-957C-12N-3 (Pieces 5 and 6, 48–62 cm).

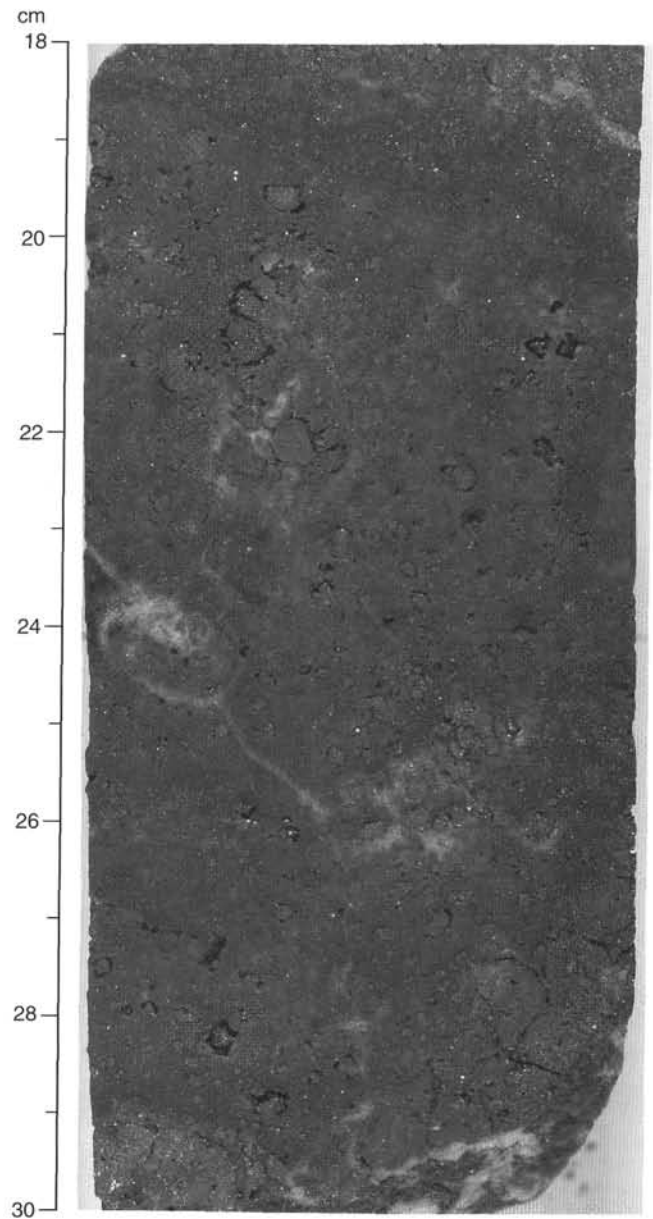


Figure 21. Pyrite-silica breccia (Type 9a) consisting of large fragments of fine-grained gray siliceous material set in a matrix of euhedral quartz. Sample 158-957C-11N-1 (Piece 3A, 18–30 cm).

In thin section, basalt clasts are cut by numerous 10- to 300- μm quartz and quartz plus pyrite veins. Pyrite is disseminated as millimeter-sized aggregates and individual crystals in veins, as small (100 μm) euhedral crystals in altered basalt (Fig. 57), and as discontinuous rims (up to 100 μm) surrounding basalt clasts. Chalcopyrite is enriched in veins as a late mineral (Fig. 58A) and in small veinlets in the altered basalt. Sphalerite and pyrrhotite are present in trace amounts as small inclusions (10 μm) in vein pyrite (Fig. 58B). Numerous leucoxene grains are present in the silicified groundmass. Some of these grains have an euhedral lozenge shape and may be titanite.

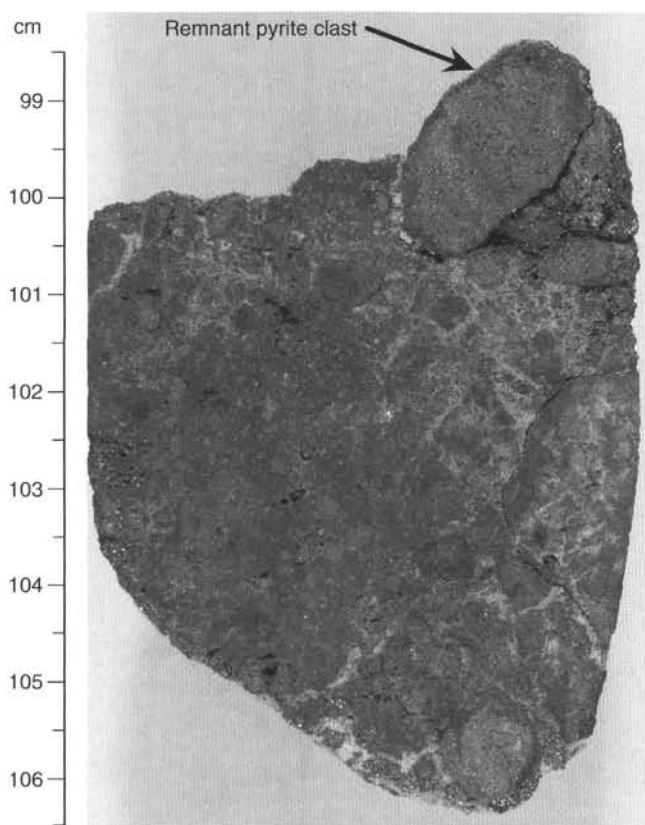


Figure 22. Large fragments of gray siliceous material and remnant pyrite clasts in pyrite-silica breccia (Type 9a). Sample 158-957C-13N-1 (Piece 17A, 98.5–106.5 cm).

Veining

Veining within Hole 957E cores consists of anhydrite veins in the upper portions of the core, passing downward into a quartz stockwork with late anhydrite veins. Within the quartz stockwork, five stages of veins have been defined, based on the mineralogy and crosscutting relationships (Fig. 59). The anhydrite veins (Type 11) discussed above correspond to Stage 5 veins in this description.

The earliest veins recognized (Stage 1) are 0.5-mm veins of dark green chlorite occurring within fragments of green chloritized basalt (Fig. 60). These veins are cut by later pyrite plus quartz veinlets that have associated gray to buff alteration halos.

Stage 2 is characterized by large (0.5–3 cm) veins of gray quartz with abundant disseminated pyrite and local chalcopyrite. The matrix material between altered wallrock fragments has the same mineralogy and is considered equivalent to the Stage 2 veins (Fig. 61). The Stage 2 veins are also texturally and mineralogically identical to the dark gray pyrite-silica breccias, but they are distinguished by their veinlike morphology and the presence of alteration halos. Buff alteration halos (0.5 cm wide) are common in the green chloritized basalt. Where rocks are uniformly gray chloritized basalt, alteration surrounding veins extends sufficiently far into the wallrocks so that the alteration is pervasive (Fig. 61). Some Stage 2 veins have coarse, granular, pyrite selvages.

Stage 3 consists of <2- to 3-mm-wide, pyrite-filled fractures (Fig. 61). These veinlets commonly have a 1- to 2-mm halo of buff clays or chlorite and pyrite, locally with minor quartz. Although the pyrite-filled fractures are separated into a distinct vein stage, no crosscutting relationships with Stage 1 and 2 veins were observed and no temporal relationships are implied.

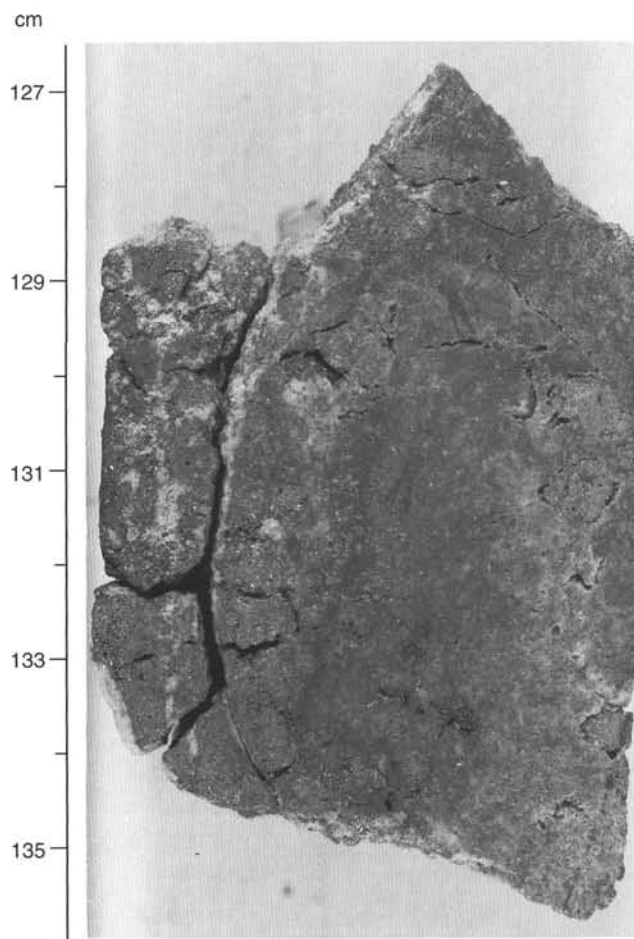


Figure 23. Large fragment of gray siliceous material in pyrite-silica breccia (Type 9a) showing partial replacement of the clast boundary by pyrite. Sample 158-957C-13N-1 (Piece 22, 127–136 cm).

White quartz and pyrite are the primary constituents of the Stage 4 veins. These veins range in width from 0.3 to 1 cm and have been divided into three substages. The three substages are separated on the basis of mineralogy only and are all considered to be related to the same general stage of vein formation. Substage 4a quartz-pyrite veins consist of euhedral white quartz with disseminated pyrite along the center or margins of the vein (Fig. 62). Substage 4b is dominated by pyrite with lesser amounts of quartz (Figs. 62, 63). White quartz veins, some with minor amounts of pyrite, characterize Substage 4c (Figs. 63, 64). Stage 4 veins are locally vuggy and commonly have a weak chloritic or buff (clays plus quartz) alteration halo.

Stage 5 consists of anhydrite veins, many of which have a chalcopyrite selvage and pyritization halo (Fig. 65). Stage 5 veins correspond to the Type 11 anhydrite veins discussed above and are identical to the middle-level anhydrite veins described in the Hole 957C core. A Stage 5 vein cutting massive granular pyrite is shown in Figure 66.

Many of the pieces of chloritized basalt breccia recovered from Hole 957E have 1- to 3-mm, continuous to discontinuous coatings of anhydrite, chalcopyrite, and pyrite on broken outer surfaces. These are most likely remnants of Stage 5 anhydrite veins.

Holes 957F and 957G

Holes 957F and 957G were drilled to recover the uppermost part of the TAG hydrothermal mound in the TAG-1 area. Cores from

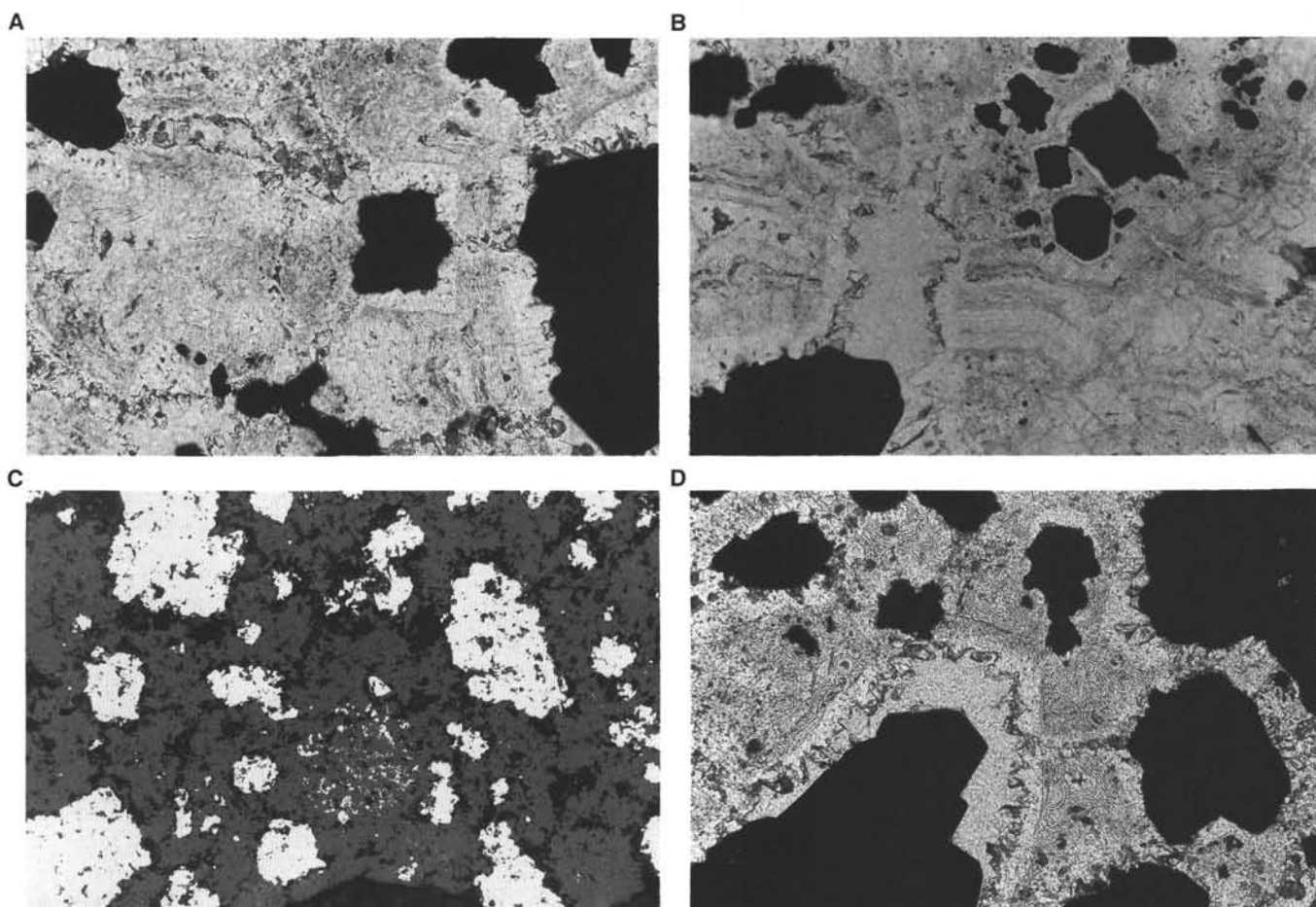


Figure 24. Representative photomicrographs of textures in pyrite-silica breccias (Type 9). **A.** Disseminated pyrite in quartz-pyrite clasts in pyrite-silica breccias. Coarse-grained recrystallized pyrite aggregates (white) are set in a matrix of euhedral quartz (dark gray). The euhedral quartz contains rare inclusions of sulfides (pyrite and chalcopyrite). Sample 158-957C-14N-1 (Piece 2, thin section from 18 to 20 cm). Reflected light, field of view = 1.5 mm. **B.** Colloform-banded quartz overgrowing disseminated pyrite grains (black). Later euhedral quartz has grown into open spaces. Sample 158-957C-15N-4 (Piece 4, thin section from 48 to 50 cm). Transmitted light, field of view = 1.5 mm. **C.** Multiple stages of colloform-banded and euhedral quartz matrix cementing disseminated pyrite aggregates (black). Euhedral pyrite is partly pseudomorphed by euhedral quartz, preserving irregular pyrite cores. Sample 158-957C-15N-4 (Piece 4, thin section from 48 to 50 cm). Transmitted light, field of view = 1.5 mm. **D.** Euhedral quartz overgrowing and partially replacing disseminated pyrite in a quartz-pyrite aggregate. Later, colloform-banded quartz fills open spaces and contains a later generation of pyrite (black). Sample 158-957C-15N-4 (Piece 4, thin section from 48 to 50 cm). Transmitted light, field of view = 1.5 mm.

Holes 957F and 957G together may be considered as forming a continuous section between 1.0 and 25.0 mbsf (Fig. 1). The following types of hydrothermal mineralization are present: (1) massive granular pyrite (Type 5c); (2) massive granular chalcopyrite (Type 5d), which is associated with porous massive pyrite; (3) nodular pyrite breccia (Type 6a); (4) pyrite-anhydrite breccia (Type 7a); and (5) siliceous pyrite-anhydrite breccia (Type 7c). A graphic log of the core is shown in Figure 67, and a listing of the visual core descriptions for Holes 957F and 957G is given in Table 7 (see back pocket).

Massive Granular Pyrite (Type 5c)

Massive granular pyrite (Type 5c) occurs in the cores recovered from below 5.0 mbsf in Hole 957F and between 12.0 and 16.5 mbsf in Hole 957G. These samples are unoriented rollers, 2 to 6 cm in diameter, coated with minor chalcopyrite and anhydrite, and may be clasts from nodular pyrite breccias (Fig. 68). Pyrite encloses patches of massive and disseminated chalcopyrite, and euhedral quartz grains or aggregates. The pyrite is generally coarse and recrystallized, and

contains scattered sphalerite inclusions (Fig. 69A). Late amorphous silica (containing very fine-grained, disseminated pyrite) was observed in pores within pyrite aggregates (Fig. 69B). The clasts in Section 158-957G-1N-1 appear less recrystallized and contain lower amounts of chalcopyrite than those in Section 158-957F-2N-1. These clasts are composed of porous colloform pyrite (Fig. 70). Complex, multiple colloform and polycrystalline growth layers with sphalerite and chalcopyrite inclusions are visible in polished thin section (Fig. 71).

Massive Granular Chalcopyrite (Type 5d)

Massive granular chalcopyrite (Type 5d) occurs as unoriented pieces in Core 158-957F-1N between 1.0 and 5.5 mbsf (Section 158-957F-1N-1). The chalcopyrite is mostly fine- to very fine-grained, but it also occurs as coarse, bladed, euhedral crystals and massive aggregates. The more massive samples (interval 158-957F-1N-1, Pieces 2–4) have a distinctive porosity, manifested as 1- to 2-mm tubular structures. Some samples are zoned (Samples 158-957F-1N-

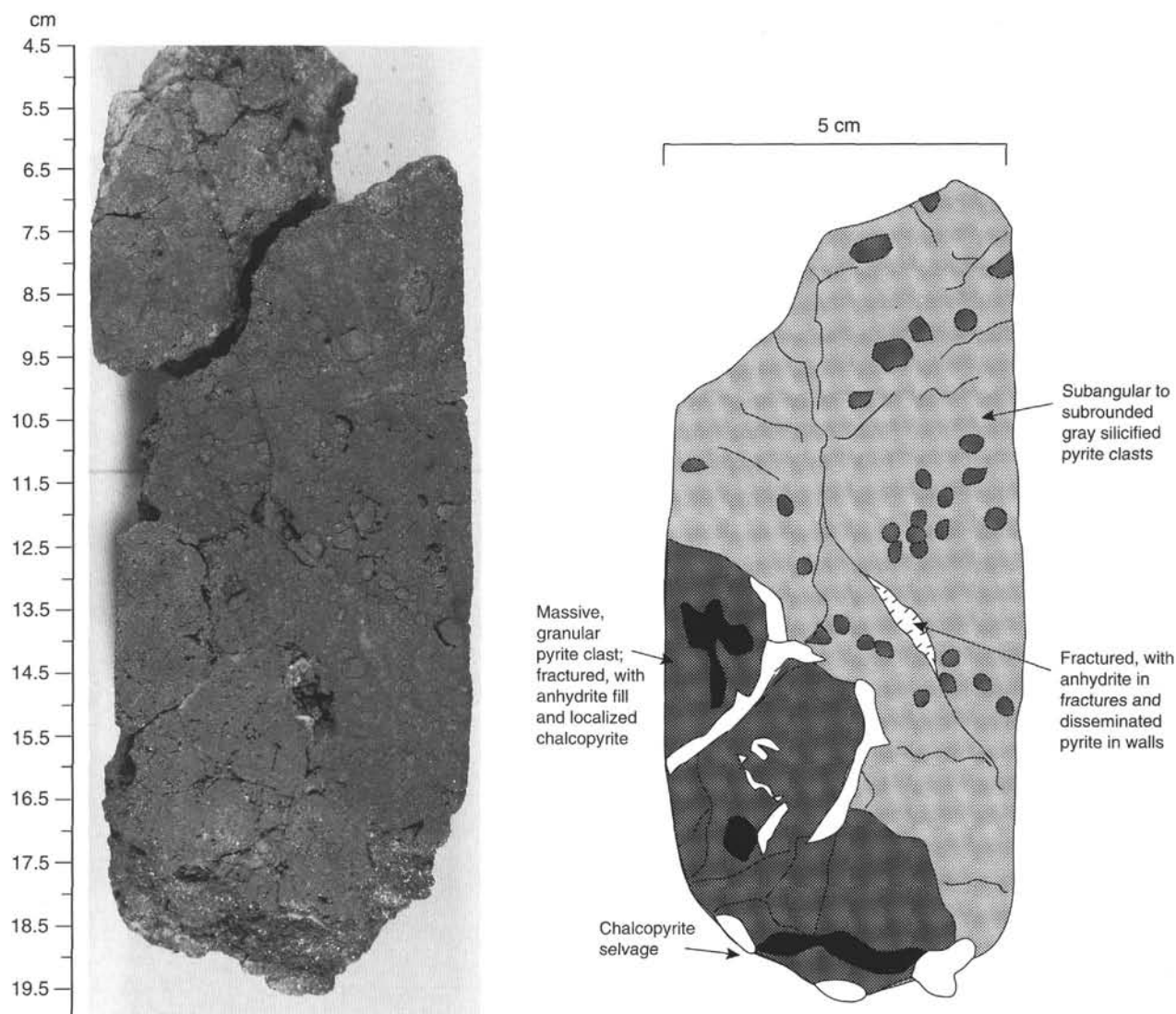


Figure 25. Photograph and sketch of Sample 158-957C-14N-1 (Piece 2, 4.5–20 cm), showing typical nodular, pyrite-silica breccia (Type 9b). The nodular pyrite aggregates occur in large clasts of gray siliceous material, and the coarse-grained pyrite is part of a pyritization halo adjacent to an anhydrite vein (not shown).

1, Pieces 1, 2, 5, and 6), with a chalcopyrite-dominated zone (up to 99% chalcopyrite) overgrown by a 1- to 6-mm growth layer of pyrite or marcasite grading out from fibrous or dendritic texture to a colloform or spherulitic carapace, and an outer layer of Fe-oxide (Fig. 72). This zonation and texture is similar to that of samples of massive sulfide crusts, or horizontal layers, recovered from the mound surface on the upper terrace, that is, on the Black Smoker Complex (Tivey et al., 1995). The presence of bladed chalcopyrite crystals indicates open space growth, either into vugs within the crust mineralization, or into black smoker conduits. However, it was not possible to distinguish between chimney and crust morphology in the samples recovered. Other samples of cemented pyrite sand and fine-grained, porous massive pyrite with varying proportions of chalcopyrite, sphalerite, and silica (Samples 158-957F-2N-1, Piece 1, and 158-957G-1N-1, Piece 2) were recovered from deeper within the hole (5.5 and 12.1 mbsf, respectively). Their mineralogy, texture, and occurrence as isolated pieces suggests that they are surface samples that may have fallen into the hole.

Pyrite Breccias (Types 6 and 7)

Nodular Pyrite Breccias (Type 6a)

The nodular pyrite breccias (Type 6a) sampled between 1.5 and 21.0 mbsf are similar in mineralogy and texture to those described between 15.0 and 30.0 mbsf in Hole 957C. In Section 158-957F-1N-1 (Pieces 8–10), the rock is grain supported with minor anhydrite (<10 vol%) in a fine-grained, pyrite-dominated matrix (Fig. 73). The main clast component is massive granular pyrite (up to 3 cm), some with porous chalcopyrite cores and pyrite rims. In polished thin section, most pyrite occurs as fine to coarse euhedral grains or aggregates (Fig. 74). The rims and porous cores of these clasts are partially filled and replaced by chalcopyrite. The angular chalcopyrite clast shown in Figure 73 is similar in texture to the innermost, monomineralic chalcopyrite lining of black smoker chimneys. Only one piece of breccia matrix material was recovered in the drilled intervals below 5.0 mbsf in Hole 957F and between 12.0 and 16.5 mbsf in Hole 957G (Section 158-957G-1N-1, Piece 6). This piece contains a high pro-

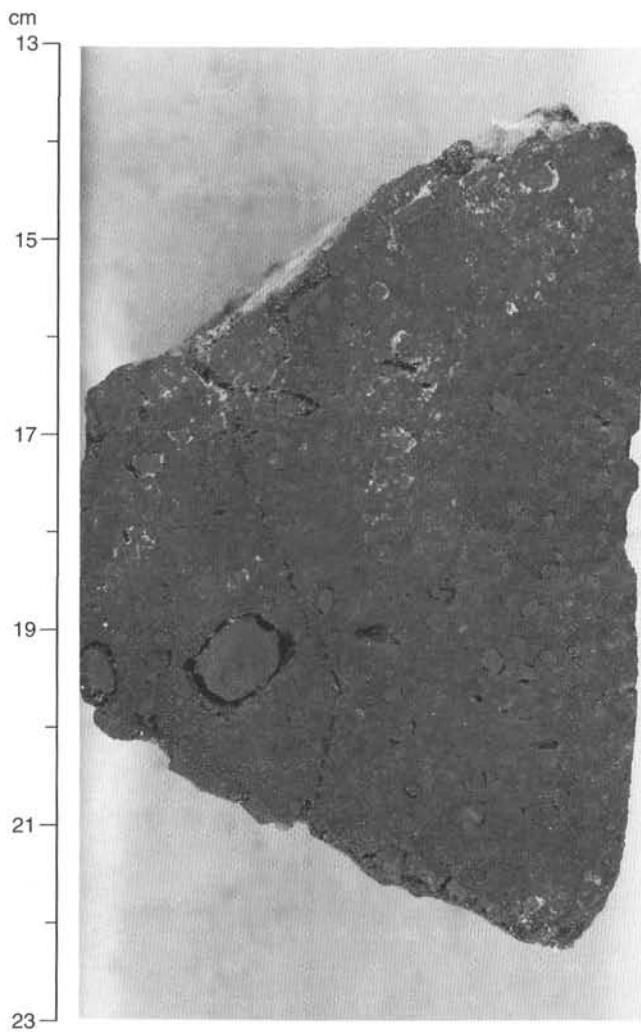


Figure 26. Close-up of nodular pyrite aggregates in nodular, pyrite-silica breccia (Type 9b). Apparent dissolution cavities occur around the pyrite clasts and some vugs are filled by late anhydrite. Sample 158-957C-16N-1 (Piece 3, 13–23 cm).

portion of anhydrite (10 vol%), which is present in the matrix and in small, irregular, 1-mm vein networks.

Massive Pyrite-Anhydrite Breccias (Type 7a)

Massive pyrite-anhydrite breccias (Type 7a) were recovered below 16.5 mbsf in Hole 957G (Samples 158-957G-2N-1, Piece 1, and -3N-1, Piece 2) (Fig. 75). A change from grain- to matrix-supported texture and an increase in the amount of anhydrite in the matrix with depth were observed. Pyrite in the matrix is generally much coarser grained than in the nodular pyrite breccias higher in the core and is associated with localized chalcopryrite aggregates. Some clasts have chalcopryrite cores or contain patches of disseminated quartz. A single piece (clast?) of massive granular pyrite from 16.55 mbsf contains an angular piece of silicified, altered basalt (Fig. 76), which is the highest stratigraphic occurrence of this clast type in the TAG-1 area.

Nodular, Siliceous Pyrite-Anhydrite Breccias (Type 7c)

Nodular, siliceous pyrite-anhydrite breccias (Type 7c) were recovered below 21 mbsf in the lowest part of Core 158-957G-3N

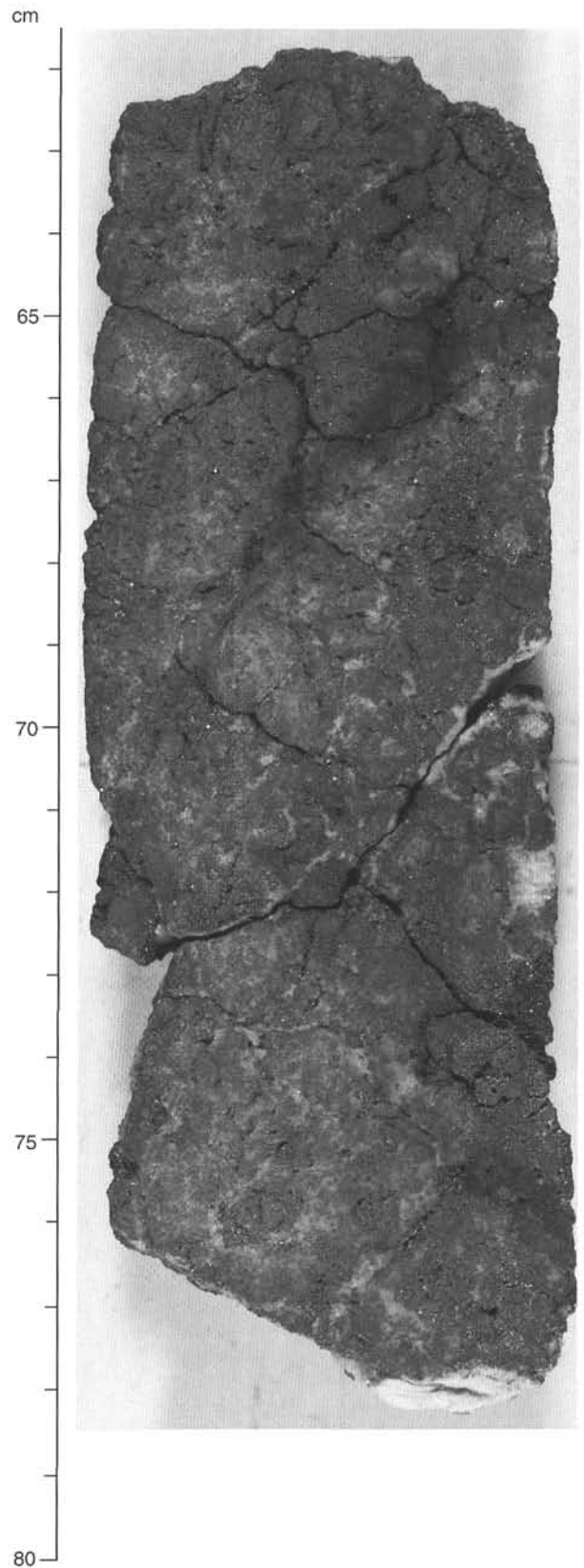


Figure 27. Silicified wallrock breccia (Type 10a) consisting of fine-grained silicified basalt clasts in a quartz-rich matrix. Silicification has obscured some clast boundaries, and the fragments are overprinted by later pyrite. Sample 158-957C-15N-1 (Pieces 9A to 9C, 61.5–80 cm).

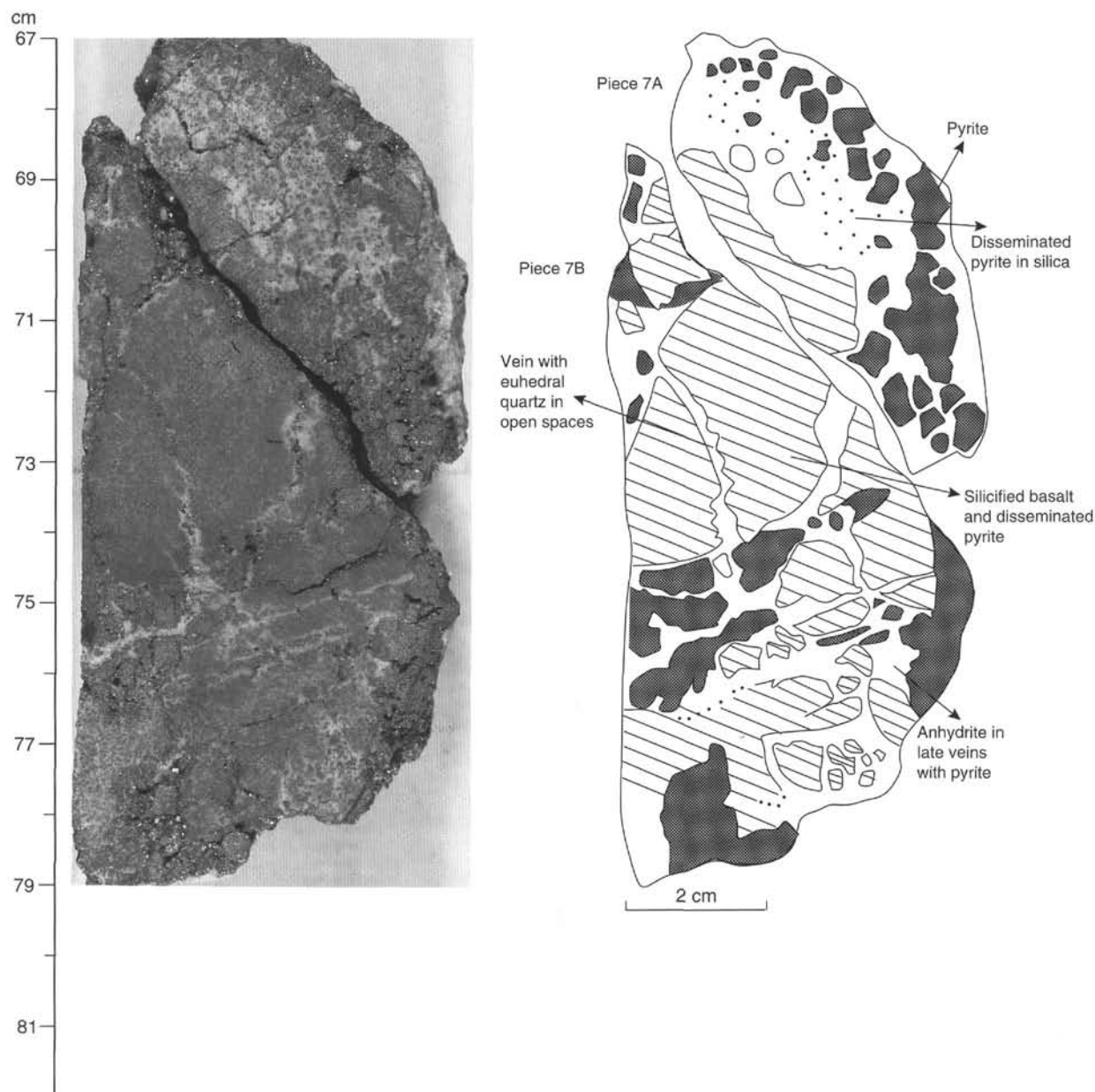


Figure 28. Photograph and sketch of silicified wallrock breccia (Type 10a) showing veinlets of euhedral quartz within fractures in the wallrock fragments and later pyrite-anhydrite veins. Sample 158-957C-16N-2 (Pieces 7A and 7B, 67–82 cm).

(Sample 158-957G-3N-1, Piece 4) (Fig. 77). The breccia is characterized by the presence of pyrite-quartz clasts in a matrix of anhydrite. The clasts are rounded to subrounded, 0.5 to 3.0 cm in size, and occasionally brecciated or rimmed by pyrite. Subangular clasts of silicified, altered wallrock and rounded pieces of red chert are minor components within this lithology (Fig. 78).

Sulfide Geochemistry

Introduction

The chemical compositions of 20 samples taken for AAS and sulfur analyses from Holes 957C, 957E, and 957F are presented in Table 8. Concentrations of S, Fe, Cu, Zn, Pb, Ag, and Cd were determined using the techniques outlined in the "Sulfide Petrology and Geochemistry" section of Chapter 5 (this volume). Three samples

were analyzed for Au by ASV (see "Sulfide Petrology and Geochemistry" section, Chapter 5, this volume). Samples were selected from depths of about 1.3 to 91.95 mbsf. The top of the stratigraphic column (1.3–5.6 mbsf) is represented by 2 samples from Cores 158-957F-1N and 2N. The intermediate levels from about 15 to 48 mbsf are represented by 16 samples from 9 cores from Hole 957C. Two samples from Cores 158-957E-9R and 12R represent the bottom of the profile, at 78.2 and 91.95 mbsf (Table 8).

Large ranges in metal contents were measured, reflecting the extreme mineralogical heterogeneity of the samples and the variable dilution of sulfides by anhydrite and silica. The Fe contents of the samples range from 20.1 to 40.8 wt% and reflect the overall abundance of pyrite in the core. The S content varies from 30.4 to 47.5 wt% and is a measure of the total amount of sulfides and anhydrite in a sample. Variations in S content are mainly the result of dilution by

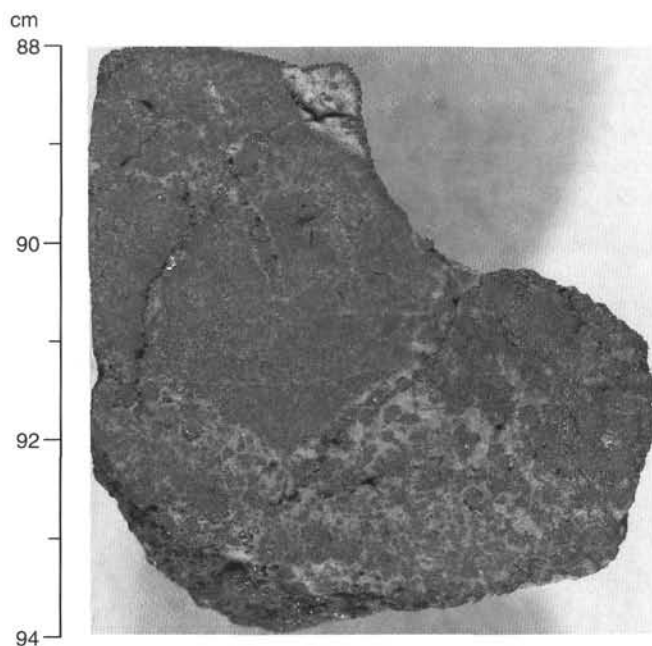


Figure 29. Close-up of silicified wallrock fragment in Type 10a breccia showing the quartz-rich matrix with abundant disseminated pyrite. Sample 158-957C-16N-2 (Piece 9A, 88–93.5 cm).

S-free minerals, such as silica and Fe-oxides. Cu contents are significantly lower, ranging from 0.01 to 6.0 wt%. Zn reaches nearly 0.2 wt% in one sample, but is generally low (<700 ppm). The concentrations of the trace metals Pb, Ag, and Cd are low and often at, or close to, their detection limits (Table 8). They range from <4 to 26, from 2.3 to 5.1, and from <0.1 to 1.2 ppm, respectively.

Chemical Composition of the Different Sulfide Types

The rock types analyzed by AAS include massive granular pyrite (Type 5c), nodular pyrite breccia (Type 6a), pyrite-anhydrite breccia (Types 7a, 7c, and 7d), pyrite-silica-anhydrite breccia (Type 8), pyrite-silica breccia (Type 9a), and silicified wallrock breccia (Type 10a). The large range of bulk compositions for individual sulfide types and overlapping concentration ranges among different types reflects the complexity of the mineral assemblages at a small scale.

Massive Granular Pyrite (Type 5c)

In the TAG-1 area, this rock type is represented by two samples, one from near the top of the sulfide mound (Sample 158-957F-2N-1, Piece 3), the other from the bottom of the profile (Sample 158-957E-9R-1, Piece 4). Their typical chemical features are high Fe (31.7–36.4 wt%) and S (35.8–44.7 wt%) contents, but low Zn (<0.032 wt%), Pb (<17 ppm), Ag (<5 ppm), and Cd (<0.1 ppm) concentrations. The samples show large differences in Cu concentrations. The sample at 78.2 mbsf has low contents of 0.65 wt%, whereas the sample from the top of the mound at 5.6 mbsf has high concentrations of 5.63 wt% because of the presence of higher proportions of chalcopyrite.

Nodular Pyrite Breccia (Type 6a)

One sample of nodular pyrite breccia (Sample 158-957F-1N-1, Piece 8) was analyzed and has high Fe (31.2 wt%), S (42.4 wt%), and Cu (5.63 wt%) but low Zn (300 ppm), Ag (5.1 ppm), Pb (15 ppm), and Cd (<0.1 ppm) concentrations (Table 8). This composition is similar to that of the massive granular pyrite described above.

Pyrite-Anhydrite Breccias (Types 7a, 7c, and 7d)

Seven samples of pyrite-anhydrite breccias were analyzed (Table 8), and they show little variation in bulk composition either between the subtypes or with depth. They typically have bulk Fe contents of 26–38 wt% and bulk Cu contents of 0.72–6.0 wt%. The high average Cu concentration (3.4 wt%) likely reflects the abundance of disseminated chalcopyrite in the matrix and in pyrite clasts within the breccias in the upper part of the core (e.g., Sample 158-957C-7N-1, Piece 6F) and in crosscutting anhydrite veins in the lower part of the core (e.g., Samples 158-957C-11N-3, Piece 8C, and 16-N-1, Piece 15). Concentrations of Zn (30–750 ppm), Ag (3.4–5.0 ppm), and Pb (10–26 ppm) vary widely and are generally low, but with slight enrichments over other sulfide types in the TAG-1 area. Sample 158-957C-11N-1 (Piece 8c) has a bulk gold content of approximately 250 ppb Au.

Pyrite-Silica-Anhydrite Breccias (Type 8)

Three samples of pyrite-silica-anhydrite breccias were taken for analysis from a relatively narrow zone (31.2–36.9 mbsf). They have a narrow range of Cu contents (2.0–2.6 wt%), but variable Fe (23.3–33.2 wt%), S (34.3–45.1 wt%), Zn (60–1830 ppm), and Cd (<0.3–1.2 ppm), and low Ag (<3.6 ppm) and Pb (<18 ppm) concentrations. Sample 158-957C-12N-2 (Piece 6) has the highest Zn (0.18 wt%) and Cd (1.2 ppm) content measured in samples from the TAG-1 area (0.18 wt%), corresponding to trace amounts of sphalerite present in the core.

Pyrite-Silica Breccia (Type 9a)

Three pyrite-silica breccias from a 2-m-wide zone between 40.5 and 42.5 mbsf were analyzed (Table 8). They have moderately high Fe contents (30–36 wt%) similar to those of pyrite-anhydrite breccias, but low Cu contents (<1.7 wt%). The concentrations of trace metals in these samples are close to their detection limits.

Silicified Wallrock Breccia (Type 10a)

Four samples of silicified wallrock breccia were selected for chemical analyses. Based on their composition, they have been divided into two groups. Samples 158-957C-15N-2 (Piece 1B) and 15N-3 (Piece 11), collected at 43.2 and 45.6 mbsf, respectively, have among the lowest S (30.4–34.3 wt%) and Fe (20.1–26.7 wt%) contents observed in all samples analyzed on board. They also have low concentrations of Cu, Zn, Ag, Pb, and Cd, which are all close to, or below, detection limits. These low metal concentrations are caused by the presence of larger proportions of silica-rich, altered basalt fragments.

The two remaining samples were collected near the bottom of the stratigraphic column (47.8 and 91.95 mbsf). They have bulk compositions similar to those of pyrite-silica breccias. Samples 158-957C-16N-2 (Piece 2) and 158-957E-12R-1 (Piece 3) contain abundant pyrite, as indicated by their higher Fe (34–40.8 wt%) and S contents (43.1–47.1 wt%) when compared with the other two samples of this type. This indicates that the sample aliquots taken from the core for chemical analyses mainly consist of the sulfide fraction of the sample. Thus, these aliquots are not representative of the bulk composition of this rock type.

Chemical Variations Along a Stratigraphic Profile in the TAG-1 Area

Variations in the metal and S contents with depth are illustrated in Figure 79. Concentrations of Cu, Ag, and Pb are erratic but, within the constraints of the sampling, appear to decrease slightly with increasing depth below about 35 mbsf (i.e., below the anhydrite-rich zone). Metal concentrations are particularly low in the anhydrite-rich vein material from Core 158-957C-12N and in quartz-rich breccias from Core 158-957C-15N. The increase in the abundance of chalcopyrite in vein selvages below about 35 mbsf is not reflected in the

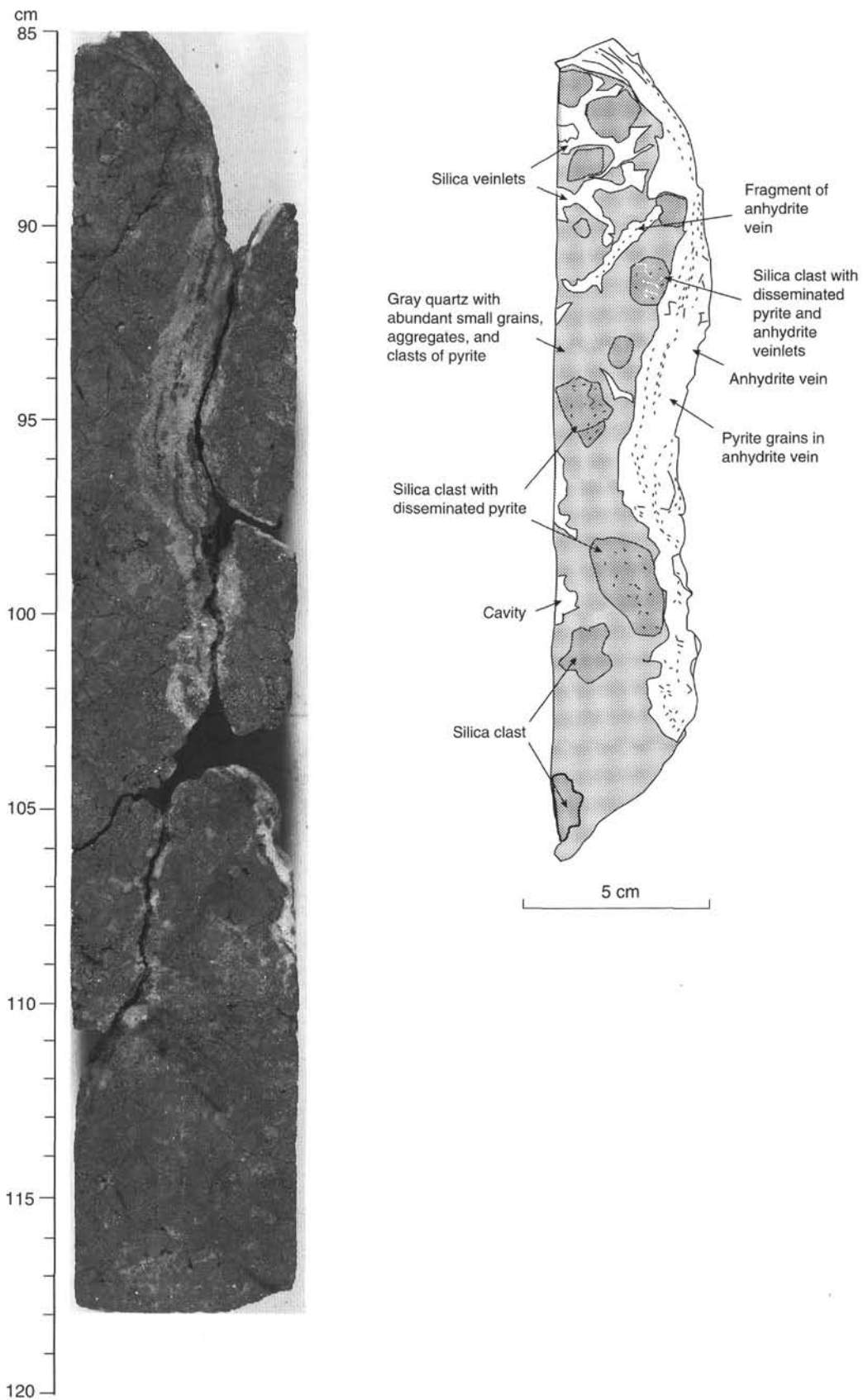


Figure 30. Photograph of interval 158-957C-15N-1 (Pieces 11A through 11F, 85–120 cm) and sketch of Sample 158-957C-15N-1 (Piece 11A), showing siliceous wallrock breccia (Type 10a), which consists of small (<5 cm) fine-grained, siliceous wallrock fragments in a quartz-rich matrix cut by a late anhydrite vein. The vein is a typical example of the deep-level anhydrite veining discussed in the text and illustrated in Figure 42.

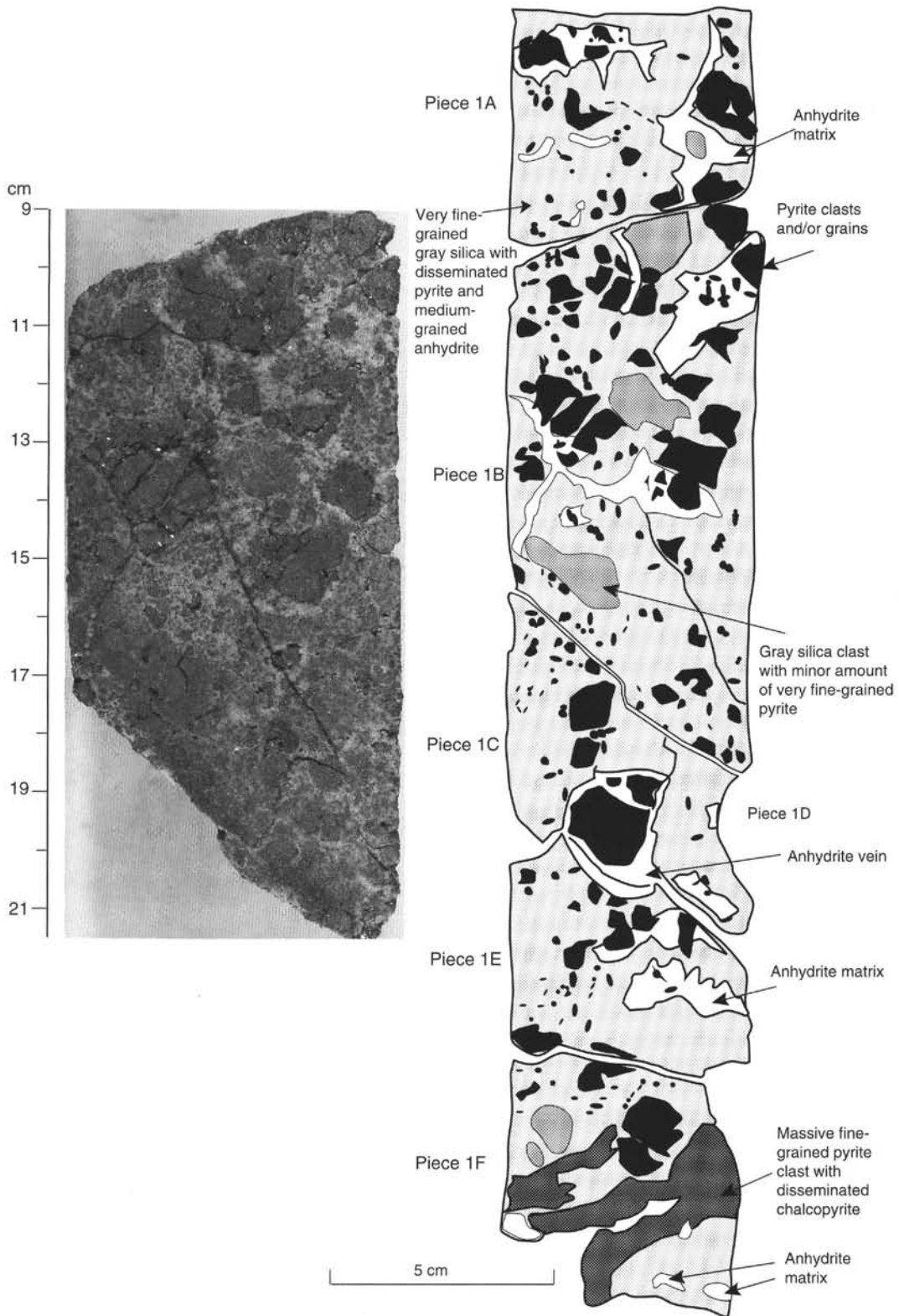


Figure 31. Photograph of Sample 158-957C-15N-2 (Piece 1B, 9–21 cm) and sketch of Sample 158-957C-15N-2 (Pieces 1A through 1F), showing siliceous wallrock breccia (Type 10a) in which some of the fragments are replaced by quartz.

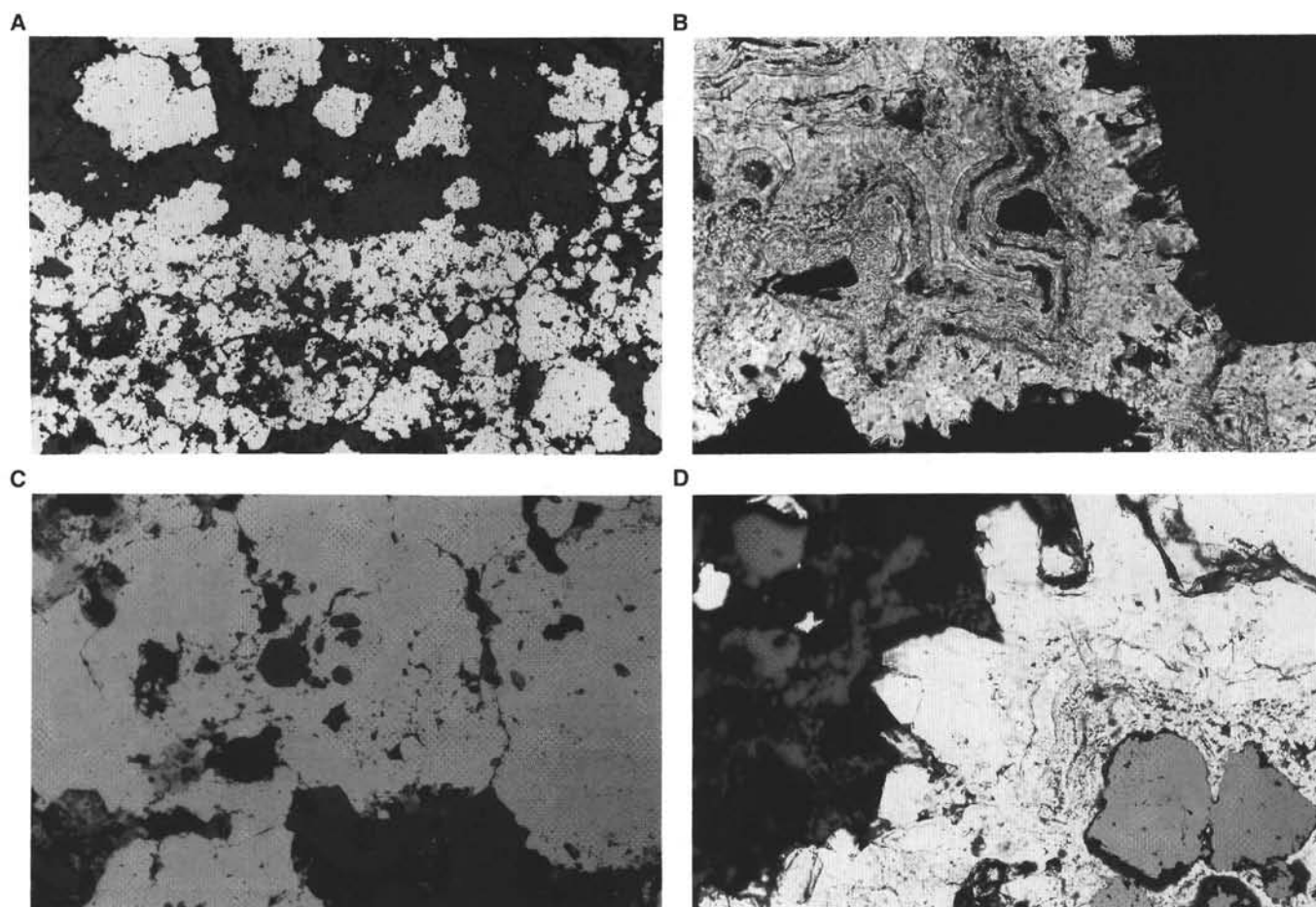


Figure 32. Representative photomicrographs of textures in silicified wallrock breccia (Type 10a). **A.** Margin of a typical coarse-grained quartz-pyrite aggregate in a quartz matrix (dark gray) within a silicified wallrock fragment. Sample 158-957C-16N-2 (Piece 1B, thin section from 6 to 8 cm). Reflected light, field of view = 6 mm. **B.** Overgrowth of euhedral and colloform-banded quartz on disseminated pyrite in a silicified wallrock fragment. Quartz has locally replaced the margins of the pyrite aggregates. Sample 158-957C-16N-2 (Piece 1B, thin section from 6 to 8 cm). Transmitted light, field of view = 0.75 mm. **C.** Granular pyrite aggregate (white) with interstitial chalcopyrite (light gray) in a silicified wallrock fragment. Note the euhedral quartz contained within the pyrite. Sample 158-957C-16N-2 (Piece 1B, thin section from 6 to 8 cm). Reflected light, field of view = 0.75 mm. **D.** Euhedral quartz overgrowing earlier colloform quartz. Colloform-banded quartz is overgrowing pyrite disseminated within the silicified wallrock fragment. Sample 158-957C-16N-2 (Piece 1B, thin section from 6 to 8 cm). Combined transmitted and reflected light, field of view = 0.75 mm.

samples selected for analysis. Zinc shows a peak in bulk concentration at about 37 mbsf, and some Zn-rich samples contain high Cd. However, well-defined correlations between the different metals were not obvious in the shipboard data.

One of the striking features of the rock types from the TAG-1 area is their very low Zn, Pb, Ag, and Cd contents despite high total sulfide concentrations in the samples (Table 8). This is in contrast to metal contents measured in samples from near the top of the sulfide mound in the TAG-2 area (Section 158-957B-1R-1) and in chimneys currently being formed at the surface in the Kremlin area, but is similar to metal contents measured in chimneys being formed at the surface of the mound on the Black Smoker Complex (e.g., Tivey et al., 1995). Table 9 compares the metal contents of two samples from Hole 957C (their compositions reflect the metal range observed in the TAG-1 area) with data from Section 158-957B-1R-1 from the metal-rich outer part of the sulfide mound in the Kremlin area. It indicates that the pyrite breccias and stockwork mineralization in core from Hole 957C (TAG-1 area) are several orders of magnitude lower in all metals except Fe, compared to samples from the lower terrace of the

mound (TAG-2 area). They also have much lower Au contents—less than 250 ppb (Sample 158-957F-1N-1, Piece 8, contains 230 ppb Au; Sample 158-957C-11N-3, Piece 8C, contains 250 ppb Au)—compared to about 3 ppm Au observed in Section 158-957B-1R-1.

Variations in absolute metal concentrations are difficult to interpret because of the dilution effects caused by metal-poor major constituents, such as anhydrite and silica, in some rock types. These effects can be minimized by looking at metal ratios. In addition, the Cu/Zn (chalcopyrite-sphalerite) zonation is one of the most definitive features of modern massive sulfide deposits on the seafloor and fossil VMS deposits on land (Franklin et al., 1981). Figure 79 shows the variation of selected metal ratios (Cu/Fe, Zn/Fe, Zn/Cu) in core samples recovered from the TAG-1 area. The Cu/Fe ratio varies from 0.0005 to 0.18 and tends to increase toward the top of the stratigraphic profile (Fig. 79). Thus, samples below 45 mbsf have Cu/Fe ratios < 0.1, whereas samples from above 30 mbsf generally have (with one exception) Cu/Fe ratios > 0.1. Between 30 and 45 mbsf, the pyrite-silica-anhydrite breccia appears to be a transitional zone with regard to Cu/Fe ratios, which range from 0.05 and 0.15. The pattern dis-

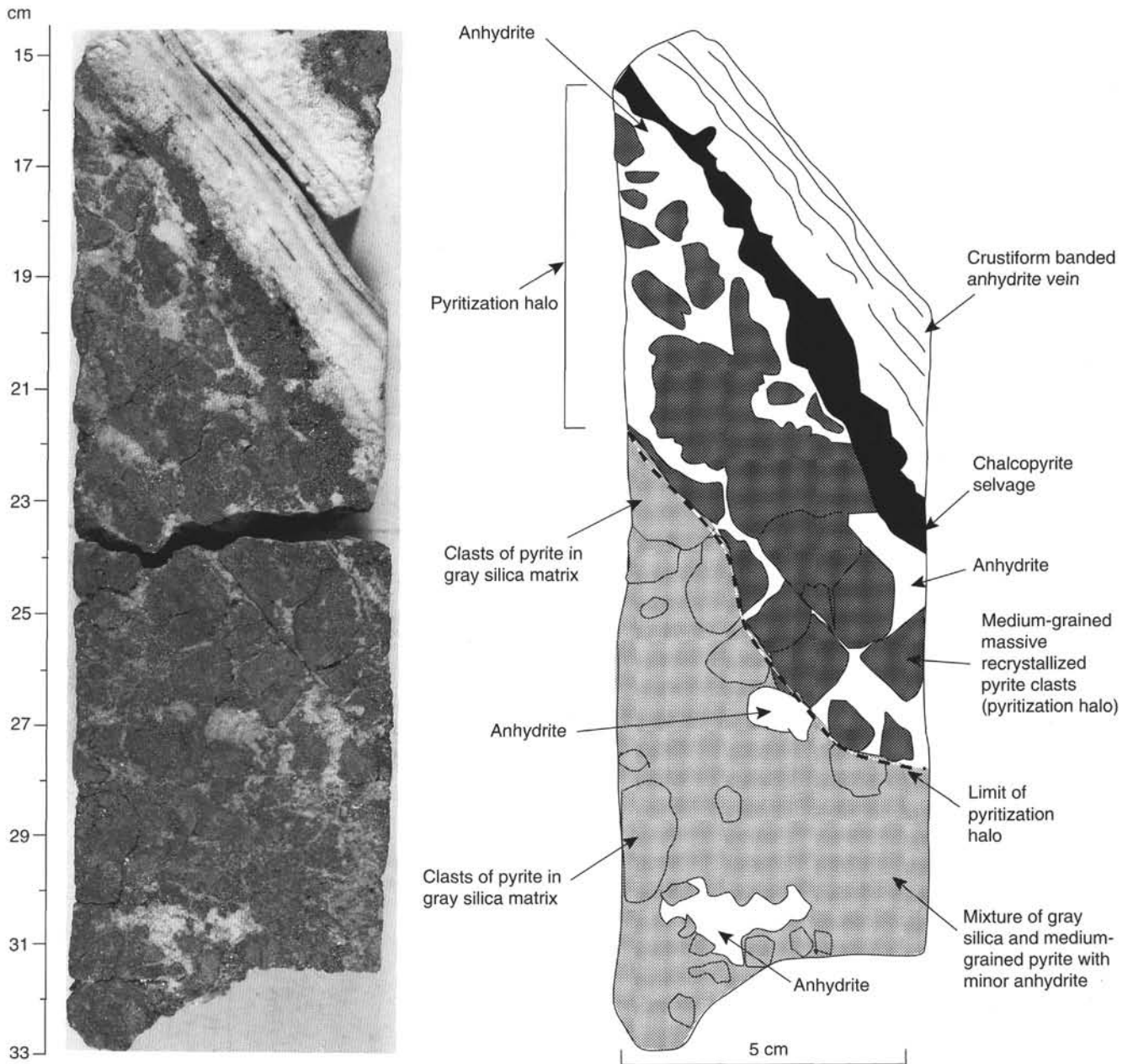


Figure 33. Photograph and sketch of a crustiform-banded anhydrite vein (Type 11) with a chalcopyrite selvage and surrounding pyritization halo. This is the type example of a middle-level anhydrite vein as discussed in the text and shown on Figure 42. Sample 158-957C-13N-2 (Pieces 3B and 3C, 14.5–33 cm).

played by the Cu/Fe ratio reflects variations in Cu concentrations, which are commonly lower than 2 wt% below 40 mbsf but increase to about 6 wt% above 40 mbsf (Fig. 79).

The patterns displayed by the Zn/Fe and Zn/Cu ratios are different in that these ratios are low at the bottom and the top of the stratigraphic profile but show an obvious maximum in between. This maximum is built up from samples belonging to the zone consisting of pyrite-silica-anhydrite breccias (Fig. 79). It is best outlined by the Zn/Cu ratio, which ranges from 0.02 to 0.2 in the transitional zone but which is 2–20 times lower below and above it. The high ratio is the result of the enrichment of Zn relative to Cu. An increase of the Zn concentrations at this level from <0.05 to 0.2 wt% occurs in Hole 957C.

The high Zn/Fe and Zn/Cu ratios most likely reflect the precipitation of minor amounts of sphalerite together with pyrite and chal-

copyrite. This occurs close to the zone where anhydrite first occurs as a major constituent of the rock matrix, that is, at the boundary of the siliceous wallrock breccia and the pyrite-silica-anhydrite breccia. The precipitation of large amounts of anhydrite suggests that this boundary zone represents a location where cold seawater can penetrate into the TAG mound and mix with circulating hydrothermal fluid. The increase in the Cu/Fe, Zn/Fe, and Zn/Cu ratios as well as the increase in Zn and Cu concentrations at this boundary suggest co-precipitation of anhydrite, pyrite, chalcopyrite, and sphalerite.

Summary

Cores from Holes 957C, 957E, 957F, and 957G provide information on the geology of the hydrothermal mound and the upper por-

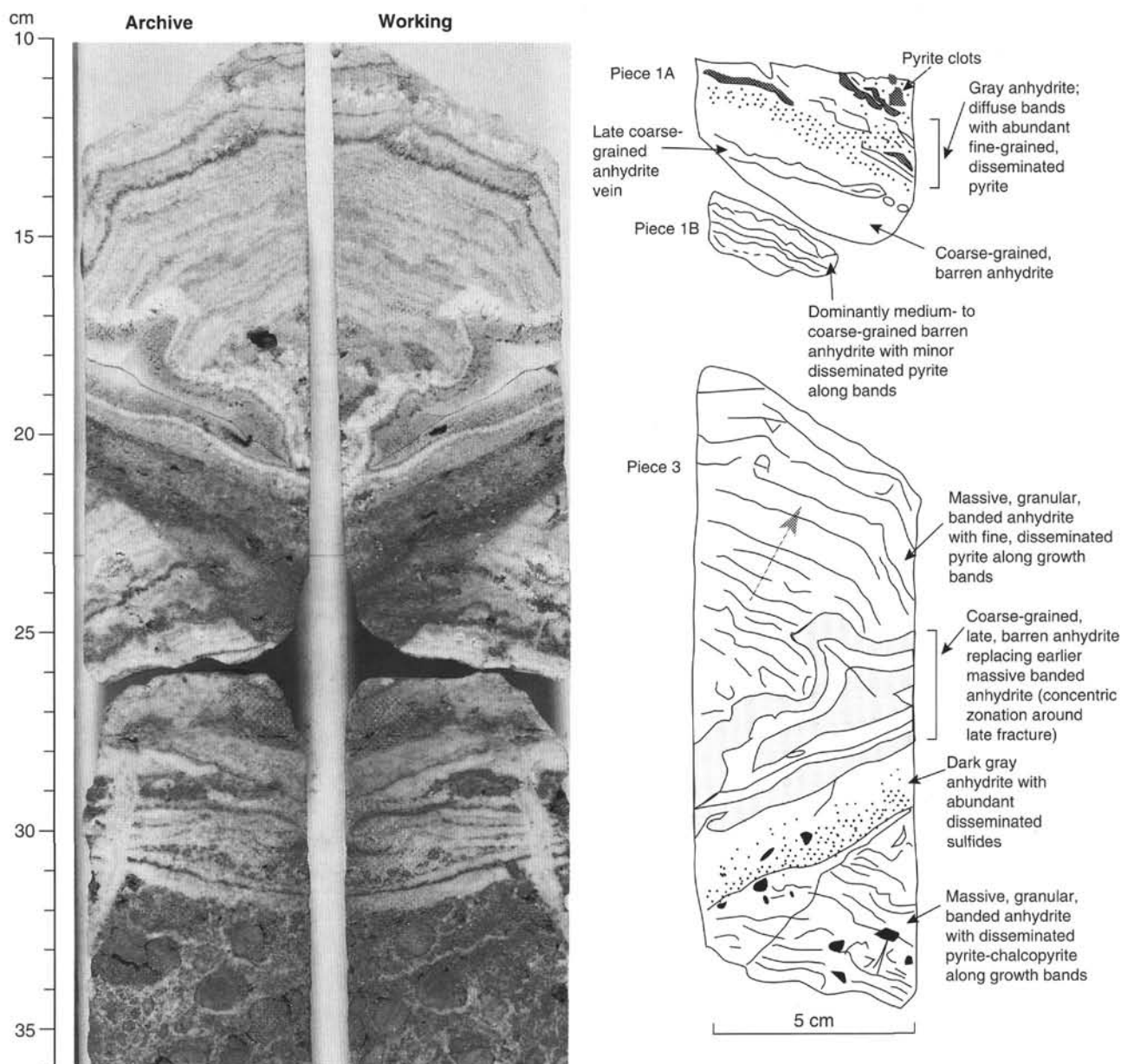


Figure 34. Photograph of archive and working halves of Sample 158-957C-7N-3 (Pieces 3 and 4A, 12–50 cm; photographed interval is from 10 to 36 cm) and sketch of archive half of Sample 158-957C-7N-3 (Pieces 1A, 1B, and 3), showing multiple generations of crustiform-banded anhydrite vein (Type 11) and minor granular anhydrite with disseminated sulfides. This is an example of a high-level, barren anhydrite vein from 22 mbsf as discussed in the text and shown in Figure 42. Shaded arrow indicates direction of crystal growth perpendicular to the walls of the vein.

tions of the stockwork zone (1–125.7 mbsf) in the TAG-1 area. The rock types are dominated by a variety of breccias and show a gradation, with increasing depth, from porous to granular pyrite \pm chalcopyrite, pyrite breccias, pyrite-anhydrite breccias, pyrite-silica breccias, and silicified wallrock breccias to chloritized basalt breccias. A subseafloor quartz stockwork occurs below approximately 50 mbsf in the silicified wallrock and chloritized basalt breccias. Anhydrite veining is abundant throughout the vertical extent of the core but is best developed in the pyrite-anhydrite and pyrite-silica breccias (15–50 mbsf).

Holes 957F and 957G recovered material from the upper portions (1–25 mbsf) of the hydrothermal mound and are interpreted to be representative of the TAG-1 area. Massive granular chalcopyrite was re-

covered only from Hole 957F, where it may represent the uppermost few meters (between 1.0 and 4.5 mbsf) of the mound. Pyrite breccias, pyrite-anhydrite breccias, and siliceous pyrite-anhydrite breccias occur between 1.5 and 25.0 mbsf. A sequence of nodular and siliceous pyrite-anhydrite breccias were also recovered in Hole 957C, where they continue down to 30.0 mbsf. If the pyrite-anhydrite breccias in Core 158-957G-1N and Section 158-957G-3N-1 are representative, then there appears to be an increase in the proportion of anhydrite with depth between 12.0 and 25.0 mbsf. There is a downward progression from grain-supported massive pyrite breccia (<10 vol% anhydrite in the matrix) to matrix-supported pyrite and siliceous pyrite-anhydrite breccia (up to 50 vol% anhydrite). Cores between 5.5 and 16.5 mbsf contain only rounded blocks of massive granular pyrite

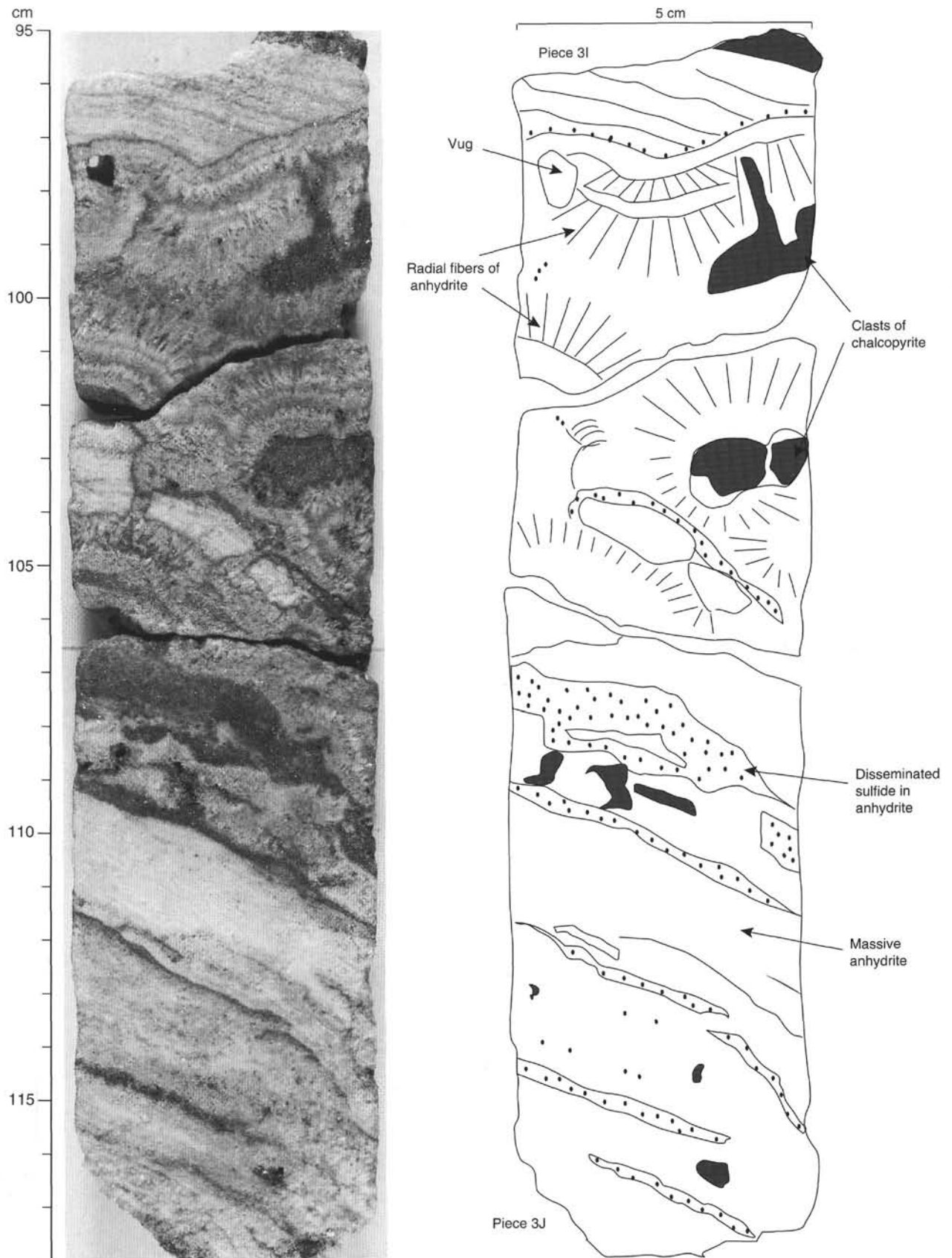


Figure 35. Photograph and sketch of the multiple generations of crustiform-banded anhydrite (Type 11) in a middle-level anhydrite vein with abundant chalcopyrite from 31 mbsf. Interval 158-957C-11N-1 (Pieces 3I and 3J, 95–118 cm). Cavities (vugs) are, in places, lined with pyrite grains.

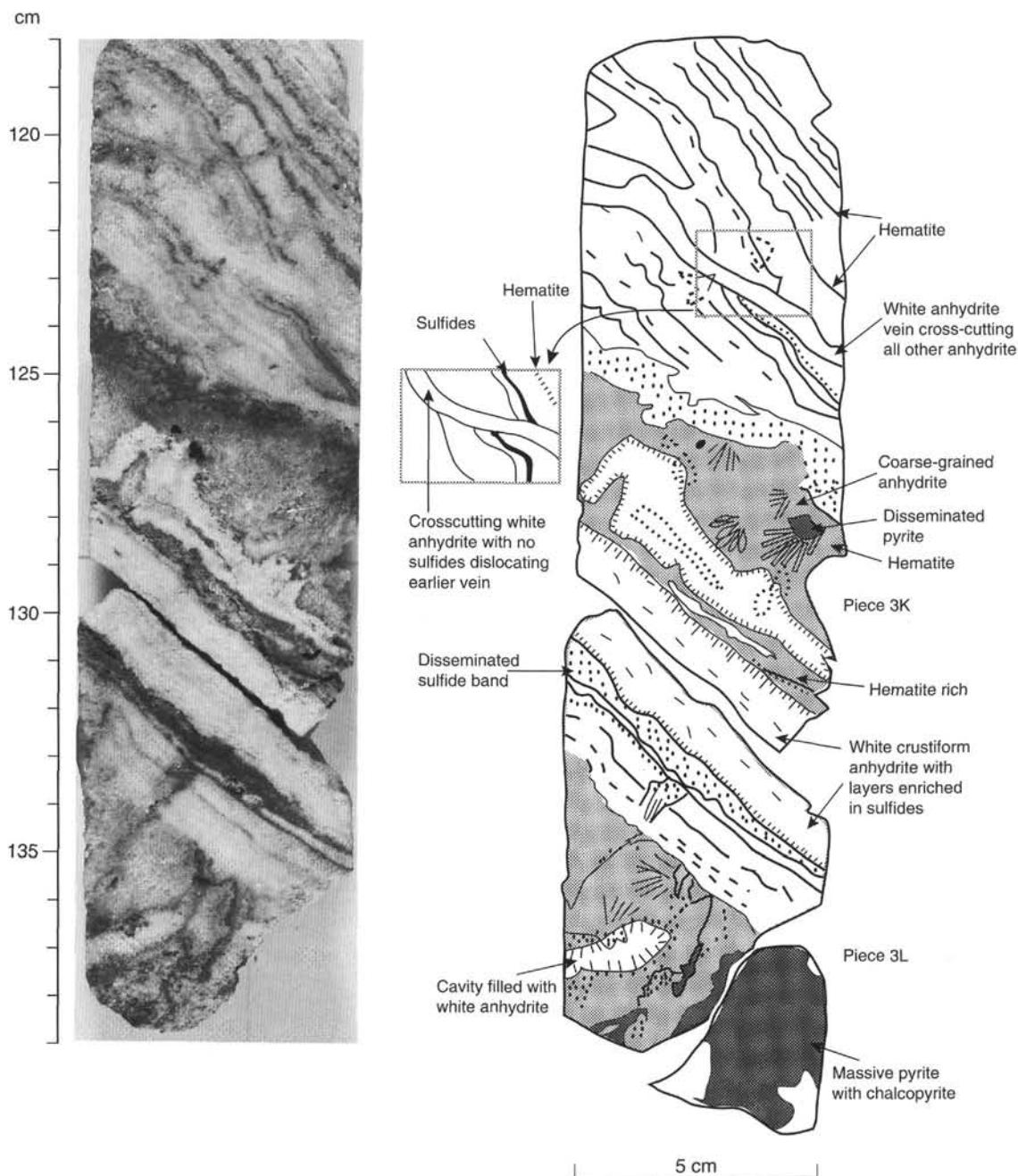


Figure 36. Photograph and sketch of the banded anhydrite vein (Type 11), showing crosscutting generations of anhydrite, coarse crystal growth in the center of late-stage bands, and minor disseminated sulfides and hematite. Continuation of Figure 35, showing Sample 158-957C-11N-1 (Pieces 3K and 3L, 118–140 cm).

(most likely large clasts or nodules) and small pieces of finer grained pyrite or anhydrite matrix. Only minor anhydrite vein material was recovered from either hole. The modal mineral composition, based on visual estimates, for a composite section of Holes 957F and 957G (Fig. 67) shows that chalcopyrite content decreases downhole, quartz is observed only below 12 mbsf, and anhydrite content tends to increase with depth.

Cores drilled from Holes 957F and 957G indicate that the upper few meters of the mound are composed of pyrite- and chalcopyrite-rich massive sulfide crusts. On the surface of the mound, similar samples are associated with seeps of black smoke exiting from cracks and

pencil-sized chimneys (Tivey et al., 1995). The pyrite breccias appear to be derived partly from this material and partly from pieces of black smoker chimneys. The silica-rich clasts that occur in the siliceous pyrite-anhydrite breccias are similar to the pyrite-silica breccias and altered wallrock breccias encountered deeper in Holes 957C and 957E, and may originate by reworking of similar siliceous rocks.

Samples of the deeper portions of the hydrothermal mound were recovered in Hole 957C. The principal rock types in Hole 957C show an apparent gradation from massive pyrite breccias near the top of the cored section, through a thick zone of nodular pyrite-anhydrite breccias between about 15 and 30 mbsf, pyrite-silica-anhydrite breccias

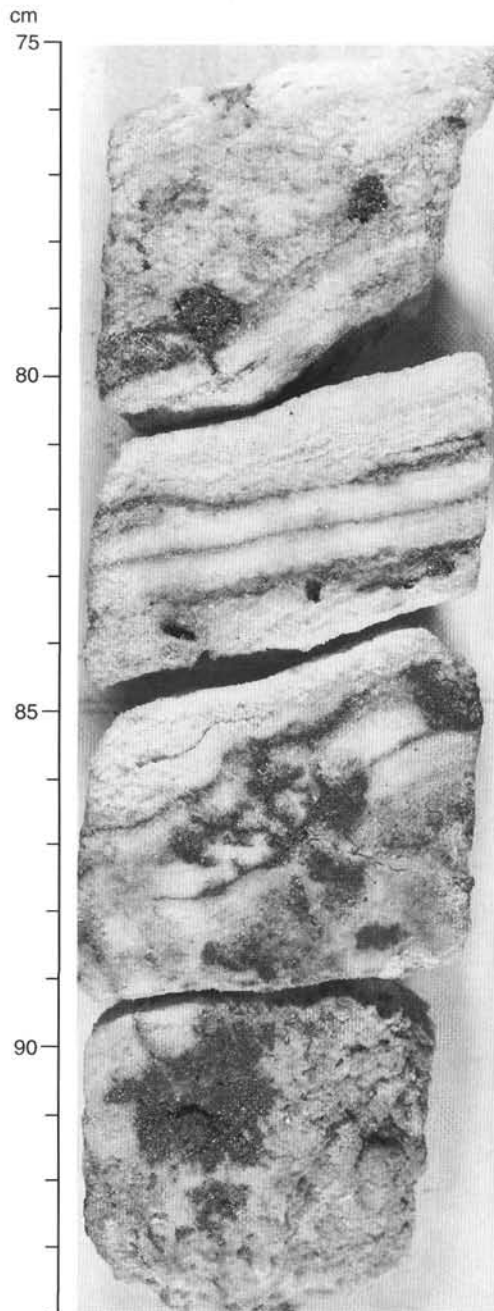


Figure 37. Concentrations of chalcopyrite and pyrite within a Type 11, crustiform-banded middle-level anhydrite vein. Sample 158-957C-12N-1 (Pieces 8A and 8D, 75–94 cm).

between 30 and 37 mbsf, pyrite-silica breccias between 37 and 43 mbsf, and siliceous wallrock breccias from about 43 mbsf to the end of the hole (E.O.H.) at 49 mbsf (see "Stratigraphy" section, this chapter). Occurrences of massive pyrite (>75 vol% pyrite) and associated chalcopyrite generally decrease downcore (Fig. 2) and are largely absent in the pyrite-silica breccias and quartz-rich stockwork. The modal mineral composition, based on visual estimates, for Hole 957C (Fig. 2) shows that below 10 mbsf quartz and the chalcopyrite contents increase downcore, and anhydrite is present in variable amounts throughout the core.

Anhydrite veining in Hole 957C is most prevalent between about 30 and 40 mbsf, with an increase in the abundance of chalcopyrite in vein selvages below about 35 mbsf (Fig. 2). The presence of chalcopyrite in the selvages of these veins suggests that, before anhydrite formation, they may have been open conduits for upwelling, high-temperature, hydrothermal fluids leading to black smokers at the seafloor. The late anhydrite that fills the veins may reflect the fact that the high-temperature episode was followed by a later stage of mixing between the hydrothermal fluids and seawater. Variations in the proportions of seawater and hydrothermal fluid within the fracture system could account for variations in the abundance of chalcopyrite selvages and the presence of trace hematite in the anhydrite veins (Tivey et al., 1995). The greater abundance of chalcopyrite in the deeper anhydrite veins may be related to a higher proportion of hydrothermal fluid in the veins at depth or may represent an earlier stage of mixing and deposition of copper during the growth of the mound. Barren anhydrite veins likely formed as a result of local fracturing of the sulfide carapace and periodic incursions of seawater into the stockwork zone.

Overall, anhydrite veins decrease in occurrence below 43 mbsf in Hole 957C. This corresponds generally to an increase in the amount of quartz cement and the occurrence of abundant quartz-pyrite breccias. The lack of abundant anhydrite veining observed at depths greater than 43 mbsf may, in part, reflect recovery. For example, rock types recovered in cores from Hole 957C between a depth of 30.7 and 49.2 mbsf include pyrite-silica breccia, pyrite-silica-anhydrite breccia, anhydrite veins, and silicified wallrock breccias, whereas rock types from a similar interval (31.5–49 mbsf) in cores from Hole 957E include only nodular-pyrite-silica breccia, semi-massive pyrite-chalcopyrite, and pyrite-silica breccia but no anhydrite veins (see Tables 2 and 6).

Breccias, which are dominantly matrix supported in the central part of the core from Hole 957C (e.g., nodular pyrite-anhydrite zone), become more framework supported toward the bottom of the core. The predominance of quartz-pyrite breccias and gray siliceous clasts below 40 mbsf resembles the quartz-rich stockworks beneath many ancient massive sulfide deposits and suggests that this is the top of the basalt-hosted stockwork zone (Franklin et al., 1981). The common occurrence of gray siliceous material in pyritic breccias higher up in the core may also be the remnants of an earlier generation of wallrock breccias, suggesting widespread replacement of wallrock material during the growth of the mound.

Hole 957E recovered core through the hydrothermal mound and into the upper portions of the altered footwall alteration and stockwork zone. The lithologies and styles of veining and alteration in the upper and central portions (31.5–100 mbsf) of core from Hole 957E are similar to those encountered in core from Hole 957C. With increasing depth in the core from Hole 957E, pyrite-silica breccias (Types 9a and 9b) grade into silicified wallrock breccias (Type 10a). At 100 mbsf, the silicification decreases in intensity and chloritization is the dominant alteration phase, giving rise to chloritized basalt breccias with recognizable basalt fragments.

The modal mineral composition, based on visual estimates, for Hole 957E (Fig. 47), shows that pyrite and quartz are the major minerals, but with variable proportions throughout the core, whereas anhydrite decreases with depth and is not observed above trace amounts below 68.3 mbsf. Chalcopyrite content occurs in minor but variable amounts from 31.5 to 120.7 mbsf but was not observed from 120.7 to 125.7 mbsf. Chlorite was first observed, in consistent quantities, at 87.1 mbsf and increases in abundance toward the bottom of the hole at 125.7 mbsf.

The type and style of veining also changes with the different sulfide lithology and alteration mineralogy in Hole 957E. Anhydrite veins (\pm chalcopyrite selvages and pyritization halos) are common throughout all cores but are concentrated in the upper and central portions of the core. In the deeper portions of the silicified wallrock breccias

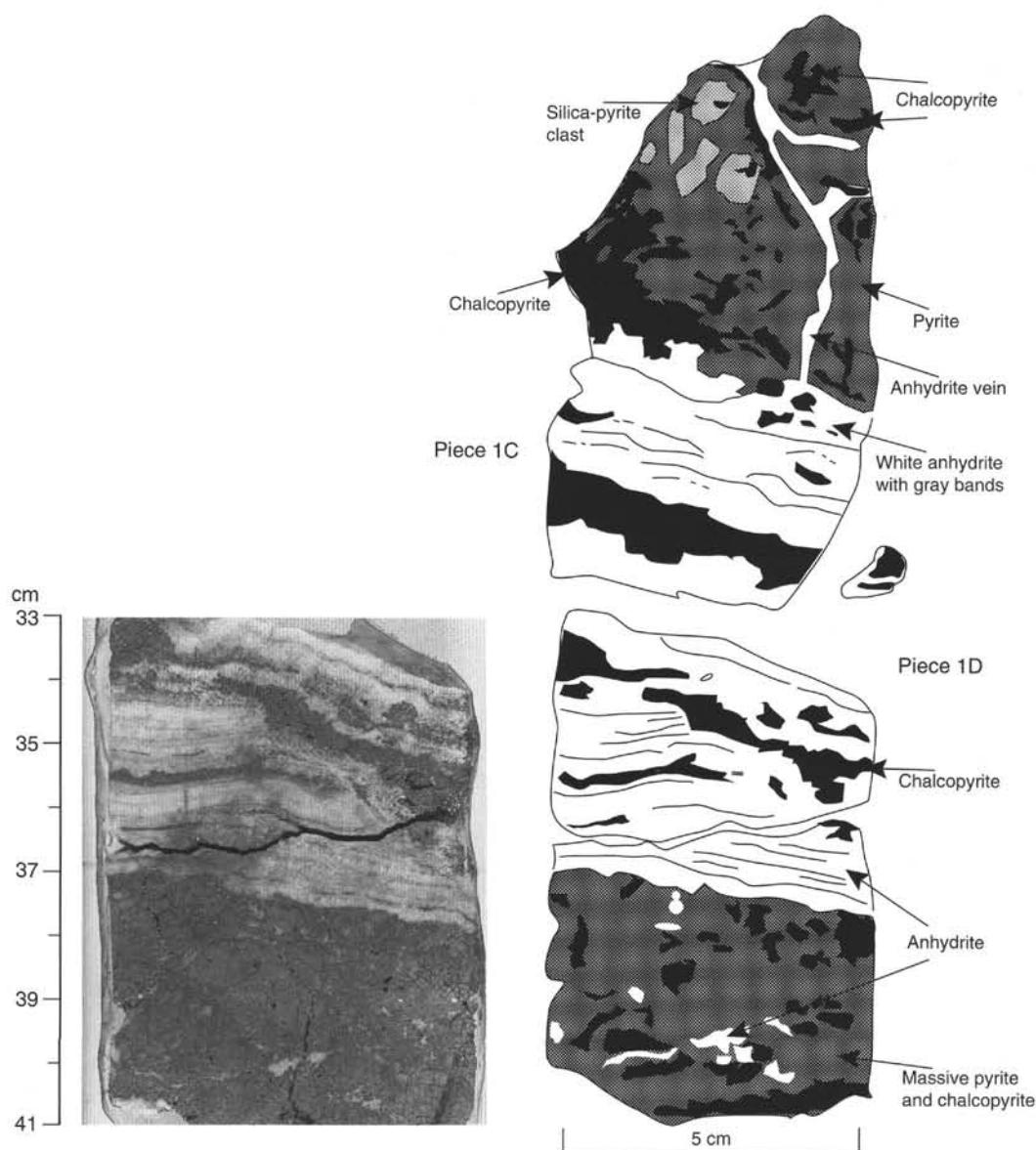


Figure 38. Photograph of Sample 158-957C-14N-2 (Piece 1D, 33–41 cm) and sketch of Sample 158-957C-14N-2 (Pieces 1C and 1D), showing the chalcopyrite selvage and pyritization halo surrounding a typical deep-level, crustiform-banded anhydrite vein (Type 11) from 41 mbsf. Chalcopyrite and pyrite also occur within the vein.

cias (below 72 mbsf), and in the chloritized basalt breccias, quartz-pyrite stockwork veins are abundant.

Genetic Implications

The following generalizations for the development of the hydrothermal mound, footwall alteration, and stockwork veining are based on hand sample descriptions and petrographic observations of representative polished thin sections. The upper 25 m of the mound in the TAG-1 area appears to be undergoing the following processes: (1) accumulation of primary sulfides (enriched in Cu) at the surface; and (2) hydrothermal reworking and recrystallization to form the sequence of massive sulfide breccias, with minor incorporation of siliceous material (possibly derived from altered basalt). On this basis, mound growth is occurring by deposition at the surface (sulfides enriched in Cu) as well as by subsurface deposition of anhydrite and Zn-

and Cu-poor, pyrite-anhydrite-silica assemblages related to hydrothermal upflow and mixing with entrained seawater.

Anhydrite- and silica-cemented breccias are the principal rock types from the lower part (25–50 mbsf) of the hydrothermal mound. The complex assemblage of fragments, at depths as shallow as 20 mbsf, in the anhydrite-cemented breccias (i.e., massive pyrite, gray siliceous pyrite, red chert, altered basalt fragments) overlying the present stockwork zone suggests that multiple episodes of brecciation and cementation occurred and that this material may have been derived from the degradation or collapse of an earlier mound/stockwork complex (i.e., a “proto-TAG”). Clasts within clasts, rebrecciation of preexisting fragments, and recementation of breccias by multiple generations of veins and matrix material suggest a complex history of mound growth. Radiometric dating suggests that pulses of high-temperature activity on the TAG mound occurred every 5,000–6,000 yr from at least 25,000 yr to 4,000 yr ago, and that a hiatus in

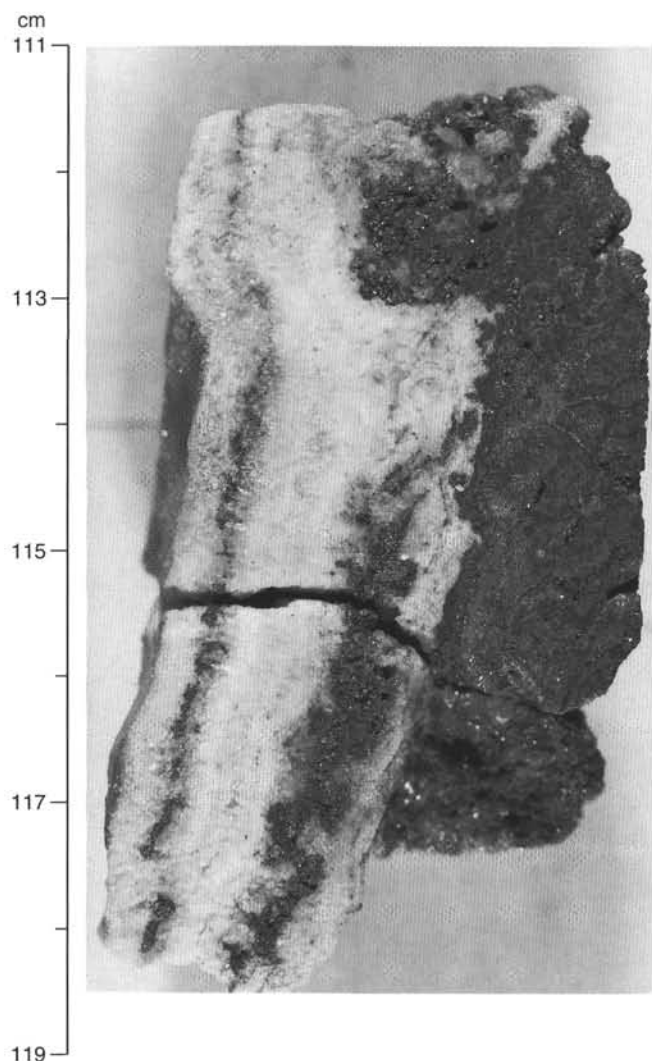


Figure 39. Detail of chalcopyrite and pyrite within a deep-level anhydrite vein (Type 11). Sample 158-957C-15N-2 (Piece 6B, 111–119 cm).

activity between about 4,000 yr and 50 to 100 yr ago was followed by resumption of the high-temperature activity at the TAG mound that continues today (Lalou et al., 1993).

Replacement textures and crosscutting relationships among veins suggest a partial paragenesis for the breccias: (1) early silicification, probably several episodes of brecciation, and mineralization of the host basalts and accumulation of massive pyrite breccias on the seafloor; (2) cementation and filling of the breccias by silica, local replacement of pyrite by quartz, recrystallization of quartz and pyrite, and multiple phases of additional pyrite growth in the lower part of the mound; and (3) development of several generations of anhydrite veins, with locally extensive pyritization of the wallrock adjacent to the veins, and further cementation of breccias by anhydrite in the upper part of the mound. Most of the sulfide lithologies found in the upper part of the mound are also present as partially replaced fragments lower down in the mound. Their presence suggests that the present distribution of lithologies through the mound is a product of several cycles of brecciation, replacement, and veining.

Below the hydrothermal mound is a footwall alteration zone containing stockwork veining. Basalts have been chloritized and overprinted by varying degrees (multiple episodes?) of silicification. In

many cases, the difference between the pyrite-silica breccias and the silicified wallrock breccias is the degree of silicification. The pyrite-silica breccias contain clasts that have been intensely silicified to the point where original igneous textures have generally been totally destroyed. In contrast, alteration in the silicified wallrock and chloritized basalt breccias has generally not totally destroyed original rock textures and basalt fragments can be identified (see the interpretation section of the "Hydrothermal Alteration" section, this chapter, for further discussion of the alteration paragenesis). Because of the intensity of alteration and vein development, it is difficult to determine accurately the depth below seafloor for the top of the stockwork zone and the base of the hydrothermal mound. One estimate is at the contact of the pyrite-anhydrite and pyrite-silica breccias (at ~30 mbsf). This coincides with an increase in the abundance of recognizable silicified wallrock clasts in the core (see "Hydrothermal Alteration" section, this chapter).

Five stages of veining have been identified in the TAG-1 area, indicating multiple generations of hydrothermal fluid flow up through the stringer zone and into the mound. Many of the samples of silicified wallrock and chloritized basalt breccias recovered have been hydraulically fractured (jigsaw fit of fragments) and healed with hydrothermal precipitate, dominantly quartz, pyrite, and anhydrite. The quartz-pyrite stockwork veins are best developed deep in the footwall and pass upward into anhydrite-dominated veins. These veins may be the channelways for the hydrothermal fluids feeding some of the active vents on the surface of the mound. The chalcopyrite content within the upper part of the stockwork zone and lower to middle portions of the hydrothermal mound is largely related to the development of selvages on the late Stage 5 anhydrite veins. Overall, the character and intensity of alteration, the change of mineralogy with depth from quartz to chlorite-dominated alteration assemblages, and the style of stockwork veining are very similar to the Cyprus massive sulfide deposits (Constantinou and Govett, 1973) and footwall alteration zones and stringer systems of numerous volcanic-hosted massive sulfide described worldwide (e.g., Franklin et al., 1981; Large, 1992).

HYDROTHERMAL ALTERATION

Hydrothermally altered basaltic material was recovered from Holes 957C and 957E in the eastern black smoker area, on the upper terrace of the TAG mound (see Fig. 3, Chapter 1, this volume). Altered basaltic material in Holes 957C and 957E was found as three general occurrences: as isolated clasts of silicified basalt, as silicified wallrock breccias, and as chloritized basalt breccia. Clasts of silicified basalt first occur at 20.08 mbsf in Hole 957C (Core 158-957C-7N) and are present sporadically in pyrite-anhydrite breccias and pyrite-silica-anhydrite breccias down to 40 mbsf, becoming more common below about 30 mbsf (see Fig. 1). Silicified wallrock breccias occur in Hole 957C from 40 mbsf to the bottom of the core at 49.2 mbsf, and between 49.0 mbsf and 101.5 mbsf in Hole 957E (Fig. 1). Chloritized basalt breccias occur in cores from Hole 957E from 101.5 mbsf to the bottom of the core at 125.7 mbsf.

Clasts of Silicified Basalt

The isolated basalt clasts occur in Hole 957C as small (1–4 cm), round to angular fragments in various types of pyrite-anhydrite and pyrite-silica-anhydrite breccias (see Fig. 10). In hand specimen, the clasts typically have a buff-colored, fibrous or feathery, microcrystalline matrix, which contains quartz and pyrite pseudomorphs after plagioclase microlites. The altered basalt fragments are always very hard and silicified, and disseminated pyrite is common. In some cases, the margins of the clast are totally replaced by very fine-grained pyrite for up to 5 mm into the clast, with the intensity of replacement

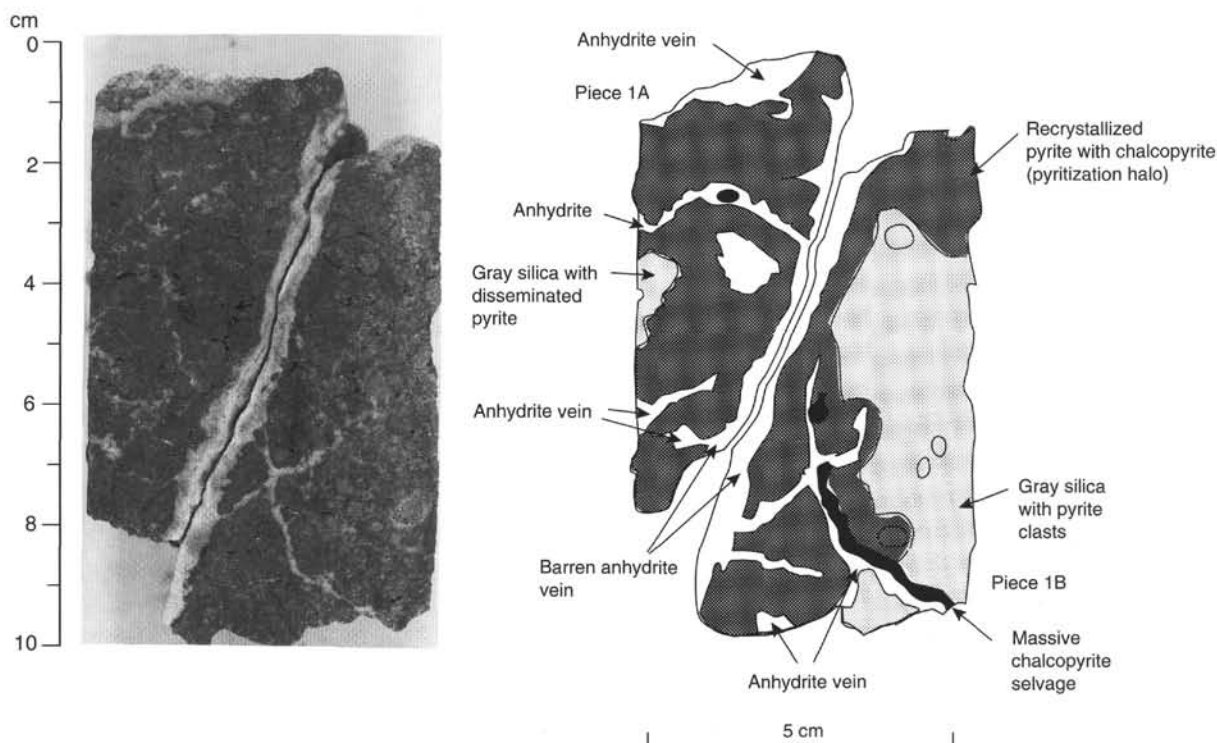


Figure 40. Photograph and sketch of Sample 158-957C-11N-2 (Pieces 1A and 1B, 0–10 cm), showing a late, anhydrite vein (Type 11) with associated chalcopyrite selvage and pyritization halo. Note that the chalcopyrite selvage and pyritization halo are also associated with thin anhydrite veins extending into the host pyrite-silica-anhydrite breccia.

decreasing inward, away from the margins. Many clasts are rounded, but in some cases small (<0.5 cm across), angular clasts cemented by quartz fit together and can be visually recombined into larger, 1- to 5-cm-sized clasts (e.g., Fig. 80). In many examples, the buff color of the fine-grained matrix in one portion of the clast fades to gray across the clast as it is progressively silicified, until the other side disappears into the surrounding siliceous matrix, leaving only a ghost or shadow of the former clast. The cements of the breccias containing silicified basalt fragments are various combinations of quartz, anhydrite, and pyrite.

Silicified Wallrock Breccias

Silicified wallrock breccias occur in Hole 957C from 40 mbsf to the bottom of the core at 49.2 mbsf (in Cores 158-957C-14N through 16N; see Figs. 1, 2), and in Hole 957E at 49.0–58.6, 63.3–68.3, 77.8–87.4, and 91.8–101.5 mbsf (Cores 158-957E-4R, 6R, and 8R–12R; see Figs. 1, 47). Interspersed with these breccias in Hole 957E are intervals of pyrite-silica breccias at 58.6–63.3, 68.3–77.8, and 87.4–91.8 mbsf (Cores 158-957E-5R, 7R, 8R, and 11R). The pyrite-silica breccias rarely contain small pieces of silicified wallrock breccia or isolated silicified basalt clasts (e.g., at about 70 mbsf in Core 158-957E-7R and at about 90 mbsf in Core 158-957E-11R; Fig. 47). The pyrite-silica breccias interspersed with the silicified wallrock breccias in Hole 957E are likely of multiple origins. They may comprise, in part, totally silicified wallrock material, in which the precursor basalt can no longer be recognized. They can also be considered as the matrix material of the silicified wallrock breccias, but some of the pyrite-silica breccia may also be veins cutting the silicified wallrock breccias.

The silicified wallrock breccias in both holes are similar and consist of angular siliceous clasts, 1–5 cm in size, veined and cemented by white to gray quartz and pyrite (Figs. 80, 81; see also Fig. 28). The

clasts are gray to buff, hard silicified basalt fragments that are identical to the isolated silicified basalt clasts described above. In rare cases, a white clay mineral is present in 1-mm patches within the hard siliceous matrix (e.g., Sample 158-957E-6R-1, Piece 6). Centimeter-sized clasts of massive pyrite are also common locally in these breccias. The altered basalt clasts are totally recrystallized to quartz, pyrite, and clay, but locally contain relict igneous textures. Subvolcanic texture was observed in thin sections, where plagioclase microlites are replaced by quartz \pm a tan-to-brown phyllosilicate, and the fine-grained interstitial material is replaced by the same tan-to-brown clay and disseminated 10- to 100- μ m pyrite and quartz (Fig. 82). The tan-to-brown phyllosilicate is unidentified, but it could possibly be chlorite(?), illite(?), or a mixed-layer phase(?). The disseminated pyrite grains are commonly surrounded by quartz, which appears to be replacing basalt outward from the pyrite grains (Fig. 54). In some samples, quartz pseudomorphs of needlelike “bow-tie” plagioclase microlite aggregates, of skeletal olivine crystals, and of rare olivine phenocrysts occur in a feathery to fibrous groundmass of tan clay mineral (Fig. 82). Locally in the groundmass, tiny, 1- to 5- μ m-sized grains of colorless granular material may be titanite or leucoxene. Vesicles are filled by tan clay, pyrite, and quartz.

The clasts are cut and cemented by 0.01- to 2-mm-thick veins of subhedral to euhedral quartz \pm pyrite; in many cases, the quartz may be replacing basalt (Figs. 83, 54). Where quartz and pyrite occur together, euhedral quartz lines the walls of the veins and subhedral to euhedral pyrite grains and aggregates, up to 3 mm in size, are present in the pore space at the center of the veins. The basalt clasts are broken into smaller fragments separated by quartz plus pyrite veins; where individual clasts are intensively veined by quartz, the clasts are more completely silicified (Figs. 84, 53). Some fragments of altered basalt become progressively more silicified toward their margin along one or more sides, with the clast being replaced by granular intergrowths of quartz and pyrite with irregular patches of tan clay, and

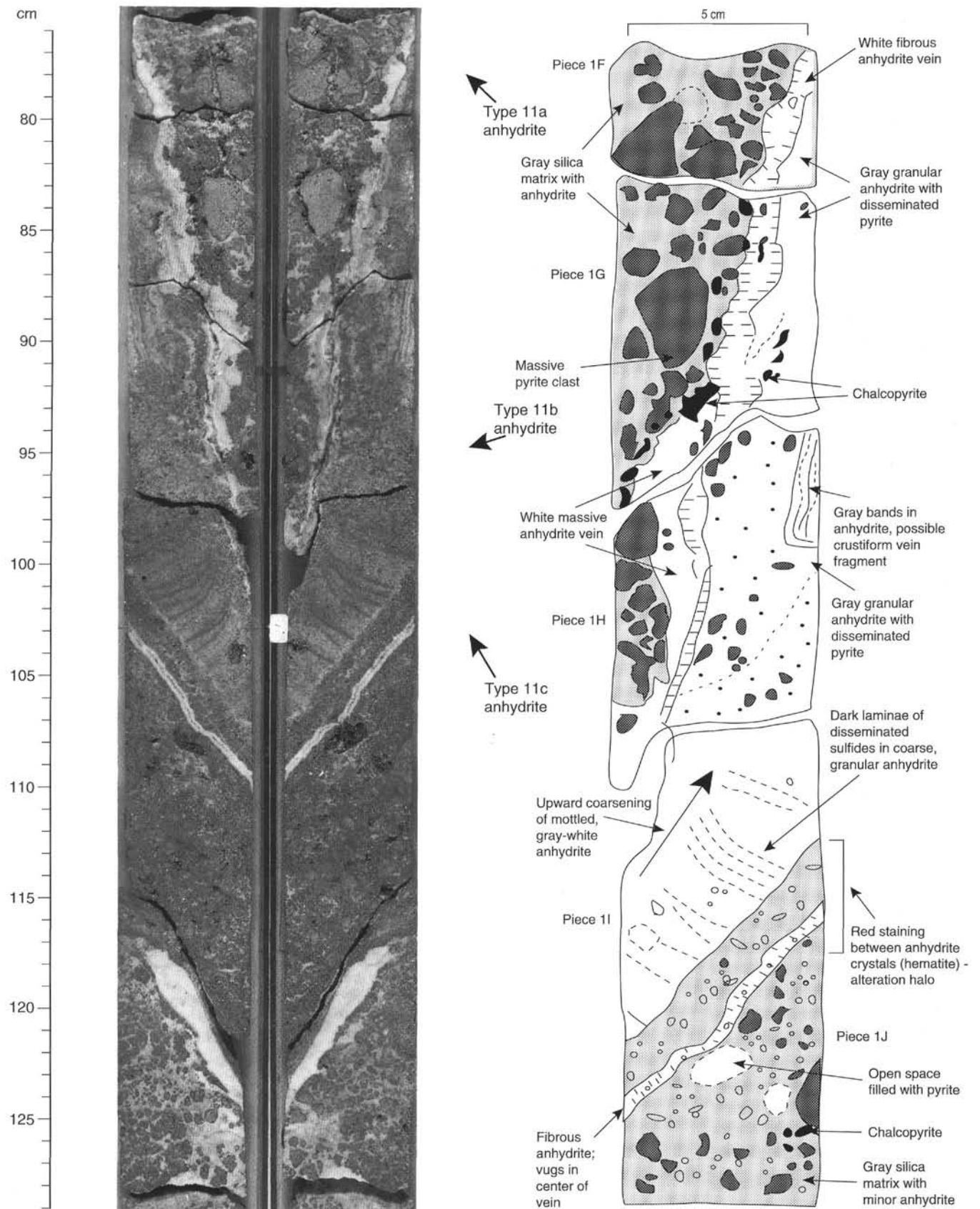


Figure 41. Photograph of archive and working halves and sketch of part of working half of a large multiple-generation, upper-level anhydrite vein. Several anhydrite types of veins with different characteristics are shown. Sample 158-957C-7N-2 (Pieces 1F through 1J, 76–129 cm). Sketch is of Pieces 1F through upper part of 1I (interval from 76 to 115 cm).

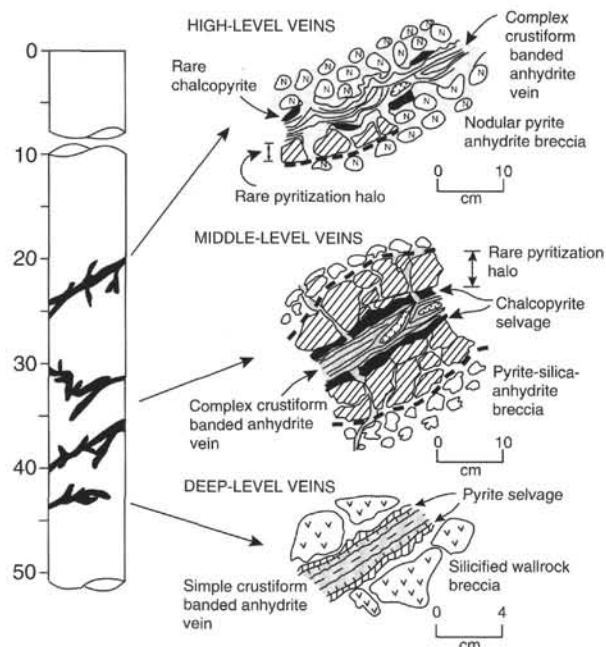


Figure 42. Schematic diagram showing variations in vein characteristics with depth throughout the vertical extent of Hole 957C. High-level, middle-level, and deep-level veins are distinguished primarily on the basis of their vein selvages and halos. Note scale difference on sketches.

consequent loss of relict igneous texture. The most intensely altered clasts consist of 5- to 100- μm -sized fragments of clay plus granular, 5- to 25- μm -diameter quartz and pyrite, lacking any relict igneous textures (Fig. 84). These clasts are surrounded by coarser grained "matrix" quartz and pyrite. In progressively more silicified areas, the clasts consist of intergrowths of granular quartz and pyrite, lacking any relict igneous texture, and grading into the coarser quartz matrix or veins. The quartz in these intensively silicified clasts appears dirty yellowish or brownish and is riddled with fluid(?) inclusions (Fig. 84), in contrast to the clearer quartz in cement and veins. Large (up to 500 μm long), anhedral quartz crystals appear "dirty" because they commonly contain numerous tiny fluid(?) inclusions, in some cases

aligned in subparallel arrays, which are probably the last traces of basaltic texture in totally silicified areas (Fig. 85). Other clasts are pyrite rich, in some cases consisting of more than 50% subhedral pyrite intergrown with and surrounded by granular quartz. These clasts may contain local patches of tan clay, but they do not preserve any relict igneous texture.

The matrix of the basalt clasts consists of 0.1- to 10-mm-sized pyrite grains and aggregates disseminated within gray, fine-grained quartz (Fig. 80). In hand specimen, this matrix material appears to be composed of hydrothermal precipitate, but, as shown by thin-section observations, it probably also contains some intensively or totally silicified basaltic material, which would likely be indistinguishable in hand specimen. Locally, small amounts of chlorite and a colorless, high birefringence phyllosilicate (talc?) occur interstitial to the quartz cement in the matrix of the silicified wallrock breccias of Hole 957C (Fig. 86). Veins of white quartz, with or without pyrite and 0.1–5 mm in width, are common cutting both clasts and matrix of the breccias in both holes. This "matrix" of the silicified wallrock breccias may actually be veins that cut the basaltic material; however, given the small diameter of the core and the small sizes of the recovered pieces, the larger scale relationships between matrix and clasts, or between veins and host rock, are not obvious.

Within the intervals of siliceous wallrock breccia in Hole 957E, many 1- to 5-cm-sized pieces of core consist of massive to semi-massive pyrite \pm quartz and chalcopyrite (in Cores 158-957E-6R, 8R, 9R, and 11R) (Fig. 53). This material occurs as isolated fragments as well as on the margins of some core pieces of siliceous wallrock breccia. These are most likely fragments of veins composed of sulfide plus quartz. Some clasts are rimmed by 1- to 5-mm-sized granular pyrite, which may be the remnant of larger sulfide veins.

Chloritized Basalt Breccias

Chloritized basalt breccias were first encountered in Core 158-957E-14R at 101.5 mbsf, and are present to the bottom of the core at 125.7 mbsf (Figs. 1, 47). The chloritized basalt clasts are mainly gray, but green chloritized basalt fragments are present along with gray ones in Cores 158-957E-16R through 18R (111–125.7 mbsf).

Gray Chloritized Basalt Breccias

The gray chloritized basalt breccias consist of 1- to 5-cm-diameter clasts of gray altered basalt in a fine-grained matrix of intergrown

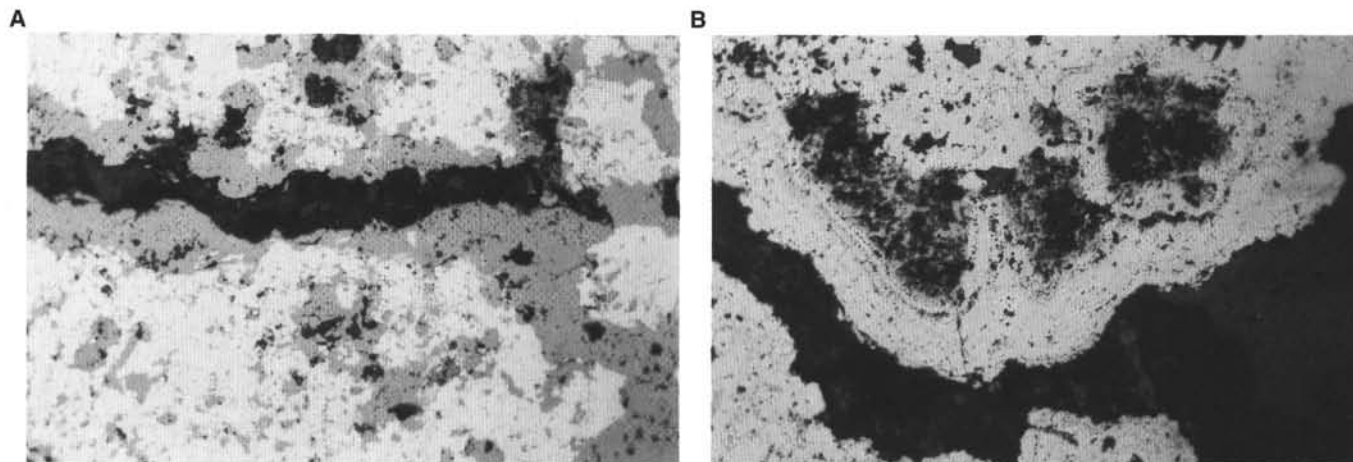


Figure 43. Representative photomicrographs of textures in massive pyrite-chalcopyrite associated with Type 11 anhydrite veins. **A.** Anhydrite vein (dark gray) crosscutting massive pyrite (white). Most of the anhydrite was plucked during polishing. The vein selvage consists of chalcopyrite (light gray). Sample 158-957C-14N-2 (Piece 1D, thin section from 41 to 44 cm). Reflected light, field of view = 1.5 mm. **B.** Colloform pyrite (white) with chalcopyrite (light gray) lining the walls of an anhydrite vein. Sample 158-957C-14N-2 (Piece 1D, thin section from 41 to 44 cm). Reflected light, field of view = 1.5 mm.

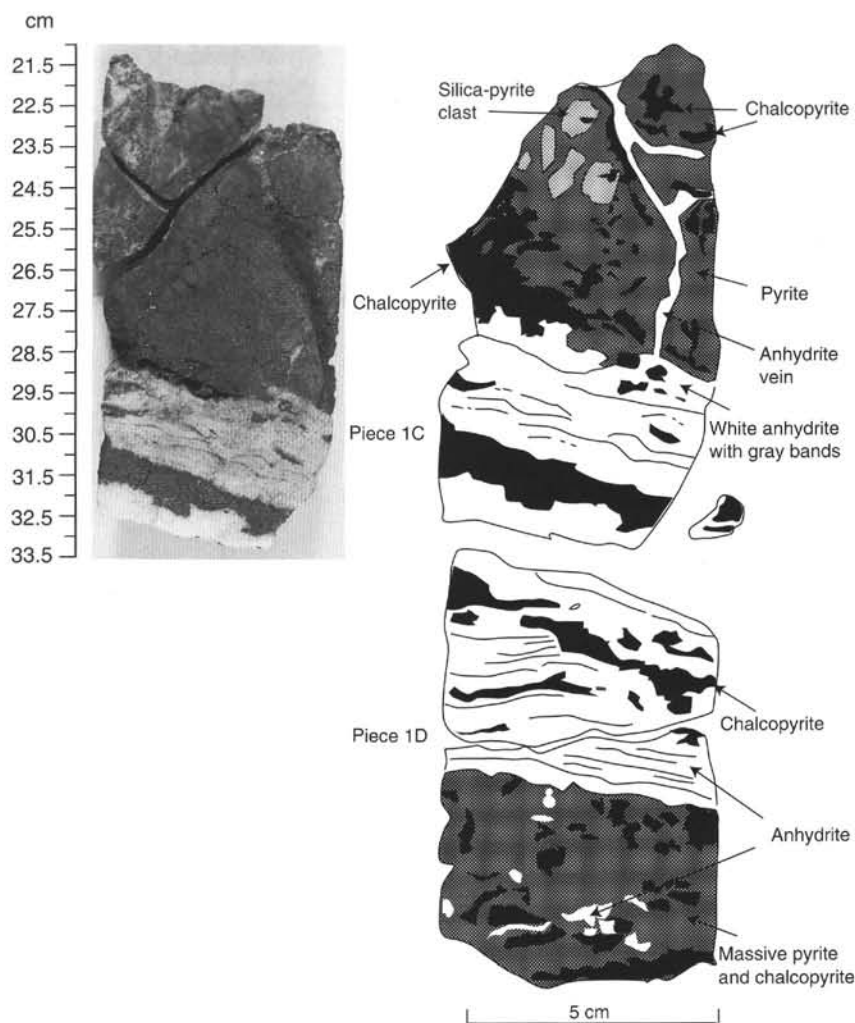


Figure 44. Photograph of Sample 158-957C-14N-2 (Piece 1C, 21.5–32.5 cm) and sketch of Section 158-957C-14N-2 (Pieces 1C and 1D), showing typical deep-level, crustiform-banded anhydrite vein (Type 11) from 41 mbsf. A narrow pyrite-chalcopyrite selvage occurs adjacent to siliceous wallrock breccia (Type 10a).

white to gray quartz and pyrite (Fig. 87). The altered basalt clasts are distinctly softer and less silicified than those in the overlying silicified wallrock breccias. Although the maximum size of clasts observed in the core is 5 cm, some of these clasts are actually single fragments of veined basalt, so the sizes of clasts or veined basalts are probably larger than indicated by the pieces recovered by drilling. In one case, a 1-mm-wide red iron oxide or oxyhydroxide band is present within a 4-cm-sized chloritized basalt clast (Sample 158-957E-15R-1, Piece 4, 6–12 cm). The band is subparallel to the margins of the clast and 1 to 4 mm from them.

A thin section of one sample (Sample 158-957E-14R-1, Piece 11, 52–55 cm) of gray chloritized basalt breccia confirms the less silicified nature of this material compared to the silicified wallrock breccias, which are quite similar in other respects. This sample exhibits relict subvolcanic texture (Fig. 88). Needlelike and bow-tie plagioclase microlites are replaced mainly by tan chlorite and to a lesser extent by quartz. The interstitial fine-grained material is replaced by tan chlorite; locally, however, feathery groundmass clinopyroxenes are replaced by orange iron oxides or oxyhydroxides plus tan chlorite. Round, 100- to 300- μm vesicles and rare 300- μm -long olivine phenocrysts are replaced by a colorless, low birefringence (first-order yellow) phyllosilicate (Fig. 88). Common irregularly shaped vugs or patches of very fine-grained groundmass (possibly formerly glass?) are filled or replaced by a colorless, higher birefringence (second-order green) phyllosilicate (possibly illite?). Disseminated 5- to 200- μm -diameter grains and aggregates of pyrite are abundant in the al-

tered basalt, and the clast is cut by numerous 10- to 200- μm -thick veins of quartz and quartz plus pyrite. Basalt clasts are more intensively silicified in these areas and, in the most intensively silicified areas, all that remains of the basaltic texture is “dirty” quartz, containing abundant oriented bands of fluid and clay inclusions.

In many cases, the margins of altered basalt clasts are rimmed by 1- to 4-mm-wide zones of pyrite (e.g., Samples 158-957E-14R-1, Pieces 10 and 11). In others, chalcopyrite-rich rims are present around clasts (Sample 158-957E-14R-1, Piece 10). These sulfide rims on clasts are probably fragments of sulfide veins plus sulfidized wallrock, and consist of 1- to 3-cm-wide, massive to semi-massive, quartz-rich pyrite (\pm chalcopyrite) material (see Fig. 56; Samples 158-957E-14R-1, Pieces 5, 10, and 11; 16R-1, Piece 3; 17R-1, Pieces 1-6; 18R-1, Pieces 1, 3, 4, and 6-9). Isolated, 1- to 3-cm-size fragments of similar sulfide material from 101.5 to 125.7 mbsf (Cores 158-957E-14R through 18R) are probably fragments of the same type of vein material. Some of these “veins” contain highly altered clasts of basalt and could also be considered as the matrix material of the breccia rather than as veins (Fig. 62).

Veins of pyrite, quartz, and quartz plus pyrite commonly cut the basalt clasts (e.g., Fig. 87). Veins appear to follow a sequence, from early pyrite and quartz plus pyrite veins, to later quartz veins that cut the earlier veins (Fig. 63). In some cases, the pyrite appears to be intergrown with quartz in the quartz plus pyrite veins, whereas in other cases pyrite appears to be relatively late, at the center of the quartz plus pyrite veins. Elsewhere, quartz veins clearly cut and form in re-

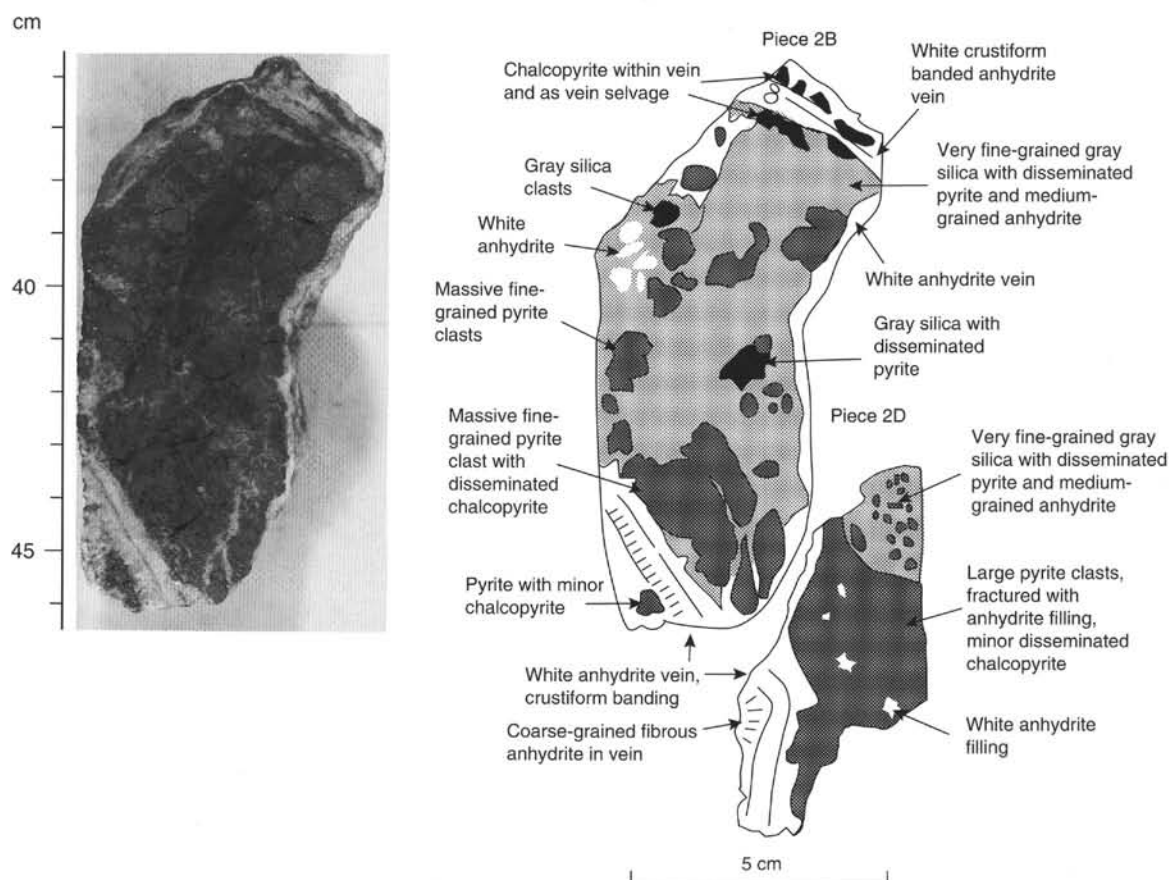


Figure 45. Photograph of Sample 158-957C-15N-2 (Piece 2B, 35.5–46.5 cm) and sketch of the working half of Sample 158-957C-15N-2 (Pieces 2B and 2D), showing brecciation (shattering and healing) of the silicified wallrock breccia adjacent to a deep-level anhydrite vein. The pyritization halo contains minor chalcopyrite.

opened earlier pyrite and quartz plus pyrite veins (e.g., Samples 158-957E-16R-1, Pieces 1 and 2; 17R-1, Pieces 3 and 7; and 18R-1, Pieces 2–4).

Many pieces have 1- to 3-mm, continuous to discontinuous coatings of anhydrite on broken surfaces. These are most likely remnants of anhydrite veins, which were lost during coring. The anhydrite veins appear to be relatively late, cutting other vein types or as the last mineral to form at the center of sulfide veins.

Some pieces have chalcopyrite plus pyrite on their margins, with an outer layer of anhydrite. These may be chalcopyrite-rich margins of anhydrite-chalcopyrite veins, similar to those observed in the better recovery from shallower depths in Hole 957C.

Gray Plus Green Chloritized Basalt Breccias

Gray plus green chloritized basalt breccias occur in Cores 158-957E-16R to 18R (111.0–125.7 mbsf; Figs. 1, 47). These rocks range from gray chloritized basalt fragments and breccias, like those described above, to green chloritized glassy basalt fragments and shards cemented by quartz (Samples 158-957E-16R-1, Piece 3; and 18R-1, Piece 5) (Fig. 89), to green, pervasively chloritized fine-grained basalt (Fig. 64), to green chloritized basalt with superimposed, 1- to 10-mm-wide, gray to buff alteration halos (Fig. 89) (Samples 158-957E-17R-1, Pieces 3 and 6; and 18R-1, Pieces 3–7 and 9).

In hand specimen, the green rocks are fine-grained and appear to be pervasively altered to chlorite, with dark green pseudomorphs of olivine phenocrysts visible in one sample (158-957E-18R-1, Piece 1). In thin section, the chloritized rock of Sample 158-957E-18R-1

(Piece 5) has an intergranular texture, with plagioclase microlites and microphenocrysts replaced by quartz, brown chlorite(?), and pyrite (Fig. 90). Fine-grained interstitial material is replaced by brown chlorite(?) and quartz. Rare olivine microphenocrysts are replaced by orange Fe-oxides or oxyhydroxides and quartz. Pyrite is abundant as disseminated grains and replacing plagioclase, and quartz is common surrounding many of the pyrite grains and aggregates. The rock is cut by 10- to 300- μ m-wide veins of quartz or quartz plus pyrite; in some cases, these veins cut or follow along discontinuous 20- to 100- μ m-wide “stringers” of pyrite.

Altered glass shards in Sample 158-957E-18R-1 (Piece 4) are replaced by chlorite having both anomalous blue and first-order yellow interference colors (Fig. 91). The latter suggest possible mixed-layering of smectite and chlorite. Tiny, 1- to 5- μ m-diameter gray granules in the chloritized glass fragments may be titanite. Rare, 100- to 150- μ m-sized aggregates of orange iron oxides or oxyhydroxides are present in the matrix, which consists of fine-grained, “dirty” quartz, riddled with inclusions of fluid and clays. In the hand specimen of Sample 158-957E-16R-1 (Piece 3), the green chlorite replacing the glassy basalt fragments is accompanied by small amounts of white clay. In both of these samples, clasts and matrix are cut by colorless to white quartz veins, 0.1–2 mm wide.

Gray to slightly buff alteration halos, 1–10 mm wide, occur around pyrite or quartz plus pyrite veins, and have sharp contacts with the green chloritized host basalt in Cores 158-957E-17R and 18R (116–125.7 mbsf) (Fig. 89; see also Fig. 61). Plagioclase microlites in these gray zones are replaced by quartz and pyrite. The fine-grained interstitial material is replaced by tan chlorite, and plagioclase

Table 5. Structural data for Hole 957C.

Core, section, interval (cm)	Piece no.	Curatorial depth (cm)	Estimated depth (mbsf)	ID no. in SVCD	Min. thickness (mm)	Max. thickness (mm)	Estimated thickness (mm)	App. dip dir. 1	App. dip 1	App. dip dir. 2	App. dip 2	Strike	Dip dir.	Dip	Comments
158-957C-															
7N-1, 41-47	6D-E	44	19.9	v1	10	13	12	270	45	0	20	200	290	47	Anhydrite vein
7N-1, 67-68	6G-7	67	20.2	v5			5	90	39	180	8	10	100	39	Anhydrite vein, dip and direction were measured by the working half
7N-1, 74-77	8A	75	20.2	v2		14	14	270	17	180	20	130	220	25	Anhydrite vein
7N-1, 79-84	8A	82	20.3	v3	3	15	9	270	42	0	45	228	318	53	Anhydrite vein
7N-1, 88-94	8B	91	20.4	v4	7	13	10	90	24	0	0	0	90	24	Anhydrite vein
7N-1, 93-98	8B	94	20.4	v5	10	24	17	270	45	180	15	165	255	46	Anhydrite vein
7N-1, 100-103	8B-C	102	20.5	v6	4	7	6	90	5	0	25	281	11	35	Anhydrite vein
7N-1, 125-133	8E	129	20.8	v7	7	17	12	270	40	180	25	151	241	44	Anhydrite vein
7N-2, 72-101	IF, G, H	87	21.7	v1	8	16	105	270	85	30	0	210	300	86	Anhydrite vein
7N-2, 72-108	IF, G, H	90	21.8		65	130									Anhydrite composite vein, estimated width incorporated into v2
7N-2, 104-111	I	108	21.9	v2		4	4	270	55	0	10	187	277	55	Anhydrite vein
7N-2, 118-126	IJ	122	22.1	v3	8	14	11	270	50	0	5	194	284	50	Anhydrite vein
7N-2, 145-148	IK	146	22.3	v4	47			90	25	180	37	58	148	42	Anhydrite composite vein, estimated width incorporated into v2 of 7N-3
7N-3, 2-7	1A, B	5	22.4	v1	40			90	16	180	25	59	149	29	Anhydrite composite vein, estimated width incorporated into v2
7N-3, 2-4	1A	3	22.3	v2	20			90	35	180	26	35	125	40	Anhydrite composite vein, estimated width incorporated into v2
7N-3, 7-10	2	9	22.4			5									Anhydrite vein, drill cuttings, estimated width incorporated into v2
7N-3, 11-21	3	16	22.4	v3	40	80		90	17	0	11	328	58	20	Anhydrite composite vein, estimated width incorporated into v2
7N-3, 23-28	3	26	22.5	v4	50			90	14	0	0	0	90	14	Anhydrite composite vein, estimated width incorporated into v2
7N-3, 21-26	3	24	22.5	v5	15	30		270	24	0	17	214	304	28	Anhydrite composite vein, estimated width incorporated into v2
7N-3, 18-23	3	20	22.5	v6	28	40	300	270	30	0	12	200	290	32	Anhydrite composite vein
7N-3, 31-34	4A	33	22.7	v7		40		270	14	0	9	212	302	16	Anhydrite composite vein, estimated width incorporated into v2
7N-3, 28-32	4A	30	22.6	v8	25			270	12	0	11	222	312	16	Anhydrite composite vein, estimated width incorporated into v2
7N-3, 31-35	4A	33	22.7	v9		7		90	75	180	67	77	167	77	Crosscutting anhydrite vein, estimated width incorporated into v2
9X-1, 1-1	1	1	24	v6											Anhydrite vein, irregular
11N-1, 25-30	3A	28	31	v1	2		2								Anhydrite vein, irregular
11N-1, 31-3	3A-B	31	31	v1		2	2	90	0	0	33	272	2	33	Anhydrite vein
11N-1, 32-40	3B	38	31.1	v2		2	2	270	71	0	24	189	279	71	Anhydrite vein
11N-1, 48-6	3D	56	31.3	v3	2	4	3	90	78	0	77	17	107	81	Anhydrite vein
11N-1, 61-72	3E	65	31.3	v4	2	4	3	270	80	350	0	170	260	80	Anhydrite vein
11N-1, 72-72	3F-G	72	31.4	v5		4	4	90	8	180	10	51	141	13	Anhydrite vein
11N-1, 72-81	3G	77	31.5	v6	5	10	8	270	85	350	0	170	260	85	Anhydrite vein
11N-1, 73-75	3G	74	31.4	v7	2	5	4	270	33						Anhydrite vein
11N-1, 82-82	3G-H	82	31.5	v8		6	6	90	6	180	25	77	167	26	Anhydrite vein
11N-1, 93-97	3H-I	95	31.7	v9	25			90	16	0	19	310	40	24	Anhydrite vein, estimated width incorporated into v17
11N-1, 102-105	3I	104	31.7	v10		15		90	26	0	32	331	61	29	Anhydrite vein, estimated width incorporated into v17
11N-1, 96-109	3I-J	102	31.7	v11		110		90	0	0	19	273	3	19	Anhydrite vein, estimated width incorporated into v17
11N-1, 107-126	3K	117	32	v12		150		90	28	0	15	333	63	31	Anhydrite vein, estimated width incorporated into v17
11N-1, 120-121	3K	120	32	v13		1		90	0	0	0			0	Crosscutting anhydrite vein, estimated width incorporated into v17
11N-1, 121-124	3K	123	32.1	v14		4		90	32						Crosscutting anhydrite vein, estimated width incorporated into v17
11N-1, 124-130	3K	127	32.1	v15	10	20		90	33	0	0	358	88	33	Anhydrite vein, estimated width incorporated into v17
11N-1, 133-136	3K	135	32.2	v16	50			270	57	0	0	180	270	57	Anhydrite vein, estimated width incorporated into v17
11N-1, 121-136	3K	131	32.1	v17	60	70	480	90	40	0	0	0	90	40	Anhydrite vein, central part of the composite vein
11N-2, 1-1	1A	1	32.1		20			270	20	180	39	114	204	42	Anhydrite vein, dip and direction were measured by the working half, estimated width incorporated into v17 of 11N-1
11N-2, 3-22	1A, B, C	13	32.2	v1	8	10	9	270	70	155	0	153	243	73	Anhydrite vein
11N-2, 47-52	1G-H	50	32.6	v2		2	2	90	46						Anhydrite vein
11N-2, 57-63	1I-J	60	32.7	v3		8	8	90	60	140	0	322	52	65	Anhydrite vein
11N-2, 55-61	H-I	58	32.7	v4		8	8	270	35	210	0	203	293	37	Anhydrite vein
11N-2, 67-76	1J, K	72	32.8	v5	50		65	270	66	221	0	219	309	71	Anhydrite vein
11N-2, 77-85	2	81	32.9		15										Anhydrite vein, drill cuttings, part of v5, just above
11N-2, 92-134	4	113	33.2		50										Anhydrite vein, drill cuttings, part of v6
11N-2, 104-110	5	107	33.2		5										Anhydrite vein, drill cuttings, part of v6, width estimated from cuttings volume
11N-2, 110	6				30										Anhydrite vein, drill cuttings, part of v6
11N-2	7				15										Anhydrite vein, drill cuttings, part of v6
11N-2	8				16										Anhydrite vein, drill cuttings, part of v6
11N-2	9	134			15										Anhydrite vein, drill cuttings, part of v6
11N-2, 134-140	10	137	33.5	v6	15		50	90	56	180	0	0	90	56	Anhydrite vein
11N-2, 143-149	11	146	33.6		14		30								Anhydrite vein, drill cuttings
11N-3, 0-4	1	2	33.6		16										Anhydrite vein, drill cuttings, estimated width incorporated into the above column
11N-3, 5-11	2	8	33.7	v1	30		30								Anhydrite vein
11N-3, 17-23	3	20	33.8		15	20									Anhydrite vein, drill cuttings, part of v6 below
11N-3, 23-34	4	28	33.9		15										Anhydrite vein, drill cuttings, part of v6 below
11N-3, 35-46	5A-B	42	34	v2	54		54	270	62	0	30	197	287	63	Anhydrite vein

Table 5 (continued).

Core, section, interval (cm)	Piece no.	Curatorial depth (cm)	Estimated depth (mbsf)	ID no. in SVCD	Min. thickness (mm)	Max. thickness (mm)	Estimated thickness (mm)	App. dip dir. 1	App. dip 1	App. dip dir. 2	App. dip 2	Strike	Dip dir.	Dip	Comments
11N-3, 57-57	5C	57	34.2	v3	3				0		0				Anhydrite vein
11N-3, 58-69	6	64	34.2	v3	100		158	90	13	0	18	305	35	22	Anhydrite vein
11N-3, 70-75	7	73	34.3	v3	10										Anhydrite vein, drill cuttings
11N-3, 75-80	8A	78	34.4	v3	38			90	0	0	7	270	360	7	Anhydrite vein
11N-3, 80-81	8B	80	34.4	v3	7			90	12	0	80	272	2	80	Anhydrite vein
11N-3, 81-87	8B	84	34.4	v4	7	10	9	270	47	0	0	180	270	47	Anhydrite vein
11N-3, 82-82	8B	82	34.4	v5		2	2	90	0	0	0	0		0	Anhydrite vein
11N-3, 83-86	8B	85	34.4	v6		2	2	270	39	0	0	180	270	39	Anhydrite vein
11N-3, 84-90	8B	87	34.5	v7		2	2	270	71						Anhydrite vein
11N-3, 88-94	8B-C	91	34.5	v8	7	9	8	90	37	0	27	326	56	42	Anhydrite vein
11N-3, 93-95	8C	94	34.5	v9	2	5	4	270	29	180	42	122	212	47	Anhydrite vein
11N-3, 97-98	8C	98	34.6	v10	2		2	90	22	0	0	0	90	22	Anhydrite vein
11N-3, 106-106	10A	106	34.6	v11	4		4	90	0	0	0	0		0	Anhydrite vein
11N-3, 109-122	10A	116	34.7	v12	5		5	90	80	0	0	0	90	80	Anhydrite vein
11N-3, 122-128	10B	125	34.8	v12				90	60	345	0	345	75	61	Anhydrite vein
12N-1, 33-33	5A	33	35.4	v1	16		16		0		0			0	Anhydrite vein
12N-1, 47-48	5C	48	35.5	v2	2		2	270	75	5	12	193	283	75	Anhydrite vein
12N-1, 66-68	6	67	35.6	v3	8			270	30	0	0	180	270	30	Anhydrite vein, estimated width incorporated into v4
12N-1, 69-74	7	72	35.6			20									Anhydrite vein, drill cuttings, width estimated from cuttings volume, estimated width incorporated into v4
12N-1, 74-97	8	84	35.6	v4		190	458		0		0			0	Anhydrite vein
12N-1, 99-127	9, 10	110	35.8		50	140									Anhydrite vein, drill cuttings, minimum width was measurement of a piece, maximum width estimated from cuttings volume, estimated width incorporated into v4
12N-2, 0-17	1, 2	10	35.9			100									Anhydrite vein, drill cuttings, width estimated from cuttings volume, estimated width incorporated into v4
12N-2, 22-26	3	24	36	v1	4		4		90					90	Anhydrite vein
12N-2, 33-37	4	35	36	v2	30		70	270	30	0	0	180	270	30	Anhydrite vein
12N-2, 37-43	5	40	36			15									Anhydrite vein, drill cuttings, width estimated from cuttings volume, estimated width incorporated into v2
12N-2, 46-50	6	48	36.1	v3	25			90	40	0	0	0	90	40	Anhydrite vein, drill cuttings, estimated width incorporated into v2
12N-2, 59-62	8	61	36.1		2	3	3								Anhydrite vein
12N-2, 80-82	11	81	36.2	v4	3		3								Anhydrite vein
12N-2, 84-88	11	86	36.3	v5		10	10	90	53	0	78	306	36	78	Anhydrite vein
12N-2, 88-93	11	91	36.3	v6		2	2								Anhydrite vein
12N-2, 96-104	12	100	36.3	v7		2	2	270	70	0	0	180	270	70	Anhydrite vein
12N-2, 111-120	14	115	36.4			50									Anhydrite vein, drill cuttings, width estimated from cuttings volume, estimated width incorporated into v8
12N-2, 125-128	15	127	36.4	v8		9	79	90	67	224	0	44	134	73	Anhydrite vein
12N-2, 129-138	16	134	36.5			20									Anhydrite vein, drill cuttings, estimated width incorporated into v8
12N-3, 17-20	2	19	36.6	v1	7		7	90	55	0	0	0	90	55	Anhydrite vein
12N-3, 17-25	2	21	36.6	v2	13		13		90					90	Anhydrite vein, irregular
12N-3, 25-25	2	25	36.6	v3	3		3		0		0			0	Anhydrite vein
12N-3, 49-51	5	50	37.4	v4	10		10	90	12	0	0	0	90	12	Anhydrite vein
13N-1, 48-53	10	51	37.7	v1		8	8	90	65	0	0	0	90	65	Anhydrite vein
13N-1, 68-75	13	72	37.9	v2	2		2	270	75	10	0	190	280	75	Anhydrite vein
13N-1, 83-83	15	83	38	v3	2		2								Anhydrite vein
13N-1, 92-94	15	93	38.1	v4	2		2								Anhydrite vein
13N-1, 128-136	22	132	38.5	v5	1		1	270	85	180	0	180	270	85	Anhydrite vein
13N-2, 6-6	2	6	38.6	v1	1		1	0	20	0	0	0	0	20	Anhydrite vein
13N-2, 7-15	2	11	38.7	v2	46		46	90	80	0	0	0	90	80	Anhydrite vein
13N-2, 16-25	3A-B	21	38.8	v3		30	30	270	50	0	0	180	270	50	Anhydrite vein
13N-2, 37-41	3D	39	38.8	v4		2	2								Anhydrite vein, irregular
13N-2, 51-57	3F	54	39.1	v5	30		30	90	0	0	0			0	Anhydrite vein
14N-1, 6-8	2	7	40.3	v1	1		1								Anhydrite vein
14N-1, 21-21	2, 3	21	40.4	v2	1	4	3		0		0			0	Anhydrite vein, irregular
14N-1, 43-45	6	44	40.6	v3	2		2	270	20	0	20	225	315	27	Anhydrite vein
14N-1, 48-50	6	49	40.7	v4	2	4	3	90	60	5	##	357	87	58	Anhydrite vein
14N-2, 0-0	1A	0	40.9	v1	1		1		0		0			0	Anhydrite vein
14N-2, 5-16	1A	10	41		1	2	2								Anhydrite vein, network
14N-2, 32-36	1C	34	41.2	v2	20	27	24	90	19	0	0	0	90	19	Anhydrite vein
14N-2, 36-37	1C	37	41.2	v3		18		90	16	0	28	298	28	31	Anhydrite vein, drill cuttings, estimated width incorporated into v4
14N-2, 38-42	1D	40	41.3	v4		28	46	90	6	180	11	62	152	12	Anhydrite vein

Table 5 (continued).

Core, section, interval (cm)	Piece no.	Curatorial depth (cm)	Estimated depth (mbsf)	ID no. in SVCD	Min. thickness (mm)	Max. thickness (mm)	Estimated thickness (mm)	App. dip dir. 1	App. dip dir. 1	App. dip dir. 2	App. dip dir. 2	Strike	Dip dir.	Dip	Comments
14N-2, 47-54	2	51	41.4			30									Anhydrite vein, drill cuttings, width estimated from cuttings volume, estimated width incorporated into v5
14N-2, 56-62	3	59	41.5	v5	10	12	41	270	46	180	20	157	247	42	Anhydrite vein
14N-2, 62-64	3	63	41.5	v6	15		55	270	12	0	0	180	270	12	Anhydrite vein
14N-2, 64-70	4	67	41.6			40									Anhydrite vein, drill cuttings, width estimated from cuttings volume, estimated width incorporated into v6
15N-1, 69-72	9A-B	71	42.8	v1		2	2	270	60	0	0	180	270	60	Anhydrite vein
15N-1, 73-75	9	74	42.9	v2		1	1	224	50	0	0	134	224	50	Anhydrite vein
15N-1, 78-78	9	78	42.9	v3	6		6	30	45	0	0	300	30	45	Anhydrite vein
15N-1, 86-114	11	97	43.1	v4	13	15	14	270	75	5	20	200	290	76	Anhydrite vein
15N-2, 28-31	1F-G	30	43.5	v1	2	3	3	270	24	180	26	132	222	33	Anhydrite vein
15N-2, 32-32	1G	32	43.5	v2	2	3	3	90	0	180	21	90	180	21	Anhydrite vein
15N-2, 34-36	2A	35	43.5	v3	8		8								Anhydrite vein
15N-2, 41-44	2A	43	43.6	v4	14		20	90	54	0	0	0	90	54	Anhydrite vein
15N-2, 34-37	2A	36	43.5	v5	2	4	3	310	65			220	310	65	Anhydrite vein, estimated width from Piece 3
15N-2, 36-43	2A	40	43.5	v6	2	4	3								Anhydrite vein
15N-2, 50-81	3	65	43.6			20									Anhydrite vein, drill cuttings, part of v4
15N-2, 83-83	4A	83	43.9		15										Anhydrite vein, drill cuttings, part of v4
15N-2, 109-119	6	114	44.2	v7	13		15	270	90	0	0	180	270	90	Anhydrite vein
15N-2, 141-148	8	144	44.4	v8	18			270	90	0	0	180	270	90	Anhydrite vein, continuation of v7
15N-3, 0-48	1, 2, 3	24	44.7		30	200									Anhydrite vein, drill cuttings, maximum width estimated from cuttings volume, estimated width incorporated into v1
15N-3, 49-55	4	52	44.9	v1	48		285								Anhydrite vein
15N-3, 56-68	5	62	44.9			30									Anhydrite vein, drill cuttings, width estimated from cuttings volume, estimated width incorporated into v1
15N-3, 69-69	6	69	45.1	v2	5	8									Anhydrite vein, drill cuttings, estimated width incorporated into v1
15N-3, 89-117	9	103	45.4			3	3								Angular fractures, anhydrite
15N-3, 117-132	10	125	45.5			1	1								Angular fractures, anhydrite
15N-3, 132-150	11	141	45.6			2	2								Angular fractures, anhydrite
15N-4, 19-26	2	23	45.9	v1	1		1	90	74	8	0	8	98	74	Anhydrite vein
15N-4, 26-26	2	26	46	v2	1	2	2	270	17	0	0	180	270	17	Anhydrite vein
16N-1, 10-13	2	12	46.3	v1	3		3	90	42	5	0	354	84	41	Anhydrite vein
16N-1, 15-18	3	17	46.4	v2	3		3	270	35	5	0	182	272	36	Anhydrite vein
16N-1, 21-23	3	22	46.4	v3	2		2	90	30	180	18	29	119	34	Anhydrite vein
16N-1, 30-32	5A	31	46.5	v4		1	1	270	28	5	0	189	279	28	Anhydrite vein
16N-1, 37-45	5B, C-D	41	46.6	v5		1	1	90	58	5	0	357	87	58	Anhydrite vein
16N-1, 54-54	7	54	46.8		6		6								Anhydrite vein
16N-1, 129-131	16A	130	47.5		8		8								Anhydrite vein
16N-2, 7-8	1	8	47.7			1	1								Anhydrite vein, irregular
16N-2, 33-43	3	38	48			1	1								Anhydrite vein, irregular
16N-2, 53-58	5B	56	48.2			1	1								Pyrite lined fracture with anhydrite
16N-2, 70-74	7A	72	48.4	v1	2	3	3	90	53	0	0	0	90	53	Silica-sulfide vein
16N-2, 77-78	7B	78	48.4	v2	2	3	3	270	21	180	10	155	245	23	Silica-sulfide vein

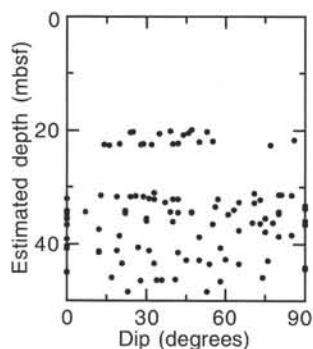


Figure 46. Plot of anhydrite vein orientations (corrected dip-angle relative to the core reference frame) as a function of depth in core from Hole 957C. The data show no apparent preferred orientations with depth.

class phenocrysts are pseudomorphed by a colorless phyllosilicate that exhibits second-order interference colors (possibly chlorite? or mixed-layer smectite-chlorite?). Rare olivine phenocrysts are replaced by orange iron oxides or oxyhydroxides surrounded by quartz, plus a colorless, high birefringence phyllosilicate (talc? or sericite?) plus pyrite.

In one example (Sample 158-957E-18R-1, Piece 4) (Fig. 60), a 0.5-mm-wide, dark green chlorite vein in green chloritized basalt is cut by a later pyrite vein and its associated gray alteration halo. Where the dark green chlorite vein in the green chloritized basalt passes into the gray alteration halo, the vein filling changes to a white phyllosilicate (Fig. 60). This white mineral continues across the gray alteration halo on the other side of the vein, and then the vein filling becomes dark green chlorite again where the vein passes into the green chloritized host basalt on the far side of the vein.

Locally superimposed on the gray to buff alteration halos and on green chloritized basalt are darker gray, irregularly shaped silicification halos (e.g., in interval 158-957E-18R-1, Pieces 4–9) (Fig. 60), which commonly contain millimeter-sized patches of relict gray to buff clays within the hard, silicified halo. These silicification halos appear to be related to adjacent quartz veins. In some cases (Samples 158-957E-18R-1, Pieces 6 and 7), dark gray silicification bands, <1 mm wide, occur at the margins of 4-mm-wide white quartz plus pyrite veins. These quartz veins contain small amounts of pyrite and dark green chlorite near the vein margins.

Preliminary Interpretations

The vein and halo relationships illustrate the sequence of alteration in the rocks. First, the rocks were pervasively altered to green chlorite(?), with concomitant formation of chlorite(?) in veins. This was followed by formation of pyrite and quartz plus pyrite veins, as well as associated gray alteration halos. Subsequent quartz veins cut earlier sulfide veins and chloritized rocks, and led to local silicification of the rocks. The first stages could conceivably be related to the reaction of large amounts of seawater with basalts during the early stages or on the margins of the hydrothermal upwelling zone. The presence of rare chlorite in the rocks (Table 10) implies temperatures of at least 200°–250°C; however, mixed-layer phases indicating lower alteration temperatures are much more common. Therefore, mixed-layer phases may be present and alteration temperatures could have been somewhat lower. This earlier alteration was followed by “main-stage” alteration, probably by upwelling “black-smoker”-type hydrothermal fluids that leached elements (e.g., K, Ca, Na) from the rocks and deposited sulfides ± quartz. By analogy with hydrothermal vent fluids and given the deposition of chalcopyrite lining veins, temperatures were probably greater than 250°–300°C. As indicated by

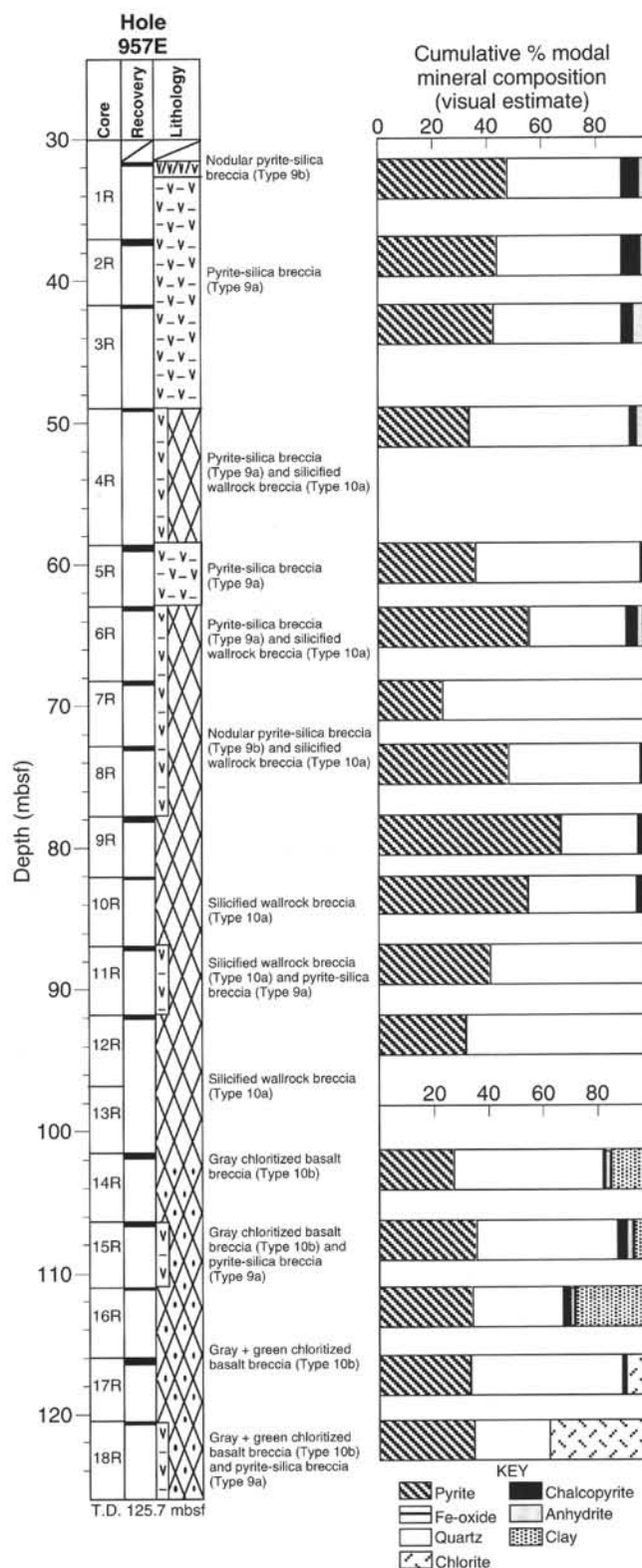


Figure 47. Detailed stratigraphic section of the most complete intervals in Hole 957E. Mineral abundances, based on visual estimates, given for each cored interval. Note that pieces of massive granular pyrite (Type 5c) were recovered in Cores 158-957E-1R, 2R, 6R, 8R, 9R, 10R, and 15R.

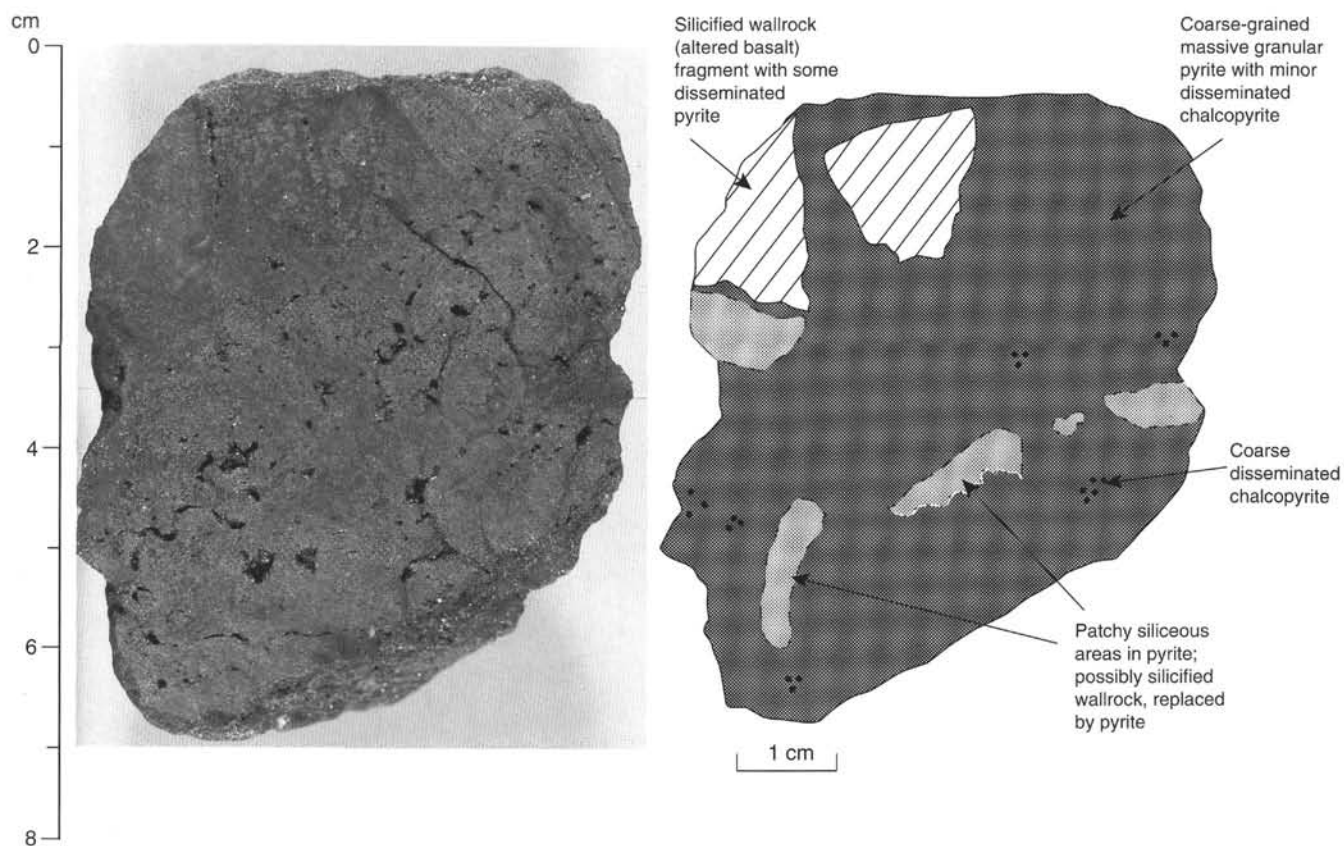


Figure 48. Photograph and sketch of massive granular pyrite (Type 5c) with disseminated chalcopyrite. Silicified wallrock fragments are enclosed in the pyrite. Sample 158-957E-9R-1 (Piece 1, 0–8 cm).

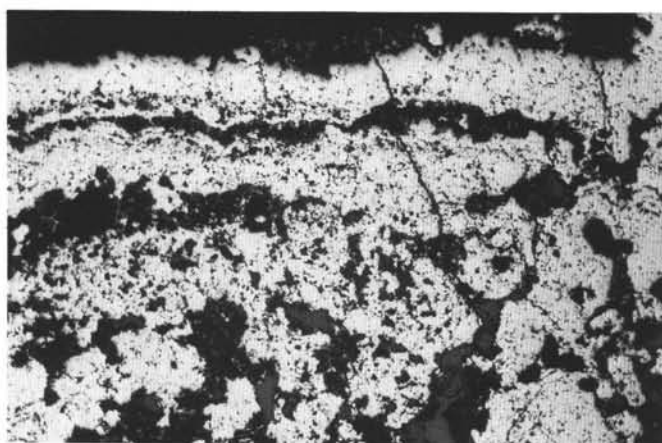


Figure 49. Photomicrograph of colloform texture preserved in massive pyrite (white). Note the high porosity (black) of the sample. Sample 158-957E-2R-1 (Piece 2, thin section from 6 to 8 cm). Reflected light, field of view = 6 mm.

the crosscutting relationships of veins, quartz (and sulfide) veins formed next and portions of the rocks were silicified, possibly during mixing of hydrothermal fluids with seawater or cooling of hydrothermal fluids during the waning stages of upwelling hydrothermal activity in these rocks. Finally, anhydrite formed in late veins as more seawater-dominated fluids penetrated the still-hot rocks. Some of the late anhydrite veins may represent the resumption of upwelling black-smoker type fluids through the rocks, and the mixing of these fluids with small amounts of seawater to form chalcopyrite plus anhydrite veins (in Hole 957C). Multiple stages of anhydrite formation

are indicated by the presence of anhydrite veins cutting across previously formed anhydrite veins (see "Sulfide Petrology and Geochemistry" section, this chapter). Dissolution features in large anhydrite veins in the upper portion of Hole 957C may reflect either periods of influx of cold seawater or of renewed upwelling of high-temperature hydrothermal fluids (see "Sulfide Petrology and Geochemistry" section, this chapter).

The general zonation upward from green chloritized basalt breccias, to gray chloritized basalt breccias, to silicified wallrock breccias in Holes 957E and 957C represents the transition from the deeper and more marginal portions of the stockwork zone into the deposit itself, from greater seawater influence on rock alteration to greater hydrothermal fluid influence.

Little evidence is present for the alteration of these rocks at temperatures less than about 200°–250°C. Possible evidence for lower temperatures is the presence of gypsum(?), which may be present in a few samples as a late euhedral mineral in vugs and veins. Some gypsum may also be present in small amounts in thin sections or in the X-ray diffractograms, but this could be the result of the sample preparation processes. The identification of gypsum in vugs is tentative, however, and all other mineralogy suggests continued temperatures >200°–250°C. No mineralogical evidence is present indicative of alteration temperatures greater than about 300°–350°C(?) (i.e., no amphibole has been observed).

PHYSICAL PROPERTIES

Introduction

The sulfide-sulfate assemblages cored in Holes 957C, 957E, 957F, and 957G on the east side of the Black Smoker Complex are characterized by a distinctive range of physical properties. Results

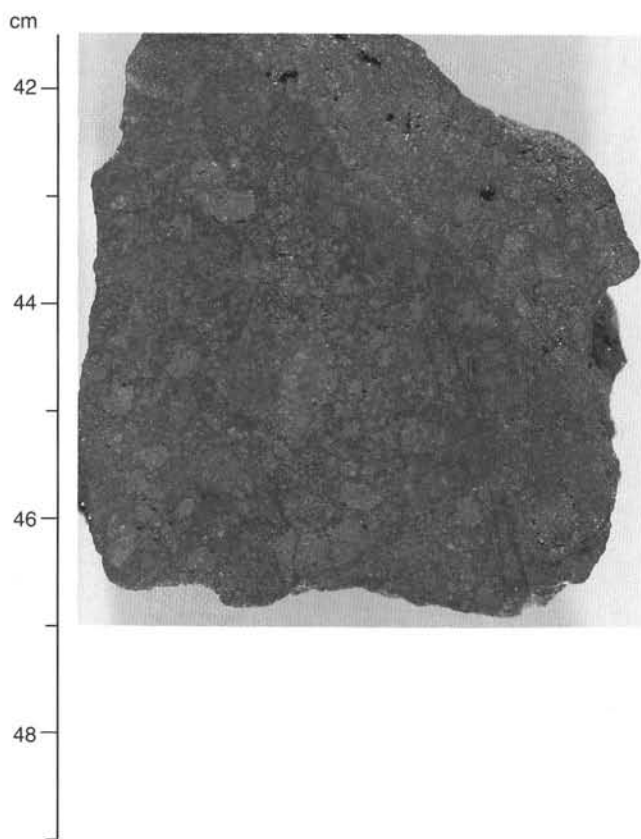


Figure 50. Pyrite-silica breccia (Type 9a). Individual clasts likely represent completely pyritized and silicified wallrock breccia fragments. Sample 158-957E-11R-1 (Piece 9, 41.5–49 cm).

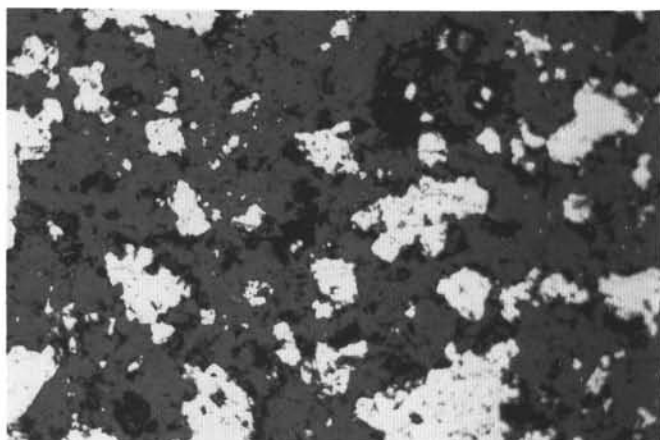


Figure 51. Photomicrograph of pyrite aggregates (white) with sphalerite inclusions (medium gray) disseminated in quartz (dark gray) in pyrite-silica breccia. Sample 158-957E-11R-1 (Piece 9, thin section from 42 to 49 cm). Reflected light, field of view = 6 mm.

are presented according to the type of measurements made for each hole. Depending on the available material (minicores or fragments), an effort was made to sample representative lithologies for each section recovered. Physical properties measurements were made on rock samples, as follows:

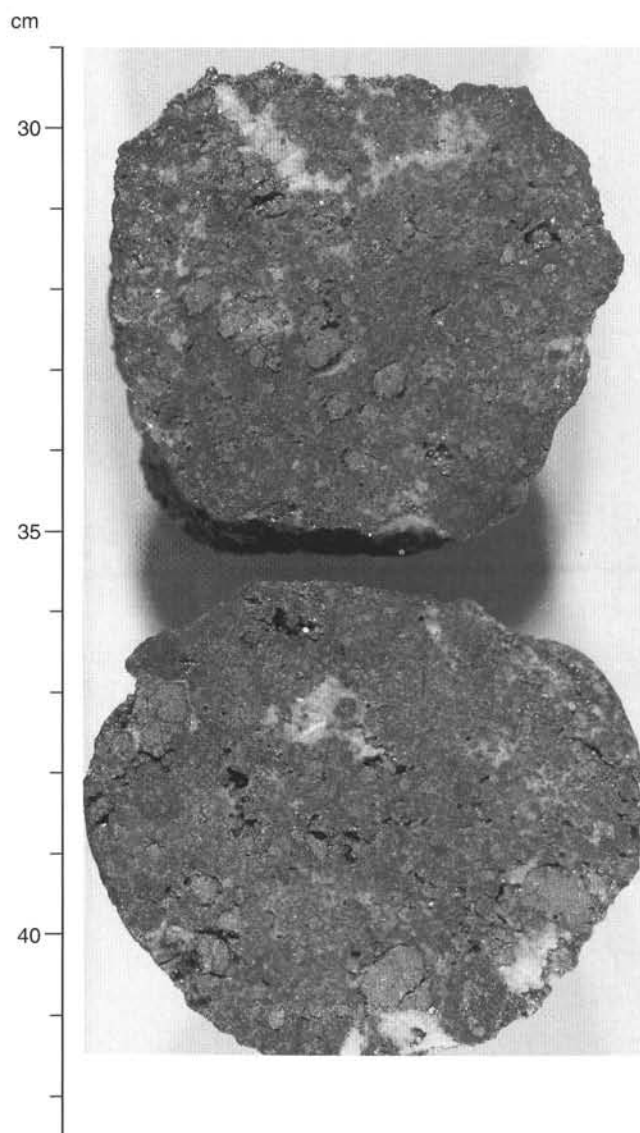


Figure 52. Nodular pyrite-silica breccia (Type 9b) with anhydrite filling open space. Dissolution(?) cavities surround pyrite clasts. Sample 158-957E-2R-1 (Pieces 6 and 7, 29–42.5 cm).

- Hole 957C: 9 sulfide minicores, 2 anhydrite minicores, 3 sulfide fragments, and 9 half-round slabs;
- Hole 957E: 12 sulfide fragments;
- Hole 957F: 1 sulfide minicore, 2 sulfide fragments, and 1 half-round slab; and
- Hole 957G: 1 sulfide minicore and 1 half-round slab.

Hole 957C

Index Properties

Index properties were measured on 1 to 2 samples from each suitable core section; these measurements are summarized in Table 11. Values of bulk density range from 2.79 to 4.31 g/cm³ and those of grain density range from 2.94 to 4.62 g/cm³. Figure 92 shows the distribution of bulk and grain density with depth based on measurements obtained on 14 discrete samples taken from Hole 957C cores (Table 11; see Method C in “Physical Properties” section, Chapter 5, this volume). The relative difference between grain and bulk density is

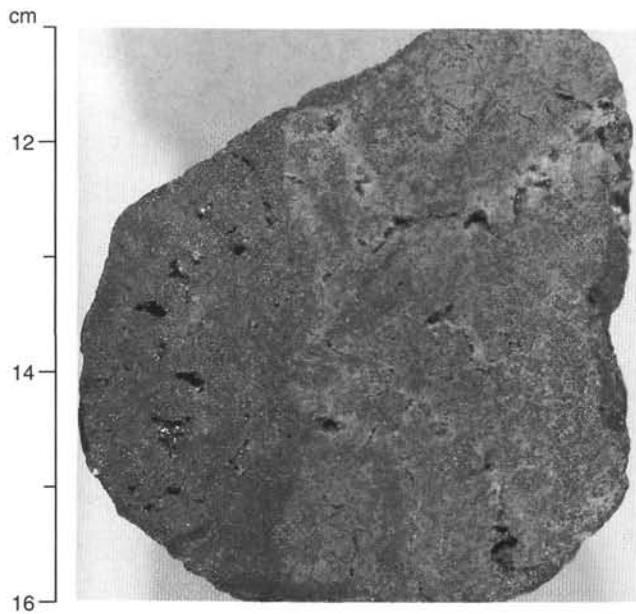


Figure 53. Massive siliceous pyrite (vein?) on the margin of a siliceous wallrock breccia (Type 10a) clast. Sample 158-957E-6R-1 (Piece 3, 11–16 cm).

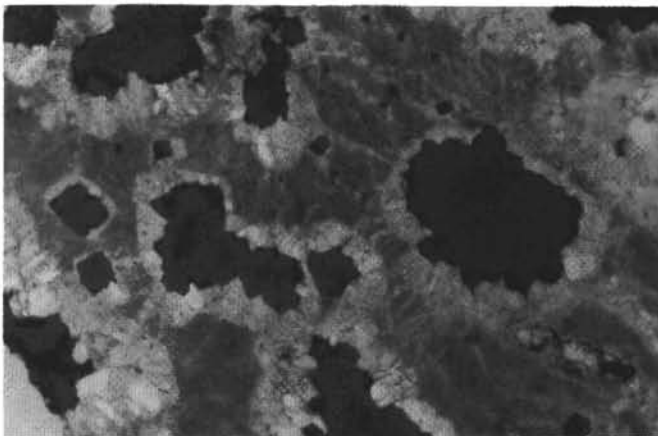


Figure 54. Photomicrograph showing replacement of altered basalt (medium gray) by pyrite (dark gray) and quartz (light gray) in silicified wallrock breccia. Relict subvolcanitic texture in silicified basalt clast. Note the continuous rim of quartz surrounding each pyrite grain, and the sharp parallel straight contact between quartz and altered basalt. This suggests that quartz has replaced basalt outward from the pyrite grain. The quartz halo preserves the morphology of the pyrite grains. The relict basaltic texture has been preserved in the quartz. Sample 158-957E-4R-1 (Piece 3, thin section from 13 to 16 cm). Reflected light, field of view = 1.5 mm.

dependent on the individual porosity of the sample. Porosity values range from 2.4% to 16.2% (Fig. 93, Table 11).

Multisensor Track

The condition of the core limited measurements to a cumulative length of 4.14 m from 4 of the 16 cores (Cores 158-957C-7N, 11N, 13N, and 15N) recovered from Hole 957C (Fig. 94). The scanned intervals are enlarged in Figure 94 to show in detail the distribution of values within each interval.

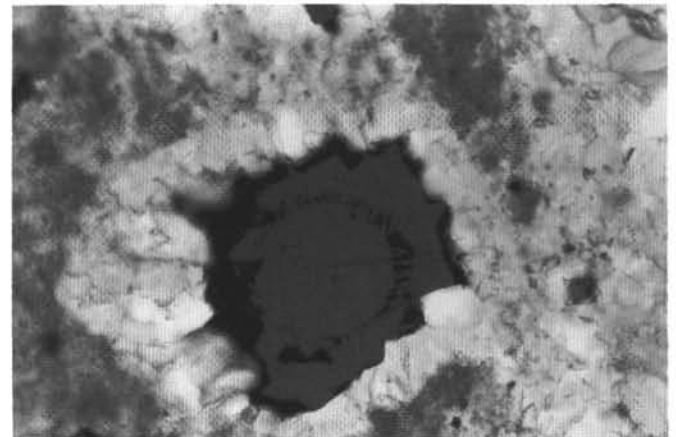


Figure 55. Photomicrograph of filling of a vesicle and replacement of surrounding basalt by pyrite (dark gray) in silicified wallrock breccia. The basaltic texture is preserved at the interior of the pyrite grain and clearly outlines the spherical shape of the vesicle. Note also the quartz (white) halo replacing basalt (medium gray) around the pyrite grain. Sample 158-957E-4R-1 (Piece 3, thin section from 13 to 16 cm). Reflected light, field of view = 750 μm .

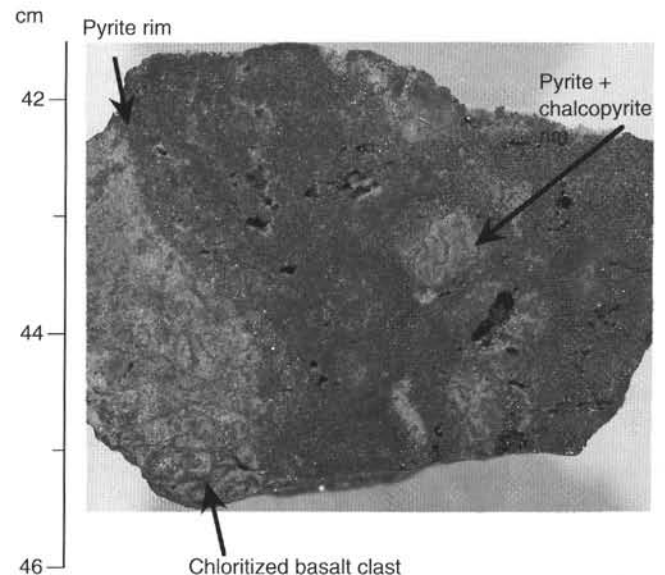


Figure 56. Chloritized basalt breccia (Type 10b) clasts rimmed by pyrite and intergrown chalcocopyrite-pyrite. Sample 158-957E-14R-1 (Piece 10, 41–46 cm).

Bulk density measurements obtained by the GRAPE instrument cluster into two groups (Fig. 94): $\geq 2.5 \text{ g/cm}^3$ and $< 2.5 \text{ g/cm}^3$. The measured cores from Hole 957C were recovered using the MDCB coring system. Core diameter varied from 55 to 61 mm. According to Figure 7 in Chapter 5 (this volume) which shows the dependence of the bulk density measured by the GRAPE instrument on the diameter of the recovered core, the actual bulk density values are 9% to 24% larger than the reported values. The range of higher values ($\geq 2.5 \text{ g/cm}^3$) is consistent with the range of discretely measured index properties for samples from corresponding core sections (Table 11), when corrected for deviation from full core diameter according to the diameter-density relation plotted in Figure 7 (Chapter 5, this volume). The range of lower values ($< 2.5 \text{ g/cm}^3$) is lower than the range of discrete-

ly measured index properties. These data are considered unreliable because of the irregularities in the cylindrical shape of the core sections scanned, probably a result of poor bit tracking and core fracturing.

Values of natural gamma radiation (Fig. 94; range: 6–12 counts/s) and volume magnetic susceptibility are generally low (Fig. 94; range: -4 to 10×10^{-5} SI units) in the samples measured, with the exception of higher values centered on 31 mbsf (Fig. 94; range: 10 to 27×10^{-5} SI units). Both the low and the higher volume magnetic susceptibility values are consistent with those made by direct measurements on minicore samples from corresponding intervals (see "Paleomagnetism" section).

Compressional (P-wave) Velocities

Compressional (*P*-wave) velocities range from 4.86 to 5.66 km/s in the six seawater-saturated, sulfide-rich minicore samples measured (Table 12).

No clear trend is visible in the variation of velocity vs. depth. However, similar rock types (e.g., pyrite-silica-breccia, nodular pyrite-silica-breccia, and pyrite-silica-anhydrite-breccia; Fig. 95) show only limited variations of 5.1 to 5.2 km/s, although their total porosities vary from 2.4% to 4.5%. The sample with the highest velocity measured (silicified wallrock breccia = 5.66 km/s) was recovered from the maximum depth penetrated (47.7 mbsf) and has a lower porosity (3.1%) than one other sample of the same rock type with a lower velocity of 4.86 km/s and a higher porosity of 3.6% recovered at a shallower depth (43.3 mbsf) (Fig. 95). Velocity could not be measured in a saturated anhydrite minicore as the *P*-wave velocity recorded (1.6 km/s) indicated primarily transmission through the seawater rather than through the anhydrite.

Electrical Resistivity

Electrical resistivity measurements were made on seven minicore samples, saturated with seawater, representing the major sulfide-anhydrite rock types recovered from Hole 957C (Table 12). The resistivities recorded ranged from 0.18 to 2.06 Ωm for five sulfide-rich samples (pyrite-silica-breccia, nodular pyrite-silica-breccia, pyrite-silica-anhydrite-breccia, and silicified wallrock breccia). A relatively high value of 2.77 Ωm was recorded in a minicore extracted from an anhydrite vein (Table 12).

Thermal Conductivity

Thermal conductivity was measured on nine half-round slabs representing the various rock types cored from Hole 957C. The thermal conductivity values of the sulfide-rich rocks are generally high (they range from 5.73 to 8.73 W/(m·K)) (Table 13, Fig. 96), and five of the eight sulfide-rich samples have thermal conductivities larger than 8.3 W/(m·K). The value of thermal conductivity measured on one anhydrite specimen (5.37 W/(m·K); Table 13; Sample 158-957C-7N-3, 10–25 cm) is consistent with published values of 5.61 W/(m·K) (Clark, 1966, table 21-2).

Hole 957E

Index Properties

Recovery from Cores 158-957E-1R to 18R allowed only rock fragments to be taken as samples for physical properties measurements. Of the suite of possible shipboard measurements, the fragments were suitable only for discrete determination of index

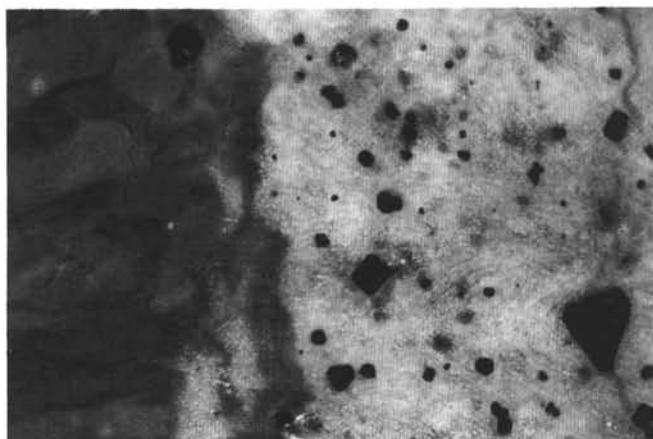


Figure 57. Photomicrograph of chloritized basalt breccia with disseminated pyrite crystals (black) in altered basalt (white). A vein of euhedral quartz crystals (left) have grown perpendicular to the surface of the altered basalt clast. Sample 158-957E-14R-1 (Piece 11, thin section from 52 to 55 cm). Reflected light, crossed nicols; field of view = 750 μm .

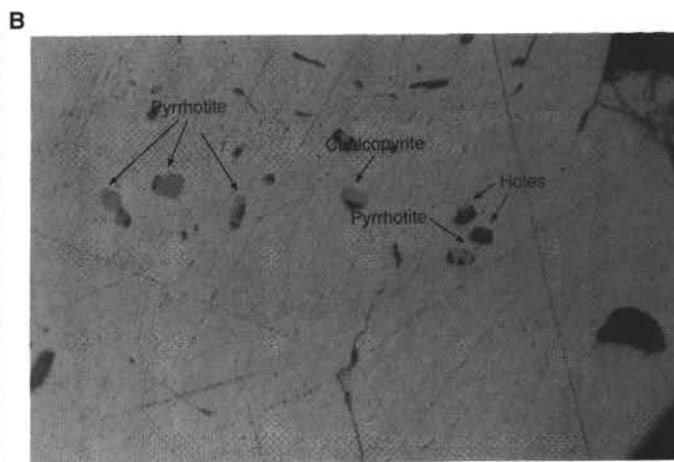
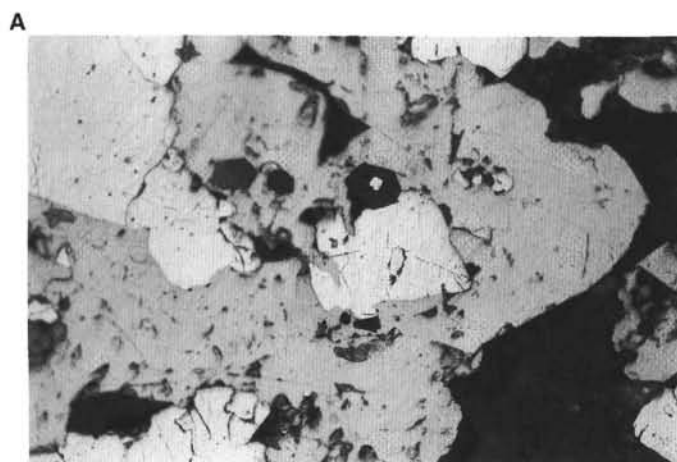


Figure 58. Photomicrograph of sulfide mineral textures in chloritized basalt breccia (Type 10b). **A.** Chalcopyrite (medium gray) overgrowing pyrite (white) and quartz (dark gray) within a quartz vein in chloritized basalt breccia. Note the euhedral quartz crystals in chalcopyrite. Sample 158-957E-14R-1 (Piece 11, thin section from 52 to 55 cm). Reflected light, field of view = 750 μm . **B.** Pyrite grain containing inclusions of pyrrhotite and chalcopyrite. Sample 158-957E-14R-1 (Piece 11, thin section from 52 to 55 cm). Reflected light, field of view = 300 μm .

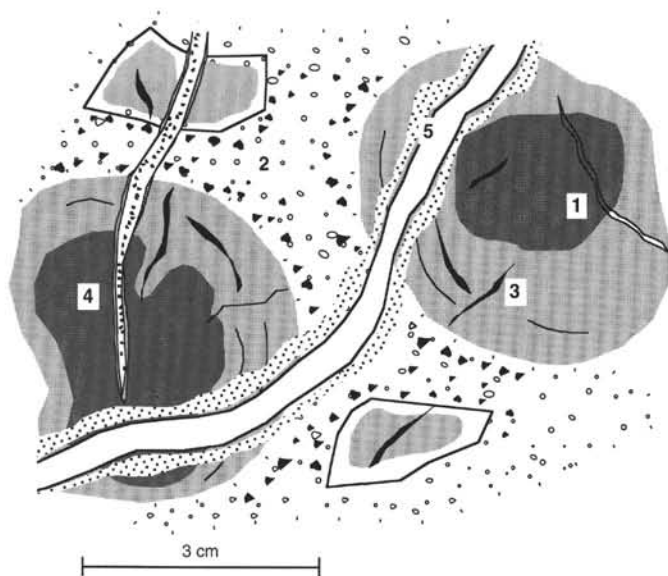


Figure 59. Schematic representation of vein stages and altered basalt clasts in core from Hole 957E. Within the basalt clasts, dark gray represents chlorite alteration, light gray represents buff (quartz and clay \pm chlorite) alteration, and white represents silicification. Numbers indicate vein stages, as follows: 1 = chlorite veins, 2 = gray quartz-pyrite veins, 3 = pyrite veinlets, 4 = white quartz-pyrite veins, and 5 = anhydrite veins with chalcopyrite selvage and pyritization halo (dot pattern).

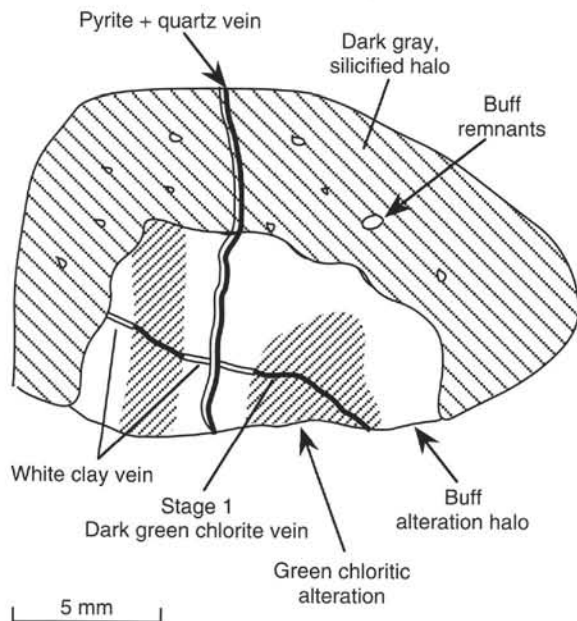


Figure 60. Sketch illustrating a Stage 1, dark green, chlorite vein in a green chloritized basalt clast, cut by pyrite plus quartz veinlet and associated gray alteration halo. The dark green chlorite vein is altered to a white phyllosilicate vein, where it is cut by the gray alteration halo. A later dark gray silicified zone is superimposed upon the gray chloritization halo, with patches of relict gray to white clay minerals in the silicification halo.

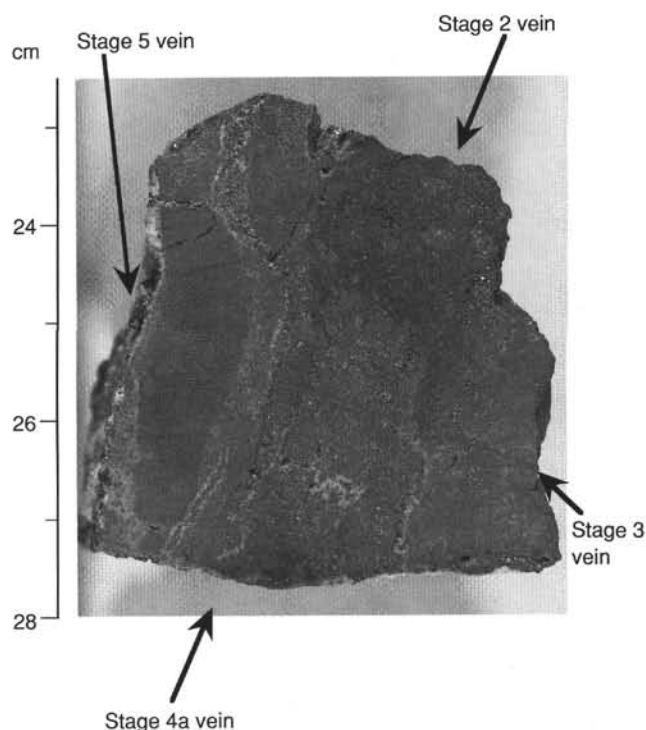


Figure 61. Stage 2 pyrite-gray quartz vein and offshoot in chloritized basalt breccia (Type 10b). Buff alteration halos surrounding the Stage 2 vein overprint the pervasive green chloritization in the breccia fragment. Tiny pyrite-filled veinlets (Stage 3) and white quartz with a central zone of pyrite (Stage 4a) are present within the basalt fragment. An anhydrite vein (Stage 5) is visible along the edge of the sample. Sample 158-957E-17R-1 (Piece 4, 22.5–28 cm).

properties. Values of bulk water content, bulk density, grain density, and porosity of rock fragments from 12 of the 18 cores are compiled in Table 11 and plotted in Figures 93 and 97.

Pyrite-silica breccia and nodular pyrite-silica breccia samples are representative of the predominant lithology between 31.57 and 87.52 mbsf and vary in bulk density from 3.19 to 3.48 g/cm³, with the highest value at 87.52 mbsf (Fig. 97). However, two samples out of that depth range (Sample 158-957E-1R-1, 7–9 cm, a semi-massive pyrite-chalcopyrite fragment; and Sample 158-957E-6R-1, 18–20 cm, a massive granular pyrite fragment), recovered at 31.57 and at 63.48 mbsf, have higher bulk densities (4.12 and 4.47 g/cm³, respectively). From 31.57 to 87.52 mbsf (Cores 158-957E-1R to 11R), porosity values generally decrease with depth (Table 11) and range from 11.4% to 4.9% (Fig. 93).

Samples taken deeper in Hole 957E (Cores 158-957E-12R to 18R; 91.96–120.96 mbsf) are representative of a change in predominant lithology to silicified wallrock breccia and chloritized basalt. In this depth range, porosity values generally increase with depth (Table 11) from 5.2% to 8.5%. Values of bulk density are all similar (3.28–3.39 g/cm³), with the exception of one sample taken at 91.96 mbsf (Sample 158-957E-12R-1, 16–18 cm), which had the highest bulk density of all samples measured in Hole 957E (4.51 g/cm³; Fig. 97). This sample is classified as a silicified wallrock breccia. However, further analysis using atomic absorption spectroscopy (AAS) yielded the highest Fe content (40.8 wt%) of all samples analyzed from Hole 957E. This sample also contains high contents of S (47.1 wt%) and Cu (4.1 wt%) (Table 8), which suggests that this sample is enriched in pyrite.

Hole 957F

Physical properties measurements were made on Sections 158-957F-1N-1 and 2N-1. A multisensor track (MST) scan (Fig. 98) of a short (50–63 cm), intact portion of Section 158-957F-1N-1 shows consistent values of wet bulk density (3 g/cm^3 , uncorrected; 3.5 g/cm^3 , corrected for actual core diameter according to Fig. 7, Chapter 5, this volume). Small range variations were observed for measurements of natural gamma radiation (8.5–10.5 cps) and of volume magnetic susceptibility ($4 \text{ to } 7 \times 10^{-5} \text{ SI}$). The corrected values of bulk density measured by the MST GRAPE device are consistent with the directly measured value (3.6 g/cm^3) for a massive pyrite breccia (Sample 158-957F-1N-1, 62–64 cm) from the same section (Table 12; Figs. 93, 97). Three massive sulfide samples (Samples 158-957F-1N-1, 19–21 cm; 1N-1, 62–64 cm; and 2N-1, 10–20 cm) exhibit a narrow range of bulk density values ($3.46\text{--}3.57 \text{ g/cm}^3$) but a wide range of porosities (9%–29%; Fig. 93). Compressional-wave velocity (5.31 km/s) and resistivity ($0.54 \text{ }\Omega\text{m}$) measured on a minicore (Sample 158-957F-1N-1, 62–64 cm) are consistent with values measured in sulfide samples from Hole 957C (Table 12, Fig. 95). Thermal conductivity measurements were performed on an intact half-round massive pyrite breccia sample (Sample 158-957F-1N-1, Piece 10B, 52–64 cm), which yielded a mean of $6.1 \text{ W/(m}\cdot\text{K)}$ (Table 13, Fig. 96). This interval represents the archive half of the core corresponding to the working half where the minicore (Sample 158-957F-1N-1, 62–64 cm) mentioned above was sampled.

Hole 957G

Physical properties measurements were made on Core 158-957G-3N-1. A multisensor track (MST) scan of a short (7–26 cm), intact portion of Section 158-957G-3N-1 (Fig. 98) shows smoothly varying values of wet bulk density ($2.5\text{--}3.5 \text{ g/cm}^3$, uncorrected; $3.0\text{--}3.9 \text{ g/cm}^3$, corrected for core diameter according to Figure 7 in Chapter 5, this volume), and narrow ranges of values for natural gamma radiation (8–10 cps) and volume magnetic susceptibility ($-1 \text{ to } 3 \times 10^{-5} \text{ SI}$). The corrected values of bulk density measured by the MST GRAPE instrument are consistent with the directly measured value (3.95 g/cm^3) for a massive pyrite-anhydrite-breccia minicore (Sample

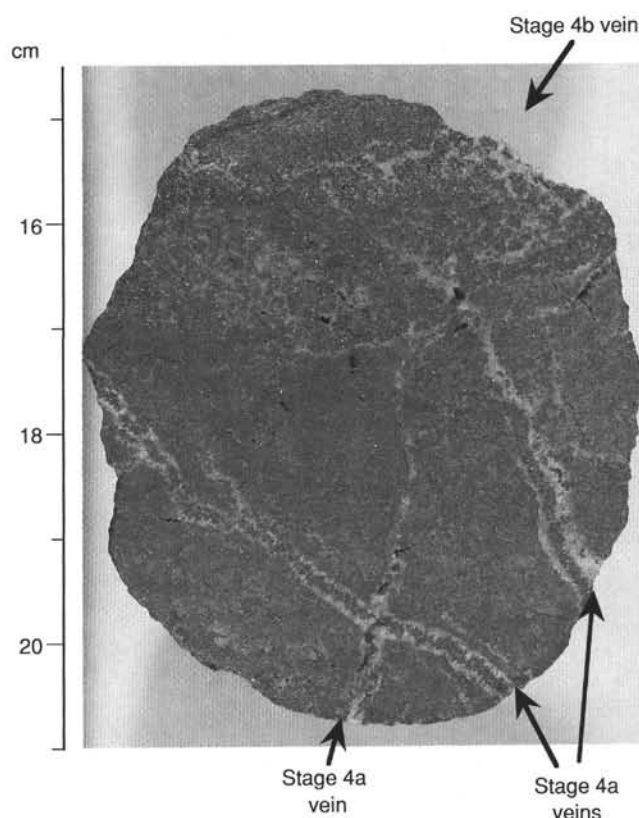


Figure 62. Two generations of Stage 4 veins: a stockwork of Substage 4a quartz-pyrite veins and a 1.5-cm, Substage 4b, pyrite-quartz vein in a gray chloritized basalt breccia (Type 10b). The larger vein contains a 5-mm fragment of chloritized and silicified basalt. The 1- to 2-mm-sized white quartz veins appear to fill reopened 1-mm-wide pyrite veins, which are broken and brecciated, with white quartz mainly filling the margins. Sample 158-957E-17R-1 (Piece 3, 14.5–21 cm).

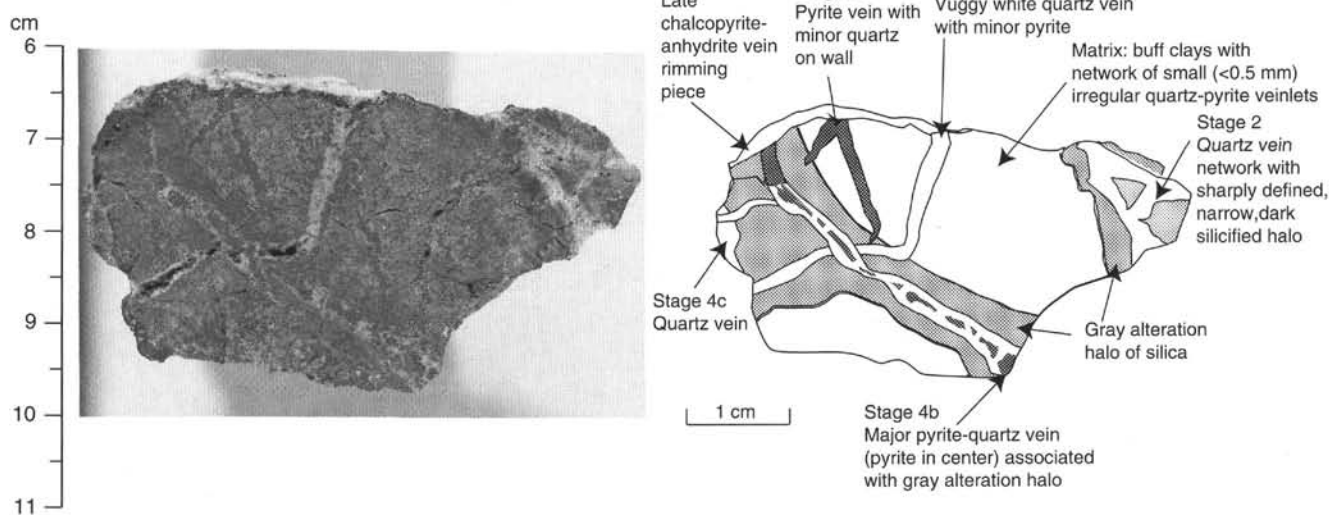


Figure 63. Photograph and sketch of five stages and substages (2, 4a, 4b, 4c, and 5) of veining in chloritized basalt breccia (Type 10b). Sample 158-957E-16R-1 (Piece 2, 6–11 cm).

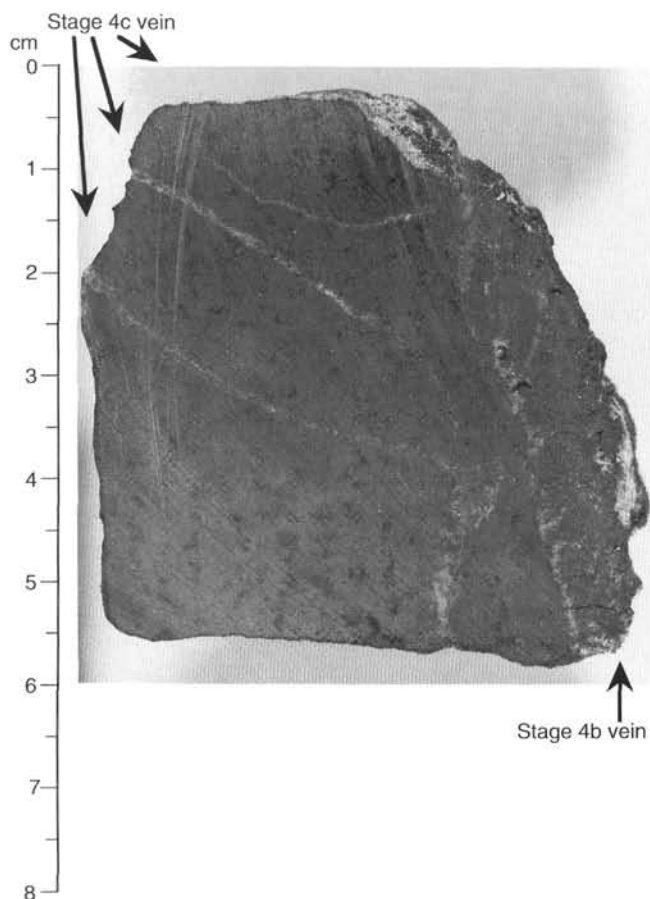


Figure 64. Stage 4b pyrite-quartz vein and Stage 4c quartz with minor pyrite veins in pervasively chloritized basalt breccia (Type 10b). Dark spots are chlorite pseudomorphs after olivine phenocrysts. Sample is cut by 1-cm-wide, massive Stage 4b pyrite vein (right) and later by 1-mm white quartz veins, which also fill the edge of a reopened large pyrite vein. Sample 158-957E-18R-1 (Piece 1, 0–8 cm).

158-957G-3N-1, 15–17 cm) from the same interval (Table 11; Figs. 97, 98). This minicore sample (Sample 158-957G-3N-1, 15–17 cm), the deepest of the physical properties samples recovered from Holes 957F and 957G (21.15 mbsf), exhibits a high bulk density of 3.95 g/cm³, a porosity of 12%, a compressional-wave velocity of 4.85 km/s, and an electrical resistivity of 0.1 Ωm (Figs. 95, 97). These values are within the range of values measured in sulfide samples from Hole 957C (Table 12). Thermal conductivity measurements were performed on an intact, half-round, massive pyrite-anhydrite breccia sample (158-957G-3N-1, Piece 2A, 6–20 cm), which yielded a mean of 8.59 W/(m-K) (Table 13, Fig. 96). This interval represents the archive half of the core corresponding to the working half where the minicore (Sample 158-957G-3N-1, 15–17 cm) mentioned above was sampled.

Summary

Sulfide specimens analyzed (11 minicores and 17 fragments) from 4 holes on the east side of the Black Smoker Complex (Holes 957C, 957E, 957F, and 957G) yielded a similar range of bulk densities (2.85–4.51 g/cm³) and porosities (2.4%–16.2%), with no consistent relations between bulk density and porosity or between these parameters and depth below seafloor. Compressional (*P*-wave) ve-

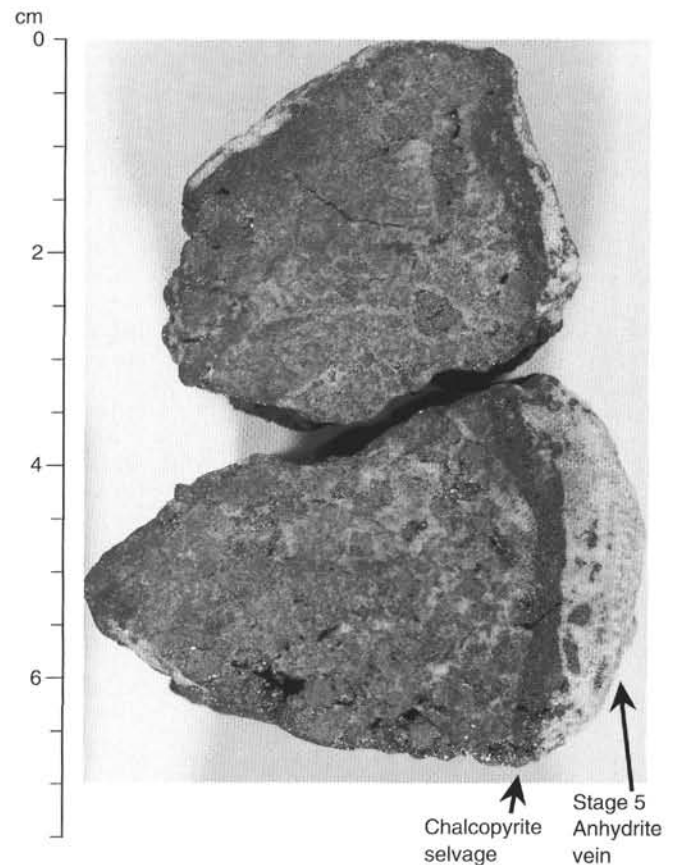


Figure 65. Anhydrite vein (Stage 5) with chalcopyrite selvage crosscutting silicified wallrock breccia (Type 10a). Sample 158-957E-4R-1 (Pieces 1A and 1B, 0–7.5 cm).

locities were measured in 9 sulfide minicores and are generally high (4.85–5.66 km/s). Electrical resistivities were measured on the same minicores and are generally low (0.11–2.01 Ωm). Thermal conductivities were measured on 11 sulfide-rich, half-round samples and are generally high (5.7–8.7 W/[m-K]).

Anhydrite specimens (two minicores) exhibit a contrast in physical properties to the sulfides measured. The anhydrite specimens have a lower range of bulk densities (2.79 and 2.85 g/cm³), higher porosities (4.9% and 9.6%), distinctly higher electrical resistivity (2.77 Ωm), and lower thermal conductivity (5.4 W/[m-K]) than the sulfides.

PALEOMAGNETISM

In this section, we report the paleomagnetic results from the TAG-1 area, located on the eastern side of the Black Smoker Complex. Although six holes were drilled in this area (Holes 957C through 957G and Hole 957L), only the cores recovered from Holes 957C, 957F, and 957G contain vertically oriented, long pieces suitable for alternating-field (AF) demagnetization and measurements using the cryogenic magnetometer.

The archive halves of Core 158-957C-7N, Cores 158-957C-11N through 16N, Core 158-957F-1N, and Core 158-957G-3N were measured using the pass-through cryogenic magnetometer. Vertically oriented sections from Cores 158-957C-7N, 158-957F-1N, and 158-957G-3N were AF demagnetized at 10-cm intervals using peak fields of 15 and 25 mT, and sections from Core 158-957C-11N were de-

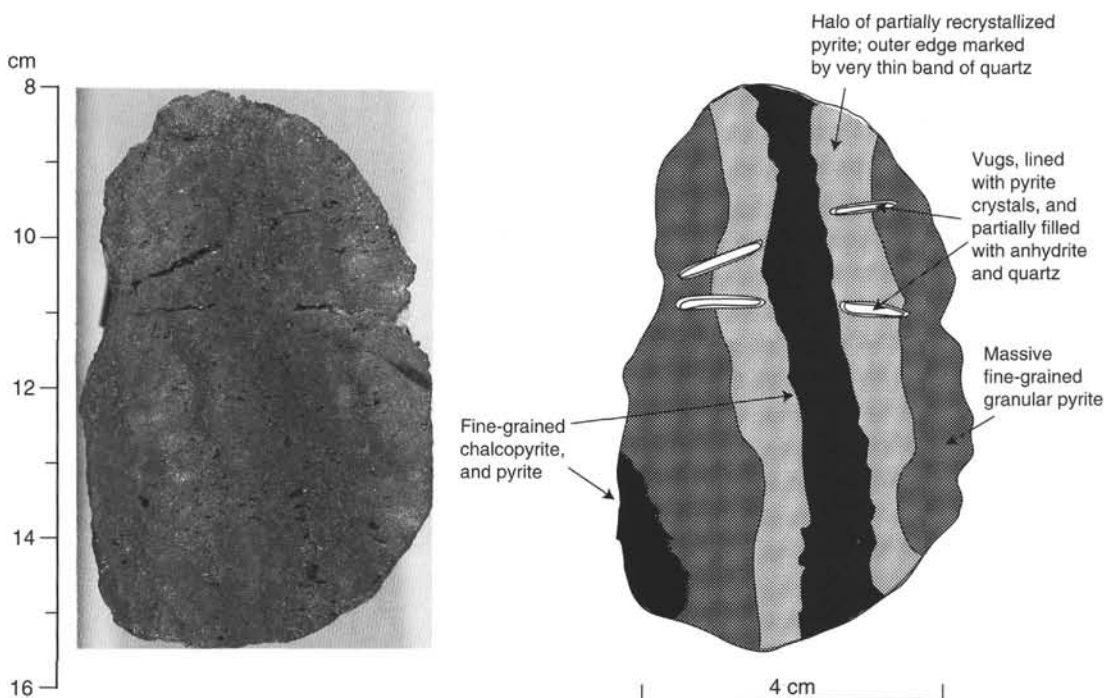


Figure 66. Photograph and sketch of Stage 5 chalcopyrite and gray quartz vein crosscutting massive granular pyrite. A pyritization halo extends from the vein into the granular pyrite. Sample 158-957E-10R-1 (Piece 2, 8–16 cm). Note that vugs do not extend through the vein, but they do occur in pyritization halo and massive granular pyrite; therefore, the vein development is later than the massive (recrystallized) granular pyrite.

magnetized with a peak field of 15 mT. Sections from Cores 158-957C-12N through 16N were measured for remanent magnetization intensities only, as these sections were not oriented with respect to the vertical dimension and were disturbed by coring. A total of four discrete samples taken from the working halves of Cores 158-957C-7N and 16N were progressively AF demagnetized up to a peak field of 80 mT, and two discrete samples from Cores 158-957F-1N and 158-957G-3N were AF demagnetized to a peak field of 60 mT. In addition, two minicore samples from Section 158-957C-11N-1 were stepwise thermally demagnetized to determine the directional stability during stepwise demagnetization, to verify the pass-through measurements from the cryogenic magnetometer, and to help identify the magnetic mineralogy. Magnetic susceptibility was measured at 3- to 10-cm intervals on four cores recovered from Hole 957C and on two sections from Holes 957F and 957G. The purpose of these magnetic measurements was to investigate the magnetic behavior of rocks recovered from the TAG-1 area. In the following, we describe the magnetic behavior of rocks recovered from individual holes in the TAG-1 area and present a summary of the magnetic results from the eastern side of the Black Smoker Complex.

Hole 957C

Whole-core Pass-through Measurements

One of the major experimental requirements in paleomagnetic research is to isolate the characteristic remanent magnetization by selective removal of secondary magnetization. As drilling at Hole 957C started with very magnetic drill collars (as evidenced by their effect on the computer screens in the ship's computer user room adjacent to the drill collar storage area), many of the cores from Hole 957C exhibited strong signs of drilling-induced remagnetization. In Figure 99, we show the natural remanent magnetization (NRM) intensities and inclinations before and after 15 mT alternating-field (AF) demagnetization observed in Cores 158-957C-7N and 11N. The aver-

aged intensity for sections in Core 158-957C-7N is 8.83 mA/m, but 24.82 mA/m for sections from Core 158-957C-11N. This approximately threefold increase in intensity appears to coincide with a change in lithology (from nodular pyrite-anhydrite breccia in Core 158-957C-7N to pyrite-silica-anhydrite-breccia in Core 158-957C-11N; see "Stratigraphy" section, this chapter). The inclinations are strongly biased toward high positive values (with a mean of 68.9°), which are significantly higher than that of the expected inclination (about 50°) at Site 957, suggesting that drilling-induced magnetization is present. Figure 99 also shows that AF demagnetization to 15 mT is not sufficient to remove this drilling-induced magnetization, as evidenced by virtually no change in mean inclination, although intensity was significantly reduced to one third of its original value. As will be shown below, it appears that only thermal demagnetization can effectively remove this drilling-induced remagnetization and isolate a stable component of magnetization.

Alternating-field and Thermal Demagnetization of Discrete Samples

Because many core sections recovered at Hole 957C contain small and unoriented pieces, long continuous and vertically oriented core sections are limited. Consequently, oriented samples for shipboard studies had to be shared between research groups. For this reason, we were able to perform AF demagnetization on only four 10 cm³ minicore samples (with one sample taken from a zone of anhydrite veins). As shown in Figure 100, progressive AF demagnetization up to 60 mT on Samples 158-957C-7N-2, 66–68 cm (pyrite breccia), and 7N-3, 15–77 cm (anhydrite vein), revealed only a single component of magnetization with inclination greater than 70° . It seems likely that this steeply downward component of magnetization is caused by coring and is very resistant to AF demagnetization.

On the other hand, thermal demagnetization on another pair of samples (i.e., pyrite breccia and anhydrite vein, respectively) suc-

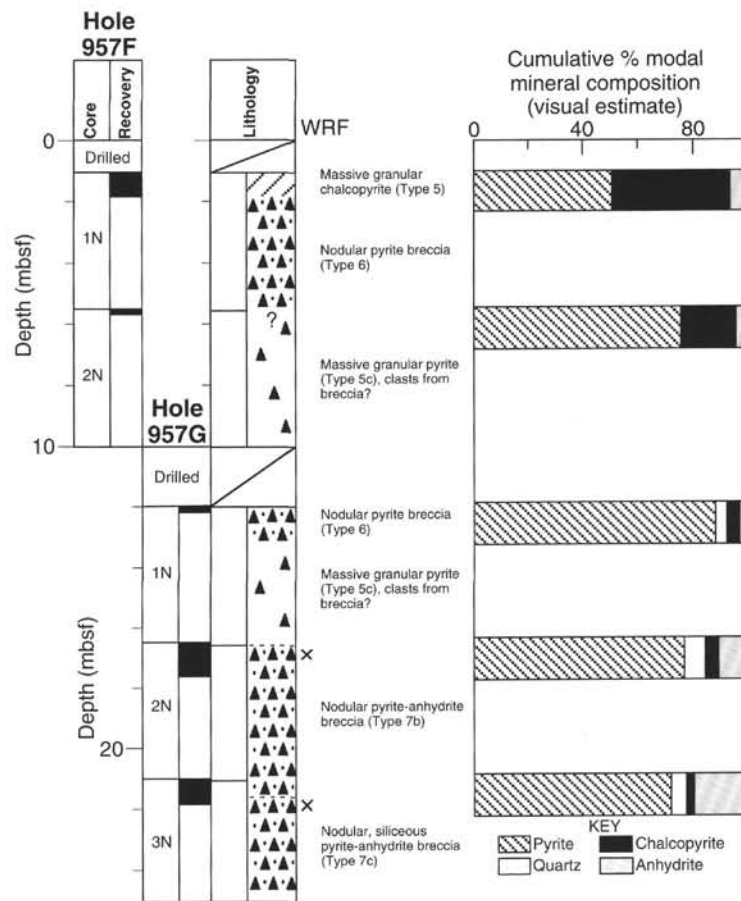


Figure 67. Recovery from Holes 957F and 957G and an idealized stratigraphic section from 0 to 25 mbsf. Mineral abundances, based on visual estimates, are given for each cored interval. WRF = presence of wallrock fragments.

cessfully removed this drilling-induced magnetization component and isolated a stable magnetization. As shown in Figure 101, the drilling-induced remagnetization component (with inclination greater than 75°) was removed after 300°C demagnetization and a characteristic component (with inclination around 55° degrees) could be identified. The pyrite breccia Sample 158-957C-11N-1, 114–116 cm, and the anhydrite vein Sample 158-957C-11N-1, 21–23 cm, displayed very similar demagnetization behavior, with unblocking temperatures very close to 400°C . Judging from the spectrum of unblocking temperatures and coercivity, it would appear that maghemite is probably the main magnetic carrier in these samples. Because of the very limited number of shipboard study samples, this interpretation awaits to be verified in shore-based studies with more representative sampling, more detailed rock magnetic measurements, and X-ray diffraction or other mineralogical identifications.

Magnetic Susceptibility

Figure 102 shows the downhole profile of magnetic susceptibility for Cores 158-957C-7N through 15N. The magnetic susceptibility values of the rocks are consistently low, averaging about 4×10^{-5} SI unit, fully in agreement with the relatively weak NRM intensities observed in these cores. These low magnetic susceptibility values are also confirmed by the results of individual sample susceptibility measurements from the six minicores that were used for demagnetization experiments. A few susceptibility maxima were observed within Core 158-957C-11N around 31 mbsf, which coincides with the beginning of the pyrite-silica-anhydrite-breccia zone (see "Sulfide Pe-

trology and Geochemistry" section), the appearance of hematitic material in veins, and the stronger NRM intensities mentioned earlier.

Holes 957F and 957G

Pass-through measurement results show that the averaged natural remanent magnetization (NRM) intensity is 1.17 mA/m for Section 158-957F-3N-1 and 5.26 mA/m for Section 158-957G-1N-1. These values are significantly lower than those in the deeper sections from Hole 957C (8.83 mA/m for Core 158-957C-7N and 24.82 mA/m for Core 158-957C-11N). Whether these differences in NRM intensity reflect different magnetic mineralogy of the sections is not clear at this time, but the inclinations cluster around the expected inclination (about 50°) at Site 957. This suggests that the nearly vertically directed, drilling-induced magnetization, which persistently exists in cores from Hole 957C, is almost absent in these two sections.

Progressive alternating-field demagnetization up to 60 mT on Samples 158-957F-1N-1, 62–64 cm, and 158-957G-3N-1, 15–17 cm, revealed straightforward demagnetization behavior with a stable component of magnetization that is univectorially decaying toward the origin (Fig. 103). The stable component of magnetization has a mean inclination about 51° , reinforcing the results of pass-through measurements mentioned above.

In summary, the cores recovered from the lower part of the TAG hydrothermal sulfide mound (Hole 957C) on the eastern side of the Black Smoker Complex appear to have a strong overprint of drilling-induced magnetization. This overprint is resistant to standard AF de-

magnetization techniques, but a stable component of magnetization with an inclination consistent with the location of the TAG mound can be isolated with thermal demagnetization. Preliminary data from unblocking temperatures and coercivity determinations suggest that maghemite is the most likely magnetic carrier in these cores. In contrast, cores recovered from the upper part of the sulfide mound (Holes 957F and 957G), which are in close enough proximity to be included in a composite section, do not show evidence of a drilling-induced magnetization and have a significantly lower intensity of natural remanent magnetization. The drilling-induced remagnetization may severely affect the external portions of the cores because the outside of the core is physically closer to the magnetized core barrel. The paleomagnetic observations from Holes 957C, 957F, and 957G suggest that a stratigraphically distinct change in magnetic minerals may exist, that the magnetic carrier may be much less abundant in Holes 957F and 957G, and that the magnetic carrier may reside mainly inside of the cores in the upper part of the section, or a combination of all these factors. These hypotheses will be tested in subsequent shore-based investigations.

FLUID GEOCHEMISTRY

Surface- and bottom-water samples were collected at Site 957 to characterize chemically two water types that, along with formation fluids, may be present in the borehole. Drilling operations introduce surface seawater into the borehole and, because of density differences between cold bottom water and hydrothermal fluid, bottom water may cascade into the borehole. It is necessary to characterize these fluids chemically to deconvolute the various chemical signals expected from mixing drilling water and/or bottom water with formation fluids.

Surface water was collected by bucket grab. Inasmuch as the position of the *JOIDES Resolution* was directly over the TAG hydrothermal mound for all holes drilled at Site 957, we consider the single surface-water sample collected to be representative of surface water for all holes at this site. Two water samples were collected using the water sampling temperature probe (WSTP) at Hole 957C in the TAG-1 area. A bottom-water sample (WSTP-2) was collected in the water

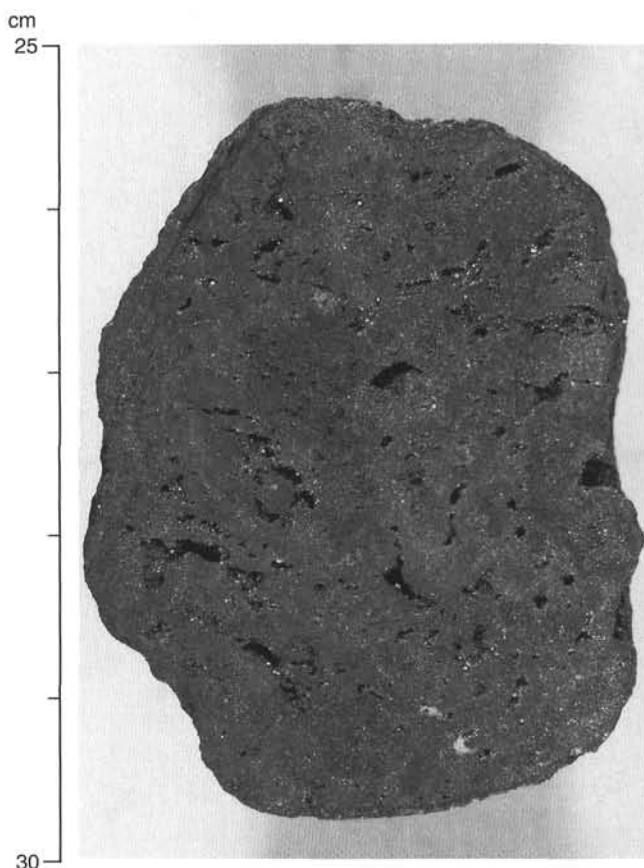


Figure 68. Massive granular pyrite, typical of material recovered in Section 158-957F-2N-1. Pieces contain disseminated chalcopyrite and minor silica in voids. The outer surfaces are coated with anhydrite, and it appears that these pieces represent clasts from a massive nodular pyrite breccia. Sample 158-957F-2N-1 (Piece 5, 25–30 cm).

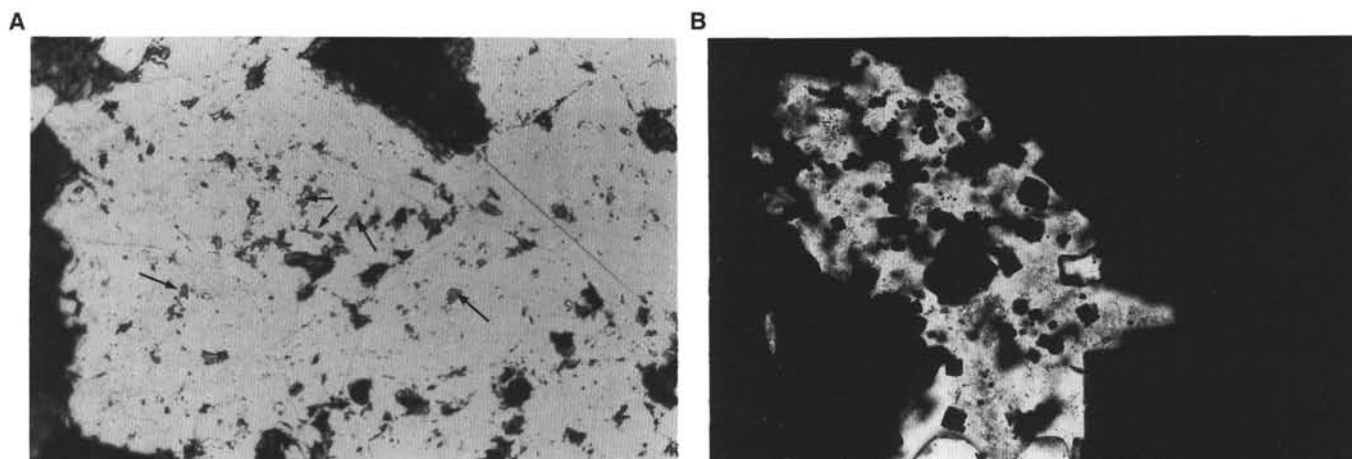


Figure 69. **A.** Photomicrograph of typical textures in the massive granular pyrite clasts. Recrystallized pyrite aggregates with numerous small sphalerite inclusions (dark gray, arrow). Sample 158-957F-2N-1 (Piece 5, thin section from 28 to 30 cm). Reflected light, field of view = 750 μm . **B.** Detail of amorphous silica lining a void within an aggregate of pyrite. The silica contains disseminated grains of euhedral pyrite. Sample 158-957F-2N-1 (Piece 5, thin section from 28 to 30 cm). Transmitted light, field of view = 750 μm .

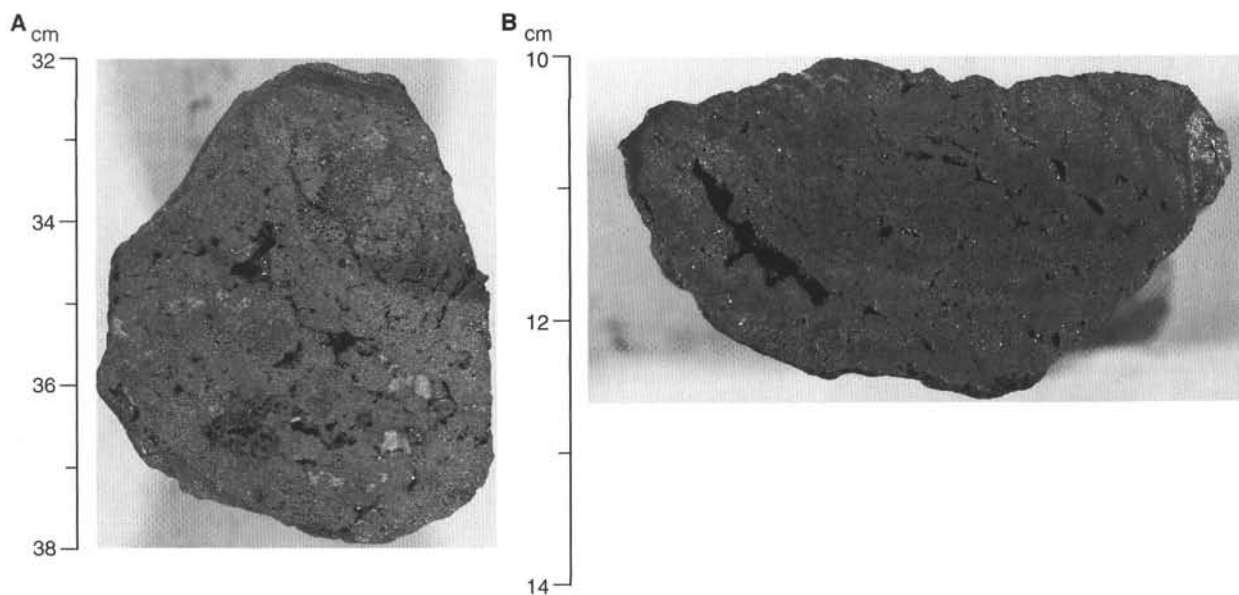


Figure 70. Massive granular pyrite, typical of material recovered in Section 158-957G-1N-1. **A.** Porous, granular pyrite with minor silica, and some anhydrite in voids. Note the generally finer grained, more porous texture compared to the sample in Figure 68. Sample 158-957G-1N-1 (Piece 7, 32–38 cm). **B.** Porous pyrite showing colloform bands. Sample 158-957G-1N-1 (Piece 3, 10–14 cm).

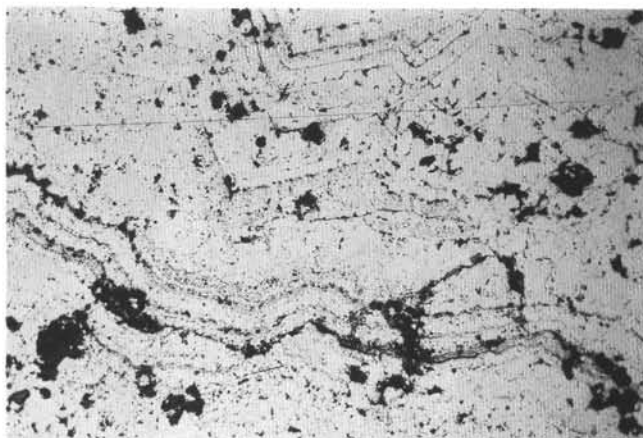


Figure 71. Photomicrograph of typical pyrite textures from massive granular pyrite. Euhedral pyrite growth layers, overgrown by colloform pyrite, now recrystallized. The pyrite contains small, irregular chalcopyrite and sphalerite inclusions. Sample 158-957G-1N-1 (Piece 3, thin section from 11 to 13 cm). Reflected light, field of view = 1.5 mm.

column approximately 10 m east of the hard-rock guide base and about 1 m above the seafloor. WSTP-2 included 10 mL contained in the titanium tube and 800 mL contained in the overflow chamber. The equilibrium temperature was not determined. A borehole sample (WSTP-3: 158-957C-10N-1, 10–15 cm) was collected at 28.65 mbsf. Fluid collected within the borehole included 10 mL contained in the titanium tube and 1 L contained in the overflow chamber.

Results

Concentrations of dissolved ions in the surface water at Site 957 have values typical of those expected for the North Atlantic (Sverdrup et al., 1942), in that salinity is between 36.5‰ and 37‰ and dissolved nutrients are very low (Table 14). Concentrations of major

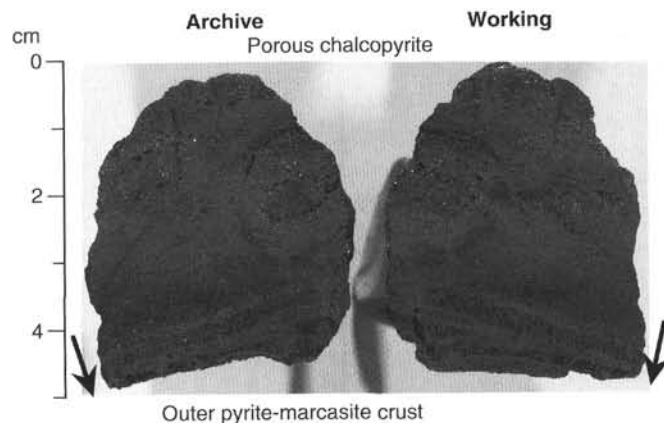


Figure 72. Massive granular chalcopyrite typical of recovered material in Section 158-957F-1N-1, 0–22 cm. Sample of fine-grained, bladed chalcopyrite that grades to a zone dendritic pyrite or marcasite (arrows). The outside of this zone is composed of a colloform carapace of marcasite with Fe-oxides. Sample 158-957F-1N-1 (Piece 1, 0–5 cm).

dissolved ions in bottom water (WSTP-2) from near Hole 957C are also presented in Table 14 and, for comparison, typical values for salinity and dissolved nutrients of natural waters expected in the vicinity of Site 957. Salinity in the bottom water from near Hole 957C is 35‰, similar to the expected salinity of North Atlantic Deep Water (34.9‰; Sverdrup et al., 1942). Dissolved silica is higher (57 $\mu\text{mol/L}$) in bottom water at Hole 957C than that measured at Hole 957A (33 $\mu\text{mol/L}$). Slightly elevated dissolved silica may result from mixing a small amount of hydrothermal fluid seeping from the TAG mound with normal bottom water, similar to that collected at Hole 957A. Dissolved silica in fluids seeping from the mound is 3 orders of magnitude higher than normal bottom water, with values near 20 mmol/L (Campbell et al., 1988). Simple mixing of bottom water similar to that observed near Hole 957A with 0.1% hydrothermal fluid contain-

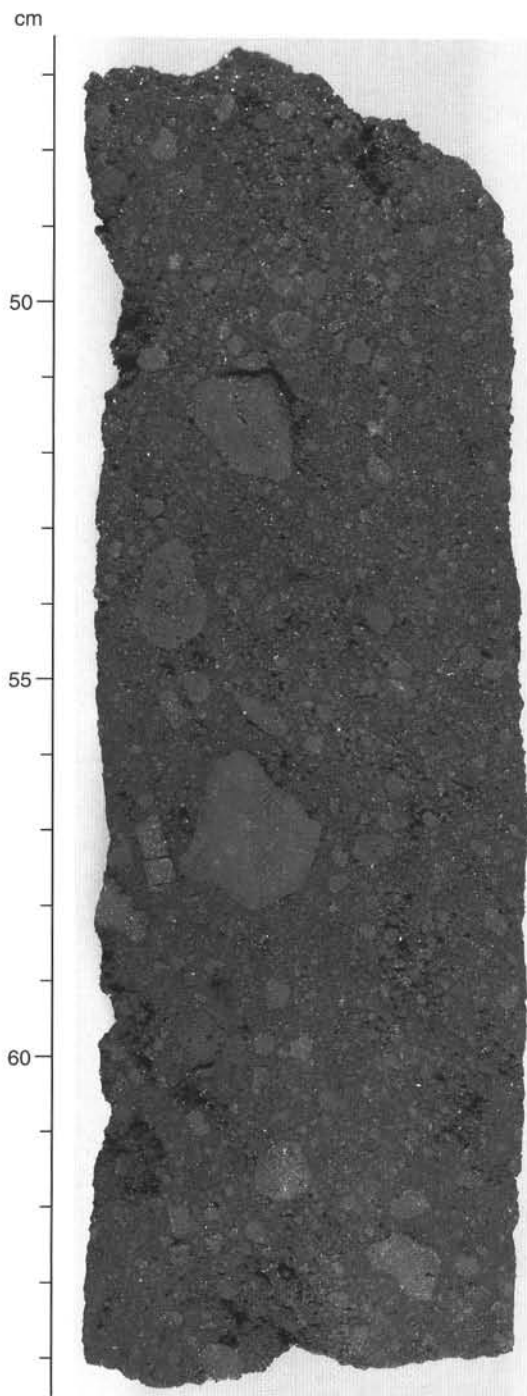


Figure 73. Porous, nodular pyrite breccia from Section 158-957F-1N-1. Coarse granular pyrite clasts are present in a matrix of fine grained pyrite, anhydrite (<10 vol%), lesser silica, and minor chalcopryite. Some clasts contain porous chalcopryite cores (e.g., at 54 cm), and there is an angular chalcopryite fragment at 57 cm. Pyrite clasts are up to 3 cm in diameter and are similar to massive granular pyrite cobbles recovered lower in Holes 957F and 957G. Sample 158-957F-1N-1 (Piece 10B, 46.5–64.5 cm).

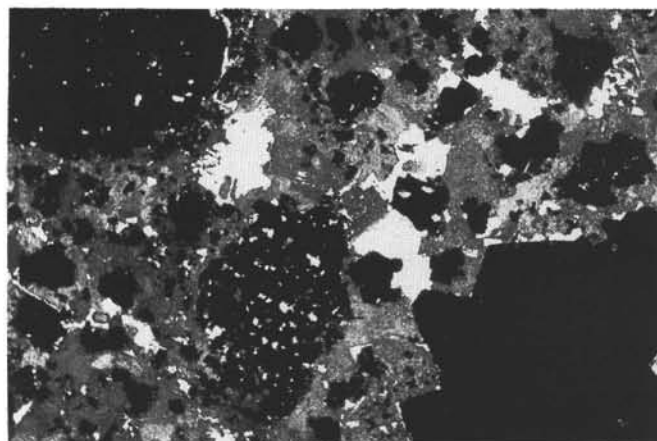


Figure 74. Photomicrograph of typical matrix texture in the nodular pyrite breccia showing anhedral to euhedral pyrite aggregates (black), some with quartz inclusions (e.g., arrow). The matrix is fine-grained pyrite and anhydrite (gray, mottled), and pore spaces in the matrix appear white. Sample 158-957F-1N-1 (Piece 10C, thin section from 66 to 67 cm). Transmitted light, field of view = 6 mm.

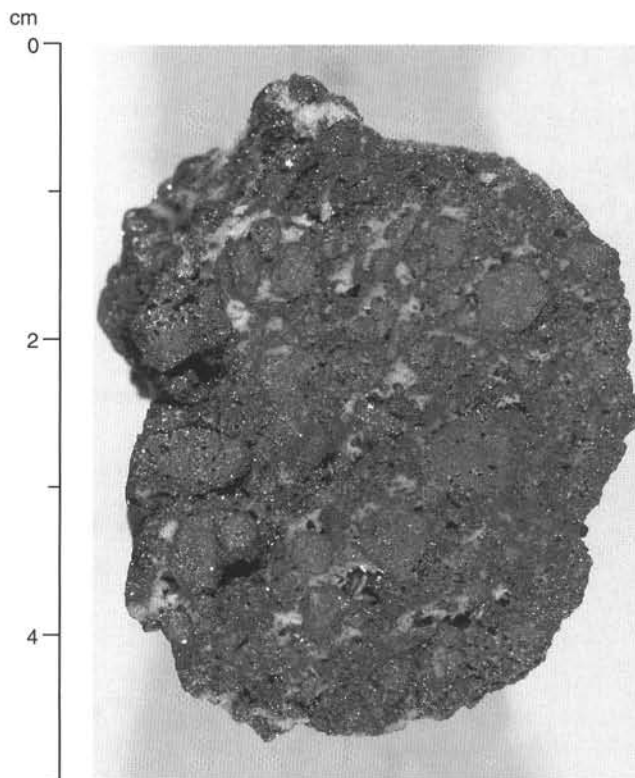


Figure 75. Pyrite-anhydrite breccia. Nodular clasts of massive granular pyrite in a matrix of coarse pyrite and anhydrite (20 vol% anhydrite by visual estimate). Sample 158-957G-2N-1 (Piece 1, 0–5 cm).

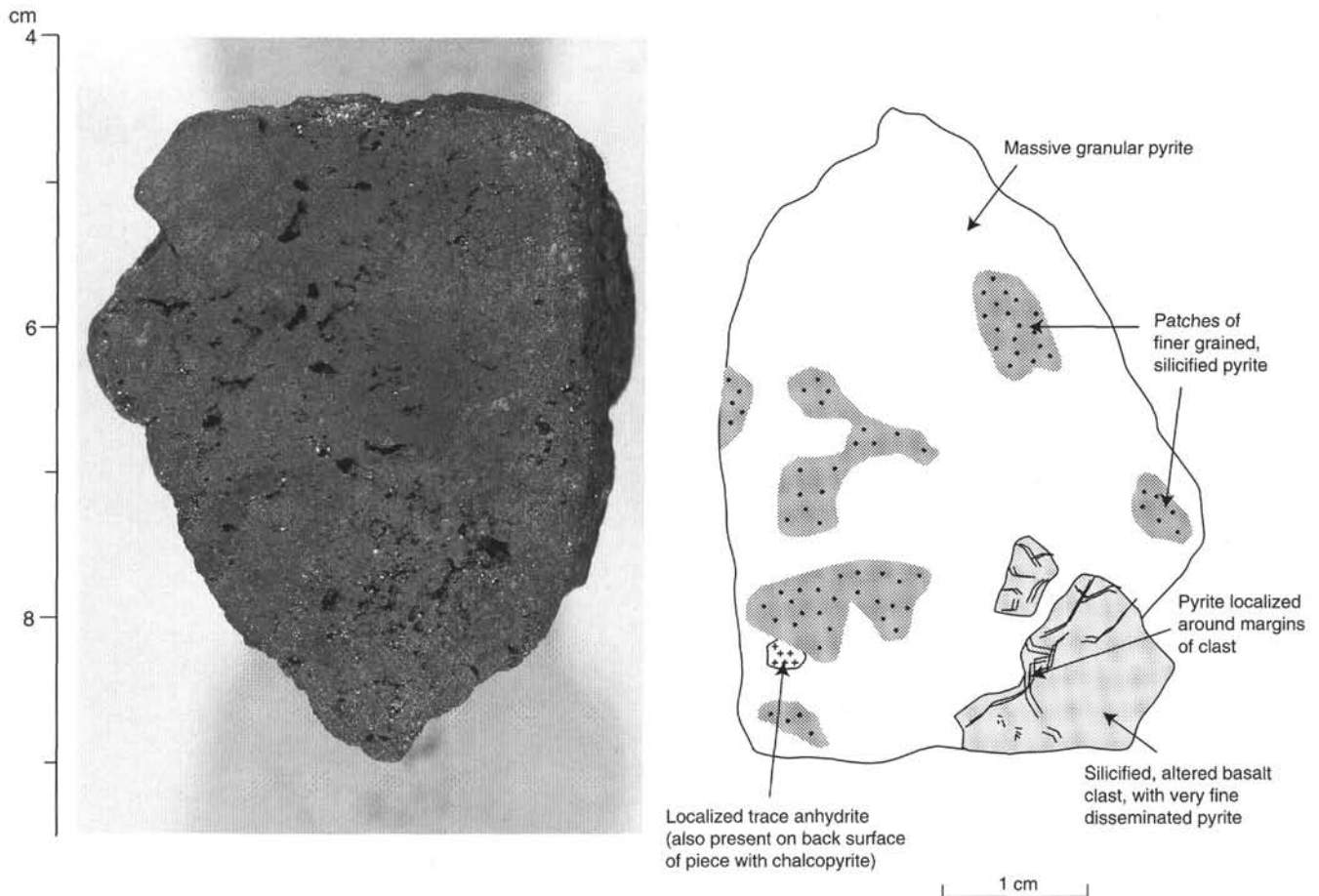


Figure 76. Massive granular pyrite with an angular clast of silicified basalt. The sample is probably a clast from the nodular pyrite-anhydrite breccia. A sketch of this sample shows the relation between pyrite and altered basalt clast. Sample 158-957G-2N-1 (Piece 2, 5–9 cm).

ing 20 mmol/L dissolved silica would increase dissolved silica by 20 $\mu\text{mol/L}$, consistent with the difference in dissolved silica at Holes 957A and 957C. Mixing of normal bottom water with 0.1% hydrothermal fluid would not be apparent in major dissolved ion concentrations (e.g., in chloride, calcium, and potassium) because the difference in concentrations of these ions in the two fluids is too small.

The chemical composition of fluid collected in the borehole (Sample 158-957C-10N-1, 10–15 cm) is dominated by surface seawater introduced during the drilling process. Measured concentrations of dissolved chloride and potassium in the borehole fluid are similar to those of surface water ($\text{Cl} = 587$ and 583 mmol/L Cl , and $\text{K} = 11.4$ and 11.1 mmol/L, respectively) (Table 14). Dissolved magnesium, calcium, and sulfate are elevated in borehole fluids relative to surface water values ($\text{Mg} = 58.4$ and 55.9 mmol/L, $\text{Ca} = 17.7$ and 11.1 mmol/L, and $\text{SO}_4 = 42.5$ and 31.6 mmol/L, respectively). The millimolar concentrations of magnesium plus calcium in excess of surface water values ($\text{Mg} + \text{Ca} = 9.1$ mmol/L) is very nearly balanced by sulfate in excess of surface water value ($\text{SO}_4 = 10.9$ mmol/L).

To determine the source of elevated calcium, magnesium, and sulfate observed in the borehole water sample, dissolution experiments were conducted on three different solids with which the borehole fluid may have reacted. Drilling mud (a mixture of bentonite clay, soda ash, and sodium hydroxide in fresh water) was circulated during the early stages of drilling at this hole (G. Pollard, pers. comm., 1994). To simulate this mud-water mixture, 0.5 g of the drilling mud was stirred with 50 mL surface seawater for 7 hr in an ice bath. Two rocks

were chosen from interval 158-957C-12N-2, 111–119 cm, for dissolution because they contained sulfate minerals (see "Sulfide Petrology and Geochemistry" section). One sample consisted of drill cuttings with a sugar-like texture. Based on visual inspection, this sample is primarily anhydrite (Sample 158-957C-12N-2, 111–119 cm a). The second sample was a hard, rounded piece of siliceous pyrite-anhydrite breccia (Sample 158-957C-12N-2, 111–119 cm b). The hard piece was broken apart using an agate mortar and pestle, and interior fragments were selected for the dissolution experiment. From each of two rock samples, 0.5 g of material was stirred separately with 50 mL surface seawater for 7 hr in an ice bath. A second aliquot of each of the rocks was stirred separately with nanopure water for 7 hr. Dissolved calcium and magnesium in the reacted fluids were determined by titration, and dissolved sulfate was determined by ion chromatography (Table 15). Fluid reacted in the presence of drilling mud had lower concentrations of dissolved chloride, magnesium, calcium, and sulfate than the starting fluid. This suggests that fresh water from the drilling mud diluted the reacted fluid. After correcting for dilution by fresh water (see drilling mud*, Table 15), chloride, magnesium, calcium, and sulfate concentrations are similar to surface seawater. From this, we conclude that the drilling mud is not a source of calcium, magnesium, or sulfate ions in the borehole fluid.

Dissolved chloride in surface seawater reacted with Samples 158-957C-12N-2, 111–119 cm a, and 158-957C-12N-2, 111–119 cm b, is consistent with that of the borehole fluid. Millimolar concentrations of dissolved calcium plus magnesium in surface seawater reacted with Sample 158-957C-12N-2, 111–119 cm a, are balanced by those

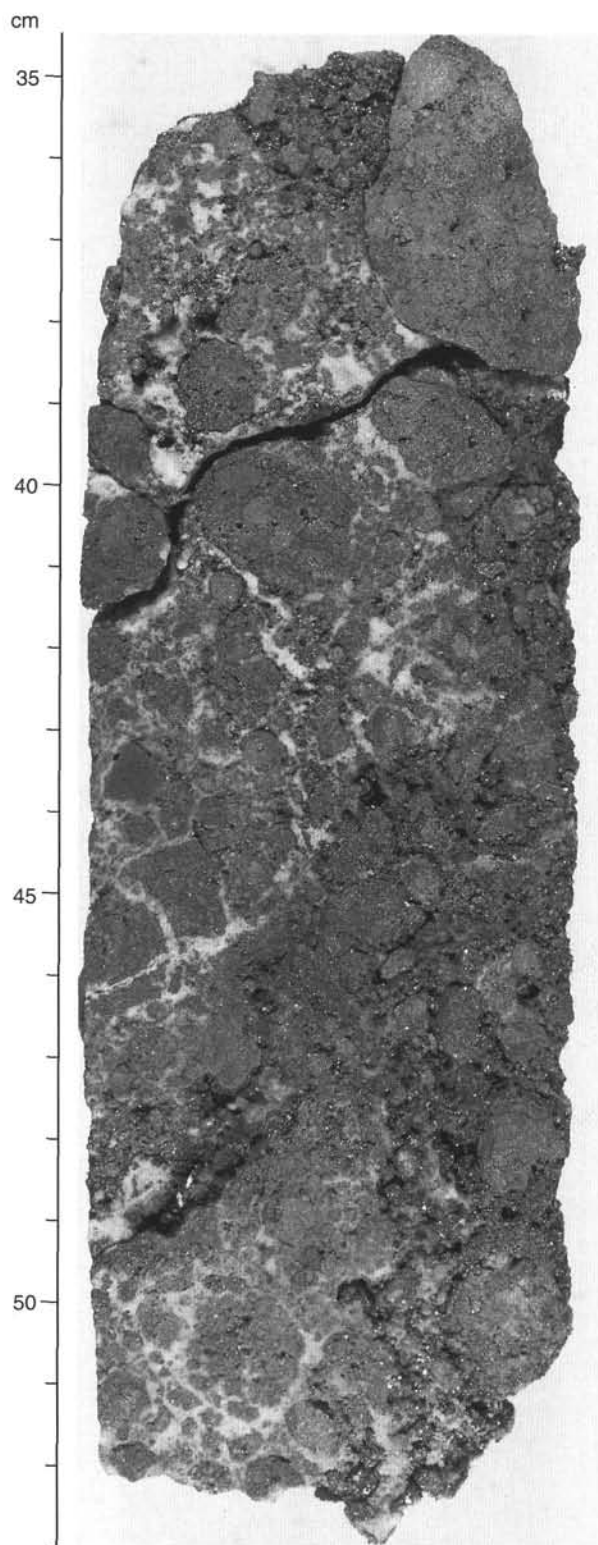


Figure 77. Nodular siliceous pyrite-anhydrite breccia. Clasts of massive granular pyrite and pyrite-silica in a matrix of anhydrite (up to 50 vol% anhydrite). Sample 158-957G-3N-1 (Pieces 4A and 4B, 34.5–53 cm).

of dissolved sulfate, a similar relative ratio to that observed in the borehole fluid. This suggests the dissolution of anhydrite and a magnesium sulfate (caminite?). In contrast, fluids reacted in the presence of Sample 158-957C-12N-2, 111–119 cm b, have relatively low dissolved calcium and sulfate in excess of that in surface seawater, indicating that anhydrite was not dissolved in this experiment. The source for the relatively high concentration of dissolved magnesium in fluids reacted in the presence of Sample 158-957C-12N-2, 111–119 cm b, has not been identified.

In experiments using nanopure water, aqueous calcium and sulfate concentrations increased (Table 15). Millimolar concentrations of Ca are balanced by those of dissolved SO_4 , suggesting that anhydrite dissolved in the nanopure water from the solid sample. In contrast to the experiments using seawater, no increase in aqueous magnesium concentration was found. This suggests either that the Mg-bearing phase is inhomogeneously distributed in the solids, or that solubility of the Mg-bearing phase is enhanced in seawater, with a high ionic strength fluid and a pH of 8, higher than the pH of nanopure water.

It is unclear from the experimental observations and from the borehole fluid chemical composition whether dissolution of calcium and magnesium sulfate solids is an artifact of drilling or the result of an ongoing process within the upper portion of the TAG mound.

REFERENCES

- Broecker, W.S., and Peng, T.-H., 1982. *Tracers in the Sea*: Palisades, NY (Lamont-Doherty Geological Observatory).
- Campbell, A.C., Palmer, M.R., Klinkhammer, G.P., Bowers, T.S., Edmond, J.M., Lawrence, J.R., Casey, J.F., Thompson, G., Humphris, S., Rona, P.A., and Karson, J.A., 1988. Chemistry of hot springs on the Mid-Atlantic Ridge. *Nature*, 335:514–519.
- Clark, S.P. (Ed.), 1966. *Handbook of Physical Constants*. Mem.—Geol. Soc. Am., 97.
- Constantinou, G., and Govett, G.J.S., 1973. Geology, geochemistry, and genesis of Cyprus sulfide deposits. *Econ. Geol.*, 68:843–858.
- Franklin, J.M., Sangster, D.F., and Lydon, J.W., 1981. Volcanic-associated massive sulfide deposits. *Econ. Geol.*, 75th Anniv. Vol., 485–627.
- Lalou, C., Reyss, J.L., Bricchet, E., Arnold, M., Thompson, G., Fouquet, Y., and Rona, P.A., 1993. New age data for Mid-Atlantic Ridge hydrothermal sites: TAG and Snakepit geochronology revisited. *J. Geophys. Res.*, 98:9705–9713.
- Large, R.R., 1992. Australian volcanic-hosted massive sulfide deposits: features, styles, and genetic models. *Econ. Geol.*, 87:471–510.
- Redfield, A.C., Ketchum, B.H., and Richards, F.A., 1982. The influence of organisms on the composition of seawater. In Hill, M.N. (Ed.). *The Sea* (Vol. 2): New York (Wiley), 26–49.
- Rona, P.A., Hannington, M.D., Raman, C.V., Thompson, G., Tivey, M.K., Humphris, S.E., Lalou, C., and Petersen, S., 1993. Active and relict seafloor hydrothermal mineralization at the TAG hydrothermal field, Mid-Atlantic Ridge. *Econ. Geol.*, 88:1987–2013.
- Sverdrup, H.U., Johnson, M.W., and Fleming, R. (Eds.), 1942. *The Oceans: Their Physics, Chemistry and General Biology*: Englewood Cliffs, NJ (Prentice-Hall).
- Thompson, G., Humphris, S.E., Schroeder, B., Sulanowska, M., and Rona, P.A., 1988. Active vents and massive sulfides at 26°N (TAG) and Snakepit (23°N) on the Mid-Atlantic Ridge. *Can. Mineral.*, 26:697–711.
- Tivey, M.K., Humphris, S.E., Thompson, G., Hannington, M.D., and Rona, P.A., 1995. Deducing patterns of fluid flow and mixing within the TAG active hydrothermal mound using mineralogical and geochemical data. *J. Geophys. Res.*, 100:12527–12555.

Ms 158IR-107

NOTE: For all sites drilled, core-description forms (“barrel sheets”) and core photographs can be found in Section 3, beginning on page 227. Thin-section data are given in Section 4, beginning on page 345.

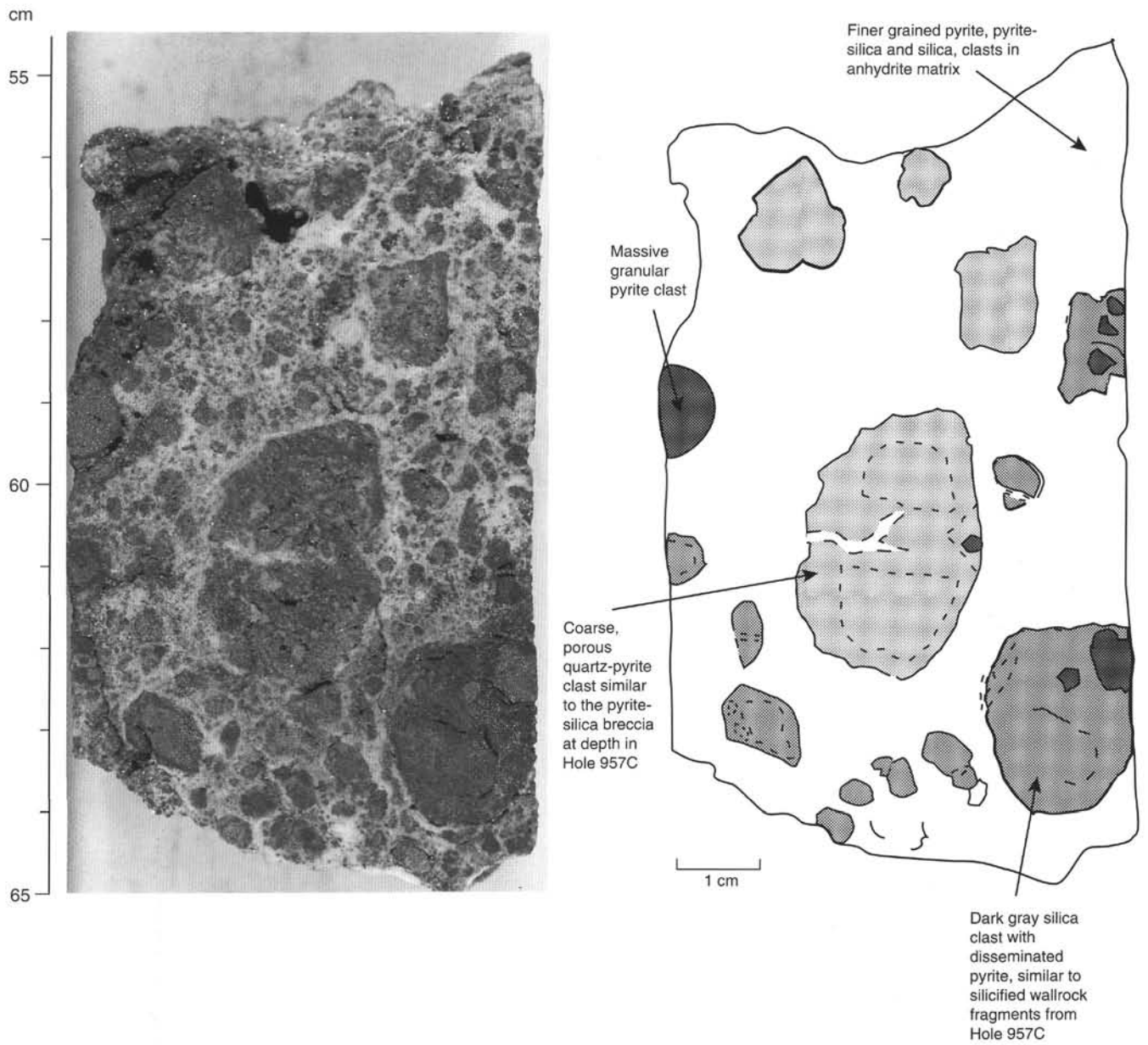


Figure 78. Detail of nodular siliceous pyrite-anhydrite breccia and sketch of the same piece, showing the different clast types that occur in the sample. Sample 158-957G-3N-1 (Piece 4D, 54.5–65 cm).

Table 8. Results of AAS, CHNS, and ASV analysis on sulfide samples from the TAG-1 area.

Core, section, interval (cm)	Piece no.	Depth (mbsf)	Rock type	S (wt%)	Fe (wt%)	Zn (wt%)	Cu (wt%)	Pb (ppm)	Ag (ppm)	Cd (ppm)	Au (ppb)
158-957F-											
1N-1, 32-35	8	1.3	6a Nodular pyrite breccia	42	31.2	0.030	5.63	15	5.1	<0.1	230
2N-1, 11-19	3	5.6	5c Massive granular pyrite	45	36.4	0.032	4.22	17	4.3	<0.1	ND
158-957C-											
5N-1, 15-48	3+5+6	15.2	7a Pyrite-anhydrite breccia	45	35.5	0.004	0.72	19	5.0	0.3	ND
7N-1, 52-56	6F	20	7c Pyrite-anhydrite breccia	45	33.7	0.003	4.68	14	4.8	<0.5	ND
7N-2, 61-69	1E	21.5	7c Pyrite-anhydrite breccia	40	25.7	0.003	3.65	14	4.8	0.5	ND
11N-1, 58-61	3D	31.2	8 Pyrite-silica-anhydrite breccia	42	33.2	0.020	2.53	12	3.6	<0.3	ND
11N-3, 90-94	8C	34.5	7d Pyrite-anhydrite breccia	44	38.3	0.072	6.00	10	4.0	0.4	250
12N-1, 53-59	6	35.5	7a Pyrite-anhydrite breccia	44	30.6	0.072	3.39	10	3.8	<0.4	ND
12N-2, 68-75	9	36.2	8 Pyrite-silica-anhydrite breccia	45	31.8	0.183	2.01	18	3.1	1.2	ND
12N-3, 86-100	9	36.9	8 Pyrite-silica-anhydrite breccia	34	23.3	0.006	2.57	<4	2.5	<0.4	ND
13N-1, 12-20	4	37.3	7a Pyrite-anhydrite breccia	48	34.3	0.075	1.88	15	3.4	0.5	ND
14N-1, 33-41	5	40.5	9a Pyrite-silica breccia	44	35.6	0.028	1.67	5	3.2	<0.4	ND
14N-2, 77-88	6	41.7	9a Pyrite-silica breccia	43	33.8	0.038	0.20	8	3.1	0.5	ND
15N-1, 36-40	5	42.5	9a Pyrite-silica breccia	40	30.1	0.047	0.61	5	3.3	<0.5	ND
15N-2, 12-15	1B	43.2	10a Silicified wallrock breccia	30	20.1	<0.002	0.01	<4	2.3	<0.5	ND
15N-3, 132-150	11	45.6	10a Silicified wallrock breccia	34	26.7	0.003	1.25	6	3.2	<0.1	ND
16N-1, 118-125	15	47.4	7d Pyrite-anhydrite breccia	44	35.1	0.035	3.51	26	3.5	0.4	ND
16N-2, 14-23	2	47.8	10a Silicified wallrock breccia	43	34.0	0.012	1.46	16	4.1	0.2	ND
158-957E-											
9R-1, 16-19	4	78.2	5c Massive granular pyrite	36	31.7	0.010	0.65	15	4.8	<0.1	ND
12R-1, 16-20	3	92	10a Silicified wallrock breccia	47	40.8	0.013	4.06	<4	3.7	<0.1	ND

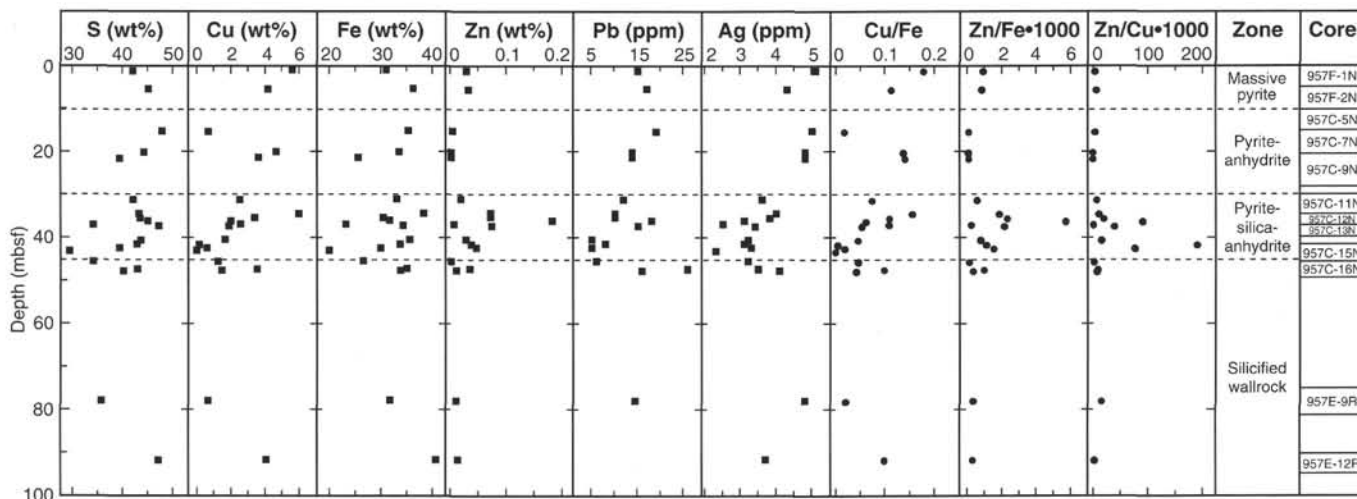


Figure 79. Variation of the concentrations of S, Cu, Fe, Zn, Pb, Ag, and the Cu/Fe, Zn/Fe, and Zn/Cu ratios down a composite stratigraphic profile in the TAG-1 area. The stratigraphy is based on AAS and CHNS analyses of samples from Holes 957C, 957E, and 957F.

Table 9. Comparison of the metal concentrations observed in Section 158-957B-1R-1 (TAG-2 area) and selected samples from Hole 957C (TAG-1 area).

Core, section	Fe (wt%)	Zn (wt%)	Cu (wt%)	Pb (ppm)	Ag (ppm)	Cd (ppm)
158-957B-1R-1	32.7	3.02	13.7	393	155	99
158-957C-						
12N-2	31.8	0.183	2.01	18	3.1	1.2
15N-2	20.1	0.002	0.01	4	2.3	0.5
Enrichment factor: concentrations in Hole 957B/Hole 957C						
957B-1R/957C-12N	1.0	17	7	22	50	83
957B-1R/957C-15N	1.6	1510	1370	98	67	198

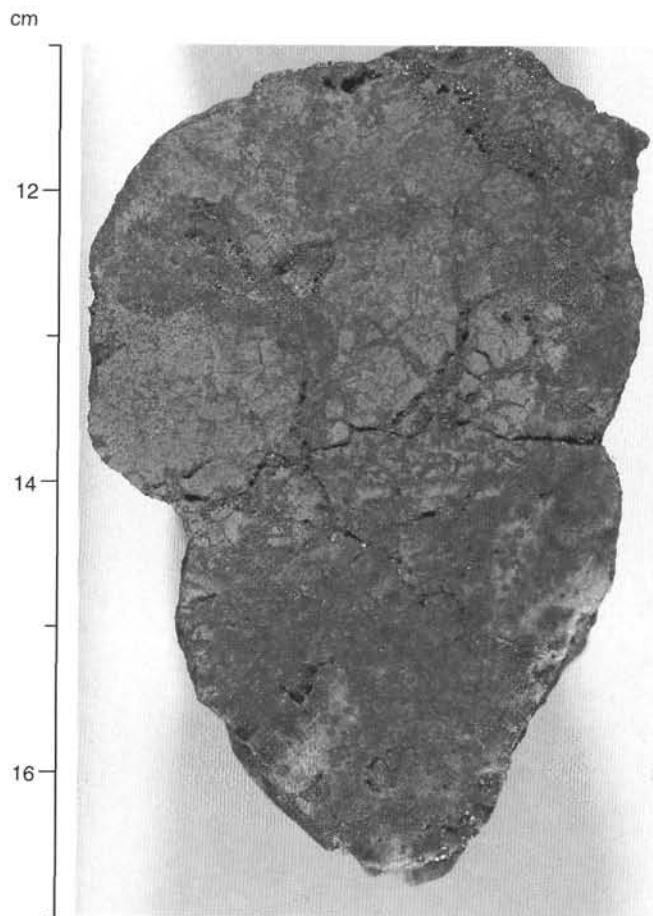


Figure 80. Silicified wallrock breccia. Gray clasts of silicified basalt (top) in a matrix of pyrite plus quartz (bottom). Smaller, millimeter-sized clasts can be visually fit back together in jigsaw puzzle fashion. Sample 158-957E-4R-1 (Piece 3, 11–17 cm).

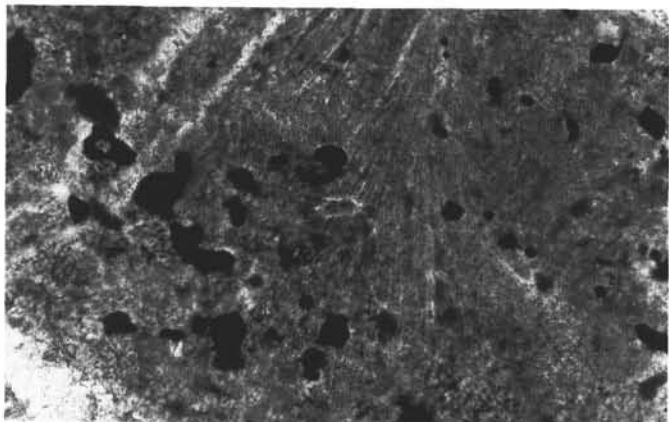


Figure 82. In this photomicrograph is a ghost of a skeletal olivine crystal (center, 50 μm in length) replaced by silica in a silicified subvariolic basalt clast. Notice disseminated pyrite scattered throughout the field of view, and quartz crystals lining the basalt clast margin (the lower left corner). Uncrossed polars, field of view = 750 μm . Sample 158-957C-16N-2 (Piece 3C, 34–36 cm).

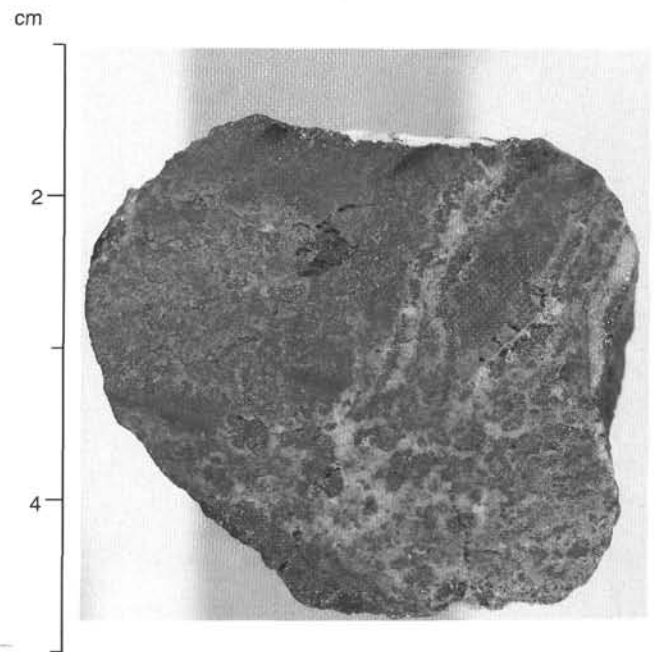


Figure 81. Intensively silicified wallrock breccia cut by numerous veins of white quartz plus pyrite. Outlines of small millimeter-sized clasts are rounded as the result of silicification, so that the clasts do not fit together in a jigsaw-puzzle fashion as in Figure 80. Sample 158-957E-11R-1 (Piece 1, 1–5 cm).

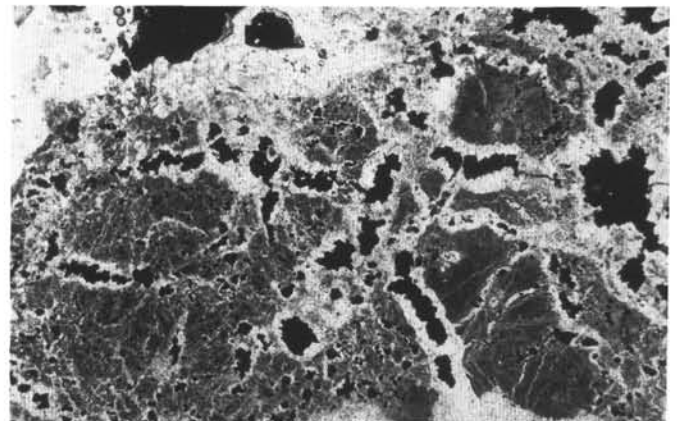


Figure 83. Photomicrograph of silicified basalt clast(s?) crisscrossed by thin quartz and pyrite veins, at selvages and centers, respectively. The subvariolic basalt texture can still be recognized in the inner parts of the clasts but it has been overprinted by silicification along the veins. Uncrossed polars, 6 mm field of view. Sample 158-957C-16N-2 (Piece 3C, 34–36 cm).

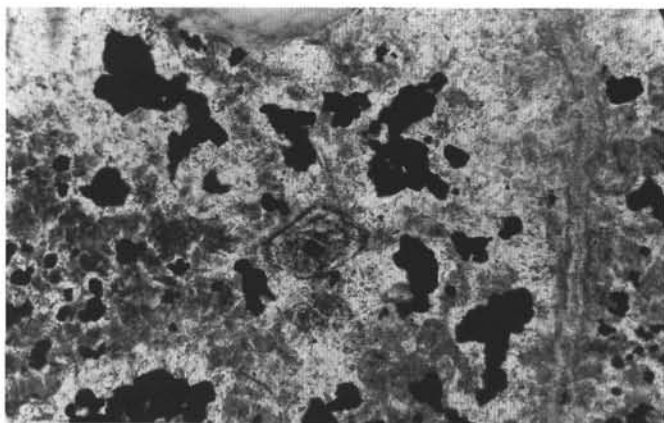


Figure 84. Photomicrograph showing that the original basaltic (subvolcanic?) texture is almost completely overprinted by silicification, exhibited by relatively coarse quartz plus disseminated pyrite. Quartz appears "dirty," as the result of abundant inclusions of fluids, clay, and rock remnants. A silicified olivine crystal (0.25 mm in length, center) is defined by outlines of iron oxyhydroxide. Uncrossed polars, field of view = 1.5 mm. Sample 158-957C-15N-2 (Piece 1B, 12–15 cm).

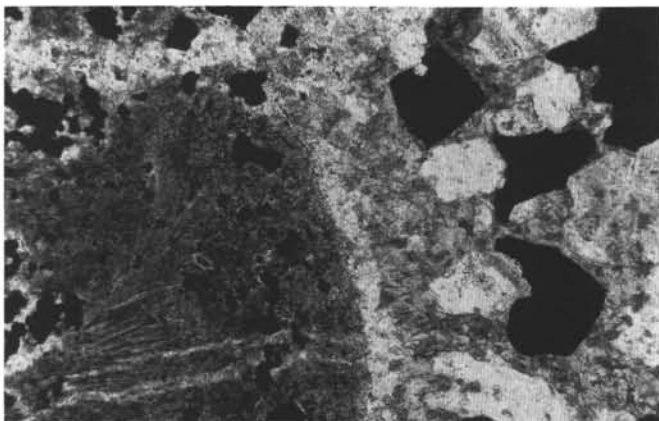


Figure 86. Photomicrograph of overgrowth rims on a silicified basalt clast. From left to right: disseminated pyrite in clast margin, a 50- to 75- μm -thick clear rim of coarse quartz (at center), a 50- to 100- μm -thick, gray rim of an unidentified clay mineral (illite?, smectite?, or talc?), and a discontinuous rim of anhedral, elongated quartz and pyrite, coarse crystals (up to 150 μm long). Uncrossed polars, field of view = 1.5 mm. Sample 158-957-C-16N-2 (Piece 3C, 34–36 cm).

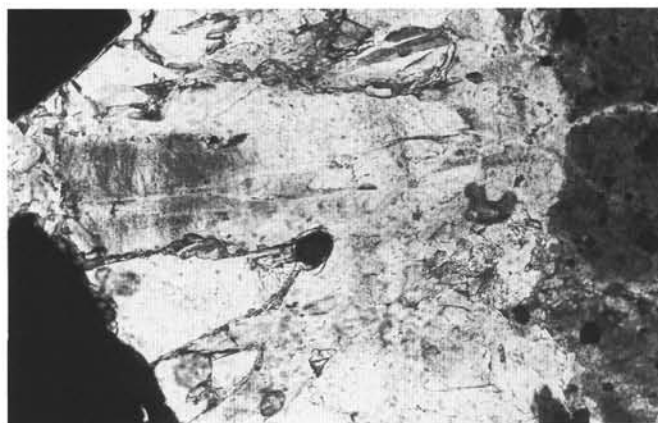


Figure 85. Photomicrograph of quartz crystals elongated perpendicular to rim of a basalt clast (right). Trails of oriented inclusions within the 500- to 600- μm -long quartz crystals may be relict basaltic texture in quartz vein replacing basalt. The quartz vein is followed outward, away from the clast, by a 800- μm -wide pyrite vein (left). Sample 158-957E-14R-1 (Piece 11, 52–55 cm).

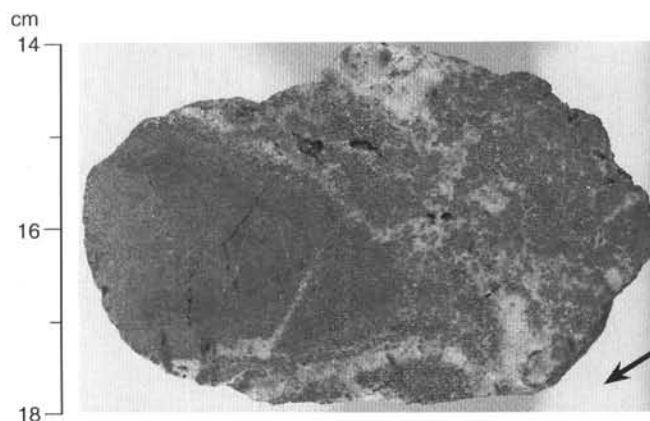


Figure 87. Gray chloritized basalt breccia with abundant white quartz plus pyrite veins. Sample 158-957E-15R-1 (Piece 4, 14–18 cm). A 1-mm-wide red Fe-oxide or oxyhydroxide band is seen within a 4-cm-sized, chloritized basalt clast (arrow).

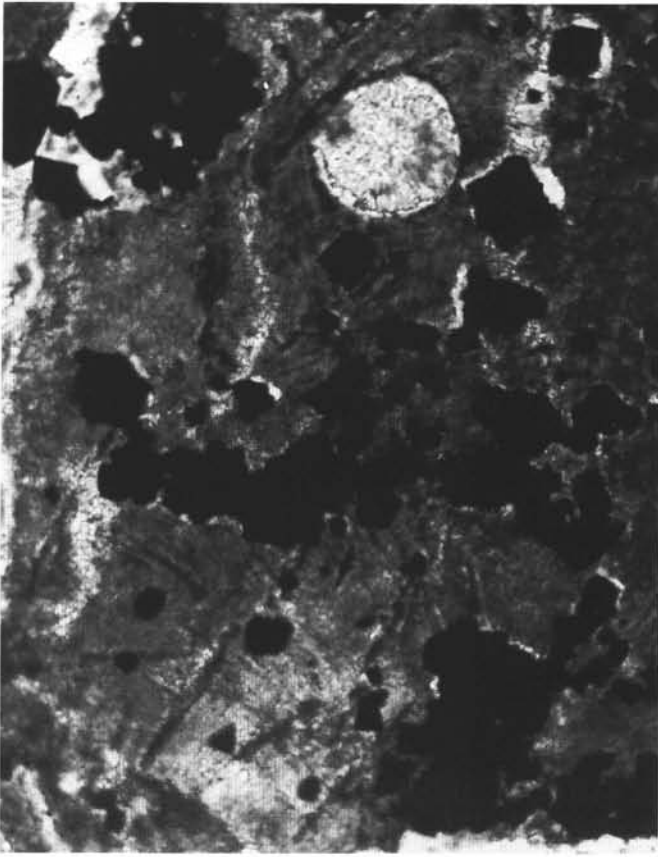


Figure 88. Photomicrograph of gray chloritized basalt clast with disseminated pyrite and a 150-µm-diameter vesicle lined by a 10-µm border of quartz and filled with an unidentified phyllosilicate mineral. Sample 158-957E-14R-1 (Piece 11, 52–55 cm).

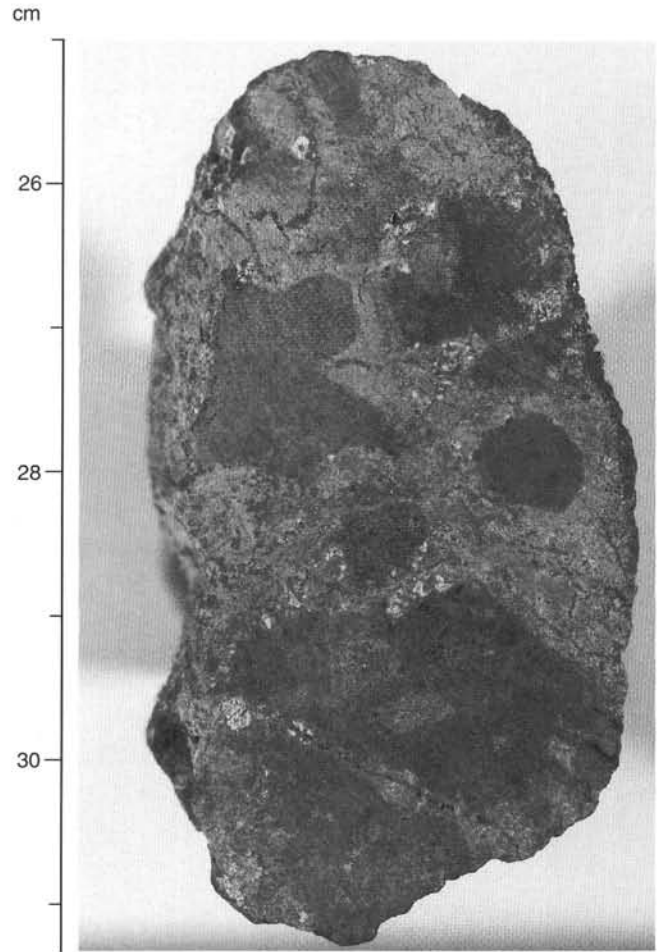


Figure 89. Green chloritized basalt breccia, with chloritized and silicified basalt glass fragments cemented by dark quartz (left side of sample), with kernels of green chloritized basalt surrounded by 1- to 5-mm-wide, gray, chloritized alteration halos. Sample 158-957E-18R-1 (Piece 5, 25–31.5 cm).

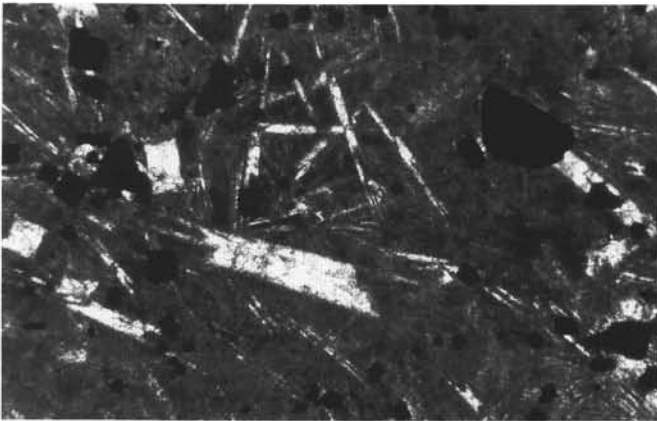


Figure 90. Photomicrograph of green chloritized basalt with intergranular texture. Plagioclase microlites are replaced by quartz and minor brown chlorite(?). Groundmass is replaced by brown chlorite(?) and disseminated pyrite. Field of view = 6 mm. Sample 158-957E-18R-1 (Piece 5, 25–27 cm).

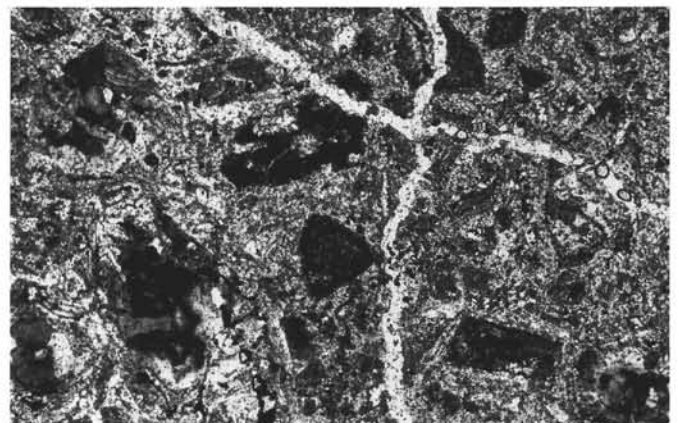


Figure 91. Photomicrograph of chloritized and silicified hyaloclastite. Angular glass shards are replaced by chlorite, pyrite, quartz, and an unidentified phyllosilicate, in a very fine-grained (<10 mm in diameter) quartz matrix. Two quartz veins crosscut both the clasts and the matrix. Field of view = 6 mm. Sample 158-957E-18R-1 (Piece 5, 25–27 cm).

Table 10. Semiquantitative determination of hydrothermal mineral samples by bulk powder X-ray diffraction analysis.

Core, section, interval (cm)	Piece no.	Lithology (from visual core description)	AA/TS	Py	Mc	Sp	Cp	Anhyd	Gyp	Qtz	Cris	Op-A	Hm	Goe	Chl	Comments
158-957A-																
3X-1, 42-46	9	Red chert	TS	*		?				***			*			Red cherty Fe-oxide
3X-1, 42-46	9	Red chert	TS	*						***			**			Brown chert
3X-1, 46-50	10	Gray silica (dark gray)	TS	***		??				*		**				
3X-1, 46-50	10	Gray silica (light gray)	TS	**		??				*	***					
158-957B-																
1R-1, 44-46	—	Fe-oxide cuttings		**		?	***			*	**					Fe-oxide, sulfide and silica
1R-1, 3-95	—	Drill cuttings (<63 µm)	AA	**		??	***			*	?					Fe-oxide and sulfide
1R-1, 3-95	—	Drill cuttings (63-420 µm)	AA	**		?	***			*	*					Fe-oxide and sulfide
1R-1, 3-95	—	Drill cuttings (>420 µm)	AA	***		??	***			*	**					Fe-oxide and sulfide
158-957C-																
5N-1, 15-48	3,5,6	Massive pyrite-anhydrite breccia	AA	***			**							?		Combined sample
7N-1, 52-56	6F	Nodular siliceous pyrite-anhydrite breccia	AA, TS	**			**	***								
7N-2, 63-69	1E	Nodular siliceous pyrite-anhydrite breccia	AA, TS	**			**	***		*						
7N-3, 7-10	2	Anhydrite vein		*			*	***								
7N-3, 67-69	5	Nodular pyrite-anhydrite breccia		**				***		**						
11N-1, 58-61	3D	Pyrite-silica-anhydrite breccia	AA	**			*	***		**						
11N-1, 130-135	3K	Anhydrite vein														Not determined
11N-2, 114-120	7	Anhydrite vein	TS					***								
11N-3, 24-34	4	Anhydrite vein						***								Soft; pink mineral in vein
11N-3, 24-34	4	Anhydrite vein						***								Hard, gray part of vein
11N-3, 70-75	7	Anhydrite vein						***								Pink mineral in vein
11N-3, 90-94	8C	Massive pyrite breccia with anhydrite vein	AA	***			**	**		**						
12N-1, 53-59	6	Massive pyrite-anhydrite breccia	AA	***			**	***		**						
12N-1, 99-124	9	Anhydrite vein		*				***								
12N-2, 9-18	2	Anhydrite vein		*				***								
12N-2, 68-75	9	Pyrite-silica-anhydrite breccia, veined	AA	***			**	**		*						
12N-2, 111-119	14	Anhydrite vein		*			*	***		**						Sulfide-rich part of vein
12N-2, 111-119	14	Anhydrite vein						***								White part of vein
12N-2, 129-137	16	Anhydrite vein						***								White part of vein
12N-2, 129-137	16	Anhydrite vein					*	***								Gray part of vein
12N-3, 32-46	4	Anhydrite vein					*	***								
12N-3, 86-100	9	Pyrite-silica-anhydrite breccia	AA	**			**	**		***						
13N-1, 12-20	4	Massive pyrite-anhydrite breccia	AA	***			**	***								
13N-2, 15-20	3A	Anhydrite vein						***								
14N-1, 33-41	5	Pyrite-silica breccia	AA	***			*	**		*						
14N-2, 47-53	2	Anhydrite vein		*			**	***								
14N-2, 76.5-87	6	Pyrite-silica breccia	AA	**			*	**		***						
15N-1, 36-40	5	Pyrite-silica breccia	AA	***			?	**		***						
15N-2, 12-15	1B	Silicified wallrock breccia	AA	**				***		***						
15N-2, 119-137	7	Anhydrite vein		*				***								
15N-3, 18-47	3	Anhydrite vein		?				***								
15N-3, 56-68	5	Anhydrite vein						***								
15N-3, 68-70	6	Silicified wallrock breccia		?										***		Mineral separate
15N-3, 89-117	9	Anhydrite vein		*				***								Soft; green mineral in vein
15N-3, 89-117	9	Anhydrite vein		?			?	***		?						Hard; green mineral in vein
15N-3, 132-150	11	Silicified wallrock breccia	AA	**			*	***		**						
15N-4, 0-19	1	Silicified wallrock breccia		*			*	***		?						
16N-1, 118-125	15	Pyrite-anhydrite breccia	AA	***			**	**		**						
16N-2, 14-23	2	Silicified wallrock breccia	AA	***			**	*		***						
158-957E-																
12R-1, 16-20	3	Silicified wallrock breccia	AA	***			**			?						
14R-1, 47-51	11	Chloritized basalt breccia	TS	**						***				?		Small unidentified peaks
158-957F-																
1N-1, 32-35	8	Nodular pyrite breccia	AA	**			***	*	**							
2N-1, 11-19	3	Massive granular pyrite	AA	***	?		**	**								
158-957G-																
3N-1, 75-76	6	Nodular siliceous pyrite-anhydrite breccia					*	***		?						

Table 10 (continued).

Core, section, interval (cm)	Piece no.	Lithology (from visual core description)	AA/TS	Py	Mc	Sp	Cp	Anhyd	Gyp	Qtz	Cris	Op-A	Hm	Goe	Chl	Comments
158-957H-																
1N-1, 60-73	13	Porous nodular pyrite breccia	AA, TS	*			**	***								
5N-1, 61-64	6	Nodular pyrite-silica breccia	AA	***				**		***						
6N-1, 14-19	3	Nodular pyrite-silica breccia	AA	**			**			***						
158-957I-																
1N-1, 33-41	6	Porous massive pyrite	AA	***	**	?										
158-957K-																
1X-1, 24-29	4	Porous massive pyrite	AA, TS	***	***	?										Small unidentified peaks
2N-1, 37-41	9	Massive granular pyrite	AA, TS	***	**	?	*									Small unidentified peaks
3X-1, 36-38	7	Massive pyrite	AA, TS	***	**	?										Small unidentified peaks
158-957M-																
1R-1, 16-47	1	Fe-oxides (<63 µm)	AA	?										***		Trace halite contamination
1R-1, 16-47	1	Fe-oxides (63-420 µm)	AA											***		Trace halite contamination
1R-1, 16-47	1	Fe-oxides (>420 µm)	AA											***		Trace halite contamination
3R-1, 57-60	14	Pyrite-silica breccia	AA	***	***	?				**						
3R-1, 123-125	28	Pyrite-silica breccia	AA	***	?		**			**						
5R-1, 90-92	15	Pyrite-silica breccia	AA	**			*			***						
8R-1, 0-4	1	Massive granular pyrite	AA	***			*			**						
158-957O-																
2R-1, 22-24	5	Nodular pyrite-anhydrite breccia	AA, TS	**			**	***								
4R-1, 45-50	9	Pyrite-anhydrite breccia	AA	***			**	**								
158-957P-																
12R-1, 0-123	—	Drill cuttings (<63 µm)	AA	**			***									Sulfide, Fe-oxide, anhydrite
12R-1, 0-123	—	Drill cuttings (63-420 µm)	AA	***			***	*		**						Sulfide, Fe-oxide, anhydrite
12R-1, 0-123	—	Drill cuttings (>420 µm)	AA	***			***	*		*						Sulfide, Fe-oxide, anhydrite
13W-2, 89-94	—	Drill cuttings	AA	***			**	?		?						Sulfide and black silica
158-957Q-																
1R-1, 95-100	—	Drill cuttings		***			**			**						Sulfide and red chert
1R-3, 70-75	—	Drill cuttings	AA	***			***			**						Sulfide and red chert
1R-4, 49-54	—	Drill cuttings		***			**			*						Sulfide and red chert

Notes: *** = abundant, ** = minor, * = trace, and ? = possible trace. Py = pyrite, Mc = marcasite, Sp = sphalerite, Cp = chalcopyrite, Anhyd = anhydrite, Gyp = gypsum, Qtz = quartz, Cris = cristobalite, Op-A = opal-A, Hm = hematite, Goe = goethite, Chl = chlorite. AA = XRD analysis of powder from shipboard AAS analysis; TS = thin section from piece. Sphalerite could only be determined indirectly by variation in peak intensities because of peak overlaps with pyrite.

Table 11. Index properties of samples recovered from Holes 957C, 957E, 957F, and 957G.

Core, section, interval (cm)	Depth (mbsf)	Bulk water content (%)	Bulk density [B] (g/cm ³)	Bulk density [C] (g/cm ³)	Grain density [B] (g/cm ³)	Grain density [C] (g/cm ³)	Porosity [B] (%)	Porosity [C] (%)	Rock type (F = fragment, M = minicore)
158-957C-									
5N-1, 25-27	15.25	4.41	3.93	3.76	4.52	4.28	16.91	16.17	Massive pyrite-anhydrite breccia (F)
7N-2, 66-68	21.51	2.00	3.91	3.74	4.15	3.95	7.63	7.29	Nodular siliceous pyrite-anhydrite breccia (M)
7N-3, 15-17	22.50	3.53	2.95	2.79	3.17	2.98	10.18	9.62	Anhydrite vein (M)
7N-3, 47-49	22.82	4.66	3.59	3.49	4.10	3.95	16.36	15.88	Nodular pyrite-anhydrite breccia (M)
11N-1, 21-23	30.91	1.71	3.37	3.28	3.51	3.41	5.62	5.46	Pyrite-silica breccia (M)
11N-1, 114-116	31.84	1.75	3.56	2.85	3.72	2.94	6.06	4.85	Anhydrite vein (M)
11N-2, 22-24	32.33	1.12	4.15	4.10	4.30	4.24	4.55	4.49	Pyrite-silica-anhydrite breccia (M)
11N-3, 118-120	34.79	1.17	3.53	3.42	3.63	3.52	4.02	3.90	Pyrite-silica breccia (M)
12N-2, 67-69	37.15	2.02	4.55	4.31	4.90	4.62	9.00	8.52	Pyrite-silica-anhydrite breccia (F)
14N-1, 18-20	40.38	0.97	3.72	3.76	3.82	3.86	3.53	3.56	Pyrite-silica breccia (M)
15N-1, 115-117	43.35	1.03	3.64	3.58	3.74	3.67	3.65	3.59	Silicified wallrock breccia (M)
16N-1, 8-10	46.28	0.74	3.37	3.30	3.43	3.35	2.42	2.37	Nodular pyrite-silica breccia (M)
16N-1, 120-122	47.40	1.44	4.50	4.26	4.73	4.47	6.34	6.01	Pyrite-anhydrite breccia (F)
16N-2, 7-9	47.69	0.81	4.03	3.90	4.13	3.99	3.17	3.07	Silicified wallrock breccia (M)
158-957E-									
1R-1, 7-9	31.57	2.83	4.29	4.12	4.72	4.52	11.82	11.36	Semi-massive pyrite-chalcopyrite (F)
2R-1, 1-3	37.01	2.33	3.39	3.19	3.59	3.36	7.72	7.27	Nodular pyrite-silica breccia (F)
3R-1, 6-8	41.76	1.87	3.51	3.38	3.68	3.53	6.40	6.16	Pyrite-silica breccia (F)
4R-1, 8-10	49.08	1.61	3.72	3.51	3.88	3.66	5.85	5.53	Silicified wallrock breccia (F)
5R-1, 4-6	58.64	1.66	3.43	3.33	3.57	3.46	5.54	5.38	Pyrite-silica breccia (F)
6R-1, 18-20	63.48	1.13	5.18	4.47	5.43	4.65	5.71	4.93	Massive granular pyrite (F)
7R-1, 19-21	68.49	1.78	3.61	3.25	3.79	3.39	6.29	5.66	Nodular pyrite-silica breccia (F)
11R-1, 42-44	87.52	1.66	3.89	3.48	4.08	3.62	6.29	5.62	Pyrite-silica breccia (F)
12R-1, 16-18	91.96	1.19	4.55	4.51	4.74	4.70	5.26	5.22	Silicified wallrock breccia (F)
14R-1, 47-49	101.97	1.45	3.65	3.39	3.79	3.51	5.17	4.80	Chloritized basalt breccia (F)
15R-1, 20-22	106.70	1.88	3.49	3.37	3.66	3.52	6.39	6.17	Chloritized basalt breccia (F)
18R-1, 26-28	120.96	2.66	3.54	3.28	3.80	3.49	9.21	8.53	Chloritized basalt breccia (F)
158-957F-									
1N-1, 19-21	1.19	8.44	3.89	3.48	5.25	4.47	32.09	28.69	Massive granular chalcopyrite (F)
1N-1, 62-64	1.62	2.66	3.71	3.57	4.00	3.83	9.65	9.28	Massive pyrite breccia (M)
2N-1, 10-12	5.60	4.10	3.69	3.46	4.15	3.85	14.76	13.85	Massive granular pyrite (F)
158-957G-									
3N-1, 15-17	21.15	3.11	4.09	3.95	4.52	4.35	12.42	12.01	Massive pyrite-anhydrite breccia (M)

Note: [B] and [C] refer to the method used to calculate bulk and grain density (see "Index Properties" section, "Explanatory Notes" chapter, this volume).

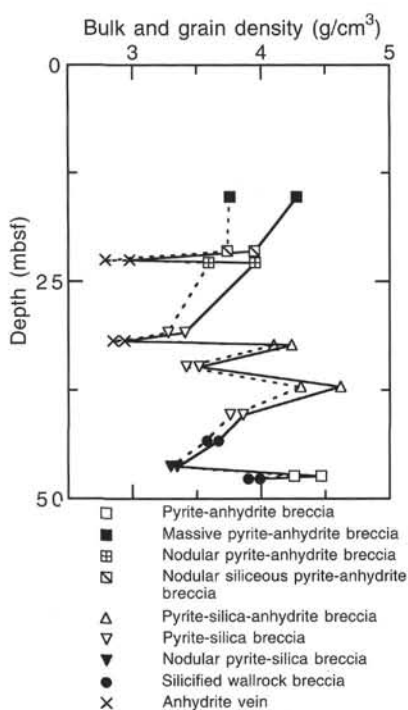


Figure 92. Bulk (dashed line) and grain (solid line) density values of samples (identified by rock type) vs. depth, Hole 957C.

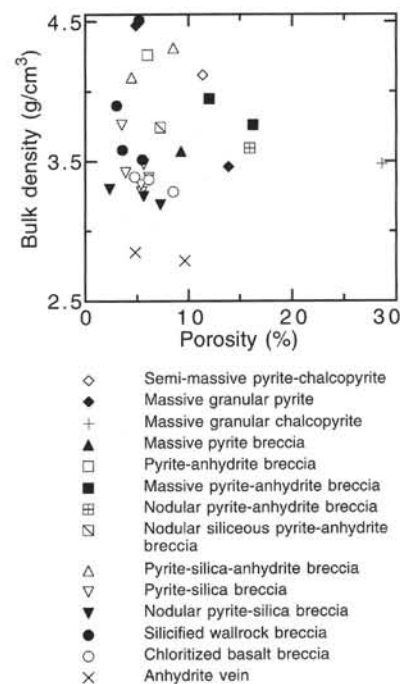


Figure 93. Bulk density vs. porosity of samples (identified by rock type) in the TAG-1 area (Holes 957C, 957E, 957F, and 957G).

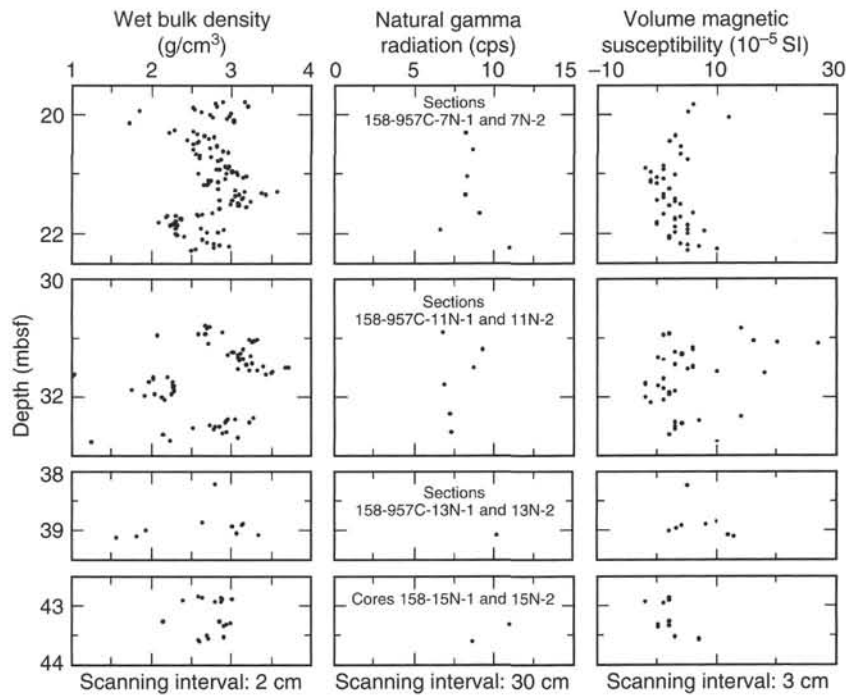


Figure 94. Results from multisensor track (MST) scans of intact sections of eight sections from Hole 957C. The measured physical properties are uncorrected wet bulk density obtained using the GRAPE instrument, natural gamma radiation, and volume magnetic susceptibility.

Table 12. Electrical resistance, *P*-wave velocity, and related properties measured in minicores recovered from Holes 957C, 957F, and 957G.

Core, section interval (cm)	Depth (mbsf)	Length (mm)	Diameter (mm)	Resistance (Ω)	Resistivity (Ωm)	Formation factor	<i>P</i> -wave velocity (km/s)	Rock type
158-957C-7N-3, 15-17	22.50	21.81	25.41	119	2.767	13.834	NM	Anhydrite vein
11N-2, 22-24	32.33	22.43	25.17	8	0.177	0.887	5.112	Pyrite-silica-anhydrite breccia
11N-3, 118-120	34.79	21.91	25.31	18	0.413	2.067	5.088	Pyrite-silica breccia
14N-1, 18-20	40.38	21.96	25.27	22	0.502	2.512	5.198	Pyrite-silica breccia
15N-1, 115-117	43.35	22.01	25.31	18	0.411	2.057	4.859	Silicified wallrock breccia
16N-1, 8-10	46.28	21.85	25.26	90	2.064	10.321	5.095	Nodular pyrite-silica breccia
16N-2, 7-9	47.69	20.88	25.28	40	0.962	4.808	5.661	Silicified wallrock breccia
158-957F-1N-1, 62-64	1.62	21.43	25.24	23	0.537	2.685	5.308	Massive pyrite breccia
158-957G-3N-1, 15-17	21.15	21.84	25.23	5	0.114	0.572	4.850	Massive pyrite-anhydrite breccia

Note: NM = not measurable.

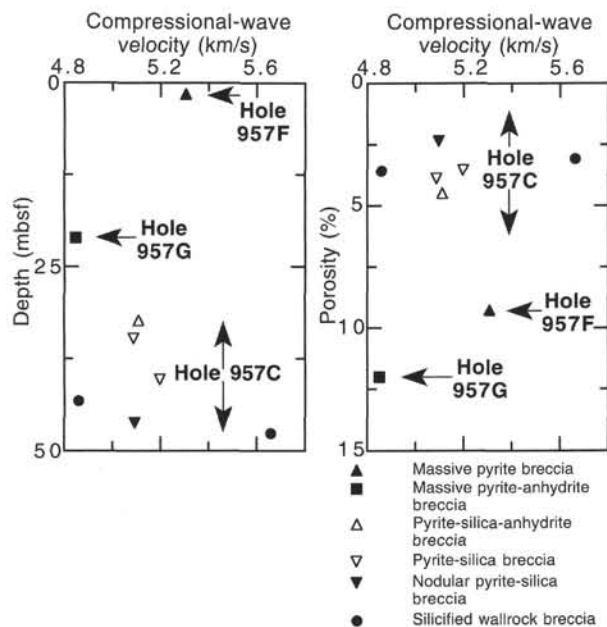


Figure 95. Compressional-wave velocity vs. depth and porosity measured from eight minicores extracted from cores of Holes 957C, 957F, and 957G.

Table 13. Thermal conductivity values measured in sulfide and sulfate samples from Holes 957C, 957F, and 957G.

Core, section, interval (cm)	Piece no.	Depth (mbsf)	Thermal conductivity (W/[m·K])	Error (W/[m·K])	Rock type
158-957C-					
7N-1, 58-68	6G	20.08	6.08	0.013	Nodular siliceous pyrite-anhydrite breccia
7N-2, 64-76	1E	21.49	8.73	0.012	Nodular siliceous pyrite-anhydrite breccia
7N-3, 10-25	3	22.45	5.37	0.012	Anhydrite vein
11N-1, 19-30	3A	30.89	8.30	0.010	Pyrite-silica breccia
11N-2, 28-36	1E	32.39	8.68	0.010	Pyrite-silica-anhydrite breccia
14N-1, 10-22	2	40.30	8.34	0.010	Pyrite-silica breccia
15N-1, 110-119	11F	43.30	8.65	0.010	Silicified wallrock breccia
16N-1, 14-22	3	46.34	5.73	0.013	Nodular pyrite-silica breccia
16N-2, 24-32	3A	47.86	8.40	0.012	Silicified wallrock breccia
158-957F-					
1N-1, 52-64	10B	1.52	6.10	0.012	Massive pyrite breccia
158-957G-					
3N-1, 6-20	2A	21.06	8.59	0.012	Massive pyrite-anhydrite breccia

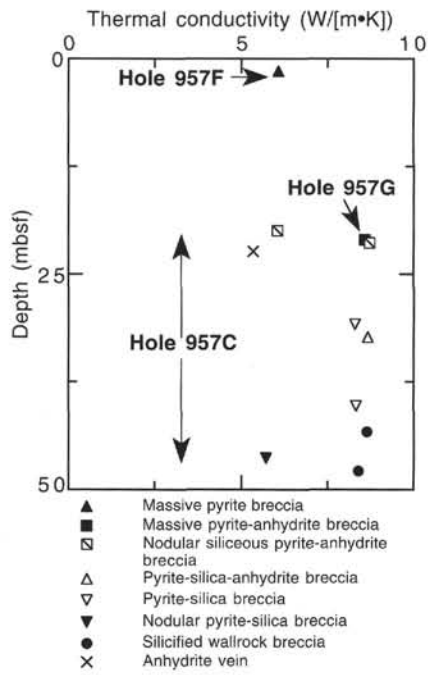


Figure 96. Thermal conductivity vs. depth based on measurement of 10 sulfide samples and one sulfate sample in cores from Holes 957C, 957F, and 957G.

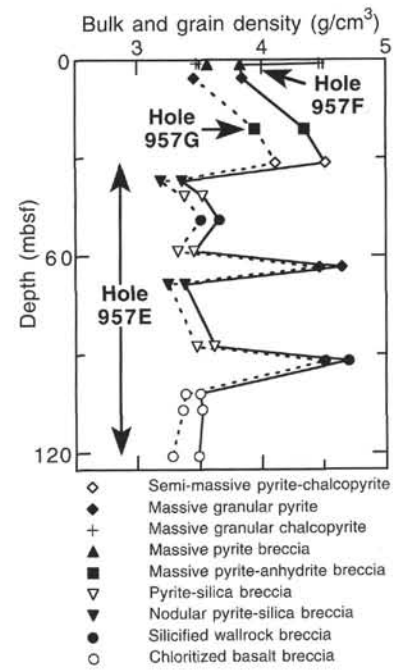


Figure 97. Bulk (dashed line) and grain (solid line) density values of samples (identified by rock type) vs. depth, Holes 957E, 957F, and 957G.

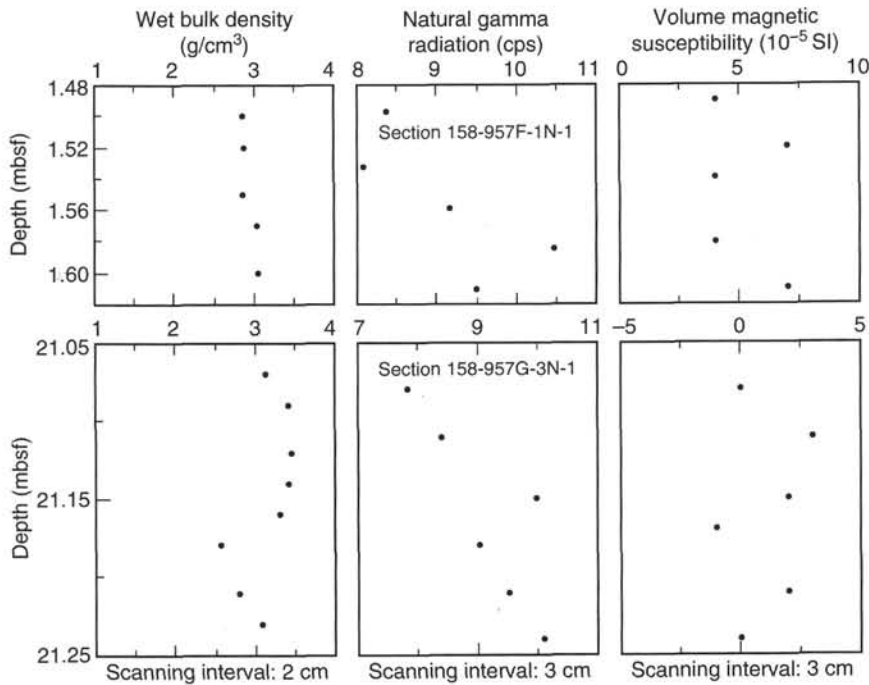


Figure 98. Results from multisensor track (MST) scans of two intact intervals (upper graphs, 158-957F-1N-1, 50–63 cm; lower graphs, 158-957G-3N-1, 7–26 cm). The measured physical properties are uncorrected wet bulk density obtained using the GRAPE instrument, natural gamma radiation, and volume magnetic susceptibility.

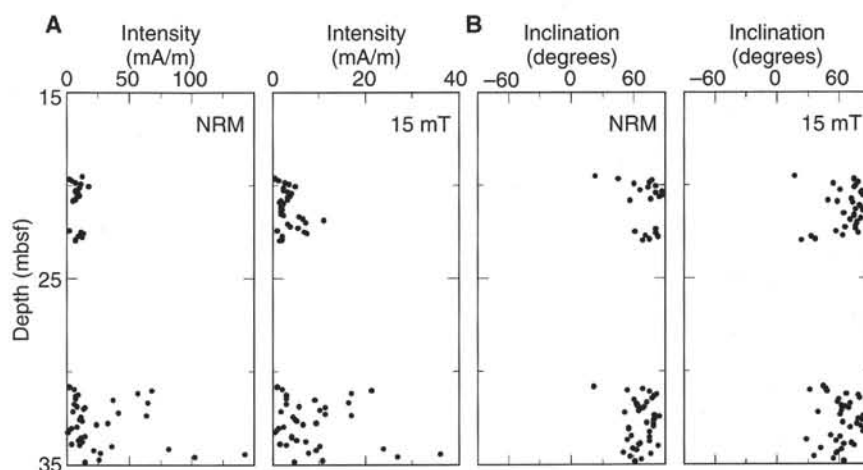


Figure 99. Downhole variation of (A) intensity and (B) inclination of NRM and magnetization after alternating-field (AF) demagnetization at 15 mT for Cores 158-957C-7N and 11N. The NRM inclinations are strongly biased toward high positive inclinations, suggesting that drilling-induced magnetization is present. AF demagnetization to 15 mT could not effectively remove this drilling-induced magnetization, as indicated by insignificant changes in inclination.

Sample 158-957C-7N-2, 66–68 cm Sample 158-957C-7N-3, 15–17 cm

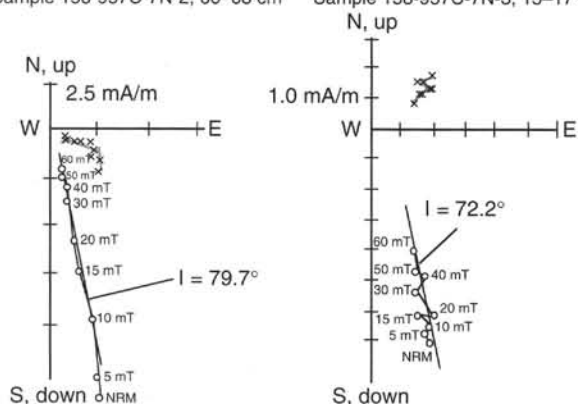


Figure 100. Representative vector endpoint diagram showing the results of alternating-field demagnetization for discrete samples from Core 158-957C-7N. The magnetic component is shown by a straight line fitting the data points, and the corresponding inclination (I) is indicated. Open circles and crosses represent vector endpoints projected onto the vertical and horizontal planes, respectively.

Sample 158-957C-11N-1, 114–116 cm Sample 158-957C-11N-1, 21–23 cm

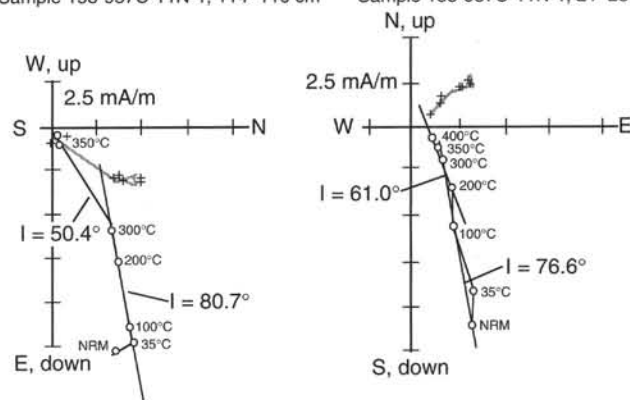


Figure 101. Representative vector endpoint diagram showing the results of thermal demagnetization of discrete samples from Core 158-957C-11N. Two components of magnetization are shown by straight lines fitting the data points. Open circles and crosses represent vector endpoints projected onto the vertical and horizontal planes, respectively.

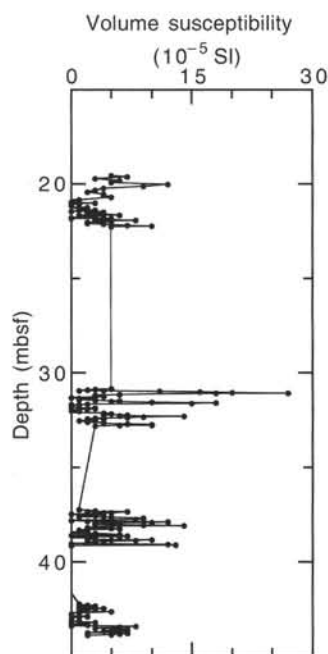


Figure 102. Magnetic susceptibility vs. depth, Hole 957C, showing that whole-core susceptibility measurements vary in a fashion similar to the NRM signals, with a mean value of about 4×10^{-5} SI units.

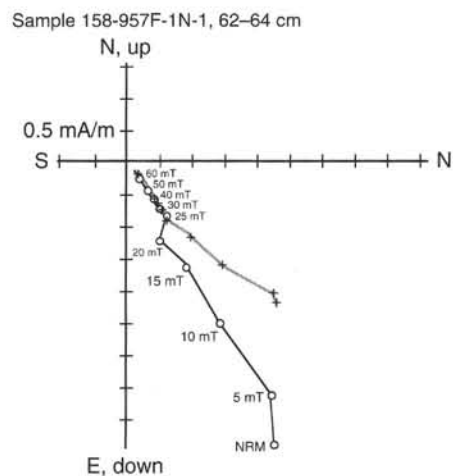


Figure 103. Vector endpoint diagram showing the results of AF demagnetization for a discrete sample from Core 158-957F-1N. Open circles and crosses represent vector endpoints projected onto the vertical and horizontal planes, respectively.

Table 14. Dissolved ion concentrations in water samples from Holes 957A and 957C.

Hole	Water depth (m)	pH	Alkalinity (mmol/L)	Salinity (‰)	K ⁺ (mmol/L)	Mg (mmol/L)	Ca ²⁺ (mmol/L)	Cl ⁻ (mmol/L)	SO ₄ ²⁻ (mmol/L)	PO ₄ (μmol/L)	NH ₃ (μmol/L)	SiO ₂ (μmol/L)
Hole 158-957A-Surface water WSTP-1	0.0	8.21	2.56	36.5	11.1	55.9	11.1	583	31.6	<0.1	3	<10
	3648.5	7.52	2.33	34.9	10.5	54.4	10.3	544	30.1	1	29	33
Hole 158-957C-WSTP-2	3648.0	7.7	2.49	35	10.7	54.5	10.2	543	28.1	1.7	31	57
	Depth (mbsf)	pH	Alkalinity (mmol/L)	Salinity (‰)	K ⁺ (mmol/L)	Mg (mmol/L)	Ca ²⁺ (mmol/L)	Cl ⁻ (mmol/L)	SO ₄ ²⁻ (mmol/L)	PO ₄ (μmol/L)	NH ₃ (μmol/L)	SiO ₂ (μmol/L)
Hole 158-957C-10N-1, 10-15 NASW NADW	28.65	8.02	2.53	38.5	11.4	58.4	17.7	587	42.5	<0.1	32	4
				36.5-37 (S)						<1(R)		<10(B)
				34.9 (S)						1-1.5(R)		20-40(B)

Notes: NASW = North Atlantic surface water, for comparison as typical values for waters in the vicinity of Site 957. NADW = North Atlantic deep water, for comparison as typical values for waters in the vicinity of Site 957. (S) = from Sverdrup et al. (1942), (R) = from Redfield et al. (1982), and (B) = from Broecker and Peng (1982).

Table 15. Dissolved Mg, Ca, and SO₄ in surface seawater reacted with rocks from Hole 957C and with drilling mud.

	Cl (mmol/L)	SO ₄ (mmol/L)	Mg (mmol/L)	Ca (mmol/L)	pH	Excess SO ₄ (mmol/L)	Excess Mg (mmol/L)	Excess Ca (mmol/L)
Surface water	583	31.6	55.9	11.1	8.21	0	0	0
10N-1, 10-15	587	42.5	58.4	17.7	8.02	10.9	2.5	6.6
12N-2, 111-119a	585	44.3	57.7	22.8	8.01	12.7	1.8	11.7
12N-2, 111-119b	585	31.8	59.4	11.6	8.03	0.2	3.5	0.5
Drilling mud	563	30.3	53.6	10.6	8.23	-1.3	-2.3	-0.5
Drilling mud*	585	31.5	55.7	11.0		-0.1	-0.2	-0.1
12N-2, 111-119a+		8.01	0.04	7.67	5.86	8.0	0.0	7.7
12N-2, 111-119b+		1.34	0.02	0.89	5.58	1.3	0.0	0.9

Notes: Excess values reported are ion concentrations after surface seawater has been subtracted. Asterisk (*) = corrected for dilution by fresh water; plus sign (+) = reacted with nanopure water.